THE UNIVERSITY *of* EDINBURGH

Neutron-Diffraction of Hydrogen-rich Molecules under High Pressure

Bernhard Massani

Doctor of Philosophy
The University of Edinburgh
July 27, 2022

Abstract

A proton and an electron form the lightest element of the periodic table: Hydrogen. Despite the simplicity of this element and an ongoing research interest, surprisingly little is known about its solid phases and structures of hydrogen-rich compounds such as water, ammonia or methane. In the particular, high pressure phases of these compounds are poorly understood.

The reason for this is of a two-fold nature; first and foremost, small, hydrogen-rich molecules have very complex phase diagrams - partially due to the quantum nature of hydrogen - and form a vast variety of crystal structures. And secondly, the only direct way of measuring the hydrogen positions in these crystal structures is neutron-diffraction. While very powerful in structure determination, this technique requires large sample volumes and, hence, the pressure range has been limited to below 40 GPa; until recently, neutron diffraction had to rely on large-volume pressure cell such as the *Paris-Edinburgh-Press*.

The overall aim of this body of work was to overcome current pressure-limitations and the concomitant limitations in data quality using single-crystals in diamond anvil cells for neutron diffraction. This attempt has been successful and the data-reduction and correction procedure reported in this work are now being used at the Snap beamline at Sns (Oak Ridge National Laboratory).

The original aim for the second half of this thesis was to use single-crystal neutron-diffraction to measure single-crystals of hydrogen (deuterium) and water. Due to the ongoing pandemic caused by Covid-19 and the restrictions to travel to Sns, this was not possible. Hence, the second half of this works tries to fill gaps in the knowledge of the high-pressure behaviour of water-gas compounds using existing techniques. In particular, studies on the water-nitrogen, water-ammonia and the water-ammonia-methane systems will be presented here.

Lay summary

Hydrogen is by far the most common element in the observable universe, followed by helium and oxygen. Although, most of the hydrogen is in its atomic form, molecular hydrogen H_2 as well as is found in vast quantities in our Solar system - in gas planets and as well as in moons. Under less extreme conditions, hydrogen and oxygen form liquid water, H_2O, which is the prerequisite for life. Crystalline water can be found - in both its pure form and mixed with other elements in gas hydrates - on Earth, on icy moons, and in cosmic dust.
With this abundance it is not surprising that many studies have been conducted to study both hydrogen and water in much detail in every possible state. However, the high-pressure crystal structures of many of these important simple molecular systems are surprisingly poorly understood. For example not even the H-H bond-length in solid hydrogen has been measured at any elevated pressure. Similarly, the high-pressure structures of many hydrogen-bonded systems are still badly characterised (see for example Guthrie *et al.* 2019).

The only direct way of measuring the hydrogen positions in crystal structures, neutron-diffraction, requires large sample volumes and, hence, limited the accessible pressure range to below 40 GPa: until recently, neutron diffraction had to rely on large-volume pressure cells such as the *Paris-Edinburgh-Press*. Smaller sample sizes and therefore the use of diamond anvil cells (DAC) remained unsuitable. Only with recent developments in diamond synthesis and the advent of bright neutron sources (e.g. SNS at ORNL, ESS) experiments at higher pressures became achievable but remain on the edge of the possible due to limitations in data quality.

The first half of this work focuses on overcoming these limitations in data quality for high-pressure neutron diffraction using crystals in a diamond anvil cell. To that end, diffraction patterns of crystals of deuterated potassium dihydrogen

phosphate (DKDP) were recorded. The same crystals were then measured in the complex sample environment of a DAC. Based on this experimental data, a data-reduction and correction procedure for single-crystal neutron-diffraction (SCND) in DACs at the SNAP beamline at SNS (ORNL) was developed. This part also sheds light on possible improvements of this technique in the future.

The original aim of this thesis was to use the obtained insights and procedures to measure the crystal structure of solid deuterium in the pressure range up to 50 GPa. However, due to the outbreak of a global pandemic in 2020, no such experiments were possible; only some preliminary results of a hydrogen single-crystal (collected in December 2019) are presented in chapter 4.

The second half of this work hence focuses on different types of gas hydrates under pressure using existing pressure methods (gas-cell and *Paris-Edinburgh Press*); data for these chapters were all collected before the COVID-19 pandemic. Chapter 8 shows the possibility to reversibly fill the channels of ice XVII with nitrogen to form an sX type hydrate. Furthermore, the surprisingly complex dissociation of nitrogen sX is presented - when heated under pressure, this hydrate undergoes various phase transitions before finally reaching the cubic hydrate stable at ambient temperature.

Chapters 6 and 7 present data on ammonia monohydrate IV. This hydrate has been known for over two decades but so far no crystal structure has been established. Here an attempt is made to find a structure using experimental neutron data and calculations based on density-functional theory. Furthermore, the behaviour of a ternary system of ammonia, methane and water is investigated.

Finally, the last chapter of this work shows a study aiming at the formation of carbonic acid from CO_2 hydrate. The corresponding neutron experiments in a PE-press were not successful since the acid reacted with the sample container; follow-up experiments were once again not possible due to the Covid crisis.

Declaration

I declare that this thesis was composed by myself, that the work contained herein is my own except where explicitly stated otherwise in the text, and that this work has not been submitted for any other degree or professional qualification except as specified.

Parts of this work have been published in J. Chemical Physics [1], in High Pressure Research [2], and in Crystals [3].

(*Bernhard Massani, July 27, 2022*)

To my parents,
Diethard and Ingrid.

For their advice, love, patience and faith.

Acknowledgements

Confitebor tibi, Domine, in toto corde meo;
narrabo omnia mirabilia tua.
Laetabor et exsultabo in te;
psallam nomini tuo, Altissime.
- Psalms 9,2

With the submission of this thesis my time as a student comes to an end and hence I would like give thanks and be grateful to a lot of people who have been there for me this whole time. First and foremost I would like to thank my supervisors Dr John Loveday and Dr Malcolm Guthrie; you taught me more than I could have ever imagined and it was a pleasure to work with you.

Furthermore, I would like to thank my parents, Diethard and Ingrid, who have supported me financially as well as morally throughout my time at university and all my degrees. I would not be able to submit this thesis without their help - be it material or immaterial help. I would also like to thank my sister Christine and my grandparents who were there for me this whole time.

Finally I would like to thank my friends, old and new, who were such a great support. Here I could write a whole litany of names but I will only name a few in person: Fr Emerson and Fr Busse for their prayers, Daniel, Max, and Kenneth for their rants, and Mops for deep conversations. But in particular I would like to mention my colleagues Liam, Hannah, Michael, Sarah, Christian, Orianna, and Caluma. Not everyone can claim that their co-workers are also their friends but I am glad that you are. You were there to discuss science and helped out when I needed you. The first words I heard in CSEC were *"Welcolm to high-pressure - where nothing works and everything sucks!"* and the depressing days when nothing worked, did suck a whole lot less with you around!

Thank you all!

Contents

List of Figures

List of Tables

Chapter 1

Where is the Hydrogen?

Hydrogen is by far the most common element in the observable universe, followed by helium and oxygen [74]. Although, most of the hydrogen is in its atomic form, molecular hydrogen H_2 is found in gas planets and as well as in moons [75]. On Earth, hydrogen and oxygen form liquid water, H_2O, which is the prerequisite for life [76]. Crystalline water can be found - in both its pure form and mixed with other elements in gas hydrates - on Earth, on icy moons and in cosmic dust [77]. With this abundance it is not surprising that many studies have been carried out to study both hydrogen and water in much detail in every possible state. Discussing the shear abundance of studies - from low pressure studies at just a few mili-bar and milli-Kelvin to shock-wave experiments at thousands of Giga-Pascal and Kelvin - would go way beyond the scope of this work. In this body of work I would like to focus on the solid region(s) in the P/T-diagram of these hydrogen-rich materials - particularly their crystal structures under pressure.

Surprisingly, the crystal structures of many of these important simple, molecular systems are poorly understood. For example, not even the H-H bond length in solid hydrogen has been measured at any elevated pressure and the space groups of the high-pressure phases remain unknown [78]. Similarly, water and its binary and ternary mixtures exhibit a wealth of phases and phenomena such as H-bond centring and superionicity [79, 80] which are poorly characterised from a structural point of view.
Accurate structural information on these systems is vital for a wide range of scientific problems. For example, the outer Solar System is dominated by hydrogen and hydrogen-rich materials and knowledge of their high pressure

properties is vital for developing models of phenomena like the existence and strength of magnetic dynamos, the internal structure of gas-giants and moons, and even to the evolution and composition of atmospheres [61, 81–86]. The long-standing problem of metallic hydrogen is the paradigmatic model for the behaviour of solids when quantum effects become significant [87–90], and the behaviour of protons in H-bonded systems like ice are proxies for more complex biological systems [76]. Finally, the recent discovery of high temperature superconductivity in hydrogen-rich systems like hydrogen sulphide [91–93] and lanthanum super-hydride [94, 95] provides further need for accurate structural information at high pressure - particularly with the discovery of the first room temperature superconductor [96]. The superconductivity is believed to be driven by the high polarisability of the hydrogen atoms which leads to strong electron-phonon coupling to phonons with high frequencies [91, 92, 97, 98]. However, to date no full structure (including hydrogen positions) of a hydrogen-rich high-temperature superconductor has been determined experimentally.

The main reason for the gap in our understanding of the crystal structure of hydrogen-rich systems is the inability to resolve the exact position of hydrogen with synchrotron X-ray measurements (see chapter 2). Neutron diffraction is the only reliable method to determine the proton (or deuteron) positions in a crystal structure. Such measurements were the first to verify the model of hydrogen bonds proposed by Pauling in 1935 [99] and to reveal the familiar bent shape of the water molecule in ice I_h in 1949 [100]. However, until the advent of bright spallation sources, the measurement of neutron powder patterns of sufficient quality for structural refinement has been limited in pressure due to the large sample volumes required for neutron diffraction (see chapters 3 and 4).

In the following introduction, I would like to shed light on the phase diagrams of hydrogen and water, and to give an overview of the structural zoo of water's binary mixtures.

1.1 Solid Hydrogen - Simple but Still a Mystery

The quantum-mechanical effect of exchange interaction forms one of the strongest bonds known: the H-H bond. In this molecular configuration, hydrogen atoms are separated by approximately 0.74 Å and show a bond-dissociation energy of approximately 4.52 eV ([69, 101]) at ambient conditions. In table 1.1 the bond dissociation energies and bond lengths of several strong bonds are compared.
To break the bond in molecular hydrogen extreme conditions are needed - at 3000 K only about 10% of the hydrogen is dissociated [102]. Pressure was subsequently proposed as another mechanism to break the hydrogen bond; more than 80 years ago, E. Wigner and H.B. Huntington predicted that, under pressure, the H-H bond would break and a new, atomic, metallic solid state of hydrogen would form [103]. It was theorised that the bonds would break at 25 GPa - an assumption that has been proven wrong. Several phases above this pressure have been discovered since (see phase diagram of hydrogen in figure 1.1).

Table 1.1 *Bond length and dissociation energies of selected specimens at ambient conditions [69]. The values for the C-C bond corresponds to the diamond configuration of carbon.*

Type	Bond length / Å	ΔH/bond / eV
H-H	0.74	4.52
C-C	1.54	3.69
N≡N	1.10	9.79
O=O	0.74	1.21

In 1968, Neil Ashcroft *et al.* suggested that metallic hydrogen might be a superconductor, up to room temperature [104]. Several years later, Egon Babaev *et al.* predicted that the the liquid, metallic state of H_2 (and D_2), would also be a superfluid, making hydrogen the first superconducting superfluid [105]. This alone makes hydrogen a unique and interesting subject to study.

Phase I hydrogen is a quantum crystal consisting of rotating hydrogen molecules in a hexagonal close packed (hcp) lattice (see structure in the inset of figure 1.1). It spans a large P-T range and remains an insulator in this phase [8].
Phase I melts, depending on the pressure, between 13.99 K (ambient pressure) and about 900 K, where the melting curve reaches its maximum at about 80 GPa [21, 106, 107].

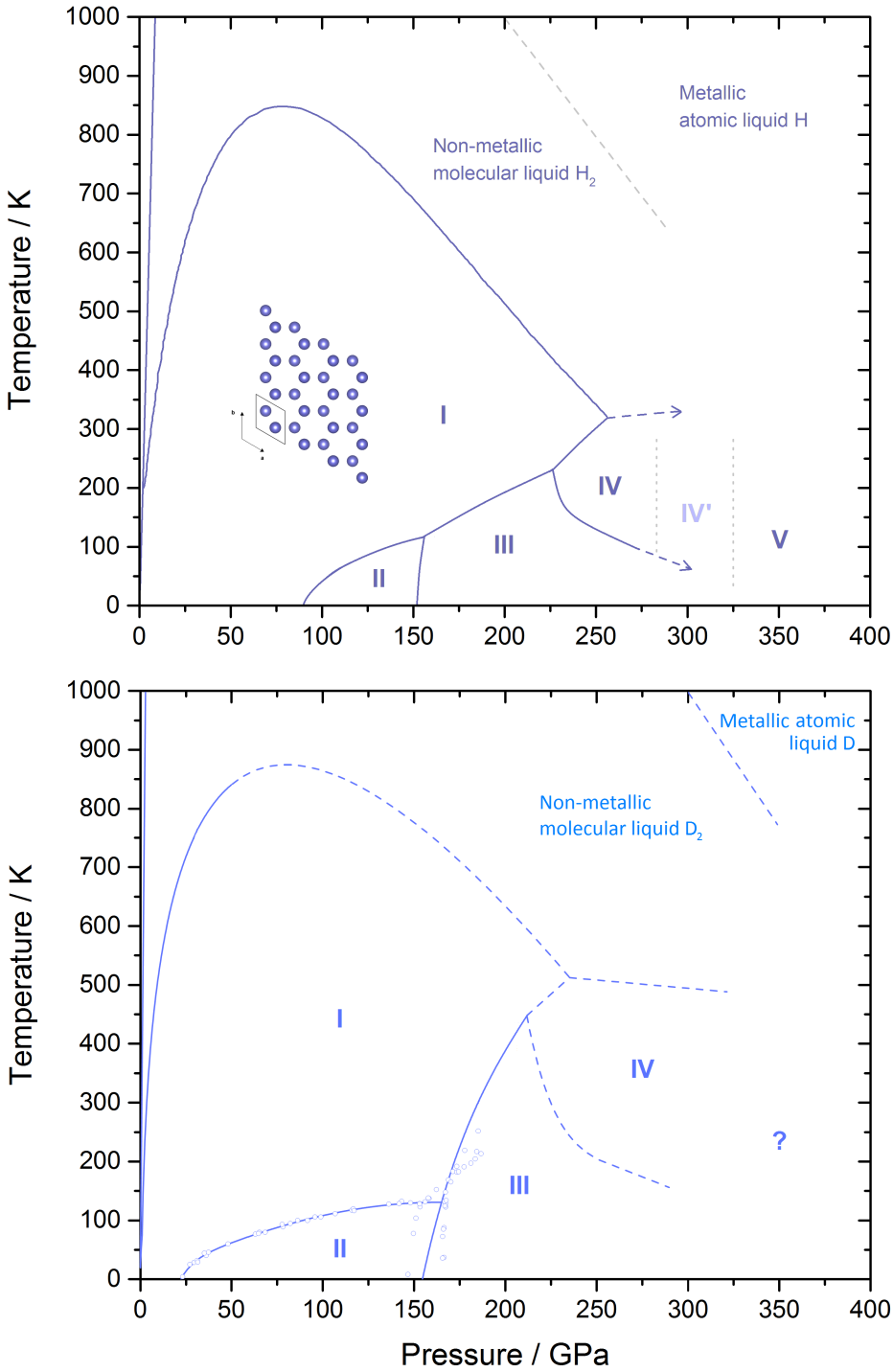

Figure 1.1 *The phase diagram of hydrogen (top) and deuterium (bottom). The solid lines are best fit curves with the form* $T(P) = a + b \cdot P + c \cdot \ln(P) + d/P + e \cdot \sqrt{P}$. *Open symbols indicate measured transition lines. The broke lines indicate assumed - but not yet measured - phase lines. Data were taken from the following sources: L-I: [4–6]; I-II: [7–9]; I-III: [6, 8, 9]; I-IV: [6]; II-III: [8, 9]; III-IV: [6] .*

Between about 30 and 150 GPa, dependent on the temperature [7, 8, 108, 109], the transition to phase II leads to discontinuous changes in the vibron spectra and changes in low-frequency excitations. These transitions arise from lowering of crystallographic symmetry (broken symmetry phase, BSP) by orientational ordering of the molecules. Goncharov *et al.* determined the I-II-III triple at 155 GPa and 125 K (shifted to 167 GPa and 142 K for D_2) [109].
Please note that, compared to hydrogen, deuterium's phase II cuts in at a much lower pressure - most likely due to the doubling of the mass of the free rotor [90]. This is a fortunate coincidence for neutron-diffraction studies of the BSP in deuterium as it significantly reduces the required pressure - usually the limiting variable for neutron-diffraction - to observe this transition.

While phase I (and to a much lesser extent II) of hydrogen have been investigated by X-ray and neutron diffraction [110–112], the exact structure of the phases at higher pressure have not been determined since this pressure regime is (yet) not experimentally accessible for neutron-sized samples. However, from Raman data Howie *et al.* were able to determine the transition lines of the phases I, III, and IV, with a triple point at roughly 225 GPa and 360 K [107, 113, 114]. Based on the calculated structures and from the shape of the transition line, it can be assumed that phase III is more ordered than both phases I and IV.

A comparison of computationally simulated structures for phases III and IV [10, 11] and the combined experimentally collected data from IR, Raman and X-ray experiments fortify this interpretation: Phase III has most likely a fixed, hexagonal structure, while Phase IV consists of hexagonal, graphene-like, sheet structure of hydrogen with intercalated molecular hydrogen between the layers. The modelled structures are depicted in figure 1.2.

Probably the most interesting transformation is the IV-IV'-V transition first reported by Dalladay-Simpson *et al.* in 2016 [6]. Although there is no distinct transition line between the phases, a remarkable Raman shift at pressures above 275 GPa can be observed [107]. Furthermore, the material properties seem to change from an insulator (in phase IV) to a semiconductor (in phase IV') due to a narrowing of the band gap. It is perceived that the H-H bonds in the graphene-like layers of molecular hydrogen in phase IV start to dissociate and form a partially atomic network resulting in conducting layers of hydrogen in

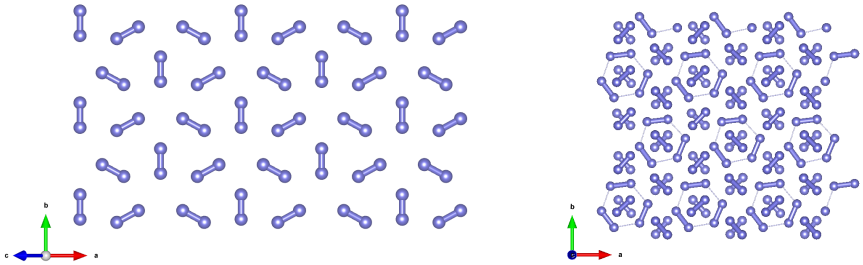

Figure 1.2 *Left: Structure of phase III [10]. Right: Structure of phase IV [11]. The structures were visualised with the VESTA software package.*

phase V. This, together with the increase of reflectivity of the hydrogen, indicates a closing of the band gap and makes phase V probably the first confirmed phase of (partially) metallic hydrogen. However, the presence of a second vibrational mode in the Raman spectrum of phase V even above 380 GPa rules out a completely dissociated hydrogen in phase V.

Another theory of the IV-IV'-V transition arose shortly after the publishing of Dalladay-Simpson's work. It is assumed that this phase transition is nothing but the transformation of phase IV into phase V, with phase IV' being a mixed phase of both phase IV and V.

Shortly after Dalladay-Simpson's publication, Eremets *et al.* published a study of hydrogen at even higher pressures of about 360 GPa and at temperatures <200 K [115]. Hydrogen at these conditions shows featureless Raman spectra, a strong drop in resistance, and absence of a photoconductive response, indicating a phase VI at this pressure and temperature [115]. This would mean an onset for the IV-V transition in H_2 at about 275 GPa (and at about 310 GPa for D_2).

Since than, several other papers have been published, claiming to have reached pressures up to 495 GPa, and showing evidence of an atomic metallic, phase of hydrogen (MH) [116, 117]. However, the setup used to do so was designed to produce pressures up to 500 GPa rather than measuring the sample at these conditions: Neither Raman scattering nor X-ray diffraction can be used at these conditions without damaging the DAC. The claim to have produced metallic hydrogen only rests on IR measurements of the reflectance of this sample. There are several arguments that the gasket rather than the sample has been measured in these studies.

1.2 Water and Gas Hydrates: Model Systems for Hydogen-bonds

Water, due to its abundance and simple geometry, is a very good candidate to study intermolecular interactions such as hydrogen bonds (H-bonds), Van-der-Waals interactions, and hydrophobic interactions. From a purely physical point of view, the hydrogen bond O-H$\cdots$O can be considered a "particle in a box", that is a simple wavefunction in a potential well. It is hence one of the only systems in which principles of quantum mechanics can be observed directly. However, the H-bond and the other interactions mentioned above are relevant to a multitude of other subjects; a chemist is interested in the properties of water as a solvent, that is its interaction with other molecules, and its reactivity [69, 118]; a biologist might be interested how water interacts with the DNA, its influence on protein-folding and - on a more fundamental level - how H-bonds in DNA and proteins behave [76]; for the astronomer water is relevant to model the evolution of planets and moons and the geologist finds high-pressure phases of water as minerals on Earth. This abundance of subjects relying on an accurate description of the small, covalently-bonded hydrogen-oxygen compound and makes water probably the most studied molecule on Earth.

1.2.1 The Phase Diagram of Pure Water

The *Encyclopædia Britannica* writes the following words about water: "Water, a substance composed of the chemical elements hydrogen and oxygen and existing in gaseous, liquid, and solid states. It is one of the most plentiful and essential of compounds. A tasteless and odourless liquid at room temperature, it has the important ability to dissolve many other substances. Indeed, the versatility of water as a solvent is essential to living organisms. Life is believed to have originated in the aqueous solutions of the world's oceans, and living organisms depend on aqueous solutions, such as blood and digestive juices, for biological processes [...] Although the molecules of water are simple in structure (H_2O), the physical and chemical properties of the compound are extraordinarily complicated, and they are not typical of most substances found on Earth." [119] This alone is reason enough to study water, its physical and chemical properties, and of course its interaction with other substances.

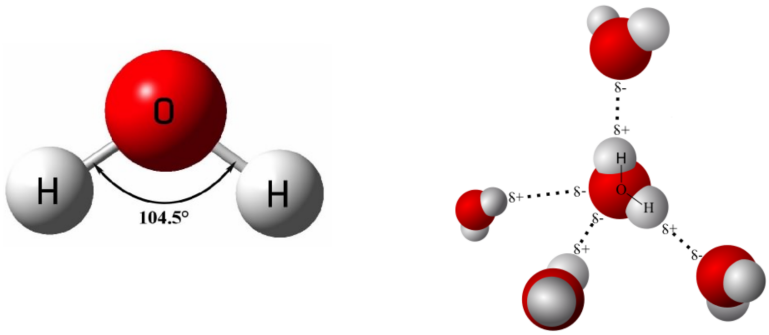

Figure 1.3 *Left: Structure of a single H_2O molecule as used in the TIPS-water model. Right: Scheme of the interaction in liquid water. The four hydrogen bonds formed between H and O are clearly visible. Structure according to Wallrafen 1964 [12].*

Water's chemical formula is H_2O: one molecule of water has two hydrogen atoms covalently bonded to a single oxygen atom. On Earth it appears in all three common states of matter. In the liquid and gaseouse state, the H-O-H angle is 104.5^o, and the distance between H and O is approximately 0.957 Å [120]. Since the water molecule is not linear and the electronegativity of oxygen (3.44 according to Pauling) is higher than that of hydrogen (2.20 according to Pauling) water is a polar molecule with an electrical dipole moment [121]; the oxygen atom carries a partial negative charge, whereas the hydrogen atoms carry a partial positive charge [122].

Water forms four hydrogen bonds which is an unusually large number for such a small molecule. These two factors give rise to the strong intermolecular interaction between water molecules, and between water molecules and other polar agents such as salts, sugars, acids, bases, and some gases. The consequences of the strong interaction can be observed in many macroscopic phenomena such as the high surface tension or the capillary effect of water. Also the strong interaction results in the high specific heat capacity of liquid water 4185.5 J/(kg·K) (per definition 1 cal/(g·K) at 15 ℃ and 101.325 kPa) as well as a high heat of vaporization of 2257 kJ/kg [123, 124]. These values are used as a reference for all other substances.

It is commonly known that water at ambient pressure freezes per definition at 0 ℃ and boils at 100 ℃ . These two points are the reference for the Celsius-

temperature scale. However there are more phases of water known than ice, water and vapour. In total the phase diagram of water contains 11 different stable crystalline ice phases (I_h, II, III, V, VI, VII, VIII, X, XI, XV, XIX). In addition, three amorphous phases (LDA, HDA, VHDA), and 8 metastable ones (I_c, IV, IX, XII, XIII, XIV, XVI, XVII) are known [125]. Furthermore, many other structures of ice are possible, if guest molecules are present [77]. Most of Earth's water is in the liquid state. The most abundant among the crystalline phases is hexagonal ice I_h which is the thermodynamically stable ice if water is cooled below 0 °C at ambient pressure. In figure 1.4 the stable crystalline phases are shown.

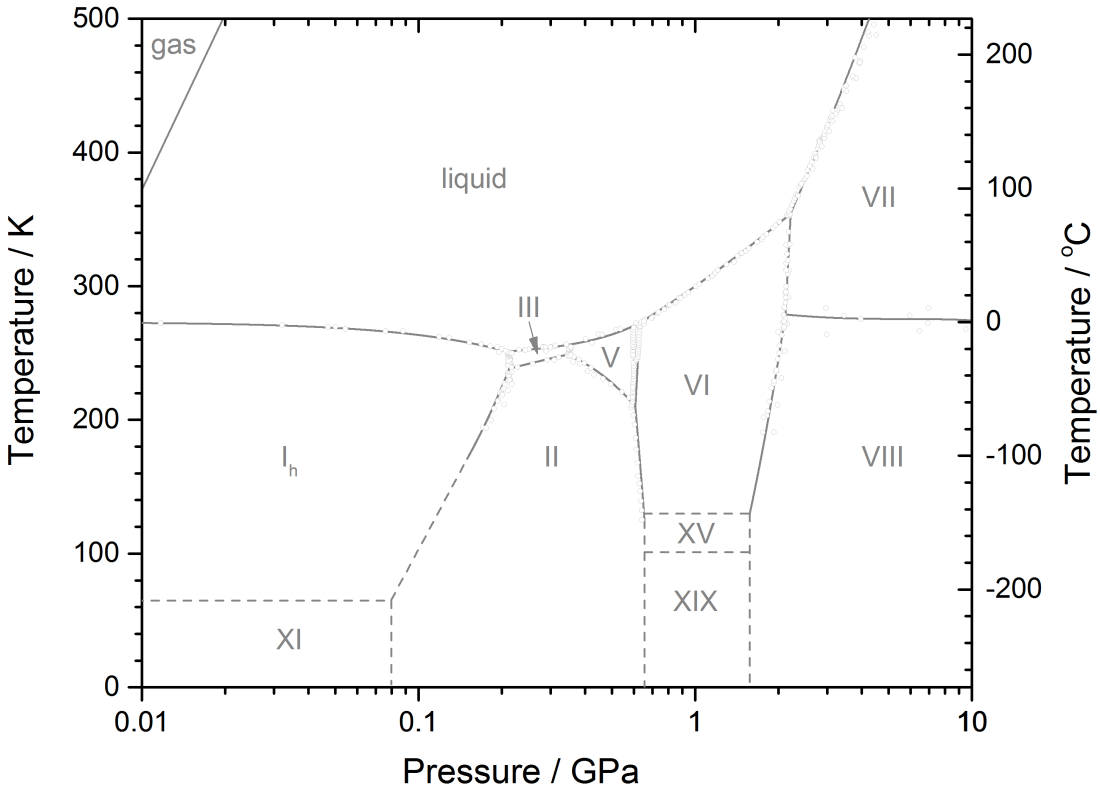

Figure 1.4 *The phase diagram of water. The grey lines are best fit curves with the form* $T(P) = a + b \cdot P + c \cdot \ln(P) + d/P + e \cdot \sqrt{P}$ *taken from [13]. The open circles indicate measured data points. The data points and phase lines were taken from the following sources: L-I: [14–16]; L-III: [14, 16]; L-V: [14–16]; L-VI: [14–17]; L-VII: [18–25]; L-X: [24, 25]; I-II: [14, 26]; I-III: [14, 26]; I-XI: [27, 28]; II-III: [14]; II-V: [14, 29]; II-VI: [29]; III-V: [14]; V-VI: [14, 29]; VI-VII: [30–32]; VI-VIII: [30, 33]; VII-VIII: [34, 35]; VI-XV: [36, 37]; XV-XIX: [37].*

If looking at the structure of solid water, ice rules are basic principles to arrange water molecules and their atoms in water ice. They are also known as BERNAL-FOWLER-rules, after British physicists John D. Bernal and Ralph H. Fowler who first described them in 1933 [126]. The rules state that:

- Each oxygen is covalently bonded to two hydrogen atoms.
- Oxygen atoms in the water molecule form two hydrogen bonds with other water molecules.
- There is precisely one hydrogen between each pair of oxygen atoms

In accordance with the previous discussion, every oxygen is therefore bonded to the total of four hydrogens, of which two bonds are strong (covalently bonded) and two are much weaker (H-bond). Every hydrogen is bonded to two oxygens, strongly to one and weakly to the other.

The resulting configurations are geometrically periodic lattices. In real ice samples, however, there is no perfect periodic lattice because of the existence of BJERRUM-defects, crystallographic defects specific to ice that violate the third rule stated above. Two BJERRUM-defects can be discriminated: The first or L-defect refers to the German word *"leer"* (engl.: empty). An L-defect accords to the missing of an hydrogen atom, so that two oxygens are linked (O$\cdots$O). The second, or D-defect refers to the German word "doppelt" (engl.: double), and occurs if two hydrogens are linked (O-H$\cdots$H-O). Another category of point defects is known: ionic defects. These defects occur if a water molecule is replaced by a ionic molecule, e.g. H_3O^+ and OH^-, violating the first of the Bernal-Fowler Rules. In addition to point defects also other defects known as dislocation or displacement defects are known [120].
Point defects are highly important for phase transitions, for most transformations start at a defect. Starting from this point the molecules reorganise, until they form a new (thermodynamically stable) phase.

1.2.2 Mixing Water and Gas - The Gas Hydrates

So far only pure water phases has been discussed. However, it is known that many other small molecules (mainly gases) can interact and be incorporated in water structures and form (gas) hydrates, which were first discovered in the early 19^{th}

century by Sir Humphry Davy (1778-1829) while leaving a mixture of chlorine and water in his laboratory [127]. Because of the cold English winter, a gas hydrate was formed by crystallisation. For example, chlorine hydrate is formed at about 9 ℃. The first big attempts to synthesise and study such compounds were made in 1930-1950 due to the discovery of hydrate-crystallisation in oil-pipelines [128]. Since 1980, gas hydrates have been studied because of their ability to store large amounts of gas: on Earth, and estimate of 50-80% of all fossil fuel is stored as methane-clathrates [129–131].
Because of the shear abundance of of gases and stochiometric combinations a vast quantity of gas hydrates exists, however, most gas hydrates have very similar structures. The two most common types of gas hydrates are **clathrate hydrates** and **filled ices** which shall be discussed in the following.

Clathrate Hydrates have their name from the Latin word *clathratus*, meaning 'with bars, latticed'. They consist of hydrogen bonded water cages, which are stabilized by guest molecules [70, 130, 132, 133] and are therefore a special form of an inclusion compound. Water molecules form as a host-lattice, in which other molecules, the guests, are enclosed. The latter are thereby essential for the formation of clathrates, since the guests stabilise the overall structure and stops the H_2O lattice from collapsing. This, however, does not mean that all cavities need to be filled in order to stabilise the structure; various filling ratios for clathrates have been reported, although, the stability usually decreases with the filling ratio. A special case of an empty clathrate is the metastable ice XVII which is obtained by pumping guest molecules out of an sX-type clathrate - a special case of a clathrate with helical channels rather than with cages (see chapter 8). This clathrate-structure can also be found in other inclusion compounds such as metal-organic-framworks (MOF) [134]. The question whether the water-analogue NH_4F also forms clathrates remains open [70].

Clathrate hydrates are by far the most common gas hydrates in our Solar System. Beside their already discussed abundance as methane-hydrate on Earth, moons such as the Jovian satellite Ganymede, consists of high-pressure ice phases including ice VI [135]. Marboeuf et al. studied the composition of ices in extrasolar planets [136]; they found that during the cooling of planetary disks CO_2 freezes as a pure condensate in contrast to CO, CH_4, NH_3 and other small gases, which form clathrate hydrates [137]. Senft et al. modeled the formation of craters on icy satellites through impact of projeticles (e.g. asteroids or comets).

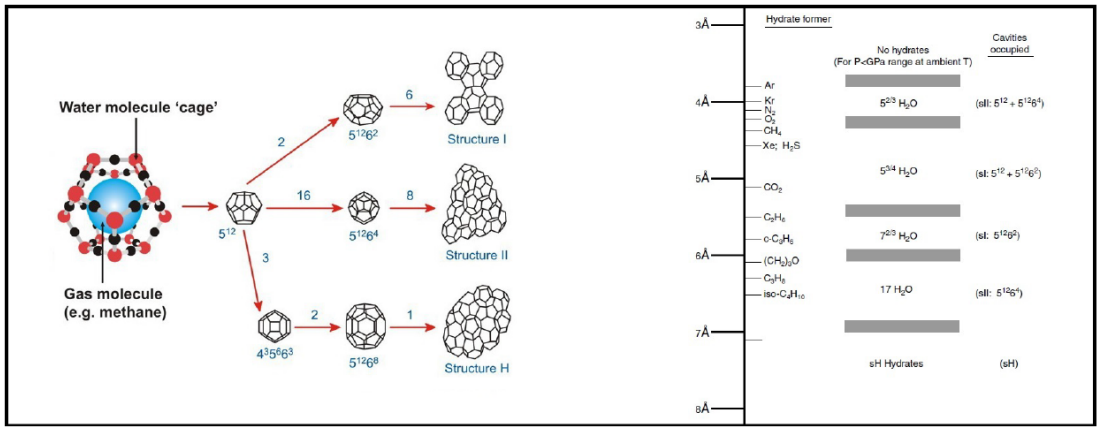

Figure 1.5 *Clathrate hydrates as an example for inclusion compounds. Depending on the size, as well as the physical properties, of the guest molecule(s), different structures can be formed, e.g cubic structure sI and sII or the hexagonal structure sH.*

They assumed pure H_2O ice for the projectiles and targets [138]. In the case of mixed ices (e.g. H_2O and CO_2) first ice VI and solid CO_2 could be generated and finally develop into clathrate hydrates.

Depending on the guest size and interaction with the water lattice, several water-cages and therefore clathrate types are possible. The water-cages are usually formed from Platonic and Archimedean solids and are described in a short notation of the constituent shape(s) and the number of respective faces of this shape as an exponent; the cage 5^{12}, for example, constitutes of 12 pentagons (a regular dodecahedron) and the cage $5^{12}6^2$ constitutes of 12 pentagons and 2 hexagons. The three most common clathrate-types sI, sII and sH are shown in figure 1.5; moreover the structures sIII, sT, and sX (s-"chi") are known. The exact composition of the structures is summarised in table 1.2. The three structures sI, sII and sH are thereby usually found at ambient pressure and which of the two is formed is dictated by the Van-der-Waals radius of the guest. Small molecules (VdW-radius <5 Å) occupy the small 5^{12} cages in sII whereas large molecules (VdW-radius >6 Å) can only occupy the largest cages in sII and sH, $5^{12}6^2$ and $5^{12}6^8$, respectively. Note that sH usually requires both a small and a large molecule to sufficiently stabilise this structure at ambient conditions. Molecules of medium size, 4 Å< r <6 Å, on the other hand usually fill the $5^{12}6^2$ cavities, which are most abundant in the sI structure. With increasing size of the guest, the preferred crystal structure for the formed hydrate is therefore sII→ sI→ sII→ sH [70, 71].

Table 1.2 *Comparison of observed clathrate hydrates [70–72]. Beside these clathrate structures, several theoretical structures based on the observed water-cages do exist; for more details on them see Sloan [70].*

	Space Group	LP / Å	Cages	n_{H_2O}	n_{cavity}
sI	$Pm3n$	$a = 12.03$	$2x5^{12}$, $6x5^{12}6^2$	46	8
sII	$Fd3m$	$a = 17.31$	$16x5^{12}$, $8x5^{12}6^2$	136	24
sIII	$P4_2/mnm$	$a = 23.18$ $c = 12.15$	$10x5^{12}$, $16x5^{12}6^2$, $4x5^{12}6^3$	172	30
sT	$P321$	$a = 35.0$ $a = 12.4$	$4^25^86^1$, $5^{12}6^2$, $5^{12}6^3$, $4^15^{10}6^3$	12	0.5
sH	$P6/mmm$	$a = 12.30$ $c = 10.20$	$3x5^{12}$, $2x4^35^66^3$, $1x5^{12}6^8$	34	6
sH-I_q	$P6/mmm$	$a = 11.99$ $c = 11.51$	$3x5^{12}$, $2x5^{12}6^2$, $2x5^{12}6^3$	40	7
sX	$P6_122$	$a = 6.28$ $c = 6.30$	helical	6	N.A.

While the sIII structure is also formed at ambient pressure, it is somewhat of an oddity; as of now it has been observed only in the bromine-water system and is as such a rare clathrate [139].

While the above discussed structures all appear at ambient conditions, several clathrate structures are known that only form under high-pressure; several of them can be quench-recovered and exist at ambient pressure as metastable structures. Figure 1.6, shows the effect of pressure on the crystal structures of various clathrate hydrates. Among the first to investigate the high-pressure behaviour of gas hydrates were Loveday *et al.* [42]. They observed that the cubic structure sI in methane hydrate (MH-I) transforms with increasing pressure into the hexagonal structure sH (MH-II) [42, 70]. At pressures above 1.8 GPa, the sH structure then forms a third methane hydrate (MH-III) which belongs to the family of the filled ice structures (FIS, see below). This behaviour of rearranging cages can be observed in nearly all other clathrate hydrates. A special place amongst the high-pressure clathrate hydrates is occupied by the sX structure; so far only observed in H_2, O_2 and CO_2, it forms helical channels rather than cages. Its structure is discussed in detail in section 1.2.3 and chapter 8.

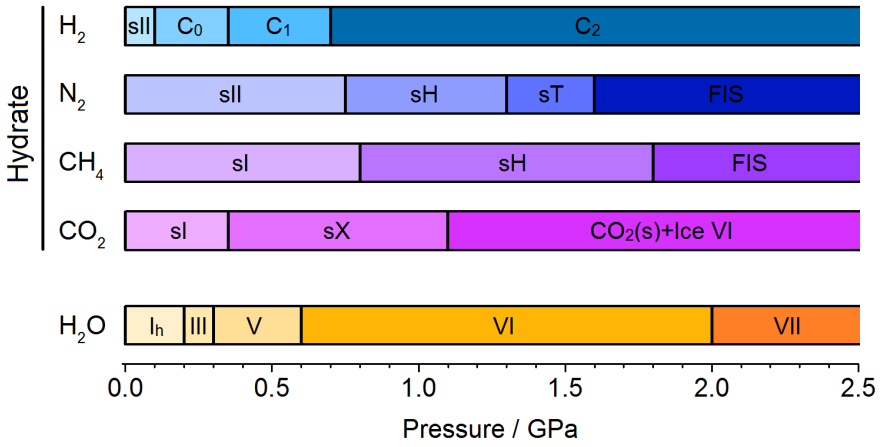

Figure 1.6 *Stability region of water ice (orange) and CO_2, CH_4, N_2, and H_2 hydrates, respectively, at a temperature of about 250 K. The transition pressures at about 250 K are taken from Loveday et al. (2008) and Massani et al. (2017) [38, 39].*

Presently many different routes to synthesise clathrate hydrates are known; starting from vapour deposition followed by an annealing procedure clathrate hydrates are formed [140–143]. Additionally liquid-liquid, liquid-gas or solid-gas interface methods exist [144–147].

Filled Ices As mentioned above, one of the first clathrates to be thoroughly studied under high-pressure was methane hydrate (MH), known as "burning ice", which forms an orthorhombic filled ice structure above 1.8 GPa. In contrast to clathrates, filled ices do not form cages to enclose the guest molecule, but rather enclose the guest in an "ice-like" structure. The structure of methane hydrate, for example, is remarkably similar to the structure of ice I with the methane molecules sitting in the channels of the H_2O network formed by the hexagonal rings (see fig. 1.7). Similar structures are known based on the ices II and XVII ("empty clathrate"). Due to the small channels in water ice, usually only rather small molecules can form this type of inclusion compound and hence it is not surprising that most other filled ices have H_2 or a noble gas a guest-molecule.

Hydrates of Polar Gases While apolar molecules and gases form inclusion compounds as a result of the hydrophile-hydrophobe interaction between water and guest, polar molecules form crystal structures which do not show a host-guest type inclusion compound. An exception to this rule is SO_2 which forms a type I clathrate despite its affinity for water [39].

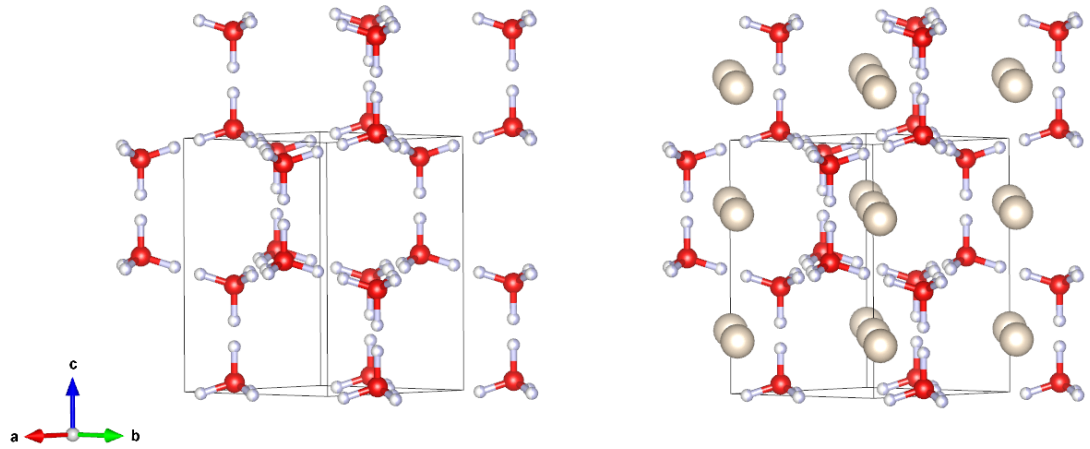

Figure 1.7 *Comparison of the structures of ice I (left) with a filled ice structure of helium.*

1.2.3 Water and Hydrogen - The Hydrogen Hydrates

At ambient pressure, hydrogen and water exist as a two-phase mixture; only at slightly elevated pressures and low temperatures a hydrate is formed. The formation of this hydrogen sII was first observed by Mao *et al.* [148], however, hints of the existence of sII were observed earlier by Dyadin *et al.* [149, 150]. Its crystal structure is the traditional clathrate structure described above. A unique feature of hydrogen sII is that multiple molecules are required to stabilise the clathrate cavities sufficiently, due to the very small size of H_2 molecules compared to other sII-guests such as N_2 or Ar. Neutron diffraction data suggest a maximum hydrogen content of 3.77 wt % with a maximum of four H_2 molecules in the large cage and one in the small cage [40]. This neutron study also showed that there is an ordering transition in the H_2/D_2 molecules below 50 K. Above 50 K the hydrogen/deuterium is randomly distributed and mobile in an approximately spherical shape in the large cage, and below 50 K the H_2 form an ordered tetrahedron.

If sII is compressed at liquid nitrogen temperature to beyond 0.1-0.2 GPa and then warmed up, two phases can be observed: C_{-1} and C_0. The former was proposed by Donnelly *et al.* only in 2016 [41]; this C_{-1} structure has a $P6_3mmc$ symmetry and at $P = 0.4$ GPa and $T = 100$ K the lattice parameters are $a = 4.5442(1)$ Å and $c = 7.1637(4)$ Å based on neutron diffraction data. This structure corresponds to an ice I_h host D_2O network with guest atoms located in the hexagonal channels making it a filled ice.

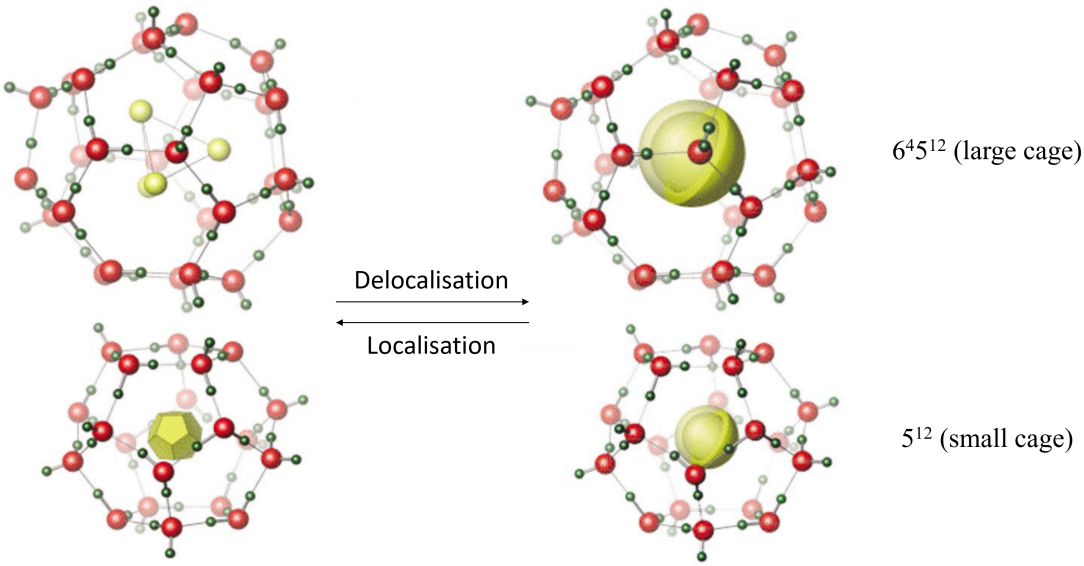

Figure 1.8 *Variation of the D_2 distribution in the cages of deuterium clathrate; the guest D_2 molecules are highlighted in yellow. Below 50 K, the guest molecules are localized but with increasing temperature, the molecules can rotate more freely, yielding a nearly spherical density distribution. Figure adapted from [40].*

On the other hand, the latter C_0 phase belongs to the sX gas hydrates and was first discovered by Efimchenko *et al.* [151]. As such it stands out; the water lattice is chiral and has channels rather than cages. It is not based on a stable ice structure (like the filled ice II structure [152]), and its network does not have an analogue in either silica or zeolite structures [153, 154]. It does, however, exist in some ternary Zintl compounds and has been suggested as a metastable group-14 structure [155–157]. The structure proposed initially was based on channels that contained sites partially occupied by non-hydrogen bonded water molecules [151]. Based on the observed high mobility of hydrogen in this structure [151] and molecular-dynamics modelling, Smirnov *et al.* proposed what emerged to be the correct structure: they suggested that the water molecules in the channels were in fact nitrogen molecules that had been absorbed from the liquid storage medium between recovery and the diffraction measurement [158]. Subsequently, del Rosso *et al.* were able to empty C_0 of hydrogen and to identify the structure as a new form of ice, ice XVII [159, 160]. Finally, Amos *et al.* found that s*X* also exists in the carbon dioxide:water system and determined the full structure of both hydrogen and carbon dioxide hydrates *in-situ* using neutron diffraction [154].

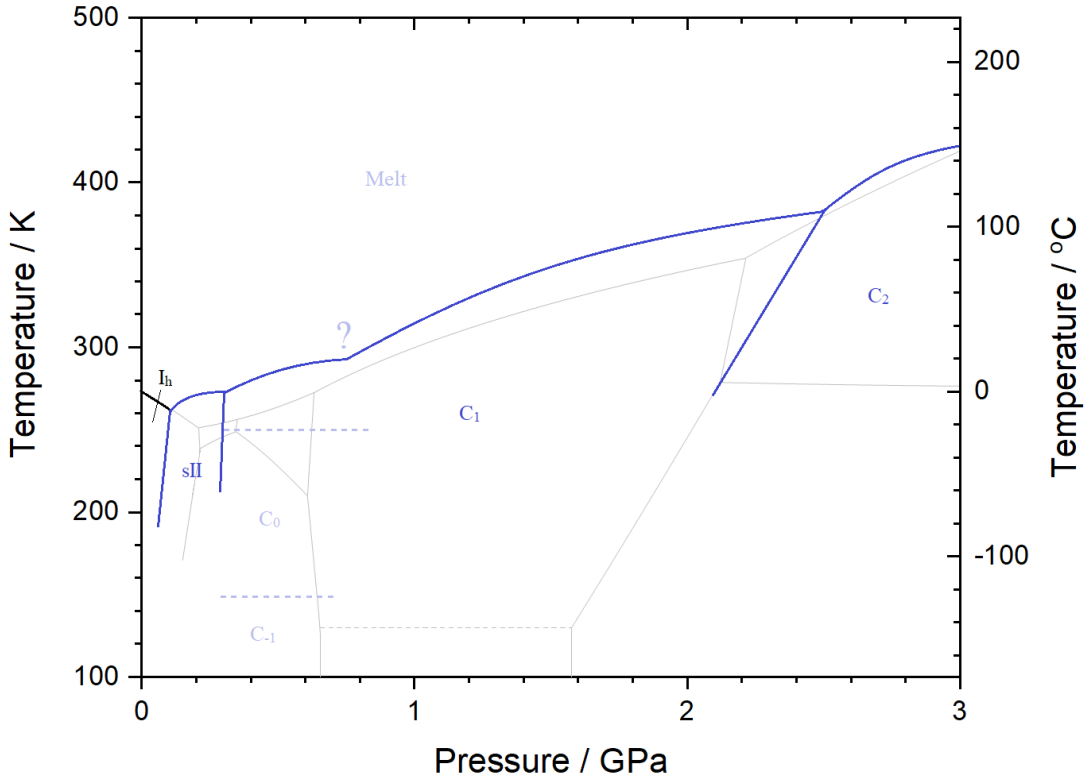

Figure 1.9 *The phase diagram of the hydrogen-water system as shown in Donnelly 2016 [41]. Please note that broken lines do not denominate phase boundaries but rather a line at which the respective other phase first appears.*

In the pressure range from 0.9-3.0 GPa the dominant phase (coexisting with C_2 from 2.3 GPa) in H_2-H_2O is C_1. Historically this was the first hydrogen hydrate that was found. Similar to C_{-1}, it is a filled-ice structure based on ice II. The same structure can be found in He hydrate, which is not surprising given the similar size and physical properties of H_2 and He. C_1 exhibits a hexagonal unit cell with $a = 12.736(2)$ Å and $c = 5.968(2)$ Å around 2 GPa, an ordered H-bond network and freely rotating H_2 located in the channel. Finally, C_2 phase of hydrogen hydrate is yet another filled ice based on ice I_c. It can be described by a cubic space group $Fd3m$ with $a = 6.43$ Å and an ordered hydrogen network similar to ice I_c, with the H_2 molecules occupying the voids. It can also be described as an ice VII analogue with one of the interpenetrating H-bond networks being replaced entirely with H_2; this results in a maximum H_2:H_2O ratio of 1:1 - about 10 wt % [161].

1.2.4 Water and Methane - The Methane Hydrates

As mentioned above, one of the first clathrates to be researched in detail was methane hydrate (MH), also known as "burning ice". Its abundance on Earth exceeds any other deposits of fossil fuel with about 50-80 % of the Earth's methane being stored as methane hydrate [129–131]. As it only forms under pressure and at low temperatures, most deposits can be found in permafrost or at the bottom of the ocean. It is not surprising that energy companies try to find a way to exploit these deposits.

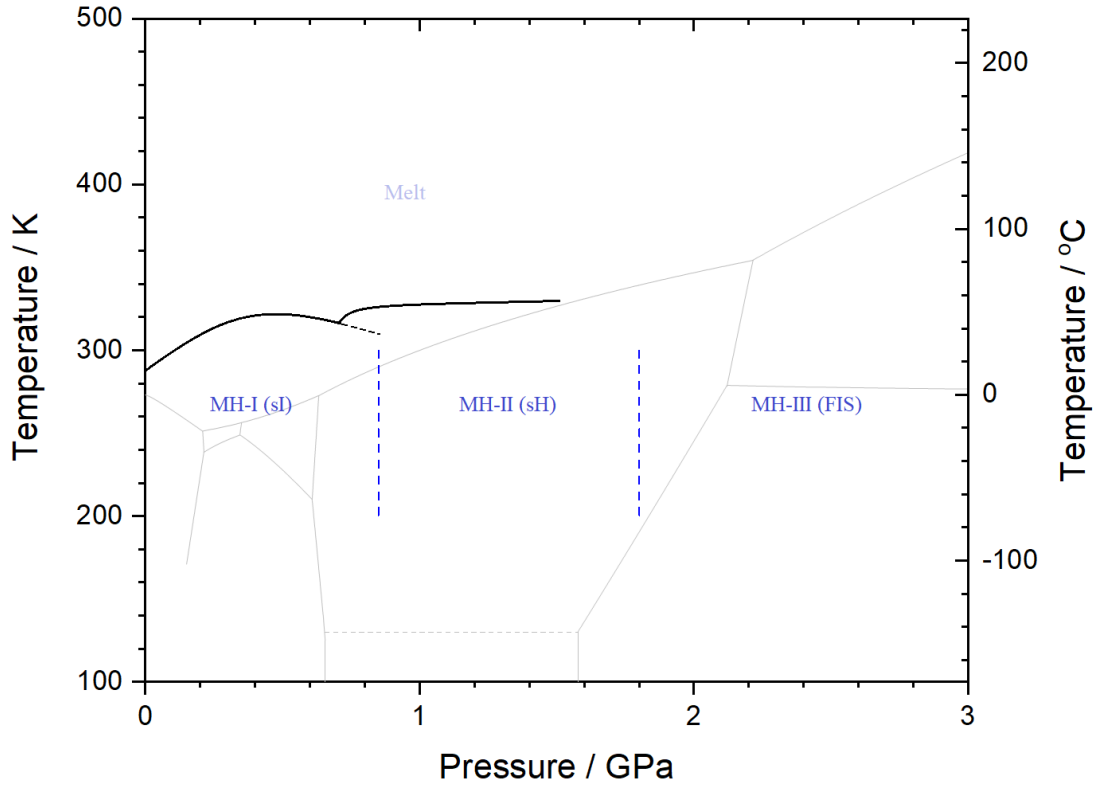

Figure 1.10 *The methane hydrate phases as given by Loveday et al. [42]. Please note that broken lines do not denominate phase boundaries but rather a line at which the respective other phase first appears.*

An interesting trivia might be that the danger of the Bermuda triangle and the disappearance of aircraft and ships under "mysterious circumstances" is a result of enormous deposits of MH. The P/T-conditions in this part of the North Atlantic Ocean are near the dissociation curve of methane hydrate so that a stream of warm water is enough to shift the equilibrium in a way that MH dissociates; large quantities of methane are released and form large bubbles on their way to

the surface - ships and aircraft which enter one of these bubbles are irrevocably doomed. Methane hydrate is also an important substance to understand the mystery of the atmosphere of Titan, Saturn's largest satellite (among other icy satellites) [42]. Conventional theory could not explain the abundant methane gas in Titan's atmosphere because the MH-I inside Titan was assumed to decompose into ice and methane around 1-2 GPa. The gaseous methane then would have escaped to the atmosphere where it would have been decomposed by radiation in the early stage of Titan's history [86].

From a structural point of view, the low-pressure phase of methane hydrate (MH-I) forms the cubic sI clathrate structure allowing for a H_2O:CH_4 ratio of 5.75:1. The melting curve of MH-I rises steeply with pressure, reaching a maximum at about 320 K and 0.5 GPa and is stable up to about 0.8 GPa at which point it transforms into mehane hydrate II. First discovered by Loveday et al. [42] in 2001, the sH clathrate structure was proposed for MH-II. Assuming an ideal occupancy of one methane molecule per cage (H_2O:CH_4 ratio of 5.67:1) this would suggest that upon the transition to MH-II methane is lost by degassing; However, Loveday *et al.* showed that in the sH clathrate some cages are occupied by more than one methane molecule allowing, for a higher methane:water ratio. Finally, at pressures beyond 2 GPa MH-II transforms into MH-III. This structure consists of an orthorhombic filled ice structure based on the lattice of ice I_h, in which methane is embedded in the hexagonal channels of hexagonal ice I [42, 162].

1.2.5 Water and Ammonia - The Ammonia Hydrates

Compared to the other gas hydrates relevant to this thesis (CH_4 and H_2), ammonia exhibits a much more complicated phase diagram. The reason for this is the strong tendency of NH_3 to form hydrogen bonds with H_2O, and therefore, no conventional clathrate or filled ice structure can be observed in NH_3-H_2O system. The N-H$\cdots$O and N$\cdots$H-O hydrogen bonds on the other hand are highly relevant as proxies for the hydrogen bonds in proteins and the DNA molecule; both types of biomolecules rely heavily on this simple bonding mechanism for their folding, replication and overall functionality (see biochemistry textbooks such as Stryer [76]). In general, the ammonia-water system forms three families of phases each based on the stochiometry: ammonia hemihydrate (AHH, $H_2O{\cdot}2NH_3$), ammonia monohydrate (AMH, $H_2O{\cdot}NH_3$), and ammonia dihydrate (ADH, $2H_2O{\cdot}NH_3$).

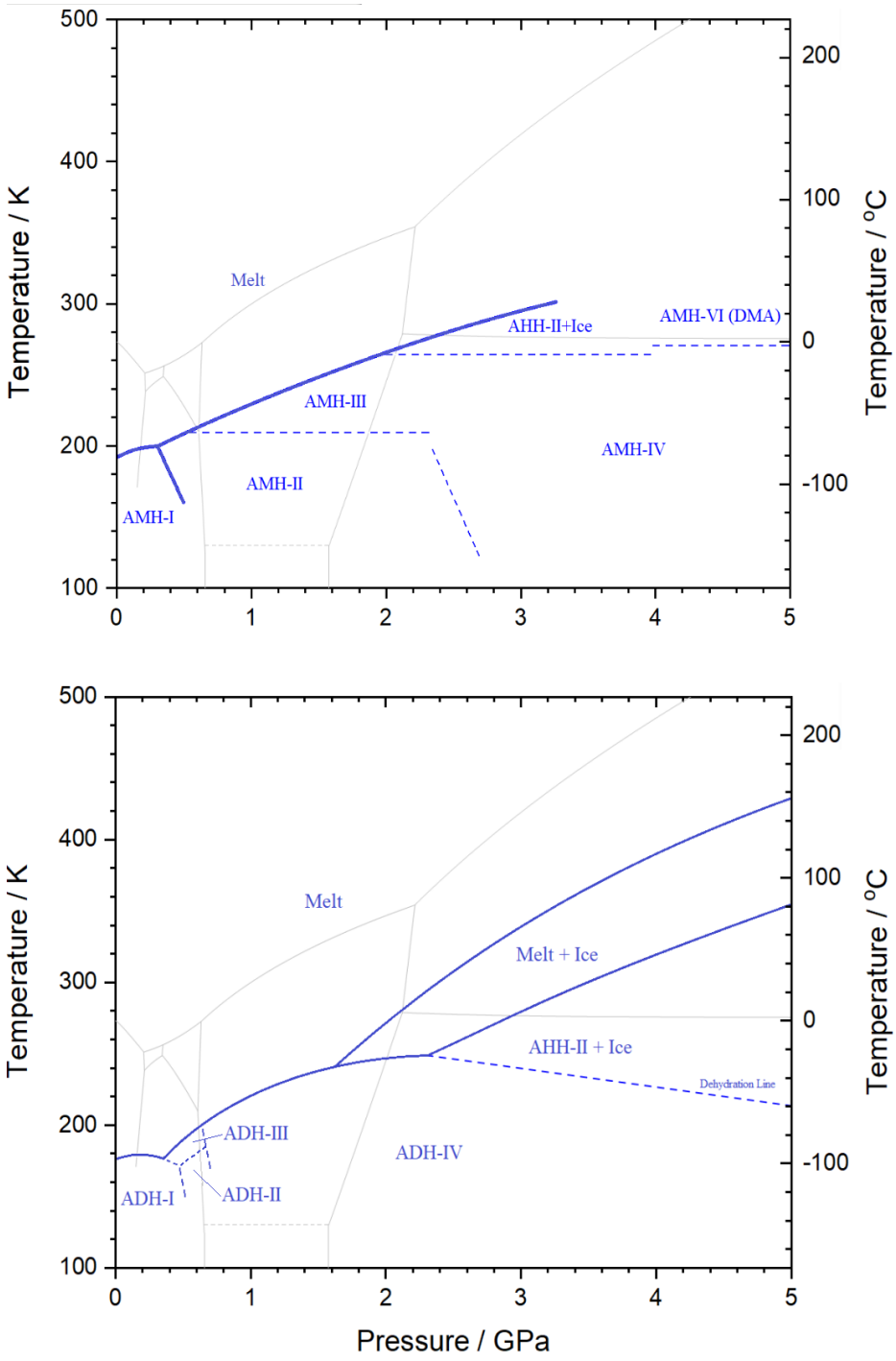

Figure 1.11 *The ammonia-water phases. For reasons of simplicity AHH-I is not shown. Please note that broken lines do not denominate phase boundaries but rather a line at which the respective other phase first appears. The grey lines in the background give the phase diagram of water as a reference. The melting curves and phase boundaries are taken from [42–47].*

The abundance of ammonia in the outer Solar System is thought to be 15 %. In contrast, the abundance of water is thought to be 45 %. This suggests that ammonia-water is one of the main phases in this region of the Solar System [163, 164]. It also explains why most studies were undertaken to investigate the water-rich ammonia hydrates AMH and ADH rather than the ammonia-rich AHH phases. However, it is noteworthy that the end-member phase of the NH_3-H_2O system at elevated pressure and temperature is usually AHH-II or DMA (see later).

AHH Ammonia hemihydrate, $H_2O{\cdot}2NH_3$, crystalises from a 1:2 solution of water in ammonia at about 195 K in the *Pbnm* space group. At 110 K this ambient pressure phase has the lattice parameters $a = 8.322$ Å, $b = 8.353$ Å, and $c = 5.280$ Å [57]. For long it has been considered the least important of the ammonia-water phases due to its unlikely presence in the Solar System. Rather recent research however suggests that it is more important than assumed since it is a precursor for AHH-II which is suspected to be abundant in the outer Solar System (see phase diagram for AMH and ADH in figure 1.11). This second ammonia hemihydrate has a monoclinic structure with space group $P2_1/c$ and the lattice parameters at 3.5 GPa. $a = 3.358$ Å, $b = 9.215$ Å, $c = 8.933$ Å, and $\beta = 94.331^o$ [46].

AMH When the phase diagram of AMH was first published, six phases were proposed [57]. Later it was found that AMH-V was actually ammonia hemihydrate II (AHH-II) which is formed upon heating AMH to about 265 K at pressures above 2 GPa. Under these conditions ammonia monohydrate dehydrates to AHH-II and ice VII/VIII [46]. The five phases of AMH are labelled in Roman numerals I-IV and VI; a full structural solution including space group and atom positions has been published for only three of them (AMH-I, II, and VI).

The ambient pressure phase, AMH-I, crystallises as an orthorhombic crystal in the $P2_12_12_1$ space group and has - at 110 K - the lattice parameters $a = 4.511$, $b = 5.587$, and $c = 9.715$ [57]. Upon pressurising to about 0.5 GPa, AMH-I transforms into AMH-II. The unit-cell parameters were obtained as $a = 18.868$ Å, $b = 6.948$ Å, and $c = 6.859$ Å (space group *Pbca*). This structure contains water molecules that are hydrogen bonded to form a crankshaft chain extending infinitely along the c-axis [56].

At about 2.5 GPa AMH-II again, turns into AMH-IV, and upon heating AMH-II to 210 K, it transforms into AMH-III - for these two phases no structural solution has been published yet; AMH-II has also been observed to coexist with ADH-II after melting of ADH I at 0.45 GPa at 179 K [44].

Finally, the last phase of ammonia monohydrate, AMH-VI, is formed by heating AMH to 270 K above 4 GPa and was solved by Loveday & Nelmes in 1999 [45]. They determined the cubic structure with the space group $Im\bar{3}m$ and the lattice parameter $a = 3.273$ Å neutron diffraction. Interesting enough, AMH-VI thereby exhibits a hydrogen-bonded disordered molecular alloy (DMA) in which the two possible atom positions in AMH-VI (0,0,0) and ($1/2$,$1/2$,$1/2$) can equally be occupied by either an ammonia or a water molecule. It has been suggested that, because of this substitutional disorder, the DMA structure could accommodate a wide range of non-stoichiometric hydrate compositions, an assumption that later was proven to be true by finding the DMA phase also in the ADH phasespace. Because of that, Wilson *et al.* suggested the nomenclature DMA-AMH instead of AMH-VI (and similarly DMA-ADH for the equivalent phase in ADH) [43, 46].

ADH Similar to AHH and AMH, an ambient pressure phase of ADH can be obtained by cooling a 2:1 solution of ammonia and water to about 180 K. The crystal structure for this ADH-I has been solved by Fortes *et al.* in 2007. They determined the space-group to be $P2_13$ with the lattice parameter $a = 7.127$ Å at 150 K [43]. By compression of ADH-I to above 0.47 GPa at 175 K, ADH-II ($P2_1/n$, $a = 6.075$ Å, $b = 6.726$ Å, $c = 7.783$ Å, $\beta = 102.107^o$) can be obtained as a single-phase. Upon warming at 0.55 GPa, the high-pressure phase ADH-II breaks down to the high-pressure AMH-II [47]. Warming of ADH II at 0.55 GPa results in a phase transformation at 190 K to ADH III and pressurising ADH-II or ADH-III to 0.6 GPa forms AMH-IV. For none of these phases a structural solution has been published so far [43].

However, if pressurised beyond 6.3 GPa or upon heating, DMA-ADH can be obtained. The fact that the AMH-IV to DMA boundary can be crossed reversibly provides the first direct evidence that (at least for the 2:1 ammonia:water composition) DMA is a thermodynamically stable phase and not a metastable form with frozen-in disorder [46].

A summary for the phase diagram of the ammonia-water system is shown in figure 1.11. Please note that broken lines do not denominate phase boundaries but rather a line at which the respective other phase first appears. The grey line in the background give the phase diagram of water as a reference.

1.3 Aim for this Work

The underlying aim as already given in the title of this thesis is the evaluation of hydrogen rich systems under pressure by the means of neutron diffraction - the only reliable method to determine the crystallographic positions of hydrogen atoms in a crystal structure. The first part of this thesis will try to push the boundaries of possibility for single crystal neutron diffraction. Namely to go to smaller sample sizes than what has been possible before. This allows for the use of diamond anvil cells in single crystal neutron diffraction - the end goal here is the reliable determination of the crystal structure of hydrogen and deuterium in the pressure range up to 100 GPa.

In the second part, I will investigate the crystal structures of gas hydrates; in particular I will shed light on the sX-hydrate formed from water and N_2 and the structure of the still unknown ammonia monohydrate IV. Furthermore, a study of the ternary system ammonia-methane-water (as it is found in planets) is presented. In the last chapter a fruitless attempt to determine the hydrogen positions in carbonic acid monohydrate is shown.

Chapter 2

On Crystallography

In general, solids can be divided into three different distinct classes as shown in figure 2.10. A crystal is, thereby, a solid material with a highly ordered microscopic structure. All constituents (atoms or molecules) are arranged in a periodic way, forming a three-dimensional lattice that extends (in the ideal case infinitely) in all directions. This leads to a macroscopic structure which is already pre-defined by the way the smallest elements of it are arranged, e.g. the geometrical shape of a quartz is that of a six-sided prism terminating with a six-sided pyramid at the end. However not all solids consist of a single crystal. It is possible that two or more crystalline domains (crystallites or grains) grow together to form a polycrystalline solid. A third possibility is that of an amorphous solid, which is a solid that completely lacks long-range order. Amorphous materials are not in thermodynamic equilibrium and are therefore metastable. They have the form of a "liquid with frozen dynamics".

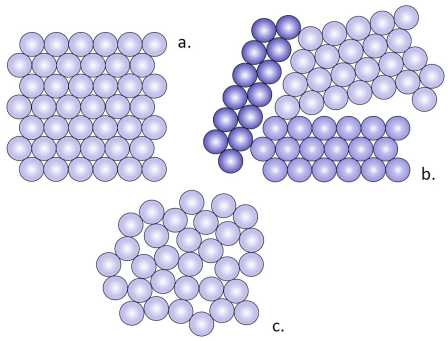

Figure 2.1 *A solid can either be (a) crystalline, (b) polycrystalline (consisting of several crystallites that grew together), or (c) amorphous.*

In this chapter only single crystals (and to a much lesser extent polycrystalline materials) are discussed. This includes a description of the microscopic structure and an introduction to various diffraction techniques which are used to find the structure of a crystal.

2.1 Describing Crystals

As aforementioned, crystals consist of an array of atoms, molecules, or ions arranged in a periodic lattice. Fundamental for the understanding of crystals is the concept of the BRAVAIS lattice (after Auguste Bravais, 1811-1863). Elements in a Bravais lattice can be atoms, ions, molecules, or even groups of molecules - a Bravais lattice only shows the underlying periodic structure in a crystal. The definition - as taken from Ashcroft and Mermin (1976) - of a Bravais lattice is "[...] an infinite array of discrete points with an arrangement and orientation that appears exactly the same from whichever point the array is viewed" [104]. Therefore, a Bravais lattice can be mathematically described by a vector $\mathbf{R}$ that goes from the origin of the lattice to any other lattice point.

$$\mathbf{R} = n_1\mathbf{a}_1 + n_2\mathbf{a}_2 + n_3\mathbf{a}_3 \tag{2.1}$$

The lattice the vectors $\mathbf{a}_i$ generate is called a *direct lattice*. In figure 2.2, the vectors of a such a direct lattice are shown. This definition of a lattice, however, is ambiguous since there are several ways to satisfy this definition. The three most important ones are given below [165, 166].

1. Primitive cells. A primitive cell is defined as an arbitrary volume of space that, when translated through the vectors of the lattice, fills all of space without overlapping itself or leaving voids. There is no unique way of choosing a primitive unit cell as long as it contains precisely one lattice point [166]. In figure 2.2 two possible primitive cells in a 2-D lattice are depicted by the light areas.

2. Wigner-Seitz cells. This type of cell is a special case of a primitive cell. It is defined as the volume element that is closer to one lattice point than to any other lattice point; as such it can be constructed by planes half way between two lattice points and perpendicular to the line joining them [166, 167]. In figure 2.2 the square cell is a W-S cell. The Wigner-Seitz cell of the reciprocal lattice (see later) is called the (first) Brillouin zone.

3. The conventional unit cell (short: unit cell). Usually, this cell is chosen to be bigger than above cells. The main difference to the above stated cells is a higher element of symmetry. The vectors of a unit cell are a *subset* of Bravais lattice vectors. Examples for such cells are the face centered cubic structure (fcc) and the body-centered cubic structure (bcc).

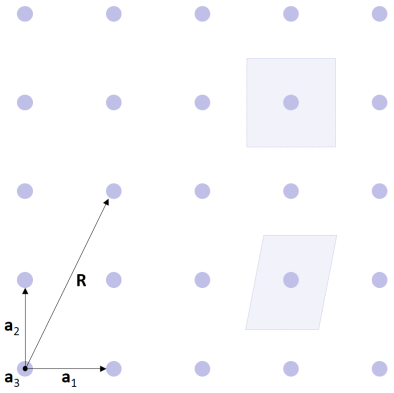

Figure 2.2 *Projection of a Bravais lattice viewed along the $\boldsymbol{a}_3$ direction. The three axis are given by the vectors $\boldsymbol{a}_1$, $\boldsymbol{a}_2$, and $\boldsymbol{a}_3$. Every lattice point can be reached by a vector $\boldsymbol{R} = n_1\boldsymbol{a}_1 + n_2\boldsymbol{a}_2 + n_3\boldsymbol{a}_3$. The shaded areas give two possible primitive unit cells.*

The numbers that specify the size and shape of a cell are the lattice constants, e.g. the lengths a, b, and c and the angles α, β, and γ.
Within a unit cell the coordinates of the respective atoms (or ions) are usually given in fractional coordinates [166].

$$\mathbf{d} = x_1\mathbf{a}_1 + x_2\mathbf{a}_2 + x_3\mathbf{a}_3 \tag{2.2}$$

To give the relative position of an atom in a cell is of particular importance for lattices with bases. For example, the sodium chloride crystal (alternating $\mathrm{Na}^+ \cdots \mathrm{Cl}^-$) can be represented as a face-centered cubic lattice with a two-atom basis (one with all the Na^+-ions and one with all the Cl^--ions). All the sodium atoms are thereby at a spatial position $\mathbf{0}$ and the chlorine ions are at the spatial positions $\frac{1}{2}$,0,0 - so shifted by a half along the $\mathbf{a}_1$ direction.

A concept equally important to solid state physics as the direct lattice is the one of a *reciprocal lattice* which is the Fourier transform of the direct lattice. In this lattice, every vector $\mathbf{b}_i$ is perpendicular to two vectors of the direct lattice and has the length of $1/d_{hkl}$, the d-spacing of two lattice planes in the (hkl) direction of the reciprocal lattice[168]. It can therefore be generated by the vectors

$$\begin{aligned}
\mathbf{b}_1 &= 2\pi\frac{\mathbf{a}_2 \times \mathbf{a}_3}{\mathbf{a}_1(\mathbf{a}_2 \times \mathbf{a}_3)}, \\
\mathbf{b}_2 &= 2\pi\frac{\mathbf{a}_3 \times \mathbf{a}_1}{\mathbf{a}_2(\mathbf{a}_3 \times \mathbf{a}_1)}, \\
\mathbf{b}_3 &= 2\pi\frac{\mathbf{a}_1 \times \mathbf{a}_2}{\mathbf{a}_3(\mathbf{a}_1 \times \mathbf{a}_2)}.
\end{aligned} \tag{2.3}$$

Since the reciprocal lattice is the Fourier transform of a Bravais lattice, it is also a

Bravais lattice. The reciprocal lattice of a reciprocal lattice, then, is the original direct lattice again. The reciprocal lattice exists in reciprocal space (momentum space, k-space), and therefore, it is possible to define a reciprocal lattice vector $\mathbf{K}$ in the reciprocal space

$$\mathbf{K} = h\mathbf{b}_1 + k\mathbf{b}_2 + l\mathbf{b}_3. \tag{2.4}$$

Another way to look at the reciprocal lattice is the following: a direct lattice with an array of lattice points at $\mathbf{R}$ can be, due to the definition of a Bravais lattice, described as a plane wave $e^{i\mathbf{k}\cdot\mathbf{r}}$. This, however, is only true for a set of wave vectors $\mathbf{K}$, that have the periodicity of the Bravais lattice. Therefore, it is possible to write

$$e^{i\mathbf{K}\cdot(\mathbf{r}+\mathbf{R})} = e^{i\mathbf{K}\cdot\mathbf{r}}. \tag{2.5}$$

Due to definition lattice and reciprocal lattice vectors satisfy equation 2.6, with δ_{ij} being the Kronecker delta ($\delta_{ij} = 0$ for $i \neq j$; and $\delta_{ij} = 1$ for $i = j$).

$$\mathbf{b}_i \cdot \mathbf{a}_j = 2\pi\delta_{ij} \tag{2.6}$$

To describe a crystal and its structure, the Miller Indices h, k, and l are commonly used. It follows from equation 2.4 that h, k, and l are the coefficients to the vectors of a reciprocal lattice. Each set of coefficients therefore corresponds to a plane (hkl) in the direct lattice. From a crystallographic point of view, the (hkl) values are a set of integers with no common factors, which are inversely proportional to the intercept of the crystal axis with the respective plane [166].

$$h : k : l = \frac{1}{x_1} : \frac{1}{x_2} : \frac{1}{x_3} \tag{2.7}$$

In figure 2.3, three such lattice planes of a simple cubic lattice are emphasised in grey. The first plane thereby intersects the crystal axis at $x_1 = 1$ and at $x_2 = x_3 = \infty$. Hence, this plane is the (100)-plane because $h : k : l = \frac{1}{1} : \frac{1}{\infty} : \frac{1}{\infty}$. If a negative integer is used to describe a crystal, it is usually written with a bar, as in $\bar{1}$ for -1 (e.g. the equivalent of the (100) plane in the -$\mathbf{a}_1$ direction is $(\bar{1}00)$).

Furthermore, different parentheses are used to describe different crystallographic properties:

- (hkl) denotes the crystallographic plane
- $\{hkl\}$ denotes the family of planes (planes that are parallel)
- $[hkl]$ denotes the crystallographic direction perpendicular to the (hkl) plane
- $\langle hkl \rangle$ denotes the set of all directions that are equivalent to $[hkl]$[166].

So far only the translation symmetries of a Bravais lattice were discussed, e.g. the translation of a lattice point along a lattice vector $\mathbf{R}$. Such a translational operation $\mathbf{T}_r$ that takes a lattice into itself is called a *symmetry operation*. In a mathematical sense a *symmetry group* of an object is the group of all transformations under which the object is invariant with composition as the group operation. For the description of the full symmetry of a crystal, therefore also the operations of rotation, reflection, and inversion have to be taken into account. For a cubic crystal system, for example, a rotation of 90° about a line in the $\langle 100 \rangle$ direction yields the same crystal structure: also, a rotation of 120° about a line in $\langle 111 \rangle$ direction does so.
The full symmetry group of a Bravais lattice therefore contains:

1. Translation through Bravais lattice vector $\mathbf{R}$
2. Rotation around or inversion through a fixed point or plane.
3. Operations by successive applications of 1. and/or 2.

Ignoring the first point and therefore the translational symmetry, one only considers operations such as rotation through an n-fold axis, reflection through a mirror plane, and/or inversion through a point. These operations are a subset of the full space group and are called a crystallographic *point group* because they leave a central point fixed while moving all other points of the crystal to a position

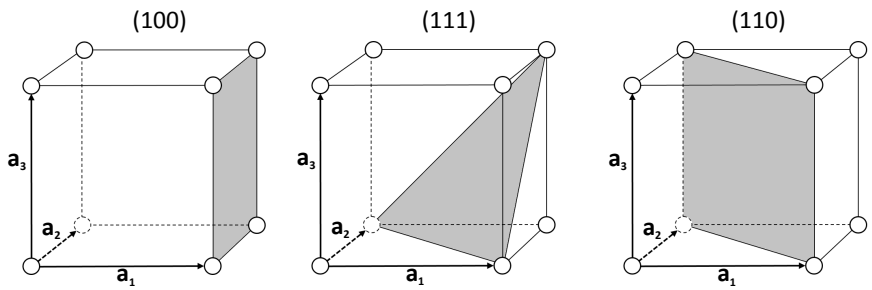

Figure 2.3 *The (100), (111), and (110) lattice planes of a simple cubic lattice.*

of the same kind. There are only seven distinct point groups that a Bravais lattice can have: cubic, tetragonal, orthorhombic, hexagonal, trigonal, monoclinic, and triclinic. Any crystal structure therefore belongs to one of these *crystal systems*. Without the translational restrictions, fourteen *space groups* are possible. Thus, from the point of symmetry, there are only fourteen Bravais lattices. The structures of these lattices are depicted in figure 2.4 (see Bravais (1845) [48] or Ashcroft (1976) [166]).

Table 2.1 *Comparrison of a Bravais lattice und a "real" crystal structure.*

	Bravais lattice (spherical symmetry)	Real crystal structure (arbitrary symmetry)
Point group	7 crystal systems	32 crystallographic point groups
Space group	14 Bravais lattices	230 space groups

A last and final step, is made to move from the ideal model of a Bravais lattice to a general crystal structure. While Bravais lattices have a 'spherical symmetry', in a real lattice arbitrary arrangements are allowed. Since the objects are no longer required to have maximum symmetry, the number of space groups is greatly increased to 230; also, the number of possible point groups increases to 32. In table 2.1 the ideal case of a Bravais lattice and the crystal structure with an arbitrary symmetry are compared.

Since a detailed discussion of these 230 space groups would go beyond the scope of this thesis, I abstain from doing one. However, the Hermann-Mauguin (H-M) notation, which is used to for labeling space groups, is worth mentioning here. The H-M notation uses 4 symbols to indicate the symmetry in a crystal, e.g. $Imma$ and $P\bar{4}2_1m$. The first letter gives the Bravais lattice of the crystal. The letters P and R stand for primitive and rhombohedral, I for body-centered (from German "Innenzentriert"), F for face-centered (from German "Flächenzentriert"), and A-C for end-centered. The following symbols indicate three highest symmetry elements in three symmetry axis with the axis of highest symmetry first. These symmetry elements are rotations along an n-fold axis (indicated by the numbers 1-4 and 6), inversion through a point (indicated with a bar over a number; $\bar{3}$), screw axes (indicated with a subscript; 3_1), mirror planes (m), and glide planes (a, b, and c) [166, 168].

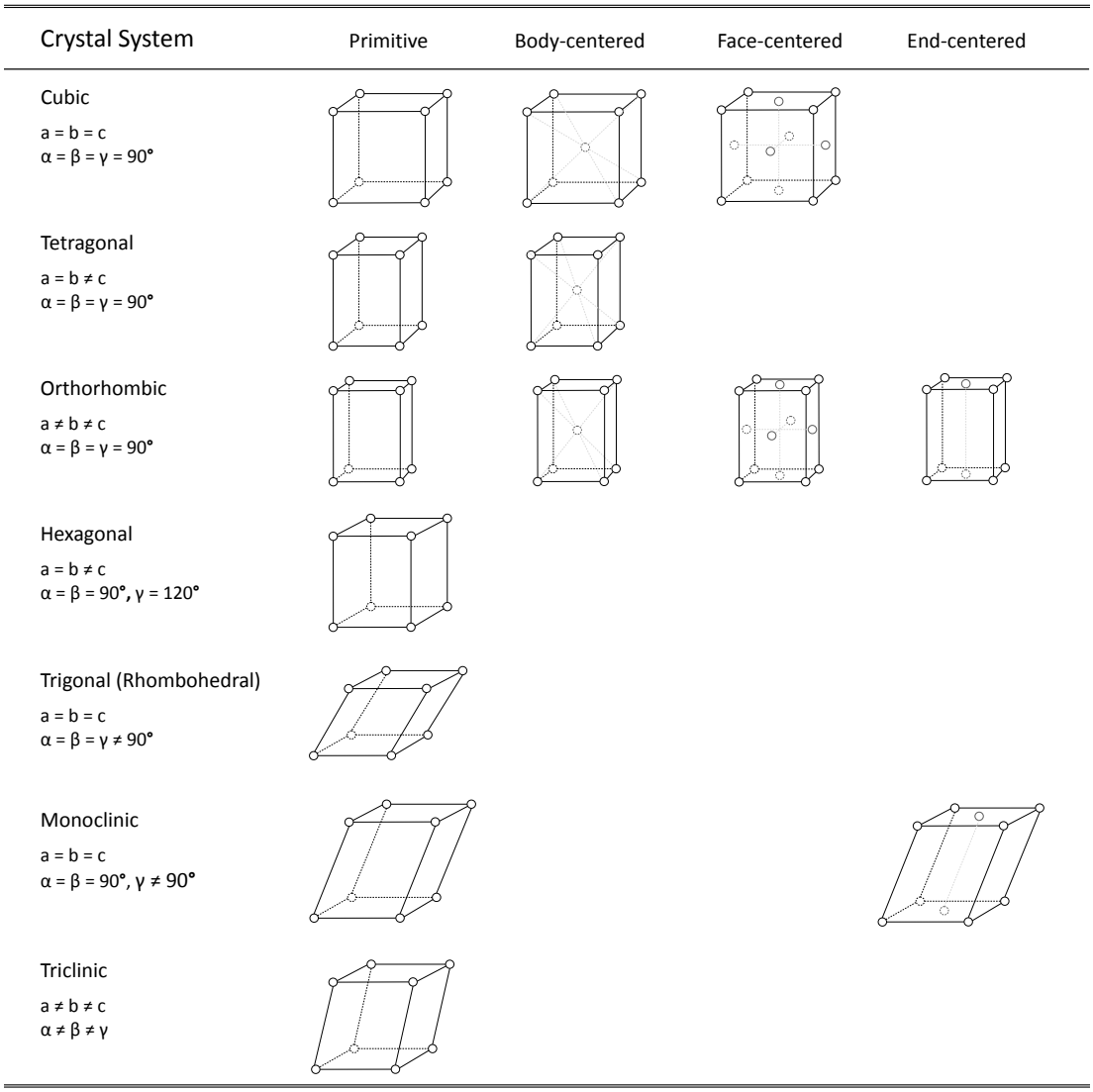

Figure 2.4 *The 7 crystal systems and the 14 Bravais lattices according to Bravais [48].*

The simplest cell with the lowest symmetry is, for example, the triclinic unit cell with no inversion center. Its H-M symbol is therefore $P111$, or in short notation $P1$. The unit cell $P6_122$, however, has as a highest symmetry element a 6-fold screw axis and two 2-fold rotational ones. This clearly indicates a hexagonal system. This notation helps to reduce the information needed to identify a crystal dramatically. The low pressure phase of CO_2 (Phase I), for example, consists of a cubic crystal system of 12 atoms. Altogether 42 parameters are needed to show its exact structure - 6 lattice parameters and the position of 12 atoms within the unit cell. The knowledge of its symmetry ($Pa\bar{3}$) reduces the needed information to only 7. Only 1 lattice parameter (it is a cubic system) and the coordinates

of one oxygen and one carbon are needed, while the other atomic positions are generated by symmetry operations (example taken from Amos [53]).

2.2 On Diffraction

When X-rays, electrons or neutrons are scattered off a periodic structure, such as a crystal, constructive and destructive interference in the scattered beam can be observed. Hereby the radiation must have wavelength comparable with the periodicity in the structure. This phenomenon can be used to determine the structure of a crystal. Thereby the incident radiation has to have a wavelength in the same order of magnitude as the distance between two lattice points (about 1 Å), such that wave interference effects occur. For electrons and neutrons the DE BROGLIE-relation ($\lambda = h/mv$) can be used to assign a wavelength to every particle. The periodic structure of a crystalline solid acts as a diffraction grating, scattering the incident beam in a predictable way and forming a diffraction pattern. From this pattern it is possible to work back to deduce the structure of the crystal producing the diffraction pattern. In brief, this technique can be split into three distinct parts:

1. How radiation interacts with lattice points, which are a) the electron shells for X-rays, b) the nuclei and un-paired electrons for neutrons, and c) charged particles (protons and electrons) for electrons.
2. How diffraction occurs in the crystal.
3. How the observed scattering can be interpreted.

The interaction mechanism of the incident beam with the lattice points is thereby non-trivial and depends on the radiation type. In general, this is the elastic scattering, where no energy is transferred from or to the crystal, the simplest form of scattering. However, other types of interaction can also occur such as inelastic scattering (energy is transferred from or to the crystal) and absorption (e.g. neutrons are captured by the nucleus).
Two approaches were made to explain diffraction, one by Max von Laue and the other by Lawrence Bragg and his father William Henry Bragg. While the latter is simpler to understand, the former is much more useful to understand neutron scattering, especially time-of-flight neutron scattering, a technique that is based on inelastic scattering of neutrons (see later). Sequentially, I am going to describe both approaches.

2.2.1 Bragg Formulation

An incoming plane wave with a wavelength and phase approaches a single crystal and is specularly scattered off two different atoms within it. Assuming that a crystal consists of parallel planes, the lattice planes, it is possible to formulate a condition at which the scattered radiation shows constructive interference. With two planes spaced a distance d apart, the path difference of two beams that are scattered in two different planes is given by $2d\sin(\theta)$, where θ is the angle of incidence. If this path difference is an integer multiple of the wave length of the incident beam, $n\lambda$, constructive interference will occur. The integer n is thereby known as the order of the corresponding reflection.

$$n\lambda = 2d\sin(\theta) \tag{2.8}$$

The relation given in equation 2.8 is also known as the Bragg-condition or Braggs' Law. However, for a beam containing a range of different wavelengths, many different reflections are observed [166, 169].

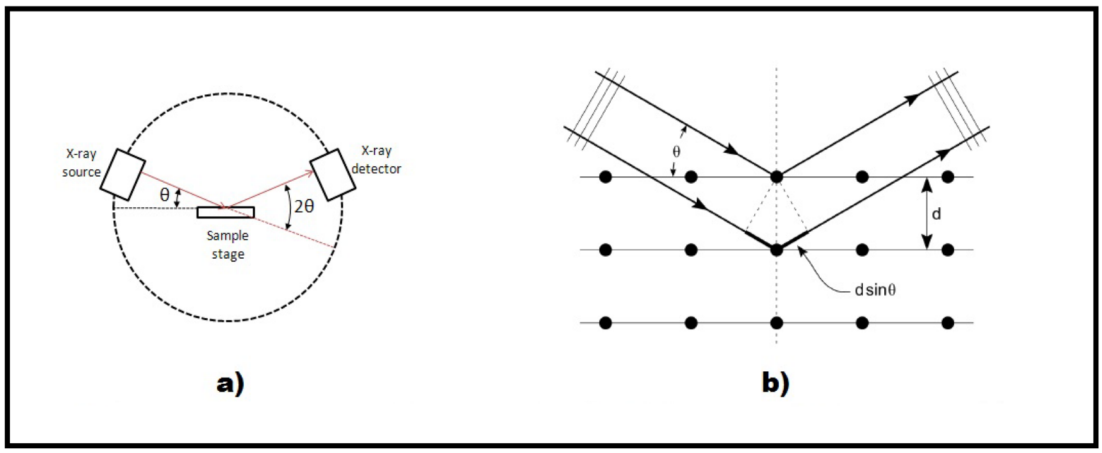

Figure 2.5 *a) The Bragg angle θ is just half the total angle by which the incident beam is deflected. b) The path difference is only dependent on the Bragg angle and the d-spacing between two lattice planes.*

2.2.2 Von Laue Formulation

This approach differs from Braggs' approch in that no lattice planes are singled out and that no specular reflection has to be assumed. He, instead, assumed a set of lattice points placed at the site $\mathbf{R}$ of a Bravais lattice that can re-radiate the incident beam in all directions. Peaks in the diffraction pattern will only be

observed if the scattered beam has the right magnitude of displacement to show constructive interference. First, we will assume a displacement of two lattice points (rather than all of them) by a vector $\mathbf{d}$ (see figure 2.5). The path difference at which constructive interference occurs can then be written as

$$d\cos(\theta) + d\cos(\theta') = \mathbf{d} \cdot (\hat{\mathbf{n}} - \hat{\mathbf{n}}') = n\lambda. \tag{2.9}$$

The wave vector $\mathbf{k}$ of the incident beam be written as $\mathbf{k} = 2\pi\hat{\mathbf{n}}/\lambda$, and for the scattered one $\mathbf{k}' = 2\pi\hat{\mathbf{n}}'/\lambda$ with $\hat{\mathbf{n}}$ being the unity vector in the respective direction. These expressions can be used to rewrite equation 2.9 to

$$\mathbf{d} \cdot (\mathbf{k} - \mathbf{k}') = 2\pi n. \tag{2.10}$$

The change of the wave vectors $\mathbf{k} - \mathbf{k}'$ is the scattering vector $\mathbf{Q}$. Since all lattice points are displaced by the lattice vectors $\mathbf{R}$, this equation becomes

$$\mathbf{R} \cdot (\mathbf{k} - \mathbf{k}') = 2\pi n \tag{2.11}$$

for an array of points in a crystal. This expression can be equivalently written in its exponential form

$$e^{i(\mathbf{k}'-\mathbf{k})\cdot\mathbf{R}} = 1 \tag{2.12}$$

If this equation is compared with the definition of a reciprocal lattice, the VON LAUE condition for constructive interference is obtained (eq. 2.13); peaks will be observed if the scattering vector $\mathbf{Q} = \mathbf{k}' - \mathbf{k}$ is a vector of the reciprocal lattice $\mathbf{K}$.

$$\mathbf{K} = \mathbf{k}' - \mathbf{k} \tag{2.13}$$

This equation can be further simplified by squaring it and assuming purely elastic scattering ($|\mathbf{k}'| = |\mathbf{k}|$) in which case it becomes

$$\mathbf{k} \cdot \frac{\mathbf{K}}{K} = \mathbf{k} \cdot \hat{\mathbf{K}} = \frac{1}{2}K. \tag{2.14}$$

In other words, the component of the wave vector of the incident beam along the reciprocal lattice vector $\mathbf{K}$ has to be half the length of $\mathbf{K}$. Equation 2.14 describes a plane in its HESSE normal form, and thus every wave vector $\mathbf{k}$ will satisfy the Laue condition if its tip lies on a plane that bisects a line joining the origin of the

k-space and a reciprocal lattice point. The planes bisecting a reciprocal lattice vector **K** are also called *Bragg planes* [166].

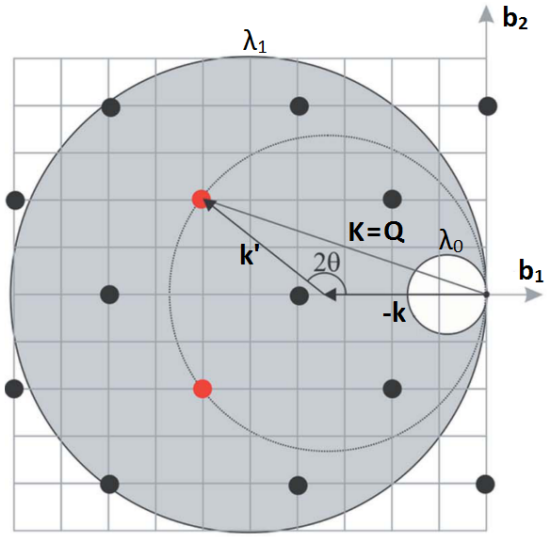

Figure 2.6 *Two-dimensional projection of the* EWALD *construction. Taken from Guthrie et al. [49].*

With this it is possible to visualise which reflections satisfy the Laue condition and to determine the wave vectors of the corresponding diffracted beam. A sphere (or a circle in case of a 2D crystal) is drawn in the k-space centered on the tip of wave vector **k** of the incident beam and with the radius $2\pi/\lambda$ (see Figure 2.6). The origin of the k-space lies therefore on the surface of the sphere. Eventually there will be a wave vector **k**' satisfying the Laue condition if a reciprocal lattice point lies on the surface of the of this sphere (see red lattice points in figure 2.6). This geometric construction is the EWALD-construction [166, 170, 171]. In general, such a sphere will not have any reciprocal lattice points on its surface, however, there are techniques to ensure that a point lies on the Ewald sphere. This also explains why radiation with long wavelengths does not lead to a diffraction pattern; the radius of the sphere ($2\pi/\lambda$) becomes too small to include any reciprocal lattice points (compare white sphere in figure 2.6).

As mentioned above, there are methods to find a geometry in which a diffraction experiment will show constructive interference.

1. The Laue method uses polychromatic rays instead of monochromatic ones. By scanning different wavelengths from λ_0 to λ_1, the Ewald sphere expands in from a radius of $2\pi/\lambda_0$ to a radius of $2\pi/\lambda_1$. Eventually, a wave vector $\mathbf{k} = 2\pi\hat{\mathbf{n}}/\lambda$ will satisfy the Laue condition. Bragg peaks in the diffraction pattern will be observed for every reciprocal lattice point lying in the region between λ_0 and λ_1. This method is particularly useful for time-of-flight neutron diffraction (see later).

2. The rotating crystal method uses monochromatic rays, however the angle of incidence is varied. This is achieved by rotating the crystal about a fixed axis. When the crystal rotates, the reciprocal lattice rotates about the same axis also. A rotation about the z-axis in figure 2.6 therefore means that the red lattice points will be removed from the Ewald sphere, however, other reciprocal lattice points will move onto the surface of the sphere.

3. The Powder method. In brief, a sample made from a fine powder or a polycrystalline solid is used - with grains that are still gigantic compared to atomic dimensions but small relative to the dimensions of the incident beam. Since all grains are randomly orientated, the diffraction is what one would produce by combining all reflections of a single crystal. Now the wave vector of the incident beam $\mathbf{k}$ is fixed and with it the Ewald sphere. Now the sample is allowed to rotate through all possible angles around the origin. Each vector $\mathbf{K}$ generates a sphere of radius K. Such a sphere intersects the Ewald sphere in a circle. Every wave vector $\mathbf{k}$' from the center of the Ewald sphere to the intersect-circle therefore satisfies the VON LAUE condition. A reciprocal lattice point therefore produces a cone of scattered radiation at an angle Φ to the forward direction, where

$$K = 2k \sin(\frac{1}{2}\Phi). \tag{2.15}$$

These cones are named after the physicists P. J. Debye and P. H. Scherrer DEBYE-SCHERRER cones and the respective rings measured by a detector placed to the forward direction DEBYE-SCHERRER rings [166, 172, 173].

So far, only the conditions for constructive interference for lattice points in a Bravais lattice were considered, e.g. that the Laue condition $\mathbf{K} = \mathbf{k}' - \mathbf{k}$ is satisfied. However, if the crystal structure consists of several bases also the scattering *within* a primitive unit cell - the scattering within this lattice point - has to be taken into account.
Assuming n identical sets of scatterers in the unit cell with the coordinates $\mathbf{d}_1, \ldots, \mathbf{d}_n$ (expressed as fractional basis vectors $\mathbf{d} = x\mathbf{a}_1 + y\mathbf{a}_2 + z\mathbf{a}_3$), the phase difference between two such sets i and j will be $\mathbf{K} \cdot (\mathbf{d}_i - \mathbf{d}_j)$. Thus, the amplitude of several scattered beams will differ by a factor $e^{i\mathbf{K}\cdot(\mathbf{d}_i - \mathbf{d}_j)}$. The amplitude of a scattered beam can, therefore, be expressed as a summation over all possible

scatterers; this is the geometrical structure factor $\mathcal{F}(\mathbf{K})$).

$$\mathcal{F}(\mathbf{K}) = \sum_{j=1}^{n} e^{i\mathbf{K}\cdot\mathbf{d}_j}, \tag{2.16}$$

This alone is not yet enough to describe diffraction completely, if the atoms are not identical. In this case, for every set of identical scatterers, j, a form factor f_j approximates the form of the respective scatterer. With this, equation 2.16 becomes

$$\mathcal{F}(\mathbf{K}) = \sum_{j=1}^{n} f_j(\mathbf{K}) \cdot e^{i\mathbf{K}\cdot\mathbf{d}_j}. \tag{2.17}$$

Note that the overall intensity of a Bragg peak will be proportional to the square of the absolute value of the amplitudes and therefore to $|\mathcal{F}(\mathbf{K})|^2$.

2.2.3 Time-of-Flight Neutron Diffraction (TOF-ND)

While neutrons in a nucleus are stable, free neutrons undergo a beta decay with a lifetime of just under 15 minutes according to

$$n \rightarrow p^+ + e^- + \bar{\nu}$$

to a proton, an electron and an electron anti-neutrino [174]. There are many ways to produce free neutrons, however free neutrons for scientific application are mainly produced in nuclear fission reactors (e.g. High Flux Isotope Reactor (HIFR) at Oak Ridge National Laboratories (ORNL)), or at spallation sources (e.g. Spallation Neutron Source (SNS) at ORNL, ISIS at Rutherford-Appleton Laboratories (RAL)). Most work in this thesis was done at one of the above mentioned spallation sources, and the process by which neutrons are produced there is therefore briefly mentioned. In figure 2.7, a sketch of the ISIS spallation source, is shown.

At an ion source, negatively charged hydrogen ions (H^-) are produced, which are then accelerated to several MeV (up to 1 GeV at SNS) in an accelerator (e.g. a linac). To convert the negatively charged hydrogen ions into protons, the ion beam is passed through a stripping foil (e.g. diamond or aluminium oxide) that strips the electrons from the negatively charged hydrogen atoms.

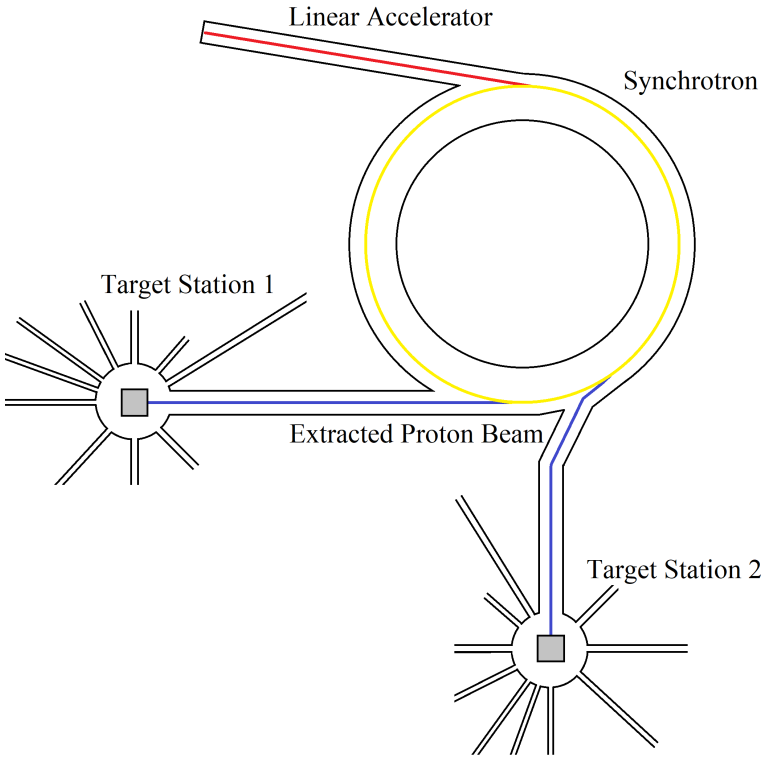

Figure 2.7 *Schematics of a spallation source. Negative H^- atoms are accelerated in a linear accelerator and then stipped of their electrons. The so produced protons are further accelerated and guided to a target where the spallation takes place [50].*

The resulting protons (H^+) are then injected into a synchrotron, where they are further accelerated. Finally, the proton beam is directed onto a target made from liquid mercury, tantalum, or tungsten, where spallation occurs. Due to the collision at high energy, per atom hit, several neutrons ("spall") are ejected. However, most of the neutrons coming out of the target have a kinetic energy not suitable for research and must be turned into low-energy neutrons; they must be moderated to room temperature or colder. The neutrons emerging from the target are slowed down by guiding them through a neutron moderator, i.e. a tank filled with H_2O, or a cold liquid such as CH_4 (at 100 K) or H_2 (at 20 K). These neutrons are than guided to the various beam-lines around the target station (see figure 2.8).

Neutron pulses reaching the beam-line are then further sharpened by a chopper, a rotating metal disc with a hole. While this is done at most neutron instruments, PEARL does not have a chopper. These neutrons are then guided through a

Table 2.2 *Comparison of neutrons with different energies. Taken from N. J. Carron (2006)[73]*

Neutron type	Moderator	Energy / eV
Cold/Ultracold Neutrons	CH_4 (at 100 K), H_2 (at 20 K)	$< 10^{-3}$
Thermal/Slow Neutron	H_2O (at RT)	10^{-3}-10^{-1}
Epithermal Neutrons	-	10^{-1}-10^{+5}
Fast Neutrons	-	10^{+5}-10^{+8}
High Energy neutrons	-	$> 10^{+8}$

flight-tube or a focusing guide (a coating inside the guide focuses the neutrons by means of total reflection) to the sample. In a last stage before the sample, the beam is collimated to the desired size by a collimator, typically made from hexagonal boron nitride. While this is not always the case on all instruments it is done on PEARL and SNAP. Detectors around the sample then register the diffracted neutrons [50, 52]; in this work, mainly large area detectors were used (i.e. Anger camera). From the geometry, the flight path chopper-to-detector, and the time stamp of the arriving neutron follow the two variables most important for time-of-flight (TOF) neutron diffraction: the Bragg angle θ, and the wavelength λ (from the flight path L and the time stamp t follows $\lambda = \frac{h}{p} = \frac{h}{m}\frac{t}{L}$).

$$d = \frac{ht}{2mL} \cdot \frac{1}{\sin\theta} \tag{2.18}$$

This means that the Bragg law can be now written in a more suitable form for ToF neutron-diffraction [168].

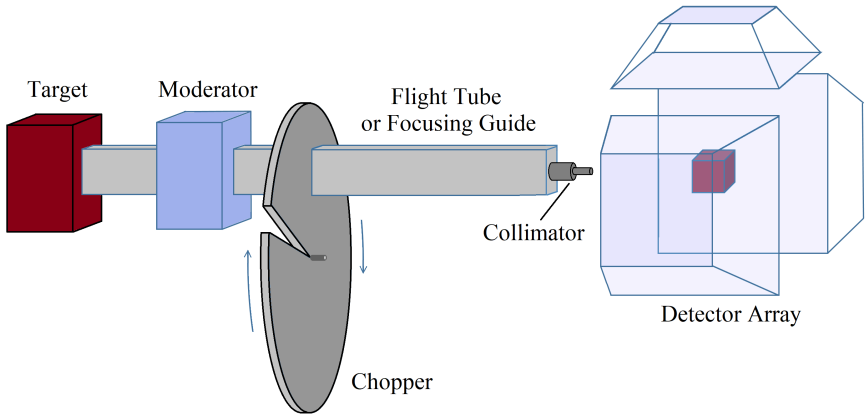

Figure 2.8 *Sketch of a beamline. The neutrons are produced in the target by spallation and then cooled down by a moderator. A chopper produces well defined pulses of neutrons which are then guided to the sample and collimated to the required beam shape [50].*

2.2.4 Neutron-Matter Interaction

While electron and X-ray diffraction is based on the interaction of the respective beam with the electron shell, neutrons interact with the nucleus; furthermore, neutrons can be scattered by magnetic materials due to their unpaired electrons. This makes neutron diffraction the method of choice for the detection of light elements without a big electron density (see figure 2.9). There are plenty ways in which neutrons can interact with matter, here, however, only elastic scattering ($k_i = k_f$) will be discussed - so scattering without an energy transfer from the neutron to the crystal. Other forms of scattering include in-elastic scattering ($k_i \neq k_f$), in which energy is transferred and absorption. However, these types of wave-matter interaction are non-trivial and are not further discussed.

In general there are two mechanisms by which neutrons can be elastically scattered. The first - and for this work more important - mechanism is the deflection from nucleus due to the nuclear strong force. This interaction occurs on a length scale of 10^{-15} m, while the wavelength of neutrons in diffraction experiments is carefully selected to be in the magnitude of 1 Å - the length scale of atomic distances in crystals. Because of the small size of the nucleus in relation to the atom and the short interaction range of the strong force, neutrons have low probability of interaction. This reduces the nucleus to a point scatterer with a spherical symmetry, that scatters in every direction equally. The interaction between the neutron and the atomic nucleus is represented by the Fermi pseudo-potential [175].

$$V(r) = \frac{4\pi\hbar^2}{m} b\delta(\mathbf{r}) \tag{2.19}$$

This potential is zero except very close to the nucleus (δ-function). The second interaction mechanism is due to the magnetic moment a neutron carries - neutrons interact with a magnetic scatterer, such as an unpaired atomic electron, and can therefore be used to reveal magnetic structures.

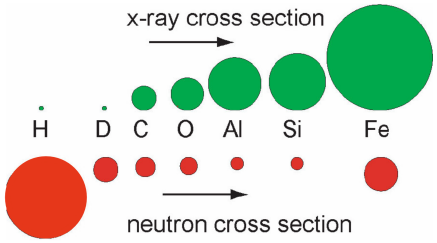

Figure 2.9 *Visualisation of the scattering cross sections of different atoms. While the X-ray scattering cross section increases with the atom size (and therefore the electrons in the shell), the neutron scattering cross section does not show such a behaviour.*

In general, neutrons that interact with matter can either be absorbed or scattered. Both phenomena can be quantified using a simple model, assuming that an interaction occurs if a neutron hits a specific area around the atom, the cross section σ_i, with b_i being the scattering or absorption length of the respective atom.

$$\begin{aligned} \sigma_a &= 4\pi b_a^2 \\ \sigma_s &= 4\pi b_s^2 \end{aligned} \tag{2.20}$$

In many cases, the absorption cross section is much smaller than the scattering cross section, and models can be applied to account for the absorption (see section 2.2.5). To describe the scattering capacity of an atom, the scattering cross section is used. The total number of neutrons scattered per unit of time, normalised against the flux of neutrons Φ_n, is thereby defined as the *total scattering cross-section* σ_t. Assuming a neutron beam entering a crystal of thickness dz, the neutron flux Φ_n of the beam will then decrease according to

$$\frac{d\Phi_n}{dz} = -n\sigma_t\Phi. \tag{2.21}$$

Solving this differential equation will lead to the exponential attenuation of the neutron beam intensity (cf. Beer-Lambert law). The total refers to all neutrons scattered through the surface of an enclosing sphere as well as all neutrons that are absorbed by the material. The scattered neutrons, however are usually not scattered equally in every direction; some orientations are preferred (see section 2.2). This however, gives rise to another cross-section, the *differential scattering cross-section* $\sigma_d = \frac{d\sigma_t}{d\Omega}$, that describes the neutrons scattered through a surface element dS, specified by the solid angle $d\Omega$.

$$\sigma_t = \int_0^{2\pi}\int_0^{\pi} \frac{d\sigma_t}{d\Omega} \cdot \sin\theta d\theta d\phi \tag{2.22}$$

The total scattering cross-section may than be recovered again by integrating over the full solid angle. The scattering cross-section of neutrons is generally

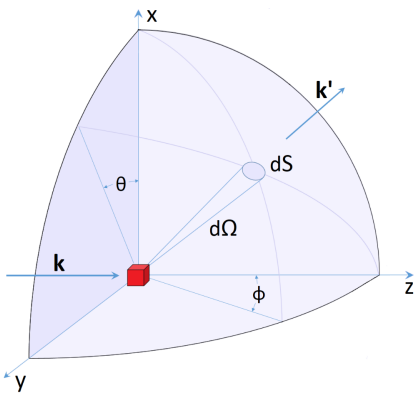

Figure 2.10 *Scattered neutrons through a surface element dS can be specified by the solid angle $d\Omega$.*

rather small and in the magnitude of
10^{-24} m^2, which means not many neutrons are actually scattered. Disadvantages that arises from this are the long collection time of more than 1 h and the relatively large sample volume of more than 0.01 mm^3, to obtain a sufficiently good quality diffraction pattern. However, since neutrons are not strongly attenuated, the actual sample can be confined in another material without a massive loss of intensity of the primary beam before it hits the actual sample [176].

Furthermore, scattering can be either coherent or incoherent, with the cross-sections σ_c and σ_i, respectively. In the first case, the scattered neutrons waves from different scattering centers interfere and thus coherent scattering contains information on the relative atomic positions - the structure of the material. In the latter case no interference occurs between the scattered neutron waves from different centers and thus the information on the relative positions of atoms is lost. The large incoherent scattering cross-section for Hydrogen (σ_c=1.76 barn and σ_i=80.27 barn) gives rise to a very large background and is the reason why deuterium (σ_c=5.59 barn and σ_i=2.05 barn) is mostly used for neutron diffraction instead [**?**].

2.2.5 Corrections in Neutron Diffraction

As described earlier, the interaction between neutrons and atoms only happens near the core, and a crystal lattice L can therefore mathematically be described as a sum of δ-functions. In one dimension a Dirac comb is given as

$$L(x) = comb_a(x) = \sum_{n=-\infty}^{\infty} \delta(x - na) \tag{2.23}$$

with a being the (equal) spacing of the δ-functions. The measured signal on a detector is the Fourier transform of the real space. For a Dirac comb, the Fourier transform becomes

$$\mathscr{F}_t\left[L(x)\right] = \int \sum_{n=-\infty}^{\infty} \delta(x - na) \cdot e^{-ikx} dx = \frac{2\pi}{a} \sum_{h=-\infty}^{\infty} \delta(k - \frac{2\pi}{a}h) \tag{2.24}$$

Note that the δ-functions becomes zero unless $\mathbf{k}$ is a reciprocal lattice vector. Similarly, for a 3-dimensional lattice a Dirac comb can be defined as $L(\mathbf{R}) =$

$\sum_{\mathbf{r}} \delta(\mathbf{R}-\mathbf{r})$. The respective Fourier transform can then be written as

$$\mathscr{F}_t\left[L(\mathbf{R})\right] = \int \sum_{\mathbf{r}} \delta(\mathbf{R}-\mathbf{r}) \cdot e^{-i\mathbf{kr}} d\mathbf{r} = \frac{(2\pi)^3}{V_c} \sum_{\mathbf{K}} \delta(\mathbf{Q}-\mathbf{K}). \tag{2.25}$$

Here, V_c is the unit-cell volume of the scattering crystal, $\mathbf{Q} = \mathbf{k}_i - \mathbf{k}_f$ is the momentum transfer to the sample and $\mathbf{K}$ is a reciprocal lattice vector. Note that $\mathbf{K} = h\mathbf{b}_1 + k\mathbf{b}_2 + l\mathbf{b}_3$ and that the factor $2\pi/|\mathbf{a}_i|$ is included in the respective reciprocal lattice vectors b_i (cf. equation 2.3).

In neutron diffraction, the differential cross section, $\mathrm{d}\sigma_t/\mathrm{d}\Omega$ is measured - to be more precise its coherent part $\mathrm{d}\sigma_c/\mathrm{d}\Omega$, that is the number of coherently scattered neutrons through angle 2θ per time into a volume element $\mathrm{d}\Omega$ normalised by the number of incident neutrons per area and time. The differential scattering cross section can be related to the structure factor $\mathcal{F}(\mathbf{K})$ as followed:

$$\frac{d\sigma_c}{d\Omega} = \frac{N_c}{V_c}(2\pi)^3 \sum_{\mathbf{K}} \delta(\mathbf{Q}-\mathbf{K}) \cdot |\mathcal{F}(\mathbf{K})|^2 \tag{2.26}$$

where N_c is the number of coherent scatterers. To obtain the number of scattered neutrons from a particular Bragg peak, we integrate over the solid angle of the detector and multiply by the incident integrated flux as follows:

$$I_c = \int d\lambda N(\lambda) d\Omega_f \frac{d\sigma_c}{d\Omega} = \int dk N(\lambda) d\Omega_f \frac{d\sigma_c}{d\Omega} \cdot \frac{-2\pi}{k^2} \tag{2.27}$$

Here, $k = |\mathbf{k}_i| = |\mathbf{k}_f|$ and $d\lambda = -\frac{2\pi}{k^2} dk$. Combining eq. 2.26 and 2.27 and multiplying by $\frac{\sin^2\theta/2}{\sin^2\theta/2}$ yields

$$I_c = V \frac{(2\pi)^4}{V_c^2 k^4} \int dk \cdot k^2 \frac{-\sin^2\theta/2}{\sin^2\theta/2} \cdot N(\lambda) \cdot d\Omega_f \cdot \delta(\mathbf{Q}-\mathbf{K}) \cdot |\mathcal{F}(\mathbf{K})|^2, \tag{2.28}$$

where V is the sample volume $V = N \cdot V_c$. The a volume element $d\mathbf{Q}$ can be written as

$$d\mathbf{Q} = \left[-2\sin^2\left(\frac{\theta}{2}\right)\right] k^2 dk \cdot \sin\theta d\theta d\phi \tag{2.29}$$

From applying equation 2.29 and integrating the structure factor can be related directly to I_c as shown in equation 2.30 [177].

$$I_c = V N(\lambda) \frac{\lambda^4 |\mathcal{F}(\mathbf{K})|^2}{2V_c^2 \sin^2 \frac{\theta}{2}}$$

$$\therefore \quad |\mathcal{F}(\mathbf{K})|^2 \propto I_c \cdot \frac{1}{N(\lambda)} \cdot \frac{\sin^2 \frac{\theta}{2}}{\lambda^4} \tag{2.30}$$

In equation 2.30, the first fraction represents the spectrum correction; this is the number of neutrons reaching the detector at a certain wavelength. To obtain this value, a nearly perfectly incoherent scatterer, e.g. Vanadium[178], is measured and the diffraction data is then divided by this spectrum. This correction is therefore often referred to as **Vanadium correction**. The second fraction is the **Lorentz correction** and takes into account the amount of time a given reflection remains in the diffraction condition. In common crystallographic convention the scattering angle is 2θ, and the Lorentz correction appears as $\sin^2\theta/\lambda^4$ [177].

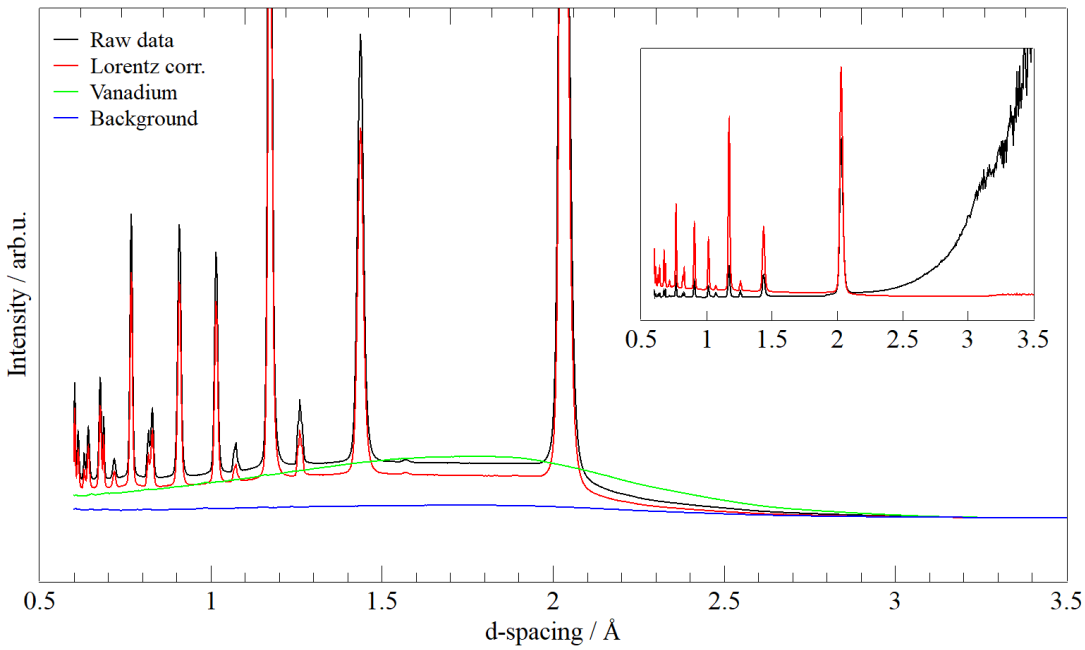

Figure 2.11 *A comparison of corrections in neutron-diffraction. The black curve gives the raw data after summing the ToF-data, the red one shows the same data set corrected by the Lorentz factor; Vanadium (green) and background (blue) spectra are shown ibid. The inset shows the raw data and the Lorentz-corrected one after division by the Vanadium and background spectra.*

Finally, scattered neutrons have to go through a proportion of the sample (and the sample environment, e.g. a DAC) and hence another correction has to be applied - the **attenuation correction**. In the most simple case, a neutron is scattered and has to go through a sample layer of thickness t before leaving the crystal again. On this way, it can be absorbed or scattered a second time.

$$I_r = I_o \cdot \sum_{n=0}^{i} e^{-N_i \sigma_i t} \tag{2.31}$$

This attenuation of the intensity of the reflected beam, I_r, can be expressed as an exponential according to equation 2.31. Here, N_i is the atom density (atoms/volume) and σ_i the respective cross section for an atom i.
Due to the small sample volume in DACs, this attenuation can be neglected, however, a more complex model for the attenuation has to be applied to take into account the attenuation caused by the diamond windows [179] or the gasket [2]. Note that, depending on the geometry, the reflected beam passes through a different thicknesses of diamond and gasket. A detailed discussion of this issue is given in chapter 4 where an in-depth procedure for the data reduction of single-crystal data in diamond anvil cells is established.

2.2.6 The orientation matrix (UB matrix)

In single crystal diffraction another problem arises, namely the orientation of the crystal relative to the diffractometer. As discussed earlier (see page 27), every reciprocal lattice point can be described as

$$\mathbf{K} = h\mathbf{b}_1 + k\mathbf{b}_2 + l\mathbf{b}_3.$$

Following Giaccovazzo *et al.*, this equation can also equivalently be written in its matrix form with a basis set $\mathbf{A^*} = (\mathbf{b}_1, \mathbf{b}_2, \mathbf{b}_3)$ and a coordinate matrix $\mathbf{h} = (h, k, l)$ [165].

$$\mathbf{K} = \begin{pmatrix} \mathbf{b}_1 \\ \mathbf{b}_2 \\ \mathbf{b}_3 \end{pmatrix} \begin{pmatrix} h \\ k \\ l \end{pmatrix} = \mathbf{A^*h} \tag{2.32}$$

Scattering occurs, if the scattering vector $\mathbf{Q} = \mathbf{k}' - \mathbf{k}$ equals the reciprocal lattice

vector **K**. For each reflection, the magnitude of its scattering vector **Q** is invariant with respect to the orientation of the crystal. However, as the crystal rotates, the direction of **Q** changes and, therefore, the wavelength (radius of the Ewald sphere) of the respective Bragg event. In figure 2.12, for example, such a rotation about an angle γ along the $\mathbf{b}_3$ axis is shown.

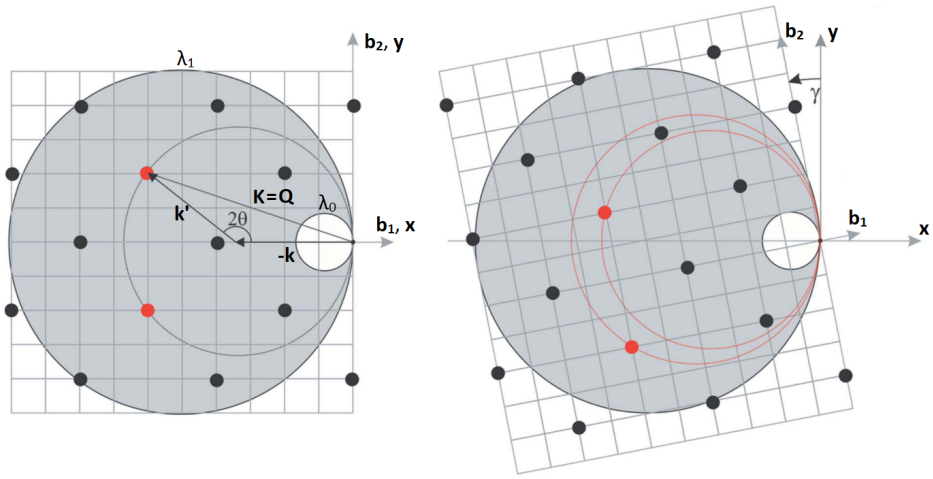

Figure 2.12 *Rotating a single crystal about an angle γ along the $\mathbf{b}_3$ axis leads to a different diffraction pattern. Taken from Guthrie [49].*

A problem thereby is that **Q** is measured in the instrument frame of reference, while the reciprocal lattice vector is not. Equation 2.33 now relates **Q** and **K**; in this equation the **R** matrix is the rotation matrix of the goniometer on which the crystal is mounted. The **B** matrix converts the coordinate system of the crystal into Cartesian coordinates and the **U** matrix represents the rotation from this Cartesian coordinate frame to the Cartesian coordinate frame of the goniometer.

$$\mathbf{Q} = \mathbf{R} \cdot \mathbf{U} \cdot \mathbf{B} \cdot \mathbf{K} \tag{2.33}$$

The orientation of the crystal with respect to the instrument frame, and therefore the incident beam **k**, is therefore given by the 3×3 orientation matrix **UB**. To obtain the **UB** matrix from the diffraction data, at least two non-colinear reflections and the lattice parameters are needed. This can be done with the ISAW package which is implemented in the the MANTID software suite (see Chatterjee *et al.*, 2002 [180]).

2.3 Data Processing and Structure Determination

Using either single crystals or powders, neutron diffraction can be used to measure the structure factor $|\mathcal{F}(\mathbf{K})|^2 \propto I_c$ for various values of (hkl). However, a direct Fourier inversion of diffraction data to yield the crystal structures is not possible because only the magnitude of $|\mathcal{F}(\mathbf{K})|$ is measured and not its phase. This is known as the phase-problem. Hence a model must be fitted to the data.

2.3.1 Le-Bail Extraction and Rietveld Refinement

The first step in any attempted structure solution is the determination of the lattice parameters; for this, the observed peak positions are used and various software packages are available [181–184]. This is followed by finding the correct space group by narrowing down the possible ones based on the systematic absence of peaks [185]. Then, an estimation of the diffraction intensities is usually done by Le-Bail extraction (LB). The advantage of this method is that it does not need any input beside the (possible) space group. An LB extraction yields best possible intensity value for all indexed peaks, by setting all $\mathcal{F}_{calc} = 1$ and then performing a steepest descent minimisation. After a convergence criterion is reached, one obtains a first estimation of the $\mathcal{F}_{obs}$. For completely overlapped reflections the intensities are apportioned according to reflection multiplicity (equal $\mathcal{F}_{calc}$) and for partially overlapped reflections the intensity will be pushed away from equal $\mathcal{F}_{hkl}$ values only as much as needed [186].

However, a Le-Bail extraction can fit any data, whether it is physically reasonable or not. Furthermore, it is not possible to directly extract the atom coordinates from a Le-Bail extraction; for that purpose a Rietveld-refinement is needed.

The principle of Rietveld's profile refinement method is to minimise a function M which analyses the difference between a calculated profile y_{calc} and the observed data y_{obs}. Hugo Rietveld defined the equation in his famous paper in 1969 [187] as

$$M = \sum_i W_i \left\{ |\mathcal{F}_{i,obs}|^2 - \frac{1}{c} \cdot |\mathcal{F}_{i,calc}|^2 \right\}^2 = \sum_i W_i \left\{ y_{i,obs} - \frac{1}{c} \cdot y_{i,calc} \right\}^2 . \quad (2.34)$$

In this formula, W_i is the statistical weight and c is a scale factor. In modern applications pseudo-Voigt functions are used to describe the peak shape - Rietveld assumed a Gaussian peak shape, however. In the Gaussian case, the peak profile of the k-th peak at position i can be expressed as

$$y_i = |\mathcal{F}_{i,calc}|^2 \cdot \frac{A}{\sqrt{H_k}} \cdot e^{\frac{B\cdot(d_i-d_k)^2}{H_k^2}} \tag{2.35}$$

with A and B being constants and H_k being the full width at half-maximum of the respective peak. The structure factor for this model is given by equation 2.16. This equation is corrected for the thermal movement of atoms using an atomic displacement parameter B_j [188]. For the isotropic case, $B_j = 8\pi^2 \left\langle u_j^2 \right\rangle$. The structure factor is then given by equation 2.36.

$$\mathcal{F}(hkl) = \sum_j b_j e^{-i2\pi(h\mathbf{b}_1+k\mathbf{b}_2+l\mathbf{b}_3)} \cdot e^{-B_j \cdot \frac{\sin^2\frac{\theta}{2}}{\lambda^2}} \tag{2.36}$$

In a more general case, the displacement is modelled as an ellipsoid - the atom displacement is then given by a second rank tensor with six independent u_{ij} displacement parameters, the 3x3 matrix $\mathbf{u}_{ij}$.

$$\mathcal{F}(hkl) = \mathcal{F}(\mathbf{h}) = \sum_j b_j e^{-i2\pi(h\mathbf{b}_1+k\mathbf{b}_2+l\mathbf{b}_3)} \cdot e^{-2\pi^2\left\langle(\mathbf{u}\cdot\mathbf{h})^2\right\rangle} \tag{2.37}$$

Beside the atom displacement, several other properties of the sample can be refined, such as peak broadening due to micro-strain or preferred orientation [187].
A similar method can be used to fit single crystal data after the structure factors and their sigmas are obtained by integrating the peaks.

2.3.2 Monte-Carlo Simulated-Annealing (MCSA)

Simulated annealing (SA) is a Monte-Carlo (MC) approach to overcome the phase problem in crystallography [189–191] and to determine the atom positions in a given unit cell and space group. It is used to explore the configuration space of a unit cell and to locate the global minimum given a suitable cost function. This cost function is usually tightly bound to the diffraction pattern; to be more specific to intensities extracted from an initial Le-Bail [186] fit or the Rietveld intensities of a related structure. Conventionally, the weighted R-factor (R_w) is used as the cost function, defined as

$$R_w = \left(\frac{M}{\sum_i w_i y_{i,obs}^2} \right)^{\frac{1}{2}}. \tag{2.38}$$

Additionally the algorithm uses the unit cell (with its symmetry, if known) and the expected cell contents (e.g. atoms, molecules or molecule fragments) as input. The latter can be defined as one or more rigid bodies, that is a body of atoms constrained into a certain geometry such as a well defined water molecule, to speed up computation time. The position parameters of this input is then randomised to generate a starting configuration, and R_w is calculated by an LB-extraction. The MC-part of the algorithm then generates a second configuration by randomly displacing atoms, and the change ΔR_w in this displacement is calculated for the two configurations. This might lead to either an improved or worse fit to the data and is repeated until a convergence criterion is met [192].

A problem of such an approach is that the algorithm often ends in a local rather than a global minimum, which might satisfy the cost function but does not give the overall best solution - in this case the solution of the correct crystal structure. To overcome this problem, the SA part of the algorithm allows the system to move away from a local minimum; a probability P of a new structure replacing the original structure even if the new one is worse than the original one is defined as

$$P = e^{-R_{wp}/T}. \tag{2.39}$$

The parameter T can be thought of as the temperature in a thermodynamic system, hence the term "simulated annealing". The process of accepting or rejecting possible structures allows for a large sampling of the configuration space. By decreasing T, that is "cooling", the configuration space gets more and more constrained after every iteration, eventually leading to a global minimum. The entire process is repeated several times and the obtained global minimum should be a recurrent solution.
Monte-Carlo Simulated-Annealing is implemented in many crystallographic software packages. For this work, the GSAS-I and GSAS-II software suites were used [181–183].

Chapter 3

Experimental Techniques: A Toolbox for Neutron-Diffraction

Atmospheric pressure, or ambient pressure, is the pressure caused by the atmosphere of Earth at sea level, and is defined as 1 atm = 101325 Pa = 0.101325 MPa. While it might be tempting to think that this pressure is "normal" in our universe, it is actually exactly the opposite - our pressure scale ranges from the (theoretical) 0 Pa value of a perfect vacuum at, under 10^{-18} Pa in outer space over several hundreds and thousands of GPa in the interior of satellites, planets and stars, up to $>10^{34}$ Pa in neutron stars and black holes [193]. Pressure thus serves as a versatile tool in the investigation of minerals that form the deep interior of the Earth and other planets.

Increased pressure alters the energy of atomic bonds by forcing atoms closer together in a smaller volume. Pressure thus serves as a powerful probe of atomic interactions and chemical bonding and allows one to tune bond-lengths in molecules as well as the separation of molecules. High pressure is a very efficient way to add energy to a system. While it takes more than 10,000 K to increase the internal energy by 1 eV per atom - a larger temperature than the one the surface of the sun - the same energy change can be achieved by a pressure increase of only about 20 GPa. This value is derived from the expression for the internal energy dU= TdS - pdV and from the bulk modulus $B_s = -V(\frac{\partial p}{\partial V})_s$. As a bulk modulus, the bulk modulus $B_S = 8.5 \cdot 10^9$ Pa of hexagonal ice was used [194]. Such a pressure is nowadays easily achieved. High-pressure thus offers a deeper understanding of intermolecular interactions, such as hydrogen bonds

(H-bonds) and hydrophilic/hydrophobic interactions [195] which are relevant to many branches of science such as chemistry (e.g. water as a solvent [69]) and biology (DNA and protein folding due to H-bonds [76]).

Finally, many novel materials can only be synthesised under high pressure [196], or change their properties dramatically if exposed to such extreme conditions, including super-hard materials and high-temperature superconductors. The record holding high-temperature superconductor (H_3S with a T_c of 203 K), for example, is formed from H_2S at about 90 GPa [91, 93, 97, 98]; and even a superconductor with a T_c of 287.7 K (C-S-H ternary at 267 GPa) has been reported but is disputed in the field [96].

3.1 Generating High Pressure: General Concepts and Pressure Devices

Understanding how matter acts under the influence of pressure is relevant to many subjects such as physics, astronomy, geology, material science, chemistry, and biology. Over the years, various devices were invented to study materials under pressure, ranging from simple gas cells (P_{max}=0.5 GPa [197]), over the piston-cylinder press (P_{max}=2 GPa) and multi-anvil press (P_{max}=25 GPa [198, 199]) to the Paris-Edinburgh press (PE-press, P_{max}=40 GPa [197, 200–202]) and finally to diamond anvil cells (DAC, P_{max} >1 TPa was reported [203, 204]). Furthermore, even higher pressures can be achieved by the use of shock wave compression (P_{max} >TPa). A name intrinsically tied to high pressure physics is hereby Percy Williams Bridgman, who received a Nobel Prize in 1946 for advancing this area of physics.

$$P = \frac{F}{A} \tag{3.1}$$

Despite the variety of pressure cells, all of them are based on the same simple principle: pressure equals force over area (cf. equation 3.1). To increase the pressure, the force has to be increased or the area decreased. While the former is limited by the strength of the pressure devices' material, the latter is limited by the required sample volume for an experiment. In general this means: the higher the pressure, the smaller the sample volume. This proves to be a problem, for

neutron diffraction (see chapter 2); due to the combination of the weak interaction of the nuclear force and the low neutron flux produced at neutron sources, large sample volumes in the magnitude of several mm^3 are usually needed in neutron diffraction experiments to improve the sample signal-to-background ratio.

3.1.1 The Gas Cell

Gas cells are a very simple device for reaching comparably low pressures and, depending on the cell material, pressures below 1 GPa can be achieved. These cells can be used for powder, liquid and single-crystal samples. In a gas cell the pressure is generated on a sample by a compressed gas such as helium, nitrogen or hydrogen. As can be seen in figure 3.1, a gas cell is composed of a cylindrical body (1) with a sample chamber (2) located in the centre that is connected to a capstan compressor pump via a sealed capillary (3) guided ino the cell through a seal plug (4); at the other end, the cell is sealed by a Bridgman seal (7-8) [205]. A sample is placed into the sample chamber, gas is compressed by the pump and led into the gas cell. In this work a gas cell of this type was used in the experiments on nitrogen sX-hydrate (see chapter 8). The cell body was composed of a 7075 Aluminium Alloy which allows for a maximum pressure of 0.45 GPa [51] due to the use of hydrogen as a pressure transmitting gas in this experiment. Comparable pressure cells made from a null-scattering titanium-zirconium alloy (TiZr) reach pressures up to 0.8 GPa, but are - due to an embrittlement caused by H_2 - not suitable for experiments with hydrogen [197].

The advantage of this pressure vessel is that it allows for a large sample volume of up to 280 mm^3. After loading and checking for leaks using helium, the cell can easily be mounted into a cryostat. Furthermore, this set-up allows changing the gas type during the experiment by pumping-off and refilling the cell.

3.1.2 The Paris-Edinburgh Press

For a long time high pressure experiments were limited to about 2.5 GPa for neutron diffraction due to the large sample volume needed. In 1992, Besson *et al.* proposed a new type of press, which was able to increase this pressure window for neutron diffraction to 10 GPa - the Paris Edinburgh press (PE-press) [197, 200]. It is a small, lightweight hydraulic press with apertures for incident and scattered radiation. It is primarily used with opposed anvils, but it has also been used with

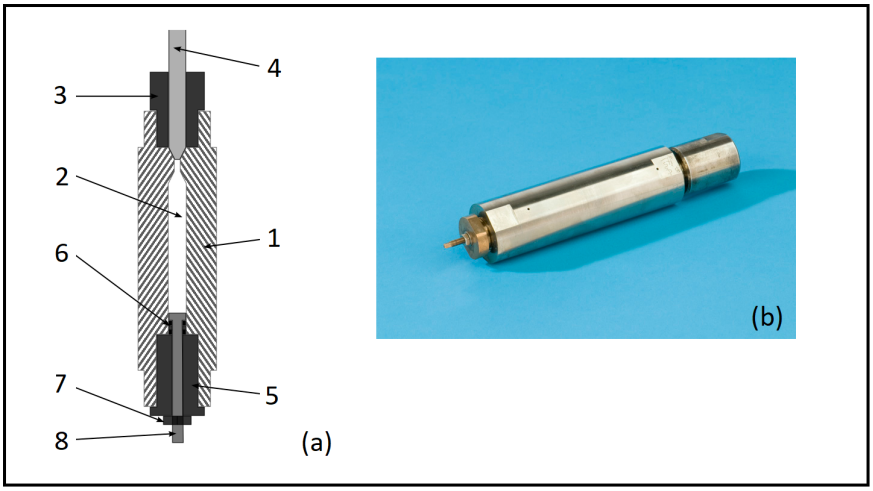

Figure 3.1 *A schematic of a gas cell (a) and a picture of a gas cell as used at the ISIS neutron facility (b) (taken from [51]). Note that the piston and lead/copper rings located at the bottom form a Bridgman seal.*

multi-anvils assemblies. For a relatively small and light frame, it provides a high load capacity of up to 250 tonnes (depending on the model) combined with a large sample volume of tens of cubic millimeters. With its sintered diamond anvils, the fourth generation is able to reach pressures as high as 40 GPa [201, 202]. It has also been modified widely to suit other purposes: PE-presses for cryo-loadings, gas loadings, heating experiments [197, 206, 207].

Principles and Design The smallest *PE*-press (VX type, see [208]) has a weight of about 60 kg and can - in theory - be carried around by one person; as such it is a "lightweight" among large volume presses. Comparable pressure devices with a similar load capacity, such as multi-anvil presses, usually are several meters square and weigh over a tonne. A schematic sketch of a *PE*-press is given in figure 3.2. The cell-body itself is usually made of steel and various sizes and designs are available. The two most common variants are the V-type cells which has four support columns between the two cell halves, and the VX-type with two support columns [197]. Not surprisingly it is the the V-type cell design that supports a greater load, however, the VX-cell offers a larger angular opening which proves beneficial in some circumstances. In both cases, the cells retain the same core design with the opposed anvil assembly at the center.

The cell-body employs two pistons; the upper piston is fixed against a removable

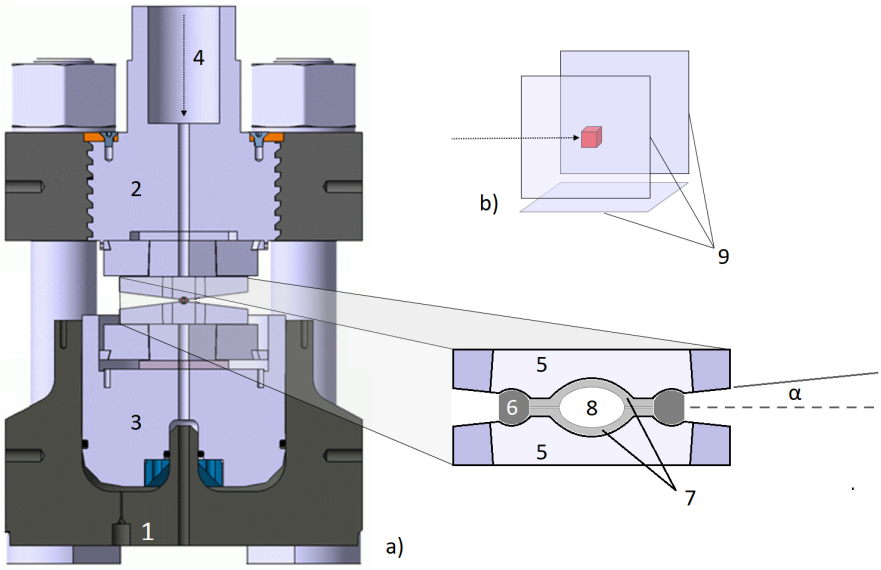

Figure 3.2 *a) Schematic sketch of a Paris-Edinburgh Press V4 with its primary parts: cell-body, pistons (2,3), collimator hole (4), anvils (5), gasket (6,7), and sample (8); The broken arrows indicate the direction the neutrons enter the pressure cell in the transverse mode.*
b) Detector arrangement (9) at a neutron beam-line with the PE-press symbolised by the red cube.

'breech' while the other one is driven by a hydraulic fluid and provides thrust. The hydraulic piston is driven by an external compressor connected to an inlet at the bottom of the press, and allows for a maximum load of 50-450 tonnes depending on the cell-design. Usually, oil is used as a hydraulic fluid, but in cryo-experiments helium is used instead. The breech is a large, threaded component which is loosened to allow access to the anvil assembly for loading and is tightened down into position before load is applied to the pistons.

A range of anvils is available for use in the *PE*-press, varying in both their construction material and profile design. Typically the anvils are machined from hard materials like tungsten carbide (WC), sintered diamond (SD), zirconia-toughened-alumina (ZTA), or cubic boron nitride (cBN), stabilised by a steel binding ring. Anvils feature either a single-toroid or double-toroid profile and a central cup to increase the sample volume [209]. The single-toroid allows for twice the sample volume compared to the double-toroid one, at the cost of the pressure performance. For all anvil designs, the surface of the anvils around the sample must be shielded in order to minimise neutron scattering by the anvils, usually by applying a thin layer of cadmium. For the experiments that required

heating, a set of zirconia-toughened-alumina (ZTA, Al_2O_3 and ZrO_2) anvils was used. This material reduces the pressure performance of the *PE*-press to below 10 GPa but allows for cryo-loading and *in-situ* heating/cooling of the sample. Using ZTA anvils, the temperature range lies between 100 K and 500 K. In brief, a heating element and a cooling system for a cooling agent is embedded in the anvils, heating the anvils, gasket and sample. For experiments that did not require heating above room temperature sintered diamond was used as an anvil material due to its better pressure performance compared to ZTA.

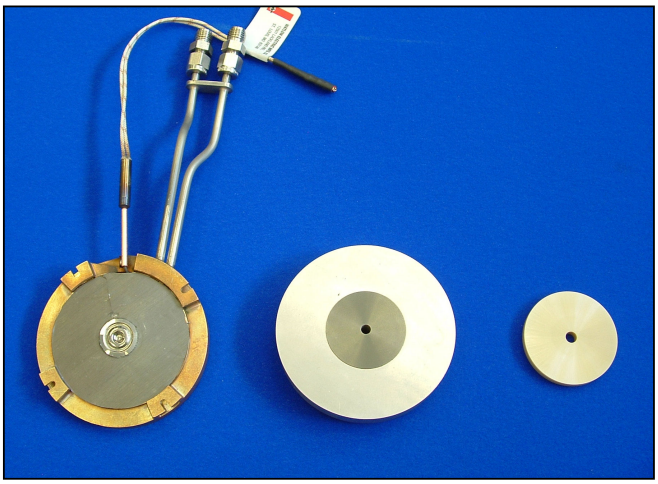

Figure 3.3 *Picture of a set of ZTA anvils that allow for the temperature range between 100 K to 500 K. Taken from the ISIS homepage [52].*

Finally, a metal gasket is used to fully encapsulate the sample and placed between the two anvils. There are several gasket designs available for the use in a *PE*-press which prove essential for the functionality of the design [197]. In its simplest form, the gasket is formed from two washers in the shape of a cup, radially supported by a toroid ring. It is sealed purely by applying a load on the press. This type of gasket has a holding capacity of roughly 40 mm^3. As both the incident beam as well as the scattered neutrons must pass through the gasket, the material used for gaskets is usually a null-scattering titanium zirconium alloy (TiZr), which does not contribute to the neutron diffraction pattern due to its zero net scattering length [200, 210].

As the press was developed for neutron-scattering, its design is such that the incident neutron beam can impinge on the sample through either through the back of one anvil (transverse mode) or through the gasket (longitudinal mode).

The different diffraction geometries allow for access of different diffraction angles; i.e. on PEARL, the transverse mode covers 81.2 deg $< 2\theta <$ 98.8 deg, while the longitudinal mode allowes for access of the low-angle (20 deg $< 2\theta <$ 60 deg) and high-angle banks (100 deg $< 2\theta <$ 160 deg). The the transverse mode uses a hole drilled from one end of the cell through to the back of one anvil, minimising attenuation of the beam before it reaches the sample. The scattered neutrons are then collected at 90^o relative to the incident beam. This is geometry that is predominately used in ToF neutron-scattering.

3.1.3 The Diamond Anvil Cell

Percy Bridgman revolutionised the field of high pressures with his development of an opposed-anvil device with small flat areas made of tungsten carbide that were pressed one against the other with a lever-arm, achieving pressures of a few GPa. In the post-Bridgman era (after 1950) this approach was revolutionised by C. E. Weir, E. R. Lippincott, A. Van Valkenburg, and E. N. Bunting, a group of scientists from different fields, by using single-crystalline diamonds as anvils [211]. This marked the beginning of the era of diamond anvil cells (DACs). Using diamonds as anvils increased the pressure range significantly and the transparent pressure windows allowed for a huge variety of experiments: Spectroscopy, Microscopy, Laser-heating, X-ray scattering [203]. Later the range of possible experiments was extended to conductivity [212] and even NMR techniques [213]. Over the last several decades, high pressure physics advanced to the current point by the use of diamond anvil cells (DACs, see figure 3.2C) which allow pressures up to 1 TPa [204].

Principles and Design The basic principle of a diamond anvil cell is simple; a DAC comprises a cell body made from hardened steel or beryllium-copper that drives two opposing diamonds together against the sample, which is contained in a small sample chamber of a metal gasket usually made from stainless steel, beryllium-copper or rhenium. With the sample an optional pressure marker and a pressure-transmitting medium (PTM) are placed in the sample chamber. The latter ensures quasi-hydrostatic conditions during the pressure increase; commonly used PTMs are ethanol/methanol mixtures, salts (KCl, NaCl), soft metals (Bi), or liquified gases (He, Ar, Ne).

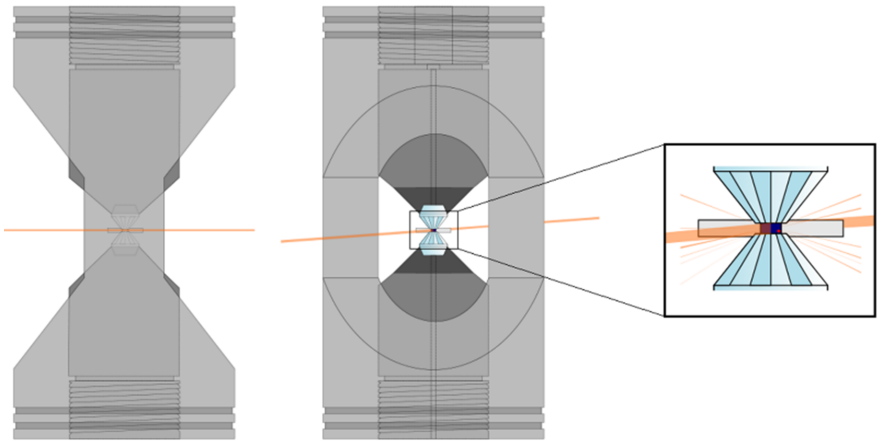

Figure 3.4 *Sketch of a large-volume diamond anvil cell for neutron diffraction as used for this work. For this type of diamond anvil cell, the primary neutron beam can enter the sample chamber either through the gasket as shown (longitudinal mode), or along the presser axis through the diamonds (transverse mode). Taken from Massani et al. [2].*

Usually the diamonds used in a typical DAC are naturally formed and of high purity. Their size varies depending on the application but are usually around 0.3 carats and cut in a similar fashion to the gem stones (brilliant cut). However, the culet (diamond tip) of both diamonds is polished to form a small flat surface varying in size from 20-600 μm wide [214]. Also, special diamond designs are available, such as partial bevelled diamonds or two-stage anvils for very high pressure up to $>$ 600 GPa [214–216] and even higher pressures of up to 1 TPa by using nano-diamonds have been reported; see for example [204].) In some cases synthetic diamonds with small electrical components embedded under the culet surface (coils for magnetic measurements), or diamonds with metal deposited onto the culet (NMR) are used. However, synthetic diamonds are usually inferior to their natural counterparts in terms or purity and hence transmission of light and X-rays.
For the large-volume DACs primarily used in this work, synthetic diamonds are used despite their disadvantages. Diamonds used in this work typically have a girdle diameter of 4 mm with a culet of 1-2 mm, and hence natural diamonds would be too expensive (3-5 ct diamonds).

To hold the anvils in the DAC, they are normally glued into the seats with a suitable glue. The seats act thereby as a bridge between the cell-body and the anvils and are made out of a hard material such as tungsten carbide. The hardened steel used for the body is too soft for this purpose; seats made from such

a softer material would cause the diamonds to deform the seat and the cell would lose its alignment (resulting in the inevitable death of the anvils). Originally, seats were just of a simple flat design and the diamonds sat on them held in position by glue, however, modern DACs mostly use the Boehler-Almax (B-A) design [217]; both the seat as well as the table of the diamond is conically polished so that the diamond perfectly fits into its negative polished into the seat. This design further stabilises and supports the anvil resulting in fewer anvil failures (such as cracking). A positive side effect is a greatly increased angular access, which is beneficial for diffraction experiments.

The seats are then mounted on the cell-body which varies depending on the application. Among the most common designs are the Merrill-Bassett cell, the plate cell, and piston-cylinder type cells [197]. The only limitation for the cell body is that it must keep the seats - and hence the diamonds in place since even a small misalignment of a few μm usually results in an anvil failure. In this work, a Merrill-Bassett type cell was used for preliminary experiments, but the main experiments at the SNS used a piston-cylinder cell as shown in figure 3.4. The exact design was published in 2017 by Boehler *et al.* and Haberl *et al.* (see [218–220]).

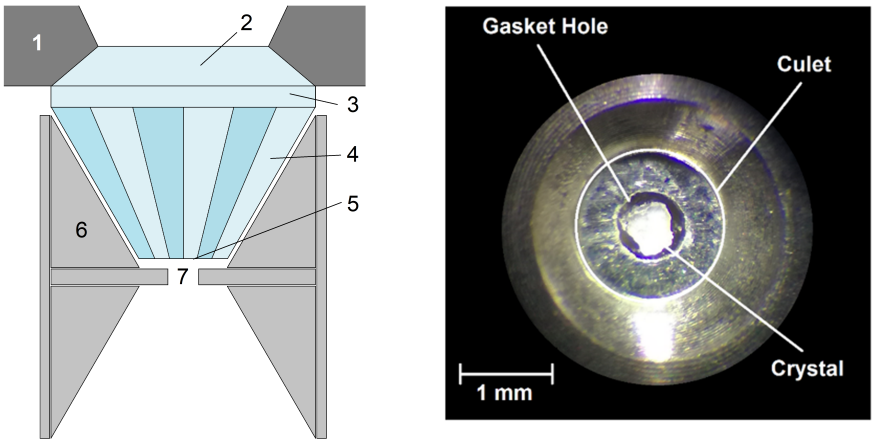

Figure 3.5 *(left) Sketch of a diamond with a 4-piece gasket as used in a large-volume diamond anvil cell for neutron diffraction. WC-seat (1), table (2), girdle (3), pavillion and facets (4), culet (5), gasket (6), and gasket-hole (7). (right) A microscope picture of a gasket taken through the top-anvil. Note that the 4-piece gasket can be seen covering the whole pavillion of the diamond-anvil. Picture taken from Massani et al. [2].*

A small metal gasket with a hole in the middle ("gasket hole") is placed between the two diamonds to encapsulate the sample. Most DACs use a simple pre-indented washer made from hardened steel or rhenium for that purpose; the gasket is first indented to the required thickness (20-60 μm) and then a hole is drilled in its centre by spark erosion (electric discharge machining) or laser drilling [197]. For all preliminary experiments carried out in the lab with a Merrill-Bessett type cell, this gasket was used.
However, for the large volume DAC, a more elaborate design of gasket was chosen. In this work usually a 4-piece gasket (see figure 3.5) is used which consists of two conical Al-washers between which a washer made from steel or rhenium is placed. These three parts are further supported by an aluminum sleeve. Similar to the primitive gasket, the assembly is indented first to 60-120 μm and then drilled (mechanically or with a spark eroder). This conical aluminium construction, despite harder to machine, radially supports the diamonds further which is crucial for the large diamond-anvils used in this kind of DAC [218, 219].

Similar to the *PE*-press, DACs in neutron-diffraction can be used in a transverse geometry where the primary beam enters the cell through a hole in the cell body and goes through the upstream diamond; but also a longitudinal mode is possible where the primary beam enters through the gasket. In both cases, a rather complex attenuation correction is required - see chapters 2 for the diamond attenuation correction [179] and chapter 4 for the attenuation correction for the 4-piece gasket.

3.2 Diffraction Instruments

While the experiments with the gas cell and the *PE*-press were carried out at the ISIS spallation neutron source at the Rutherford Appleton Laboratory (RAL), the DAC experiments needed a brighter neutron source (high neutron flux and low lower divergence). To this date, the Spallation Neutron Source (SNS) at the Oak Ridge National Laboratories (ORNL) is the only facility with a flux high enough for this type of experiment. The experiments were carried out on the PEARL instrument (ISIS) and at TOPAZ and SNAP (SNS).

Both neutron sources use large area detectors with several modules and data are collected as time-of-flight spectra in each pixel of these modules. Subsequently,

the collected data are then put through a preprocessing procedure known as 'focussing' in which the ToF-spectra for each pixel in a module are converted into d-spacing using Bragg's Law (see chapter 2) and summed together. An advantage of this approach is that the diffaction pattern for each module (theoretically for each pixel) can then be processed on its own. The combined diffraction patterns for all pixels/modules together then give the diffraction pattern that can be used for analysis. The error in the number of counts detected in each pixel (N) for a given ToF (the intensity) is given by a Poisson statistics and hence by $\sqrt{N}$ and is carried through the focussing procedure. Since this is a standard procedure, it is not tested further in this work. During this process several corrections are usually applied (see chapter 2).

3.2.1 PEARL

The PEARL instrument is a specialised high-pressure powder-diffraction beamline and is optimally designed to be used with Paris-Edinburgh presses. PEARL has a primary flight-path of 12.8 m (methane moderator to sample) and is equipped with three ZnS scintillator detector banks consisting of multiple modules each which are either 0.8 m or 1.2 m from the sample [52]. The detector banks are located at 90^o ($81.2^o < 2\theta < 98.8^o$), a low angle bank covering a range of $20.0^o < 2\theta < 60.0^o$, and a back-scattering bank covering a range of $100.0^o < 2\theta < 160.0^o$. Though this may seem like a large area of detector coverage in the standard Paris-Edinburgh press geometry only some of these detectors can be accessed at any one time. In transverse mode (through-anvil) the banks at 90^o are the only ones that can be accessed. In longitudinal mode (through-gasket) the other banks can be accessed, with the 90^o bank being shielded by the press itself [221].

Corrections on PEARL In the transverse geometry, the incident beam first passes through one of the anvils and the gasket. After reaching the sample the beam is diffracted and traverses through the remainder of the sample and gasket again; the diffracted beam is hence attenuated and the attenuation depends on the geometry of anvil, sample and gasket material and the scattering angle. The attenuation correction for this is built into the focusing routine used in Mantid on PEARL and is based on a Monte-Carlo ray-tracing approach [221].

3.2.2 TOPAZ

TOPAZ is the dedicated single-crystal instrument at the Spallation Neutron Source. TOPAZ is a high-resolution single-crystal diffractometer using time-of-flight Laue technique with a decoupled poisoned hydrogen moderator (i.e. H_2 with Cd to prolong the lifetime of the H_2) [222, 223] and an array of neutron area detectors distributed spherically about the sample. The wide neutron wavelength band of 3.1 Å is well suited for efficient 3D-mapping of Bragg scattering in reciprocal space in the Q-range 0.45-25.00 $Å^{-1}$ (d-spacing range 0.25-14.00 Å). As such, TOPAZ is well suited for determining atomic positions and displacement parameters of light elements, such as hydrogen. The high real-space resolution down to 0.25 Å d-spacing, allows for precise measurements of atom-distances in H-bonds. Currently, TOPAZ has 24 of 48 detector ports populated with Anger camera modules covering about 3.0 sr in solid angle. TOPAZ uses a 18 m long bent focussing guide which focusses the beam to 2.0-4.0 mm. The high-precision goniometer is fixed to $X = 135^o$ and samples can be freely rotated about two axis, Φ and Ω (see chapter 4, in particular figure 4.6) [224].

3.2.3 SNAP

The Spallation Neutrons and Pressure (SNAP) instrument is a high-flux diffractometer primarily used for powder diffraction under high pressure. SNAP uses area detectors of the same type as TOPAZ arranged in two 3x3 detector banks. The position of the two detector benches can be rearranged along a circle around the sample according to the experiment design. This allows for an angular coverage of $26^o < 2\Theta < 138^o$, depending on the detector positions (horizontal and vertical coverage: $\pm 22.5^o$). Compared to the neutron optics used on TOPAZ, the beam-focusing optics on SNAP are significantly shorter (guide length: 2.4 m; source-to-sample distance: 15 m), allowing for a high neutron flux at the expense of a higher divergence and complex beam profile. Hence, the instrument is well suited to deal with various complex sample environments for high-pressure studies.

Corrections on SNAP and TOPAZ Since most experiments carried out on these two instruments are part of the development of single-crystal neutron-diffraction in diamond anvil cells for the SNAP beam-line, all corrections are discussed in detail in chapter 4.

3.3 Ancillary Techniques and Pressure Scales

3.3.1 Raman Spectroscopy

In 1928 C. V. Raman and K. S. Krishnan first published their paper on "A New Type of Secondary Radiation", a study that is the basis for what is now known as Raman Spectroscopy [225]. This technique proved to be an immensly useful tool for the investigations of molecules. In the simplest case it can be used to identify the presence of different molecular species in a sample. As such it can be used to confirm a successful loading of a DAC especially if the sample can not be seen by microscopic techniques (e.g. gases). Since the spectrum of a sample is dependent on its environment, it can also be used to observe phase transitions by tracking the Raman spectrum as a function of pressure and temperature. Usually such changes can be observed by discontinuities, peak-shifting, and peak-splitting. Raman spectra can thereby easily be recorded through the two diamond windows which are transparent to the laser light used in Raman spectroscopy.

In this work, Raman spectroscopy is only used as a secondary technique and for preliminary measurements. Hence, only a basic introduction to this theory is provided here. A more thorough explanation and discussion of this technique can be found elsewhere (c.f. Smith and Dent [226]).

When light is scattered by molecules, the electromagnetic wave can either be scattered elastically or inelastically (see figure 3.6); the former scattering process of light is known as *Rayleigh* scattering, while the latter is *Raman* scattering [225]. In both cases the electromagnetic wave is absorbed by the molecule which is promoted into a higher virtual state: the molecule becomes a small radiating dipole. The light is re-emitted shortly afterwards and the molecule drops back to a lower energy state. While in the case of Rayleigh scattering (elastic scattering) the re-emitted photon has the same frequency as the initially absorbed photon, in the case of (inelastic) Raman scattering the frequency changes. This second process, Raman scattering, is by far weaker, only occurring approximately once in every 10^7 Rayleigh scattering events [226].

In cases where the Raman scattering process causes a transition in the vibrational or librational mode of the molecule from a lower to a higher energy level, the

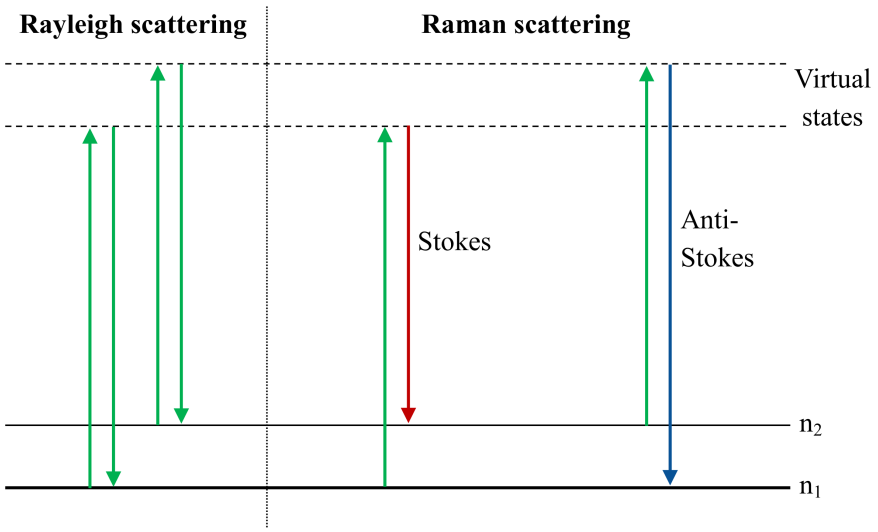

Figure 3.6 *Showing the energy state transitions involved in the Rayleigh and Raman scattering processes. The colouring shown for Stokes and anti-Stokes scattering types indicates the shift in the re-emitted photon towards the higher (blue) or lower (red) end of the electromagnetic spectrum (no shift occurs in the case of Rayleigh scattering). Taken from Amos 2015 [53].*

emitted photon carries a lower energy than that absorbed, and the process is referred to as Stokes scattering. In the opposite case, where the transition is from a higher energy vibrational or librational mode to a lower energy level, the photon is emitted with more energy than that of the absorbed photon, and is referred to as anti-Stokes scattering [226].

Whether Stokes or anti-Stokes scattering will occur is highly dependent on the population of the respective states involved. The population of the starting and end state is dependent on the temperature of the sample which can sucessively be described by a Boltzmann statistic. This means that Stokes scattering is always stronger than anti-Stokes scattering even-though the two cases can reach a similar likelihood at high temperatures. From the ratio of Stokes and Anti-Stokes scattering events it is furthermore possible to determine the temperature of a sample [226].

As discussed above, a molecule that has been excited into a virtual state vibrates about its equilibrium position. The amount of possible vibrational or librational modes that can be excited in Raman scattering depends on the type of molecule. Assuming N atoms in a molecule, each atom can move along the three axes in

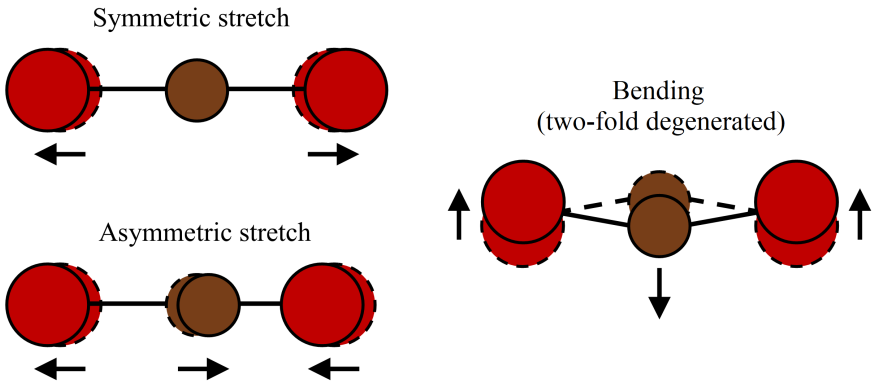

Figure 3.7 *Illustrating the four possible vibrational modes of a triatomic, linear molecule. Note that the bending mode is 2-fold degenerate. Taken from Amos 2015 [53].*

space which results in $3N$ degrees of freedom. The number of vibrational modes is therefore $3N$ minus the number of translational and rotational degrees of freedom; $3N$–5 for linear and $3N$–6 for nonlinear molecules. This means a linear triatomic molecule such as CO_2 has four vibrational degrees of freedom (see figure 3.7); a bent triatomic molecule such as H_2O has three degrees of freedom. Each of these modes appear in a Raman spectrum as a peak shifted relative to the frequency of the radiation which caused the excitation - the Raman shift.

3.3.2 Ruby Fluorescence - A Handy Pressure Scale

In high-pressure experiments it is essential to determine accurately the pressure of a sample. Initially the only reliable way to determine the pressure of a sample were diffraction experiments and the determination of the lattice parameters of a pressure-calibrant (see section 3.3.3). It was not until 1975, that an accurate pressure measurement was possible without diffraction [227–229].

In Raman scattering the incident photon is not fully absorbed and exciting its vibrational or rotational energy states. A related process is fluorescence which occurs if a photon is completely absorbed causing the molecule to jump to a higher electronic state. Upon return to a lower energy state, light is emitted again. It was observed that the fluorescence of chromium-doped corundum (ruby) is highly pressure sensitive. Piermarini *et al.* used this to calibrate the wavelength of the $R1$-line, the strongest and sharp fluorescence line of ruby, against pressure. This resulted in a highly accurate pressure scale up to 195 kbar for the ruby fluorescence

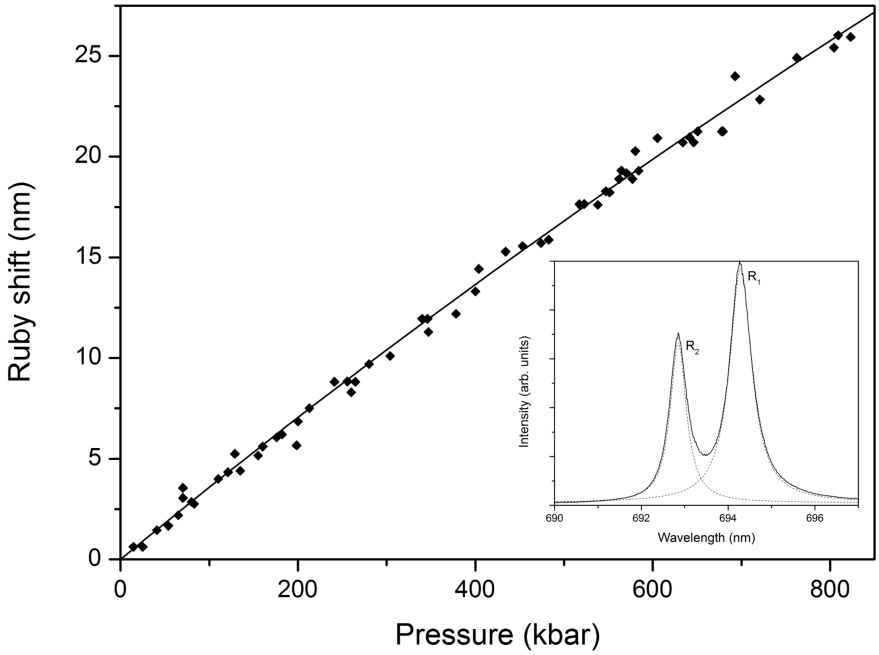

Figure 3.8 *The ruby pressure scale: The shift of the R1-line of the ruby fluorescence spectrum as a function of pressure up to 800 kbar by Mao et al. [54]; Inset: R1- and R2-lines of the fluorescence spectrum of ruby. Taken from Amos 2015 [53].*

shift [227]. As can be seen in figure 3.8, the ruby pressure scale has been greatly extended to higher pressure [54]. By simply adding a small amount of ruby to a sample, it hence became possible to readily measure the pressure in a DAC utilising the transparent window the diamond-anvils offer.

Two problems of this pressure scale shall be discussed here. First, the ruby method is sensitive to deviatoric stress, caused by non-hydrostatic conditions (e.g. by compressing a sample that is not in a fluid state). The two strong ruby lines that are close together (see inset in figure 3.8) broaden and an overlap of these spectral lines can give an indication of the presence of this type of stress. As such, ruby fluorescence can be used as an indicator for the loss of hydrostaticity due to the solidification of the pressure transmitting medium. Second, the ruby method is sensitive to temperature. The $R1$-peak also shifts with temperature. However, this problem can easily be overcome by simultaneously measuring the temperature of the sample and correcting for the effect of the temperature.
This method is now standard in DAC work and will hence not be further discussed here.

3.3.3 Other Pressure Calibrants: Equations of State

Before ruby was used as the standard method to determine pressure other methods had to be used for this purpose, namely mixing a material with a very well defined equation-of-state (EoS) into the sample. From the diffraction pattern the lattice parameters of this pressure calibrant are determined which allows for the accurate calculation of the pressure in the sample.

$$P(V) = \frac{3B_0}{2}\left[\left(\frac{V_0}{V}\right)^{\frac{7}{3}} - \left(\frac{V_0}{V}\right)^{\frac{5}{3}}\right]\left(1 + \frac{3}{4}(B_0' - 4)\left[\left(\frac{V_0}{V}\right)^{\frac{2}{3}} - 1\right]\right) \tag{3.2}$$

This EoS method is still frequently employed if the sample is not optically accessible as it is the case in the *PE*-press; the opaque anvils and gasket do not allow for a measurement of the ruby fluorescence spectrum. A standard EoS used in this work is the Birch-Murnaghan equation of state as given in equation 3.2 (see [230, 231]). To that end, a material with a well defined EoS is mixed with the sample and the diffraction pattern of the added material can be used as a pressure calibrant. While this method is highly accurate, it is prone to systematic errors; it heavily relies on an accurate measurement of the calibrant's lattice parameters and is therefore sensitive to inaccuracy in the calibration of the used neutron instrument. Furthermore, the inclusion of a second material means that the sample volume is reduced, leading to longer data collection times. It is also possible that the peaks of the sample and the pressure calibrant overlap; this can cause problems in the data analysis. Finally, the pressure calibrant - if not chosen carefully enough - can chemically react with the sample compromising the whole data. In order to overcome these problems, a pressure calibrant is employed only when needed and in a minimal amount.

For experiments in a *PE*-press, lead (Pb) - which is a cheap and readily available material - is used; the EoS used here was measured by Straessle *et al.* in 2014 against NaCl [232]. In some cases it was also possible to use the EoS of the sample (e.g. due to excess water) as an internal standard for this method.

3.3.4 Density Functional Theory (DFT)

Beyond the experimental techniques discussed above, for this work DFT (density functional theory; an *ab initio* method) was used to predict or verify structures obtained from neutron diffraction data. A detailed theoretical background for

this technique would go beyond the scope of this thesis, so only the basics are mentioned here; for an in-detail discussion I would like to refere to a textbook on density functional theory, such as written by Sholl and Steckel [233].

In brief, DFT uses the energy of a structure based on the calculation of the inter-atomic forces of a given arrangement of atoms [233]. To solve a many-electron wavefunction for a large system (e.g. the sI type clathrate 46 water molecules) would by far exceed any computational capabilities. In order to overcome this problem, the Kohn-Sham ansatz is used, in which the interacting system is replaced by a non-interacting one. This ansatz corresponds to a mean-field approach, where the wavefunction is decomposed into a product of single-electron orbitals. However, the so obtained Kohn-Sham orbitals have no physical meaning and are only used to reproduce the correct electron density. A lowest-energy solution for the system can then be obtained iteratively.

After obtaining the energy and density map of the starting structure, the atoms are moved similar to MCSA but based on the calculated forces that they experience. The calculations are repeated and (hopefully) an energetically favourable arrangement is found. In this work, only simple functionals such as the local density approximation (LDA) or the generalized gradient approximation (GGA) have been used. While they producing accurate results for the structural and energetic properties of a structure, they fail when it comes to describing the band-structures of semiconductors and insulators by underestimating their band-gap [234, 235].
Furthermore it should be mentioned here that the semi-local exchange-correlation functional used for these calculations does not fully account for longer range dispersion interactions which may be present. As a result, the pressure estimations for calculated structures are higher than seen in experiment, an effect well known for ice [236].

DFT techniques can be used to predict high pressure phases that are not experimentally accessible or for which no sufficient data is available by applying this method to a large numbers of pseudo-randomly generated structures. Examples thereof are the programs AIRSS (*Ab Initio Random Structure Searching*) [237, 238] and CALYPSO (*Crystal structure AnaLYsis by Particle Swarm Optimization*). The latter, CALYPSO, was initially used for a structure prediction in chapter

6 but did not yield any useful results. More relevant to this thesis, however, is the application of this technique to verify experimental observations, i.e. to see whether a structural arrangement based on experimental data is plausible. This is particularly useful for data of poor quality, or when the structure is too complicated for solution from powder diffraction data alone - either of which is usually true for neutron-diffraction under high-pressure.

For this work, the *Castep* software suite [239] was used and the author would like to state that all DFT calculations shown in chapter 8 were carried out by Lewis Conway under the supervision of Dr. Andreas Herrman (see the publication based on this chapter [1]). All other calculations were carried out by the author himself.

Chapter 4

Quantitative Single-Crystal Neutron-Diffraction in DACs

As outlined in chapter 2, the pressure limit for quantitative neutron diffraction has for a long time been limited by the large sample volumes needed. However, recent developments in diamond synthesis have paved the way for new large-volume diamond anvil cells (DAC) [218, 220, 240]. Combined with extremely bright neutron sources, available at the Spallation Neutron Source (SNS) a facility located at the Oak Ridge National Laboratory, neutron diffraction up to a pressure up 110 GPa has been made possible [240, 241]. This technique has, so far, mainly been used for powder diffraction and, as such, has its limits. For many crystallographic studies, single-crystal techniques are critical in that they provide a much higher (real-space) resolution by enabling access to short d-spacing Bragg reflections that would be heavily overlapped in a powder study. At pressures >50 GPa powder methods, for example, give the same solution for a 1-site and 2-site model of a hydrogen bond in high-pressure ice (cf. Guthrie *et al.* [241]).

Of equal importance, single-crystal methods avoid the need to deuterate samples. The concentrated signal from sharp single-crystal Bragg spots remains visible on top of the incoherent scattering originating from hydrogen ^{1}H that would overwhelm distributed powder intensities. Use of DACs for high-pressure single-crystal neutron diffraction (HP-SCND) therefore paves the way for studies of hydrogen-rich systems to pressures currently inaccessible and with unprecedented structural detail.

However, quantitative single-crystal neutron diffraction (SCND) studies under high pressure in DACs remain challenging, albeit sucessful attempts have been made. Binns *et al.* published a set of experiments at ANSTO's KOALA, a neutron Laue diffractometer, using a Merrill-Basset-type diamond cell with conical Boehler anvils ($\varnothing_{culet}$=1 mm). It demonstrated sufficient data quality for refinement on crystals of typical X-ray diffraction sizes [242]. Furthermore, at Heinz Maier-Leibnitz Zentrum (MLZ)'s four- circle diffractometer HEiDi, monochromatic neutron diffraction was performed in a panoramic DAC with conical Boehler anvils and achieved high-quality data under compression to 1 GPa. Another successful test of the cell/anvil setup with 1.5 mm culets reached 7 GPa [243]. These studies are mainly aiming for magnetic materials and large unit cells, but do not report a good enough resolution in the high-Q range to investigate H-bonds.

The goal here is to benchmark SNAP, a high-pressure time-of-flight diffractometer at the SNS for the quantitative structure analysis of single crystals containing hydrogen or other light elements in a DAC. As a reference, a similar set of experiments was carried out on TOPAZ, a well-established single-crystal instrument also at the SNS. Here, a set of trial experiments to investigate the relationship between sample volume and data quality is presented. These properties are inversely related to one another yet, unavoidably, the former is strictly limited in high-pressure studies. The systematic study of the crystallographic limitations of progressively smaller sample volumes is a critical first step in the development of routines for quantitative single crystal structure refinement in a DAC.

Furthermore, the influence of the complex sample environment consisting of diamonds, gasket, and cell body on the data quality is shown. To that end, a structural refinement of the deuterated ferroelectric potassium dihydrogen phosphate (KD_2PO_4, DKDP) is carried out. Finally, the data reduction procedure and all necessary corrections were tested against an ice VI single-crystal grown in a diamond anvil cell and an initial trial to obtain structure factors of a single-crystal of hydrogen H_2.

4.1 Material and Methods

DKDP is a classic example of a short hydrogen-bonded system, which has already been heavily studied – its structural properties are therefore well known [244]. DKDP (KD_2PO_4), is a tetragonal body-centred crystal (space group $I\bar{4}2d$; N^o 122), with lattice parameters at ambient conditions of a=7.469(1) Å and b=6.976(1) Å (unit cell volume 387.29 Å^3). A unit cell contains four hydrogen-bonded formula units of KD_2PO_4, with all the hydrogen bonds lying in the ab-plane. It is well known that the DKDP's deuteration ratio has an influence on its lattice parameters; in the figure 4.1, the lattice parameter a=b and the c/a ratio are plotted as a function of deuteration (data taken from Wang *et al.* [245]). The red dots at 94% thereby give the lattice parameters for one of our measurements. Our data, fits the trend as published by Wang *et al.* and Nelms *et al.* quite well.

The DKDP was synthesised at SNS by dissolving KDP (potassium dihydrogen-phasphate, KH_2PO_4) in D_2O and recrystallising out of the solution. This procedure was repeated three times and two sample crystals were cut from the deuterated crystal. The larger of the two had a volume of 1.028 mm^3 and the small one had a volume of 0.028 mm^3 (disc-shaped; $\varnothing$=0.6 mm, h=0.1 mm) [244]. The latter volume was chosen because it is suitable to fit the sample chamber of diamond anvil cells for neutron diffraction [218].

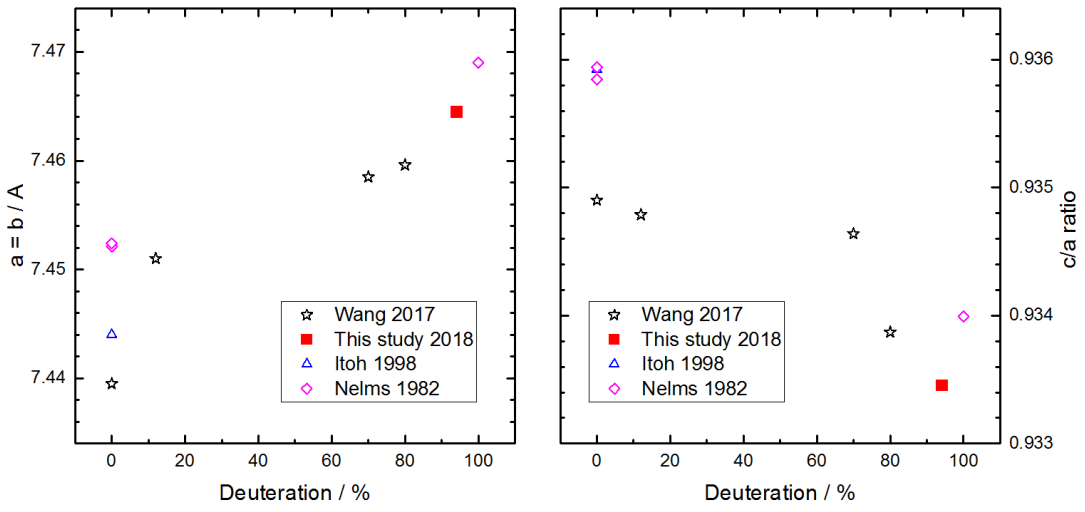

Figure 4.1 *Influence of the deuteration ratio on the lattice parameter $a = b$ of KDP and DKDP as found in literature.*

As outlined in chapter 2, SNAP is a diffractometer designed for high-pressure experiments. This instrument has so far mainly been used for powder studies, its capabilities for a full structural refinement of SCND data have so far not been tested. TOPAZ on the other hand is the dedicated single-crystal instrument at SNS; its design does not allow for the use of large pressure cells. For a more detailed discussion of the instruments used here, please refer to this chapter.

However, for the data reduction - particularly for the absorption correction - the geometry of the two instruments is important and has to be mentioned here. For both instruments, the primary beam enters the sample along the z^+ axis and the sample can be rotated relative to the primary beam. On TOPAZ, the goniometer allows for a rotation of the Φ and Ω angle with X being fixed to 135^o; on SNAP, only a rotation about the y-axis (angle Ω) is possible, with X and Φ being fixed to 0^o (see figure 4.6).

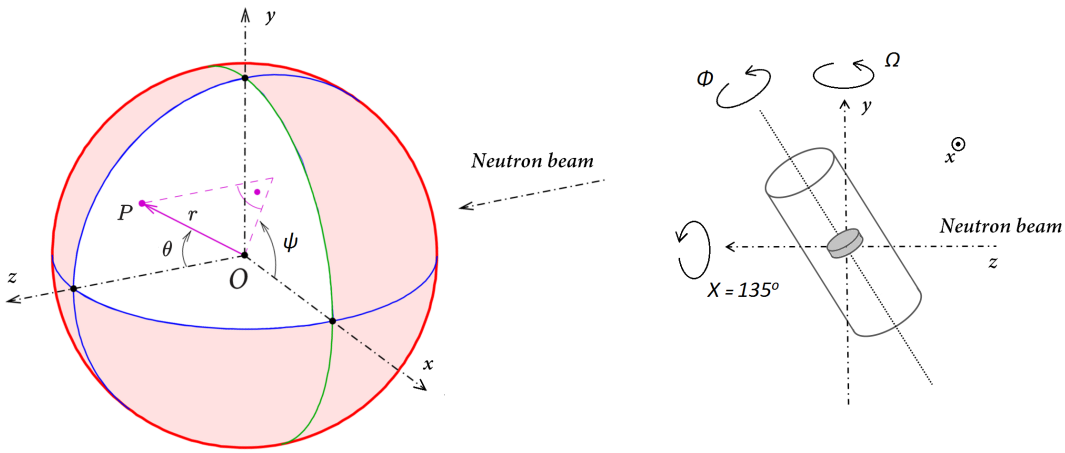

Figure 4.2 *Left: Coordinate system on TOPAZ and SNAP. The beam direction is along the z-axis. The angles θ and Ψ give the direction of the diffracted beam. Right: The goniometer angles X, Φ, and Ω. On TOPAZ X is fixed to 135^o; on SNAP X and Φ are fixed to 0^o. Taken from Massani et al. [2].*

Patterns of the bare crystals were collected for about 3 h per orientation both on SNAP and on TOPAZ. From this initial measurement on TOPAZ it was possible to refine the deuteration ratio of the DKDP to be $> 94\%$; this value was fixed for all subsequent refinements. Please note that the lattice parameters of KDP/DKDP are strongly dependent on the deuteration ratio (see figure 4.1 and table 4.5).

Subsequently, the small crystal was placed in a DAC (SNAP) and a "mock-DAC" (TOPAZ). The "mock-DAC" was used because the sample stage on TOPAZ cannot support the weight of a real DAC. A DAC is is formed by a metal gasket with a small sample chamber between two diamonds held together by a cell body made from hardened steel or beryllium-copper alloy. For the detailed design see chapter 2 or the original publications by Boehler and Haberl [218–220]. The "mock-DAC" had the same basic parts but held together by a much lighter aluminium scaffolding instead of the heavy cell body to be able to mount it on the goniometer on TOPAZ. In both cases a collimator of 3 mm in diameter was chosen. Patterns of the crystal were then collected in the "mock-DAC" on TOPAZ for ten orientations (3x10h and 7x6h). Similarly, six orientations on SNAP were recorded (the sample rotation on SNAP is limited to a single vertical axis whereas TOPAZ has a two-axis orienter). On SNAP data collection was limited to only 3 h collections per orientation.
The data reduction was carried out using the MANTID data analysis and visualization package [246]. All crystallographic refinements were carried out using EXPGUI [181], the graphical user interface for GSAS-I [182].

4.2 Initial observations

4.2.1 Single Crystals on SNAP: Improvement of Data Quality

The main aim for these experiments is to extend the pressure range for SCND on SNAP and by doing so, improve the data quality of high-pressure neutron-diffraction experiments. However, the possibilities and limits of single-crystal diffraction under ambient conditions on SNAP had to be investigated first. To that end, the large (1 mm^3) crystal was measured on SNAP and the same data reduction procedure as used on TOPAZ was applied to obtain the structure factors. In total, 1027 structure factors for this crystal were obtained (after outlier removal). An initial refinement of this dataset based on the crystal structure of DKDP resulted in an overall R_w value of 0.067; this model has two hydrogen atoms placed between two oxygen atoms, each of which has an occupancy of 0.5. In figure 4.3 the left plot gives the observed structure factors F_{obs} versus the calculated structure factors F_{cal} for this refinement; note that in the case of a perfect match between the model and the data, all data points should lie on the dotted line.

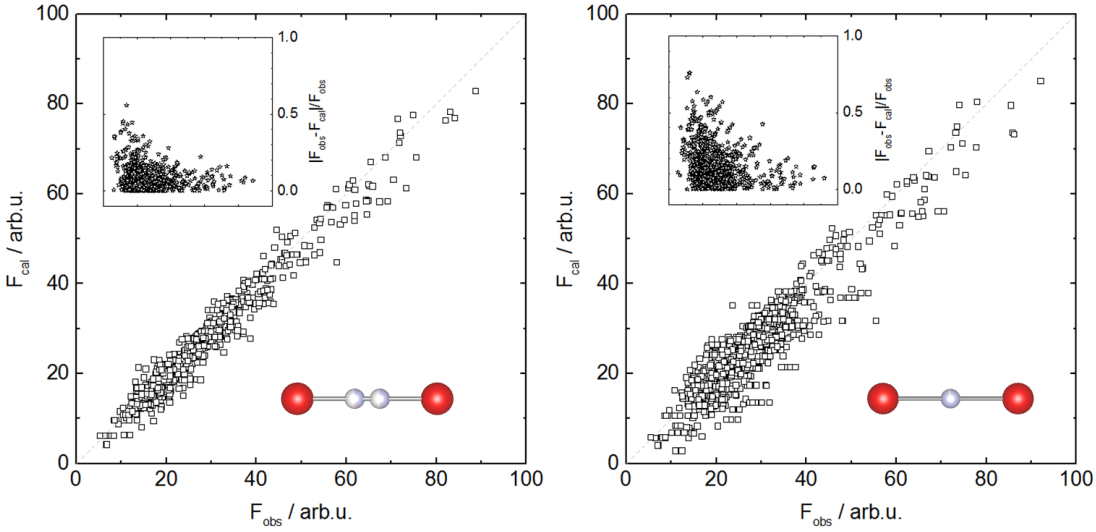

Figure 4.3 *Left: Refinement of DKDP with two symmetrical hydrogen positions with an occupancy of 0.5. Right: Model of a centred hydrogen atom with an occupancy of 1 between two oxygen atoms.*

To see whether the hydrogen positions are clearly resolved, a second (wrong) model of a perfectly centered hydrogen bond was used (right plot in figure 4.3). From the F_{obs} vs F_{calc} plot of this completely symmetrical bond it is evident that the data points are spread out more and hence allows for the conclusion that the quality of the fit to the wrong model decreases. This was also quantified by a worse overall R_w value of 0.123. Simultaneously, it is evident from the $—F_{obs}\text{-}F_{cal}—/F_{cal}$ that small structure factors (high-Q) fit worse than large structure factors (low-Q). This is not surprising as the information of the hydrogen positions is given by the high-Q structure factors.

This latter observation was hence used to determine a possible cut-off for high-Q data. In Figure 4.4, the root-mean-square displacement of atoms from the "ideal" structure as a function of a d-spacing cut-off is shown. For the various data points, structure factors with a smaller d-spacing than the cut-off were ignored for the refinement. It is – once again – evident that the oxygen positions are hardly affected at all by a high-Q cut-off, while the hydrogen atoms are no longer at the right position if all reflections <0.9 Å are ignored.

These initial measurements all indicate that SNAP is perfectly suited for single-crystal diffraction, albeit that the angular coverage is smaller than that of a dedicated single-crystal diffractometer.

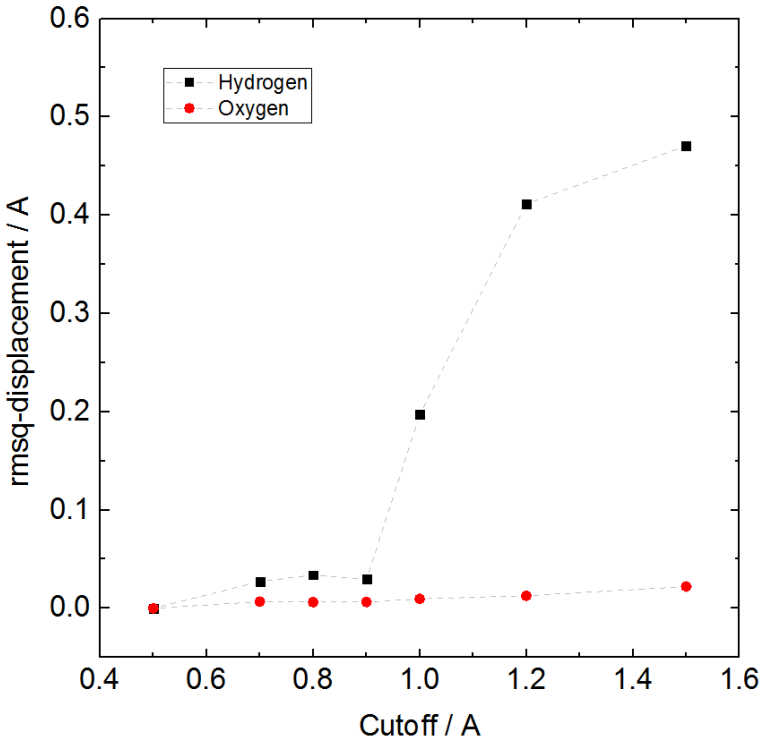

Figure 4.4 *Root-mean-square displacement of the hydrogen atoms in comparison to the true positions as a function of the data cut-off.*

4.2.2 Effects of the Sample Size and Deutration Ratio on the Data Quality

As a first step, the volume restrictions were investigated and the influence of the sample environment on the data quality using a fully benchmarked instrument. To that end the small, DAC-sized crystal was measured on TOPAZ, the dedicated single crystal instrument at SNS. This marks the smallest crystal measured on this instrument to date. As mentioned above, ten orientations of the crystal were measured for 3 h each; each orientation contributed about 100 reflections to the overall data set of 1044 reflections, after removing outliers.

The structural refinement of the dataset obtained from this experiment yielded values consistent with those reported in literature (see Tibballs *et al.* [244]). The respective structural information is given in table 4.4 (cf. appendix to this chapter). This data set was used as a baseline for all subsequent measurements. In general, the deviation of the structural parameters from the literature values is very small and might be a feature introduced by a slightly different deuteration

ratio of our sample compared to that of Tibballs *et al.* As mentioned above, the ratio of KDP ($a = 7.4521(4)$ Å, $c = 6.974(2)$ Å, $a/c = 0.936$) to DKDP ($a = 7.469(1)$ Å, $c = 6.976(1)$ Å, $a/c = 0.934$) has a large influence on the lattice parameter $a = b$; KDP expands more in the ab-plane than along the c-axis when deuterated. This behaviour is due to all the H-bonds being arranged in this plane. However, the obtained structural parameters are afflicted by larger errors of about one order of magnitude higher compared to the results published by Tibballs *et al.* Note that this is a direct result of the small sample volume, with the low intensites (high-Q) having a greater statistical uncertainty.
In general, our measurements are accurate albeit not as precise as the literature values. Still, these results show that even in a DAC-sized crystal it is possible to resolve the exact hydrogen/deuteron positions accurately on a well-calibrated neutron diffractometer.

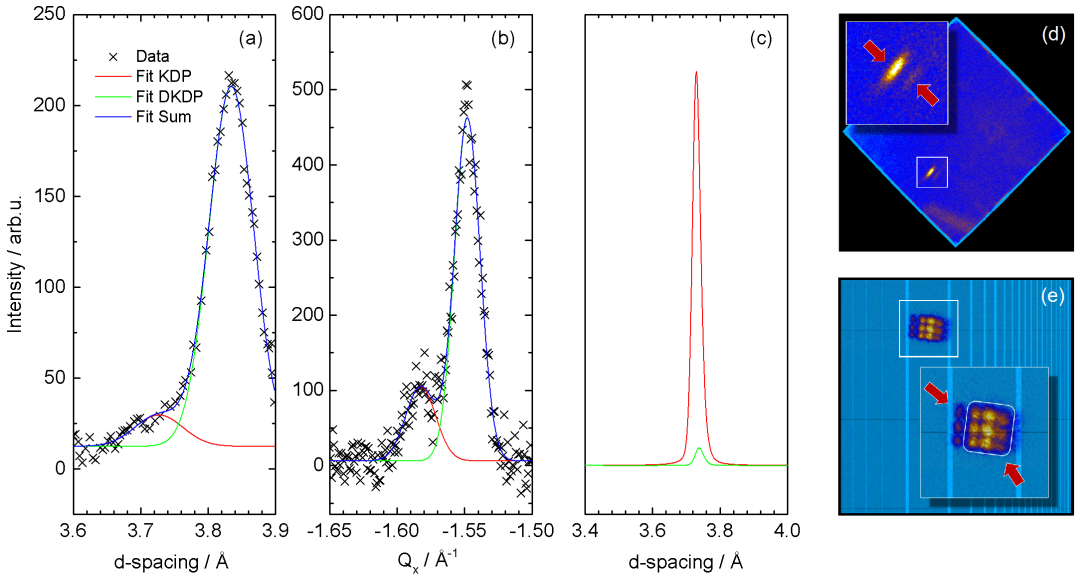

Figure 4.5 *(a), (b) The observed doublet in d-spacing and along Q_x. In both cases two Gaussians were fitted to the data to obtain the peak maxima. (c) Simulated peak for KDP (red) and DKDP (green). (d) Pictures of the split-peak on a detector module on TOPAZ. (e) Pictures of the doublet on a detector module on SNAP. Note that the peak itself consists of a 3x3 "checkboard" pattern as a result of the short guide (cf. section 4.3.3).*

By examining the diffraction patterns it was possible to identify a shoulder on some Bragg reflections. This shoulder was only visible in the most intense Bragg reflections. In figure 4.5, the 020 peak at about 3.8 Å is shown with such a

shoulder in *d*-spacing (Fig. 4.5 a) as well as along the Q_x direction in the lab frame-of-reference (Fig. 4.5 b). In both cases two Gaussians were fitted to the data to obtain the position of the peak maxima and their intensities. Due to the small *d*-spacing difference of about 0.1 Å, a twinned or broken crystal can be excluded. From simulated patterns of KDP and DKDP (Fig. 4.5 c), it is apparent that in those patterns the 020 reflections are also shifted by about 0.1 Å as a result of the effect of deuteration on the lattice parameters [244, 245]. Therefore, it was concluded that a small part of the crystal is undeuterated KH_2PO_4 (KDP). Based on the intensities of the split 020 reflections (as seen in Figure 4.5) it can be estimated that ∼4% of the crystal was KDP; this is in the same order of magnitude as the established deuteration of ∼94% obtained by refinement of the whole data set. As the 4%-estimate is only based on one reflection, a rather large large error can be assumed on this value.

Possible explanations for the existence of KDP in the sample are either an incomplete H-D exchange during the synthesis of the DKDP or the exchange of H and D on the surface of the crystal due to hydrogenous water in air. The former explanation would suggest that hydrogen is incorporated in the whole bulk of the crystal and thus a shift and a broadening of the peak should be observed. However, the existence of a shoulder indicates that particular regions of the crystal are less deuterated than others. This favours the second theory of an H-D exchange due to H_2O in air and the formation of a KDP layer on the outside of the crystal.

As mentioned above, the shoulder was only visible in low-Q (high d-spacing) peaks; thus, a separate integration of the peaks was not possible. Based on the assumption that the splitting is a result of the deuteration ratio, it was ignored and the split reflections were integrated together. However, the deuteration ratio for all the subsequent refinements was fixed (94%) to take peak broadening into account.

4.3 Establishing a Data Reduction Procedure

4.3.1 Problems obtaining the peak positions: The Limits of TOPAZ's Automated Algorithm

Subsequently, the crystal was placed in a DAC (SNAP) and a mock-DAC (TOPAZ) and patterns were recorded. Several crystal orientations were measured and then analysed with the standard procedure used on TOPAZ. That is, a UB was manually constructed from the observed Bragg reflections of the first orientations, which was then applied on all other orientations by rotating the UB about the same axis as the crystal. Using the UB, the position of the SXL-Bragg peaks in Q-space were then predicted and integrated using the Mantid algorithms *PredictPeaks* and *IntegrateEllipsoids*. All these steps are thereby automated and hence user-friendly. The so-obtained list of structure factors, F_{obs}, was then used for a refinement. This precedure, although yielding a good fit for a bare crystals, led to a very unstable refinements for the very same crystal in a DAC environment.

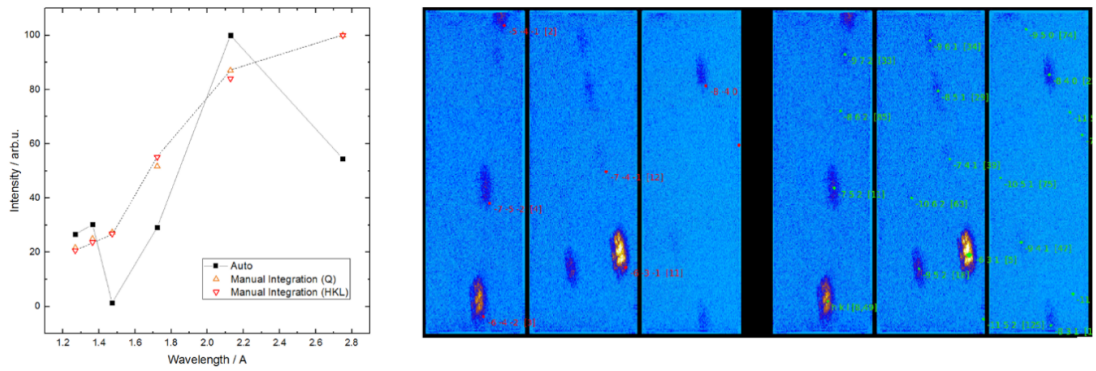

Figure 4.6 *(Left) Uncorrected raw data as a function of the wavelength. The intensities of the (211) reflections are plotted for the case of TOPAZ's automated integration mechanism and a manual integration in Q- and HKL-space. (Right) wrongly predicted peak positions (red) and actual peak positions (green) on a SNAP detector.*

In the left panel of Figure 4.6 the intensities of the (211) reflections as obtained from the standard, automated, procedure are depicted as a function of wavelength. This family was chosen because its peaks are strong and spatially separated from any powder line (produced from the gasket) and from the diamond's single-crystal peaks. As a reference, the same reflections were

integrated completely manually. In order to do that a box was drawn around the respective Bragg peak in Q-space using the Mantid slice viewer function. The obtained peaks were then background corrected and a Pseudo-Voigt function was fitted to them using Origin1. No corrections have been applied to this data. (Corrections usually applied to SCND are λ^4, Vanadium, Lorentz, and absorption correction, in which case all intensities of the same family should have the same reduced, structure factors squared F^2; see chapter 2. Here, however, only the raw data was of interest.) From the λ^4 dependency of the intensities, it would be expected that the values for the intensity of the same peak family increases with wavelength. While the manual integration follows this trend (in both cases, the integration in Q and in HKL space), TOPAZ's automated integration does only to a certain degree; some intensities are a lot smaller than what the trend would suggest (e.g. at 1.48 and 2.81 Å), indicating that this integration method is not suitable for diffraction experiments in a DAC. The UB often predicts peak positions off-centre the actual peak resulting in wrong intensities, e.g., the integration of the (211) peak at a wavelength of 1.48 Å gave this peak zero intensity, indicating that the predicted peak location did not coincide with the actual reflection at all. This can also be seen in the right panel of figure 4.6; most predicted peaks (red) are way off the centre of the actual peak (green). In order to overcome this problem, a separate orientation-matrix for every crystal-orientation had to be constructed; based on this individual UB, the peaks were integrated and the resulting intensities were combined for the subsequent data reduction.

4.3.2 The Effect of the DAC on Data Quality

Due to the contributions of the single-crystal diamond peaks, and the powder lines of the steel gasket, an increased background, and an increased signal-to-noise ratio, routines that are well established on TOPAZ failed here. In the following, problems and approximations used for the data reduction and analysis are discussed.

Increased Background While light elements (e.g. C, N, O, F, Ne) cause mainly the emission of an alpha or beta radiation, heavier elements (e.g. Fe and Re) produce gamma radiation if exposed to a neutron beam [247]. Anger cameras as used on SNAP and TOPAZ to detect neutrons but are also sensitive to gamma rays. Since steel, beryllium-copper, or rhenium gaskets are most commonly used

in DACs, the background is significantly increased if the primary beam hits the gasket.

While it is possible to minimise the gamma ray emission if the primary beam enters the cell through one of the diamonds, this geometry limits the accessible orientations of the single-crystal. Far more orientations can be measured if the primary beam enters the cell through the gasket, inevitably resulting in a significant background increase.

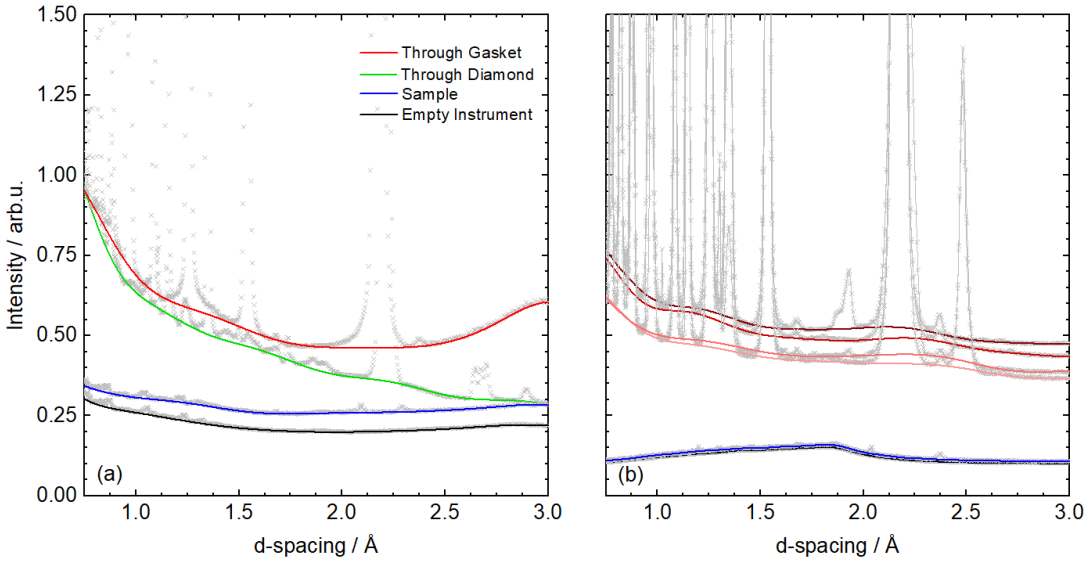

Figure 4.7 *Comparison of background levels on SNAP (a) and TOPAZ (b) for the empty instrument (black), the sample on a vanadium pin (blue), and the full assembled DAC. SNAP: the green curve shows the background in which the primary beam enters the cell through the diamonds only, while the red curve is the background for the case in which the primary beam enters the cell through the gasket. TOPAZ: The four red curves give the background on TOPAZ for various orientations of the cell. All plots are normalised to the proton-current and vanadium-corrected.*

For SNAP, the diffraction patterns for the empty instrument (black), the sample on a vanadium pin (blue), and the full assembled DAC are given in figure 4.7 (a) (all plots are normalised to the proton-current and vanadium-corrected). The green curve shows the background in which the primary beam enters the cell through the diamonds only, while the red curve is the background for the case in which the primary beam enters the cell through the gasket. Please note, that the background level for the high-Q data are of a similar magnitude in both cases; the background increases significantly in the high-Q regime if the gasket is in

the primary beam path. For most elements the absorption cross section σ^a is inversely proportional to the wave vector $k = \frac{2\pi}{\lambda}$. This leads to more neutrons being absorbed at higher wavelengths and hence more gamma rays being emitted [176]. In figure 4.7 (b) the same data are shown for an experiment on TOPAZ and similar to the experiments carried out on SNAP, an increased background is observed. (The four red curves show the variation of the background levels for four cell orientations.) However, the background does not increase at low-Q to the same extend as on SNAP.
A background reduction could possibly be achieved by a reduction of the beam diameter from 3 mm to the actual dimensions of the sample chamber.

Gasket Contamination Gaskets for these experiments consist of poly-crystalline steel and add a parasitic signal to the data. Unlike the parasitic signal from the single crystal diamond - which is well defined in 3D-reciprocal space - powder lines emanating from the metal gasket pollute entire d-spacing ranges on the detector. In figure 4.8 (a) a sample reflection on top of a powder line is shown. Technically, it should be possible to fit the powder-line and subtract it from the peak. Such an algorithm has yet not been written for MANTID; hence all sample reflections overlapping with the d-spacing range of gasket-lines were excluded. This approximately halved the accessible Q-range for this experiment.

Signal-to-Noise Ratio While it is not possible to reduce the background with a longer collection time, the signal-to-noise ratio (s/n-ratio) improves with time. As a threshold $s/n = 3$ was chosen, meaning a peak that is thrice as intense as the noise of the background. For the measurement of one orientation, the number of integrable reflections above the s/n ratio increased with time; the number N was roughly proportional with the $\sqrt{t}$ - after 3, 6, and 8 h the number of integrable reflections were 5-10, 20-30, and >45, respectively.

Attenuation Correction I - Cell The sample volume of the DAC-sized crystal was about 0.028 mm^3. In comparison, a metal gasket having a diameter of 6.0 mm and a height of 0.5 mm has a volume of 14.137 mm^3 - about 500 times more than the sample volume. Even if the neutron beam does not immerse the whole gasket, its illuminated volume exceeds the sample volume. For the attenuation correction only the contributions of the steel gasket were taken into consideration.

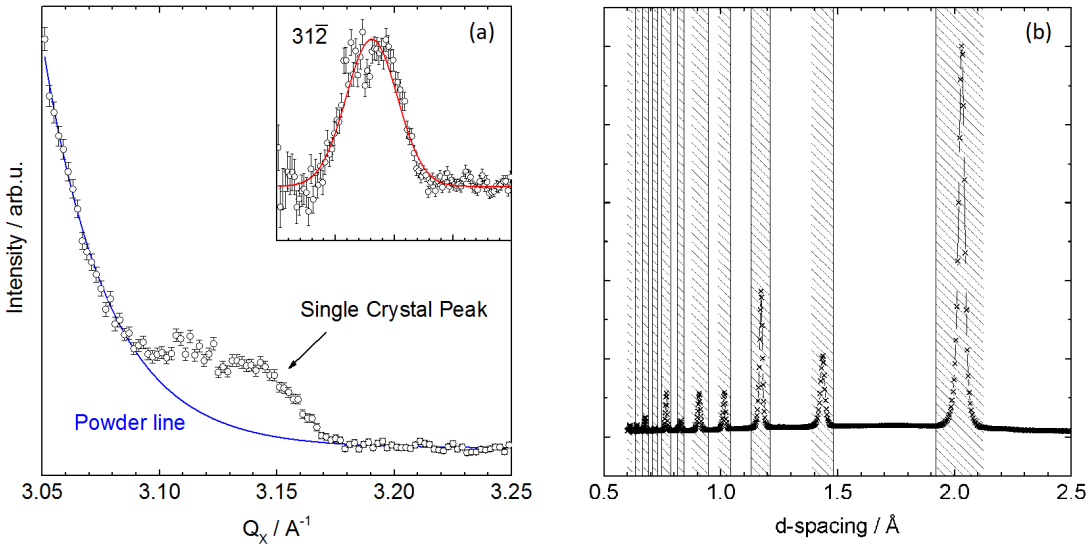

Figure 4.8 *(a) A single crystal peak on top of a powder line with the blue curve being a fit of the powder-line. The inset gives the single crystal peak after a subtraction of the powder-line. (b) Powder-lines caused by the steel gasket. Peaks in the shaded d-spacing regimes were excluded during the data reduction.*

For the data reduction, a spherical model was used, i.e. the gasket was modeled as a (hollow) sphere and hence the attenuation was uniform for all scattering angles. The radius of the attenuation sphere was chosen to be 1.5 mm. - the diameter of the beam used for this experiment - and consisted of Fe, Cr and Ni in their respective abundance. Stainless steel as used for this experiment is an alloy composed of roughly 70% Fe, 20% Cr, and 10% Ni. The other elements in stainless steel such as Mg, Si, P and C were omitted from this model as their abundance is usually less than 2%.

Furthermore, it was tried to improve the attenuation model using an analytical beam-tracing approach; to that end, a 3-dimensional model of a diamond anvil cell was created in Python (cf. inset in the left panel of figure 4.9). This model has the same frame of reference as the TOPAZ instrument and is freely rotatable in 3D about Φ, χ and Ω (cf. TOPAZ specification sheet[224]). Instead of a diamond with an angle of 82^o (as in a real DAC), the diamond was modeled as a cylinder with the same radius as the culet. This simplification can be justified by two reasons. Firstly, as can be seen in figure 4.9 (b) the overall path-length through the diamond is small compared to the path-length through the gasket. And secondly, the scattering cross-sections of carbon (σ_s=5.551 barns, σ_a=0.004 barns) relative

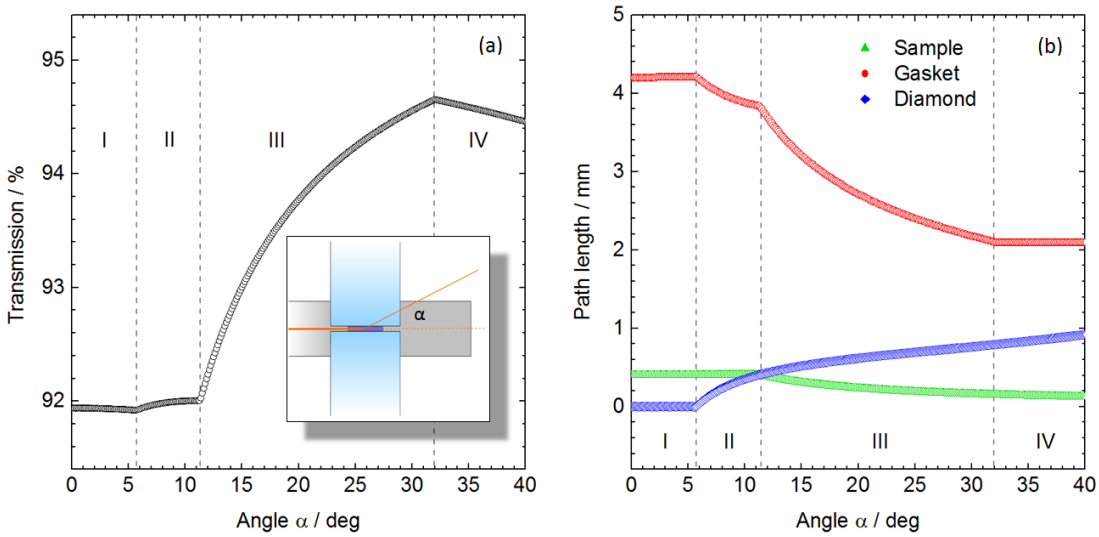

Figure 4.9 *(a) Transmission of a steel gasket for the geometry Φ=-15°, X=135° and Ω=0°. The model of a DAC used for this experiment is shown in the inset. For the beam, four cases for the path can be distinguished: (I) diamond-only, (II) diamond-gasket, (III) gasket-diamond-gasket, and (IV) gasket-only. (b) The respective path lengths through diamond and gasket.*

to those of iron (σ_s=11.62 barns, σ_a=2.56 barns), chromium (σ_s=3.49 barns, σ_a=3.05 barns), and nickel (σ_s=18.50 barns, σ_a=4.49 barns) results in a smaller contribution of diamond to the total attenuation[176].

The total beam-path $D_i = d_i^{in} + d_i^{out}$ was calculated, with d^{in} and d^{out} being the path lengths through the respective materials to the centre of the sample chamber and from the centre out of the cell, respectively. The un-attenuated intensities, I_0, can then be calculated according to Beer's law from the observed intensities, I_{obs} as

$$I_{obs} = I_0 \cdot \prod_{i=1}^{n} \exp\left(-\rho_i D_i \sigma_i^s - \rho_i D_i \sigma_i^{a,\ddagger} \cdot \frac{m_{neut}\lambda}{h} \cdot 2200\frac{m}{s}\right). \tag{4.1}$$

In this equation ρ_i are the atom densities in atoms/m^3, D_i are the path-lengths, σ_i^s are the scattering cross-sections and $\sigma_i^{a,\ddagger}$ are the absorption cross-section at 1.798 Å (v=2200 m/s) [168, 176]. For most nuclides, the scattering lengths and cross-sections are independent of the incident neutron wave vector in the thermal neutron region, while the absorption cross-sections are inversely proportional to v, the velocity of the neutron [176, 248].

The so obtained transmission as a function of the angle α (the angle of a beam relative to the gasket plane) for the geometry Φ=-15^o, X=135^o and Ω=0^o is given in figure 4.9. It can be seen that the intensities of the reflected beam in this case vary by about 3%, with beams that are in plane with the gasket being attenuated the most. This model, although more accurate than the spherical model, did not improve the R_w for the refinements significantly.
An attempt to refine anisotropic thermal parameters was made but proved unstable because the number of observed reflections was insufficient.

Attenuation Correction II - Diamond Dips In a TOF neutron diffraction experiment, the incident neutron beam travels through a single-crystalline diamond. Neutrons with a certain wavelengths will fulfill the Bragg condition and hence be scattered. This can be seen in the transmission spectrum by "diamond dips", which further decreases the intensity of incident neutrons around certain wavelengths [179]. Guthrie et al. showed that this effect is negligible at low pressures but becomes more pronounced with pressure. Since experiments in this work were a) carried out in a way that the primary beam enters the cell through the gasket and b) were not carried out at high enough pressures, this effect was ignored here. At higher pressures and other geometries, an additional correction for "diamond dips" also has to be applied.

Extinction Correction For the extinction correction a first-order Lorenzian model from GSAS-I was used. A better result for the bare crystal was obtained using the extinction models by Becker and Coppens 1974 [249] as employed by the JANA software package, but was not used here since all other error sources for this experiment outweighed the error due to extinction.

Integration and Refinements Several routines for the integration of the Bragg reflections obtained from the experiment were investigated. In figures 4.10 and 4.11 the plots show the calculated vs the observed structure factors, F_{calc} and F_{obs}, respectively, for the investigated integration and data-reduction routines. In an ideal case, F_{calc} from the structural model and F_{obs} obtained from the experiment are the same, F_{calc}=F_{obs}, indicated by the broken grey line. The insets in the respective plots show the relative difference between F_{obs} and F_{calc} ($|F_{obs} - F_{calc}|/F_{obs}$) as a function of F_{obs}.

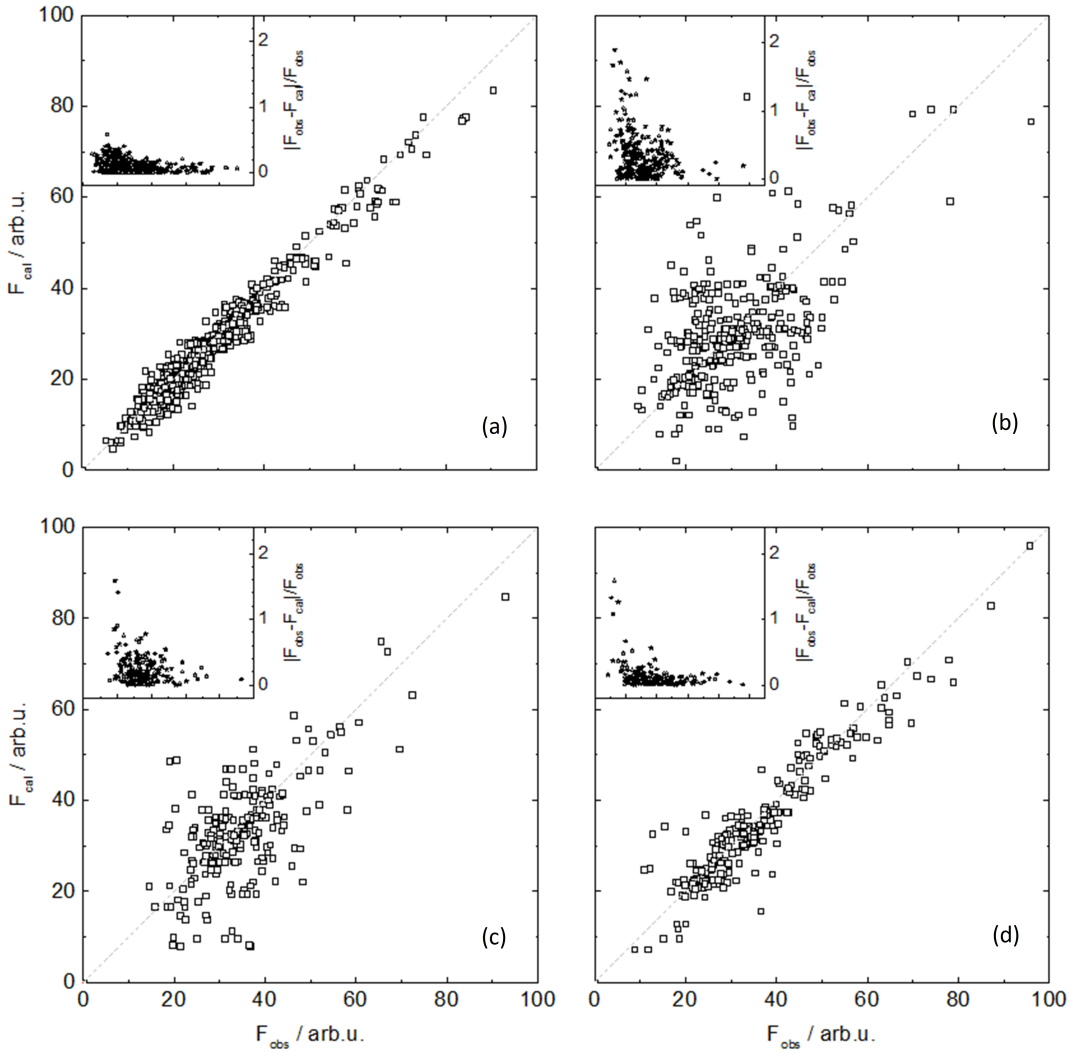

Figure 4.10 *Observed versus calculated structure-factors for: (a) The bare crystal without a sample environment, (b) using the standard TOPAZ algorithm (DAC_a), (c) a refined UB for every orientation (DAC_{UB}), and (d) a selected subset of peaks (DAC_s). The insets give the relative difference between observed and calculated structure-factors as $|F_{obs} - F_{calc}|/F_{obs}$ as a function of F_{obs}.*

First, the integrations were carried out using the standard TOPAZ algorithm (DAC_a), which automatically predicts peaks, finds a UB, and integrates the respective peaks. This automated algorithm failed here (see section 4.3.1), as can be seen by strong scattered structure factors in figure 4.10 (b). It is not surprising, that small structure factors (usually high-Q structure factors) fit particularly poorly. This refinement gave an overall R_w of 0.201, with R_w being the residual factor (R-factor)

$$R_w = \sqrt{\frac{\sum |w|F_{obs} - F_{calc}||^2}{\sum |wF_{obs}|^2}}. \tag{4.2}$$

With a refined UB-matrix for every orientation (DAC_{UB}), R_w was reduced to 0.145, suggesting still a bad fit of the model to the data. Hence the peaks were picked manually in order to ensure that the Bragg reflections actually used for the refinement were not on a powder line or close to a detector edge and had a sufficient s/n-ratio for the integration. Using this subset of peaks (DAC_S), R_w of 0.117 was obtained, a much better result than for the other routines. The F_{obs} vs F_{calc} plots for the DAC_{UB} and DAC_S routine are depicted in figure 4.10 (c) and (d), respectively. The integration discussed above was carried out using the *IntegrateEllipsoids* algorithm [250, 251].

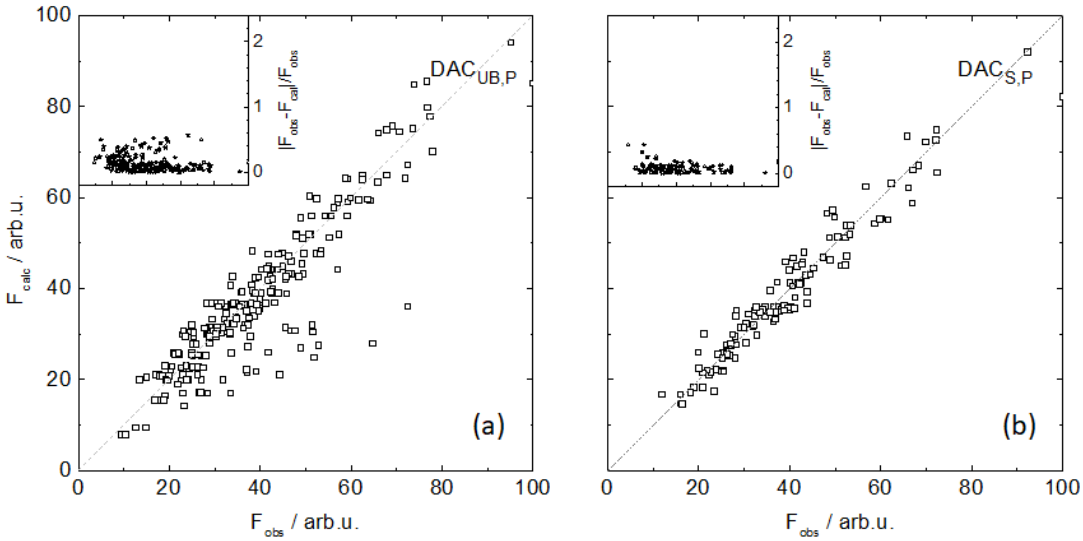

Figure 4.11 *Observed vs Calculated Structure factors for (a) a refined UB for every orientation ($DAC_{UB,P}$), and (b) a selected subset of peaks ($DAC_{S,P}$). The integrations were carried out using the IntegratePeaksProfileFitting algorithm. The insets give the relative difference between observed and calculated structure factors as $|F_{obs} - F_{calc}|/F_{obs}$ as a function of F_{obs}.*

The same data sets as used in DAC_{UB} and DAC_S were then re-integrated using the *IntegratePeaksProfileFitting* algorithm ($DAC_{UB,P}$ and $DAC_{S,P}$, respecively). This algorithm uses two Gaussians to fit a peak in Q-space, an actual fitting technique. Compared to the *IntegrateEllipsoids* algorithm, the intensities and sigmas of the fitted peaks are in a better agreement with the data, particularly for weak reflections close to the s/n threshold [252]. The best fit of the data by the model was obtained using this method (cf. figure 4.11) with R_w of 0.110 and 0.087, respectively.

The respective results for all the refinements are given in table 4.4 in the appendix. Furthermore, all structural parameters are within 1σ of the data obtained from the bare crystal and hence comparable. Note that the data set integrated using the *IntegratePeaksProfileFitting* is not only more accurate than the data from the other routines, it also is 2-3 times more precise. Full structural refinements from single-crystal data in DACs are therefore possible on well calibrated diffractometers with Anger cameras.

4.3.3 Is Quantitative Structure Refinement of Hydrogen-Rich Systems in a DAC on SNAP Feasible?

SNAP is the dedicated high-pressure diffractometer at SNS, and, by design, has a much higher flux than TOPAZ, a feature that is needed for high-pressure experiments. However, SNAP has primarily been used for powder studies and fully quantitative SXL work on systems containing light elements has not been explored yet - hence its capabilities for single-crystal diffraction had to be tested. To that end, a single crystal of DKDP (about 1 mm^3) was placed on a vanadium pin and and diffraction patterns of ten orientations, each measured for 3 h, were collected. Compared to TOPAZ the detector coverage is more limited and the sample stage deployed for this experiment allowed for rotations about the vertical omega axis only. These limitations reduce the Q-space coverage in comparison to TOPAZ. It was possible to utilise TOPAZ data-reduction procedures for SNAP. The results of the refinements for the data collected are given in table 4.5 (cf. table 4.5 appendix). A total of 1027 reflections were observed and an R_w of 0.067 was obtained. All structural parameters are within 1σ of the reference measurement carried out on TOPAZ (see section 4.2.2). Note that the larger deviation in the lattice parameter $a = b$ stems from the limited rotation geometry which leads to an under-representation of reflections along the c-axis.
Compared to TOPAZ, SNAP has a shorter focusing guide which allows for a higher flux, a feature needed for high-pressure powder diffraction. The guide's curvature profile is not ideally suited to its location at the instrument leading to a more complex beam profile and a splitting of a peak into 9 distinct spots in a 3x3 "check-board pattern" on the detector (see figure 4.8 (e)). The integration was carried out over the whole area of the respective peaks, with the peak maximum forced to be at the centre of the 9 spots as this corresponds to the direct beam, not affected by the guide.

Subsequently, this experiment was repeated with a DAC-sized crystal and similar results for the refinement were obtained (cf. table 4.5). A total of 279 reflections from six orientation (3 h each) were observed and an R_w of 0.090 obtained. Even though the number of observed reflections dropped by a factor of 4, the structural parameters remained well within 1σ of the larger crystal and within 1-2σ of the reference measurement on TOPAZ. Please note that the error-bars only tripled by reducing the volume by a factor of 35 from 1.028 mm^3 to 0.028 mm^3.
These results show that SNAP as it is setup presents some limitations but in principle similar data quality as on TOPAZ can be achieved and as such can yield accurate structural data.

Finally, the small crystal was placed in a real diamond anvil cell for neutron diffraction and measured as well. (Rotations about omega only; the primary beam entered the cell through the gasket). The DAC was rotated about omega to six orientations and patterns were collected for 3 h each. Despite the short collection time, 56 Bragg peaks with an acceptable I/σ ratio were found and integrated. The empirical $3n$-rule (three structure factors per refinement parameter) suggests that for an isotropic refinement of DKDP (4 atoms) at least 48 reflections are needed - which was achieved here. Lattice parameters and structural parameters of this experiment are shown in table 4.5. The fractional refinements carried out on this small data set resulted in an overall R_w of 0.336. The atomic coordinates obtained from this data set are still correct, but due to the reciprocal space coverage explored, the uncertainties are very large and in the order of 0.05-0.20 Å. With a similar collection time as on TOPAZ (6-8 h), better results should be possible.

4.4 Application on Samples Under Pressure: A Structural Study of Ice VI

In order to asses the methods developed here for SCND in a real environment, a single-crystal of ice VI of a similar size as the small DKDP crystal was grown in a diamond anvil cell by repeatedly melting and re-crystalising a powder of ice VI in an ammonia-water pressure medium (Sigma-Aldrich, ND_4OD-D_2O, 25% , >99.99% deut.). Note that the ammonia-water mixture at 1.1 GPa and room temperature exists as a two-phase system of an ammonia-rich liquid and solid ice VI (see chapter 1.2.5).

To grow a single crystal of ice VI, the gasket hole was filled with the ammonia-water solution ($\varnothing_{culet}$=1.43 mm; steel gasket, $\varnothing_{hole}$=800 μm, indented to 136 μm), and the sample was pressurised to about 1.1 GPa to form a powder (pressure from the EOS of ice VI [62]). At this pressure, the melting point of the mixture lies just above room temperature. The sample was melted by heating the whole cell on a hot plate and the gasket hole was observed through a microscope (see figures 4.12). The sample was carefully melted melted in a way that only one crystallite survived; from this small nucleus a single crystal was grown by cooling the sample back to room temperature.

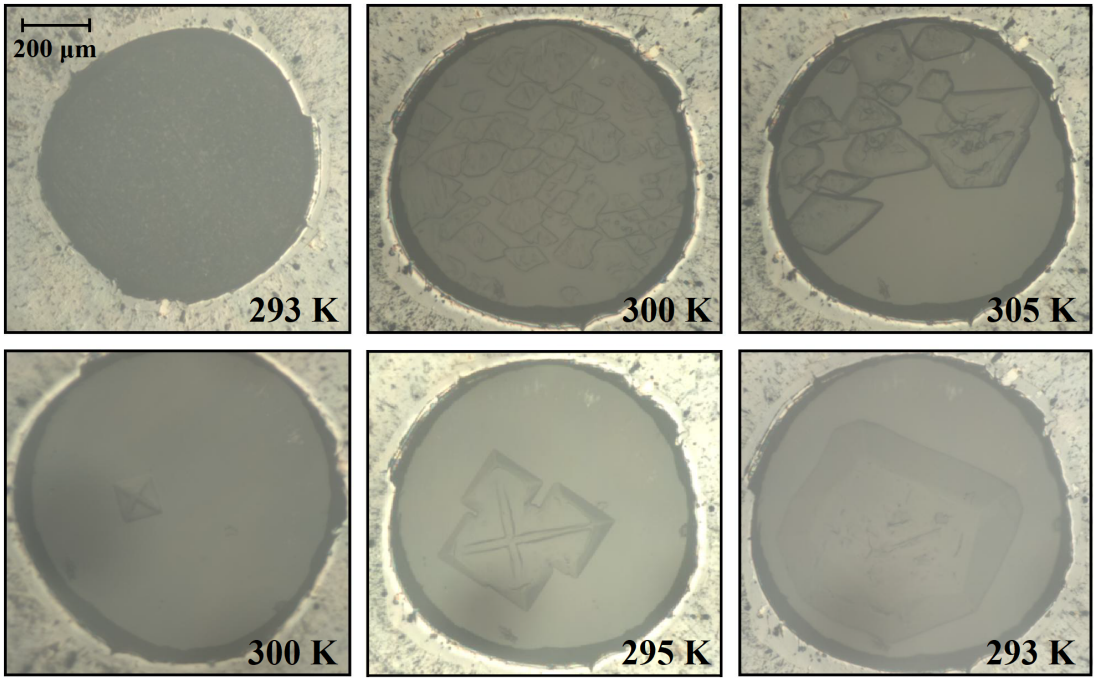

Figure 4.12 *Microscope pictures of the gasket hole loaded with a powder made of 25% ND_4OD-D_2O. The powder was melted by heating the sample and subsequently a single crystal was formed using a single crystallite as a nucleus. Taken from Massani et al. [2].*

To test our method against a sample under pressure, a single crystal of ice VI was measured. The cell containing the sample was aligned on the SNAP instrument and patterns for three orientations were collected (about 12h per orientation). Altogether, 84 structure factors were obtained after the data reduction procedure and an outlier removal. From the orientation matrices, the lattice parameters of the single-crystal were found to be a=b=6.2053(61)Å and c=5.7087(22)Å.

Similarly to DKDP, ice VI is a well known structure and has been studied thoroughly [55, 62, 253–256]. Ice VI shows a tetragonal crystal system with the space group $P4_2/nmc$; its unit cell contains 10 water molecules and has the dimensions a=6.1845(1)Å and c=5.6981(1)Å at 1.26 GPa [62]. The oxygen atoms are on 2a and 8g sites, and the hydrogens are located on three 8g sites and one 16h site - hence, only 17 parameters are needed for a structural refinement with isotropic atomic displacement parameters.

Table 4.1 *Comparison of structural parameters of ice VI as reported by Kuhs et al. [55] (top) and this study (bottom). Data were collected on SNAP.*

	x	y	z	Occ.	U_{iso}
O1 (2a)	0.7500(00)	0.2500(00)	0.7500(00)	1	0.0299(49)
O2 (8g)	0.7500(00)	0.5295(43)	0.1339(38)	1	-
D1 (8g)	0.7500(00)	0.4628(92)	-0.0137(86)	0.5	0.0380(51)
D2 (8g)	0.7500(00)	0.3703(64)	-0.1365(101)	0.5	-
D3 (8g)	0.7500(00)	0.6872(10)	0.1248(18)	0.5	-
D4 (16h)	0.1325(41)	0.5307(51)	0.7844(51)	0.5	-
O1 (2a)	0.7500(00)	0.2500(00)	0.7500(00)	1	0.0208(25)
O2 (8g)	0.7500(00)	0.5337(25)	0.1306(23)	1	-
D1 (8g)	0.7500(00)	0.4450(40)	-0.0120(50)	0.5	0.0211(27)
D2 (8g)	0.7500(00)	0.3850(60)	-0.1423(29)	0.5	-
D3 (8g)	0.7500(00)	0.6799(32)	0.1330(40)	0.5	-
D4 (16h)	0.1333(27)	0.5330(30)	0.7930(25)	0.5	-

A preliminary refinement for the 17 parameters in an ice VI crystal resulted in an overall weighted R-factor of R_w= 0.1302; constraining the isotropic atomic displacement parameters for the D and O atoms slightly increased the R_w to 0.1477; this was done to compare the structure with the published structure. (Similar to the DKDP a refinement with anisotropic thermal parameters was attempted but gave no physically sensible results.)

The structural parameters for ice VI as given by Kuhs *et al.* [55] and the values for this refinement are shown in table 4.1. Although only three orientations were measured for this study, the obtained values are fairly close to the published structure of ice VI (within 1-2σ). In the right panel of Figure 4.13 the two structures are depicted on top of each other to highlight the small differences. Furthermore, the oxygen positions are in accordance to published single crystal X-ray data (see for example Kamp *et al.* [254]).

Table 4.2 *Comparison of atomic distances (Å) and angles (deg) of ice VI as reported by Kuhs et al. [55] and this study.*

	Kuhs '84	Here		Kuhs '84	Here
O1-O2	2.788(24)	2.796(15)	O1-D2	0.986(48)	1.04(4)
O2-O2	2.726(38)	2.69(4)	O2-D1	0.937(55)	0.98(9)
O2-O2	2.778(28)	2.84(3)	O2-D3	0.976(51)	0.91(3)
avrg.	2.774	2.775	O2-D4	0.939(32)	0.94(2)
			avrg.	0.961	0.968
D1-D2	0.906(21)	0.81(8)			
D3-D3	0.976(38)	0.99(8)			
D4-D4	0.780(24)	0.87(2)			
avrg.	0.887	0.89			
O2-O1-O2	128.02(45)	127.1(4)	D2-O1-D2	115.51(2.29)	115.6(2)
O2-O1-O2	76.60(73)	78.1(6)	D2-O1-D2	97.97(4.77)	98(8)
O1-O2-O2	89.32(78)	89.0(5)	D1-O2-D4	105.67(3.40)	108(3)
O1-O2-O2	128.30(96)	129.0(3)	D1-O2-D3	113.07(4.86)	110.5(15)
O2-O2-O2	76.90(92)	76.7(5)	D4-O2-D4	101.29(3.40)	101(3)
O2-O2-O2	128.45(75)	128.3(3)	D3-O2-D4	114.97(2.92)	125(13)
avrg.	108.15	104.60	avrg.	109.4	109.5

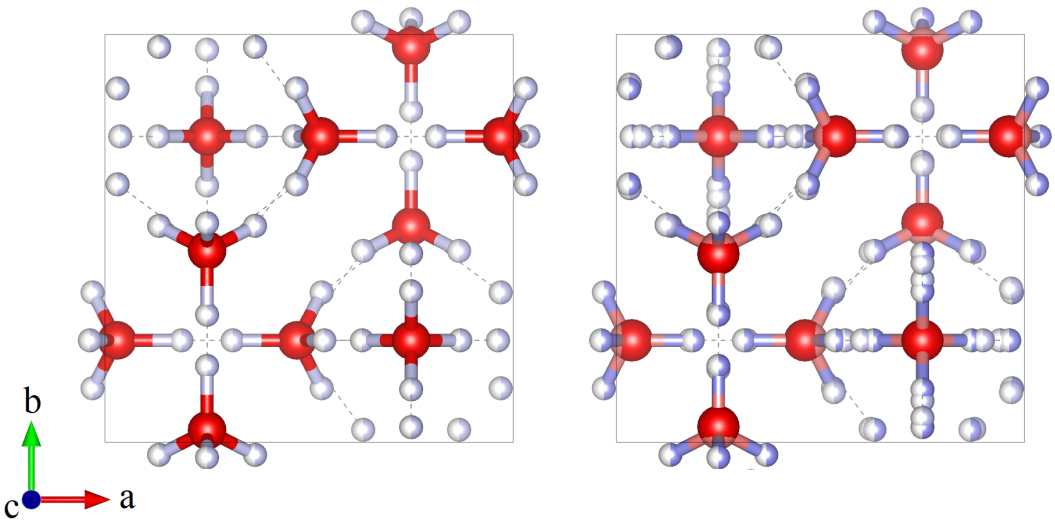

Figure 4.13 *Left: The structure ice VI as reported by Kuhs et al. [55]. Right: An overlay of the published structure of ice VI and the atomic coordinates obtained by HP-SCND in this study [2].*

Finally, the differences in the atomic distances (Å) and angles (deg) is given in Table 4.2. Being able to resolve hydrogen bonds in water with the same accuracy as established techniques finally proves that the reduction procedure and the corrections established here are robust and can be used to study single-crystals in diamond anvil cells on SNAP. This adds this technique to SNAPs repertoire and opens the possibility of a wide range of experiments.

4.5 Application on Samples Under Pressure: A Single Crystal of H_2

The development of this technique was aimed to one certain goal - namely the study of hydrogen/deuterium at pressures up to 100 GPa. Finally, as a proof-of-concept experiment a neutron DAC was loaded with a mixture of hydrogen and helium. For this the ORNL gas loader was used.

In brief, an open DAC was placed in the loading chamber of the gas loader; the gasket material was rhenium (0.25 mm thick) and the initial diameter of the gasket chamber was 0.8 mm (V=0.25 mm^3) but collapsed drastically to about 0.4 mm after compression to 9.5 GPa. Here, another gasket material had to be chosen since steel reacts with hydrogen and hence can not be used for this type of experiment. Please note the very unfavourable absorption cross-section of Re (σ_s=11.5 barns, σ_a=89.7 barns) relative to iron (σ_s=11.62 barns, σ_a=2.56 barns). As a better material tungsten (σ_s=4.6 barns, σ_a=18.3 barns) or a BeCu alloy (Cu: σ_s=8.03 barns, σ_a=3.78 barns; Be: σ_s=7.63 barns, σ_a=0.0076 barns) should be used in the future.

Gaseous helium was compressed to 1.5 kbar. Then the gas bottle was changed to a hydrogen H_2 cylinder and hydrogen was compressed as well. The overall pressure of the gas loading was 2.7 kbar, at which both H_2 and He were in a supercritical state. Assuming ideal behaviour of both fluids, this pressure ratio results in an approximately 50:50 mixture of He an H_2 in the loading chamber. The DAC was closed with a torque of 100 ft.lbf and the excess gas released, and then the DAC was quickly brought to a pressure of about 9.5 GPa. At this pressure, helium is still a fluid while hydrogen crystallises as phase I.

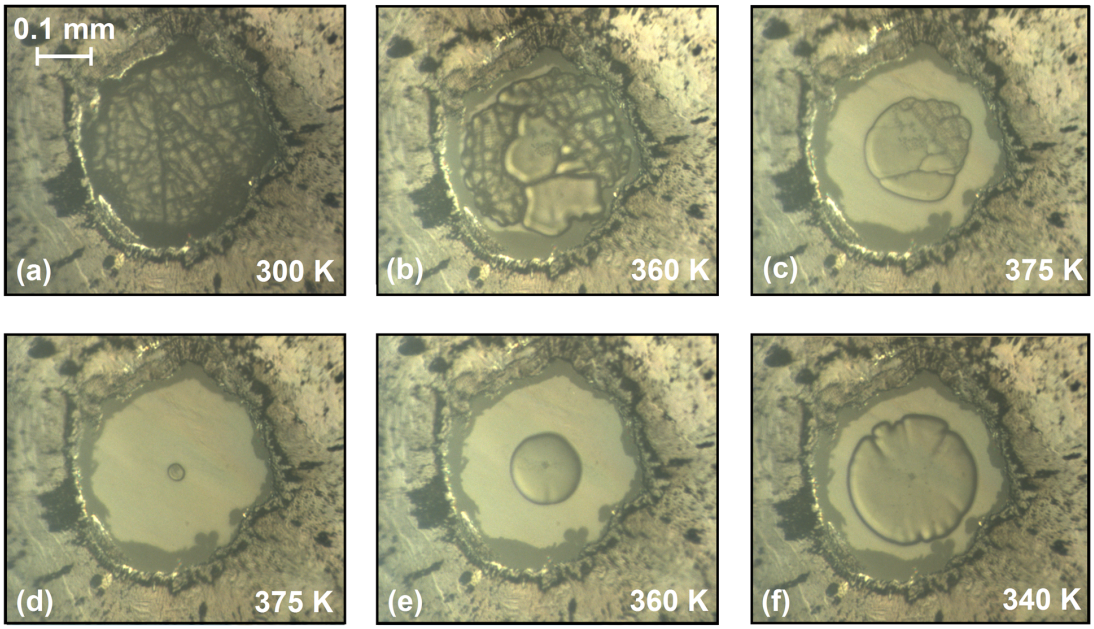

Figure 4.14 *Microscope pictures of the gasket hole loaded with a H_2 powder in a He matrix. The powder was melted by heating the sample and subsequently a single crystal was formed using a single crystallite as a nucleus.*

Compressing hydrogen this way results in a powder with crystallites too large for conventional neutron powder diffraction. Furthermore, hydrogen and deuterium crystallites forming within a diamond anvil cell have a well-defined orientation, with the c-axis of the hcp lattice oriented paralell to the axis of the anvil [110]. In figure 4.14 (a) this powder is depicted. From this powder a single-crystal was grown by repeatedly melting and re-crystalising in the same fashion as the ice VI single crystal was formed; during this process the pressure dropped to about 8.45 GPa. The progress of the crystal growth is shown in figure 4.14.

The cell containing the sample was aligned on the SNAP instrument and a data set for one orientation was collected for about 24 h. Altogether, two reflections were recorded. The detector views (right detector bank only) are given in Figure 4.15 and the two reflections are highlighted by a red circle. Please note that hydrogen phase I is a highly symmetric phase, and has a small unit cell with only two molecules on the ($^1/_3$,$^2/_3$,$^1/_4$) and ($^2/_3$,$^1/_3$,$^3/_4$) sites. So far only very few reflections have ever been reported - the (100), (010), (1$\bar{1}$0), (101), (110), (1$\bar{1}$0) and (002) reflections [78].

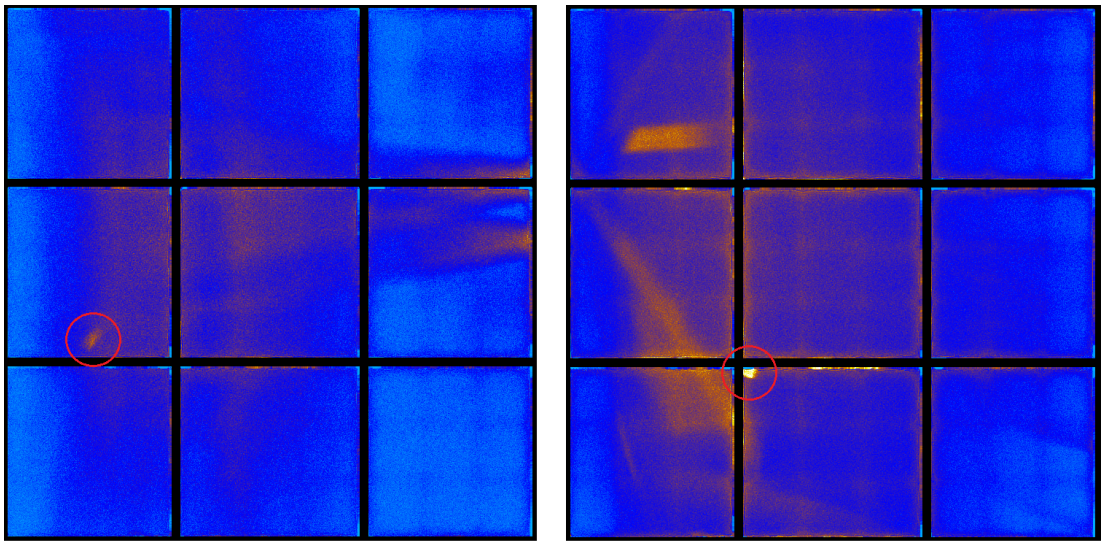

Figure 4.15 *Detector views for the left modules in the d-spacing ranges 1.0-1.4 Å (left) and 2.0-2.4 Å (right). The red circles indicate the (100) and (103) peaks of hydrogen H_2 and the detector area over which the peak-integration was carried out.*

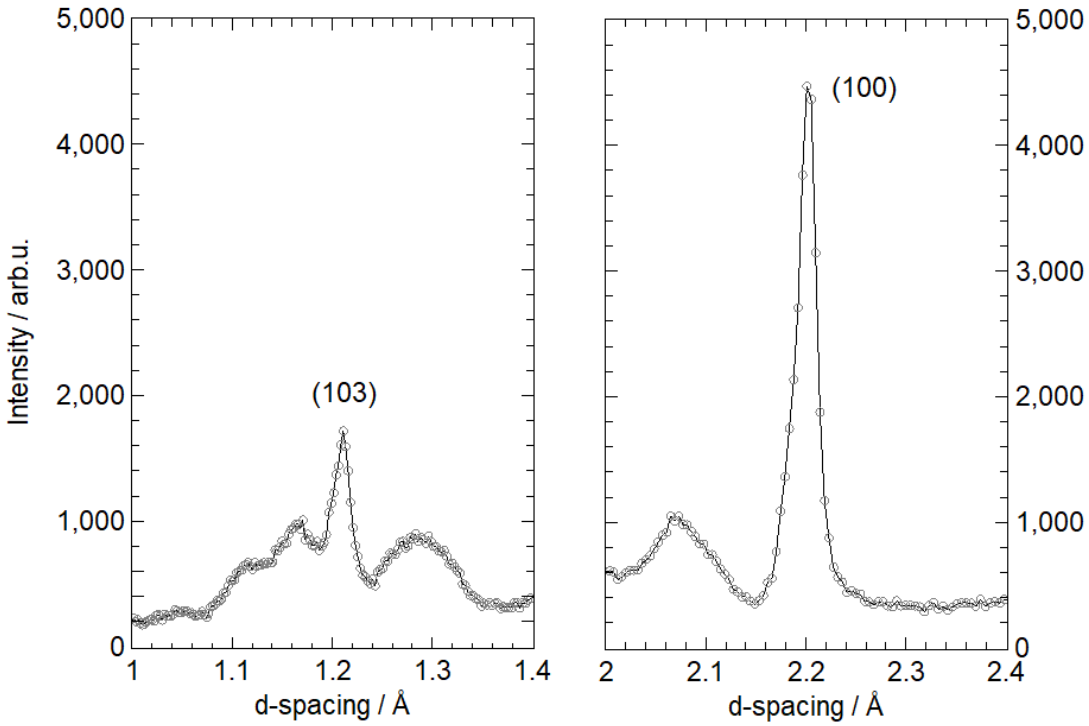

Figure 4.16 *The diffraction intensities around the reflections at 1.210 Å and 2.198 Å of hydrogen H_2 after integrating in d-spacing the two circles in Figure 4.15. In both cases a complicated background can be seen.*

The H_2 crystal of about 0.3 mm in diameter is at this point the largest one that has been grown in a DAC and still the smallest crystal measured on the SNAP instrument. It is surprising that this data could be obtained for two reasons. First, a hydrogenous sample rather than a deuterated one was used here; for neutron diffraction usually hydrogen is avoided due to its high incoherent background. And second, the gasket added a high contribution to the background and produced many parasitic powder lines. For these reasons recording two reflections is a huge success in itself especially since only one orientation was measured.

The red circles in Figure 4.15 were integrated, resulting in the peak intensities as shown in figure 4.16. The two reflections were used to construct a UB matrix to the crystal; due to only two reflections available it was not possible to assign errors to the resulting UB matrix.

From this it was possible to assign the first peak at 2.198 Å to the (100) reflection and the peak at 1.210 Å to the (103) reflection. The UB matrix was suggests the lattice parameters were a=2.541 Å and b=4.340 Å; the c/a ratio is thus 1.708. Please note that these values differ from the lattice parameters at 8.45 GPa. At this pressure the BM-EOS for hydrogen would suggest $a = 2.539$ and $c = 4.138$ and a c/a ratio of 1.630 [110]. This can be explained by the small sample of peaks, the clipping of the (100) peak at the detector edge, and the broad peak profile, in particular of the (103) reflection. Those problems should be overcome by using a deuterium D_2 sample.

4.6 Conclusion and Outlook

Several neutron-scattering experiments were performed on the TOPAZ and SNAP beamlines at the Spallation Neutron Source (SNS) at Oak Ridge National Laboratory (ORNL). As samples, deuterated potassium dihydrogen-phosphate (DKDP) and water ice VI were used. Results of the initial suite of experiments on single-crystal neutron-diffraction in diamond anvil cells are summarised in table 4.3.

In a first trial experiment it was shown that it is possible to obtain data of high quality from a DAC-sized crystal. The results are in good agreement with the crystal structure published by Tiballs *et al.* [244], indicating that it is feasible to reduce the sample size to a volume smaller than that of a typical neutron-DAC cavity. The experiment was repeated in the sample environment of a diamond anvil cell. Despite the - not surprising - loss of data quality, it was possible to obtain enough structure factors to refine the structure with the same accuracy as in the case of the bare crystal, however, the errors on the structural parameters increased significantly.

Table 4.3 *Summary of the refinements for the DKDP crystal in a DAC-sample environment for SNAP and TOPAZ, respectively. The collection time per orientation is given as well as the number of reflections after outlier removal. Only best refinements are shown - for detailed information see tables 4.4 and 4.5 in appendix.*

Crystal	Small	Large	Small	DAC	DAC
Instrument	TOPAZ	SNAP	SNAP	TOPAZ	SNAP
Orientations	10	6	6	10	6
Collection time / orientation	3 h	3 h	3 h	6-8 h	3 h
Reflections	1044	1027	279	167	56
R_w	0.045	0.067	0.090	0.087	0.336

In a second step, SNAP, an instrument primarily used for powder diffraction, was bench-marked for quantitative analysis of single crystal data. It was possible to show that single crystal diffraction on SNAP is feasible and that the data is of similar quality to TOPAZ. Subsequently, patterns of a DAC-sized sample were collected to test the volume limitations of SNAP. Altogether 279 structure factors were obtained - enough to refine the structure to R_w=0.090.

Finally, patterns of a single crystal in a diamond anvil cell were collected on SNAP. Due to time restrictions, only 56 reflections from 6 orientations were obtained (measured for 3 h each); a similar experiment carried out on TOPAZ (10 orientations for 6-8 h each) in comparison resulted in about 300 structure factors. Nevertheless it was possible to refine the structure from the obtained data, however, the large errors on the atomic coordinates suggest that a similar collection time as on TOPAZ is needed for precise results.

The data reduction procedure was then tested against a crystal of ice VI which was grown in a DAC. Diffraction patterns of three orientations (measured for 12h each) resulted in 84 observed structure factors - enough to carry out a refinement that reproduced the published structure of ice VI, proving that HP-SCND on SNAP is possible.

Based on this promising result, a proof-of-concept experiment was conducted; a single crystal of hydrogen was grown in a diamond anvil cell at about 8 GPa. This crystal was then measured on SNAP as well and - despite it being a hydrogenous sample - it was possible to obtain two well defined peaks. A further analysis of this crystal was not possible and all additional beamtime to investigate the actual crystal structure of hydrogen and deuterium was cancelled due to the global pandemic hitting the world in 2020. However, based on these preliminary results more experiments will be scheduled as soon as possible.

Table 4.4 *Comparison of refinements of data of DKDP in a diamond anvil cell. The data was integrated using the standard TOPAZ algorithm (DAC_a), a refined UB for every orientation (DAC_{UB}), and a selected subset of peaks (DAC_s) to exclude peaks on powder lines. While the first integration was carried out using the IntegrateEllipsoid algorithm, the last column (DAC_p) was treated as the DAC_s data but it was integrated using the IntegratePeaksProfileFitting algorithm.*

Crystal	KDP*	DKDP*	Small	DAC_a	DAC_{UB}	DAC_S	$DAC_{UB,P}$	$DAC_{S,P}$
Note	Nelmes82	Nelmes82	TOPAZ	TOPAZ	TOPAZ	TOPAZ	TOPAZ	TOPAZ
Obs	-	-	1044	359	216	222	323	167
Rw(Fobs)	0.022	0.055	0.045	0.201	0.145	0.117	0.110	0.087
a	7.4521(4)	7.4645(3)	7.4505(12)	7.4534(10)	7.4534(4)	7.4660(7)	7.4713(3)	7.4652(8)
c	6.974(2)	6.9678(4)	6.9679(8)	6.9701(8)	6.9732(4)	6.9733(6)	6.9722(2)	6.9779(7)
a/c	0.936	0.934	0.933	0.935	0.936	0.934	0.933	0.934
O-O	2.4944(5)	2.5286(4)	2.5322(4)	2.37(2)	2.3923(4)	2.51(2)	2.507(9)	2.511(9)
O-P	1.5402(4)	1.54207(19)	1.53717(16)	1.51(1)	1.59568(16)	1.551(10)	1.545(4)	1.541(7)
O-D	1.0657(12)	1.0419(3)	1.062(8)	1.13(9)	0.97830(14)	1.071(11)	1.05(1)	1.05(1)
D-D	0.367(3)	0.4511(4)	0.420(16)	0.31(8)	0.44359(6)	0.404(6)	0.45(2)	0.42(6)
x(D)	0.14757(12)	0.14861(2)	0.14844(23)	0.1331(21)	0.1444(18)	0.1528(23)	0.1467(10)	0.1474(18)
y(D)	0.22559(15)	0.22011(2)	0.2217(10)	0.258(11)	0.2204(11)	0.2250(40)	0.2222(12)	0.2220(35)
z(D)	0.12161(47)	0.12041(3)	0.1196(10)	0.146(6)	0.12173(6)	0.1140(40)	0.1229(14)	0.1250(40)
x(O)	0.14839(3)	0.14888(1)	0.14891(11)	0.1438(17)	0.15215(14)	0.1472(15)	0.1494(5)	0.1486(9)
y(O)	0.08264(3)	0.08073(1)	0.08070(11)	0.0909(13)	0.08957(12)	0.0836(12)	0.0822(6)	0.0818(11)
z(O)	0.12584(5)	0.12643(2)	0.12566(11)	0.1166(9)	0.12942(8)	0.1299(21)	0.1254(4)	0.1258(8)
UISO (D)	-	-	0.0279(8)	-0.017(6)	0.17(6)	0.0288(16)	0.0256(16)	0.033(4)
UISO (O)	-	-	0.0183(12)	0.045(9)	0.064(26)	0.0179(21)	0.0146(8)	0.0166(20)

Table 4.5 *Sequentially deteriorating data quality with crystal size and the complexity of the sample environment .*

Crystal	KDP*	DKDP*	Small	Large	Small	DACm
Note	Nelmes '82	Nelmes '82	TOPAZ	SNAP	SNAP	SNAP
Obs	-	-	1044	1027	279	56
Rw(Fobs)	0.022	0.055	0.045	0.067	0.090	0.336
a	7.4521(4)	7.469(1)	7.4505(12)	7.4988(1)	7.4865(8)	7.4773(10)
c	6.974(2)	6.976(1)	6.9679(8)	7.0037(2)	6.9927(9)	7.0001(31)
a/c	0.936	0.934	0.933	0.934	0.934	0.936
O-O	2.4944(5)	2.5286(4)	2.5322(4)	2.535(3)	2.530(8)	2.42(8)
O-P	1.5402(4)	1.54207(19)	1.5371(16)	1.5478(12)	1.544(4)	1.61(5)
O-D	1.0657(12)	1.0419(3)	1.062(8)	1.056(3)	1.066(8)	0.99(12)
D-D	0.367(3)	0.4511(4)	0.420(16)	0.430(5)	0.404(13)	0.5(3)
x(D)	0.14757(12)	0.14861(2)	0.14844(23)	0.14868(24)	0.1487(10)	0.142(14)
y(D)	0.22559(15)	0.22011(2)	0.2217(10)	0.22150(18)	0.2233(8)	0.219(15)
z(D)	0.12161(47)	0.12041(3)	0.1196(10)	0.1199(4)	0.1209(15)	0.124(20)
x(O)	0.14839(3)	0.14888(1)	0.14891(11)	0.14901(11)	0.1488(5)	0.161(4)
y(O)	0.08264(3)	0.08073(1)	0.08070(11)	0.08096(10)	0.0810(5)	0.088(5)
z(O)	0.12584(5)	0.12643(2)	0.12566(11)	0.12577(13)	0.1260(5)	0.121(8)
UISO (O)	-	-	0.0183(12)	0.02612(4)	0.01755(5)	0.006(10)
UISO (D)	-	-	0.0279(8)	0.01664(5)	0.01709(8)	0.023(33)

Chapter 5

A Novel N_2 sX Hydrate

Amongst the hydrate water networks, sX, first discovered as part of the C_0 structure of hydrogen hydrate [151], stands out: it is chiral, has channels rather than cages, is not based on a stable ice structure (like the filled ice II structure [152]), and its network does not have an analogue in either silica or zeolite structures [153, 154]. It does, however, exist in some ternary Zintl compounds and has been suggested as a metastable group-14 structure [155–157]. The structure proposed initially was based on channels that contained sites partially occupied by non-hydrogen bonded water molecules [151].

Based on the observed high mobility of hydrogen in this structure [151] and molecular-dynamics modelling, Smirnov *et al.* proposed what emerged to be the correct structure: they suggested that the water molecules in the channels were in fact nitrogen molecules that had been absorbed from the liquid storage medium between recovery and the diffraction measurement [158]. Subsequently, del Rosso *et al.* were able to empty C_0 of hydrogen and to identify the structure as a new form of ice, ice XVII [159, 160]. Finally, Amos *et al.* found that sX also exists in the carbon dioxide:water system and determined the full structure of both hydrogen and carbon dioxide hydrates *in situ* using neutron diffraction [154].

Due to the high guest-host ratio, the reversibility of the filling and emptying, and the high mobility of hydrogen in the cavities, the sX/ice XVII system has been proposed as a possible hydrogen storage material [257, 258]. Other possible applications, however, have not been discussed. With its channel structure, and high surface area, ice XVII resembles activated charcoal and could therefore

be used as a low-temperature molecular sieve. Here, high-pressure neutron diffraction data is shown that indicates that ice XVII can, indeed, absorb nitrogen molecules. Furthermore it is shown that nitrogen sX undergoes a series of transformations into other, exotic, hydrate types before forming the stable sII structure.

5.1 Experimental Procedure and Methods

This experiment was conducted in a gas pressure cell made from aluminium (c.f. section 3.1.1) at the PEARL beam-line, the dedicated high-pressure powder instrument at the ISIS neutron source at the Rutherford Appleton Laboratory (RAL, Oxfordshire, UK) [221]. This instrument has access to a d-spacing range out to beyond 4 Å, which is necessary to record sX's (101) Bragg reflection at 4.1 Å. This peak is very sensitive to the guest-site occupation. The analysis of the diffraction patterns was carried out by either Rietveld or LeBail profile refinement using the GSAS-II crystallographic software package [183].

Furthermore, a computational study is mentioned here; the respective calculations were performed by Lewis Conway and were essential in the data analysis process. The enthalpy calculations based on density functional theory (DFT) were performed using the CASTEP code [239] on sets of approximate sX structures with a range of tractable guest-host ratios as well as fully filled nitrogen hydrate III (NH-III). Exchange-correlation effects were described within the generalised gradient approximation (GGA) using the Perdew-Burke-Ernzerhof (PBE) functional [234] and ultra-soft pseudo-potentials as generated 'on-the-fly' by CASTEP with radii cut-offs of 1.1 Bohr for oxygen and nitrogen, and 0.6 Bohr for hydrogen. Geometry optimisations were performed with plane wave cut-offs of 1000 eV and a Monkhorst-Pack [259] k-point spacings of no more than $2\pi \times 0.04$ Å^{-1}.

The calculations were performed on water networks with hydrogen arrangements to give a zero net dipole moment per unit cell. To calculate stable compounds enthalpy values were compared according to $H = U + PV$ where U is the internal energy per molecule and P and V are the pressure and molecular volume respectively. Calculations on ices XI, IX, XV, VIII and the relevant phases of α-, γ-, and ϵ-N_2 were performed as well to compare the enthalpy values with the

ones of the pure molecular phases [260]. The nitrogen hydrate compounds which form the convex hull of the relative formation enthalpies (see equation 6.1), are thermodynamically stable against decomposition.

$$\Delta H(x) = H((H_2O)_x(N_2)_{(1-x)}) - xH(H_2O) - (1-x)H(N_2) \tag{5.1}$$

An initial leak test was performed and showed no significant pressure drop with time in the setup. Deuterated water (D_2O, Sigma, 99.9% D) was frozen to produce ice I_h and ground under liquid nitrogen to a fine powder. The powder then was filled into a cooled hydrogen-compatible gas cell at 77 K and pressurised with hydrogen gas to 0.300 GPa. To control the temperature in the cell during the experiment, an ILL patented 'Orange' helium cryostat was used. Upon heating to 195 K at 0.300 GPa, the H_2-I_h mixture undergoes transitions first to the C_{-1} hydrate at 160 K and than to C_0 (H_2-sX) above 180 K. The respective diffraction patterns for the two transitions are shown in figure 5.1 and will not be discussed here; for more information see Donnelly (2016) [41] and Donnelly *et al.* (2018) [261].

After the full transformation to C_0, the sample was cooled to 80 K and the pressure was released. It is well known that ice XVII can be easily formed by pumping off the hydrogen in sX [159], however, the same can be achieved by heating the hydrogen hydrate at ambient pressure to 130 K [41]. As the hydrogen left the structure, the volume of the unit cell started to decrease, indicating the emptying of the channels in sX. To ensure that the starting material for the experiment is pure ice XVII, diffraction patterns were collected every hour. The transformation was considered complete after about 12 h, at which point the volume of the unit cell did not shrink any further with time (see left panels in Figure 5.2). Furthermore, the Rietveld refinements carried out on the last diffraction pattern suggest completely empty channels.

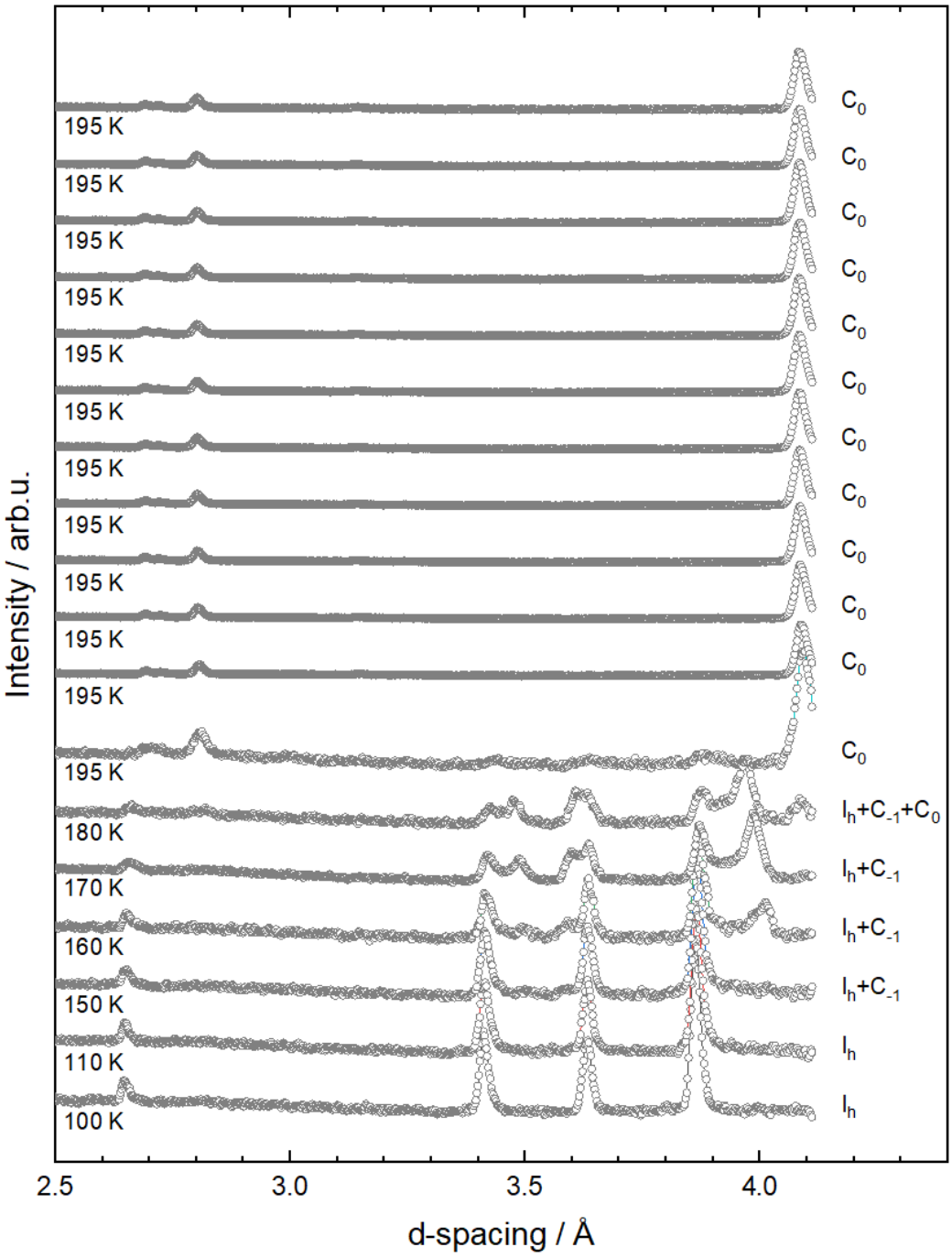

Figure 5.1 *Powder diffraction patterns of the subsequent formation of C_{-1} and C_0 from a mixture of deuterated ice I_h and hydrogen H_2 upon heating to 195 K.*

5.2 Results and Discussion

The emptied C_0 hydrate (ice XVII) was then pressurised with nitrogen to 180 bar (0.0180 GPa; the pressure of a full gas bottle) at 130 K. Upon that, an uptake of gas was observed. Firstly, the pressure in the cell dropped with time and additional gas had to be added to the system regularly (every half hour) to maintain the pressure of 180 bar. And secondly, upon analysing the diffraction patterns an expansion of the unit cell volume was observed (see right panel in figure 5.2). This volume increase was most pronounced along the *c*-axis of s*X* (the axis that contracts most on removal of hydrogen) as can be seen in the c/a ratio in the plot *ibid.*

5.2.1 Structure of Nitrogen sX Hydrate (NH-V)

After about 7 hours no changes in pressure and lattice parameters were observed, indicating that the structure was saturated with nitrogen. Data were then accumulated for about 5 h for full structural analysis. The results of a Rietveld profile refinement are shown in figure 5.3, together with the refined crystal structure. It was possible to fit the known pattern of the s*X* structure to our data [154]. The space group is $P6_122$ or $P6_522$, but lower symmetry space groups were initially tested as well.
While most other reported s*X* hydrates (H_2, CO_2, Ne, Ar) crystallise in $P6_122$ or $P6_522$, an Italian group around Catti *et al.* found that oxygen, a diatomic molecule of similar size to nitrogen, forms a $P6_1$ structure [262]. Attempts with lower symmetry space groups, however, led to unstable refinements and were hence discarded.

From the refinement the lattice parameters $a = 6.240(3)$ Å and $c = 6.065(2)$ Å were obtained; the respective Rietveld fit to the data is shown in figure 5.3. According to the established numbering methodology, the name nitrogen hydrate V (NH-V) for this new s*X*-type hydrate is proposed. To model the disorder in the H-bonded water lattice, a 2-site model was used; two deuterium atoms with an occupancy of 0.5 were placed along the O-O axis, one representing the covalent O-D bond, the other the D$\cdots$O hydrogen bond.

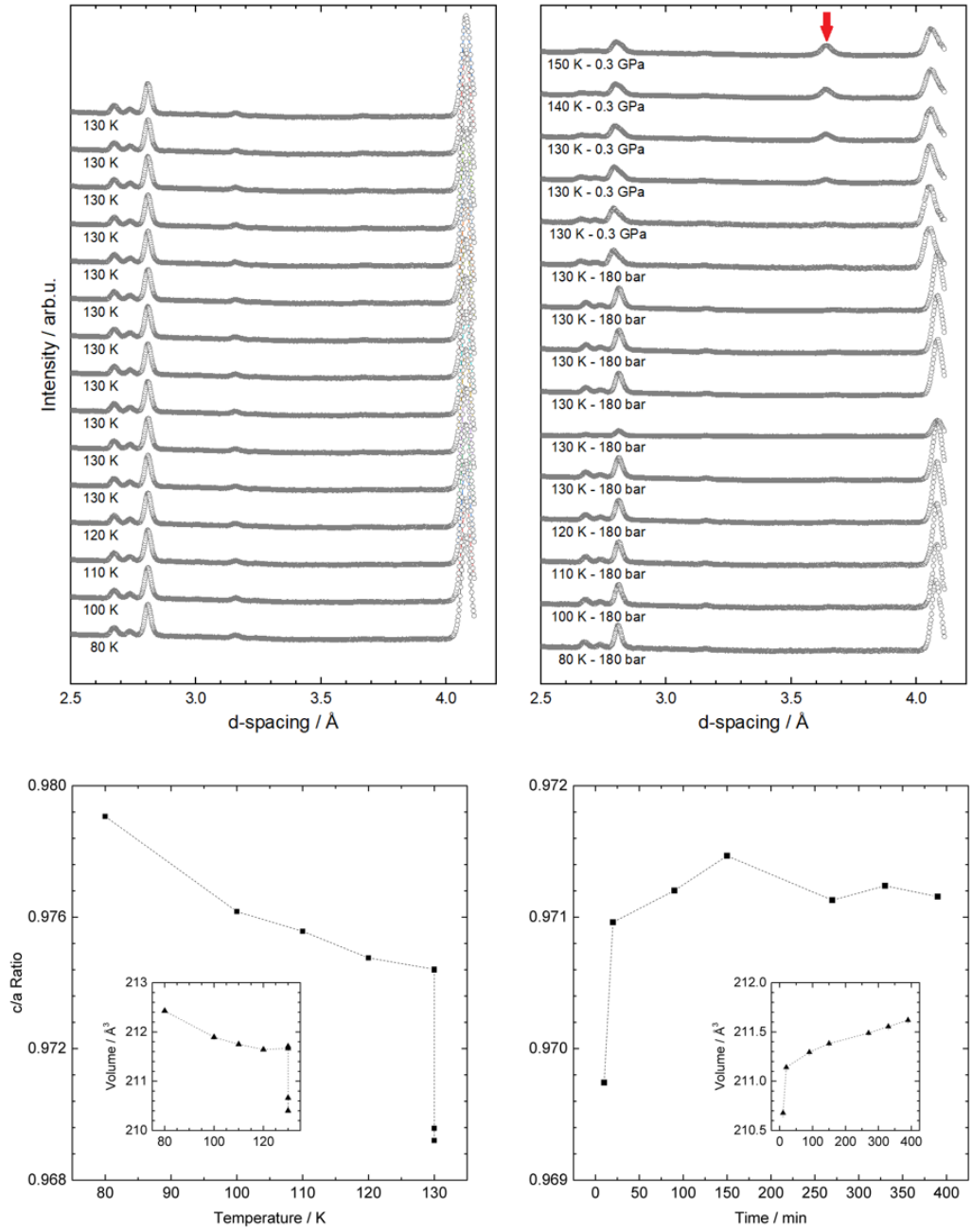

Figure 5.2 *Top: Diffraction patterns of the emptying (removal of H_2, left) and subsequent filling of the water network with N_2 (right).*
Bottom left: The c/a ratio and overall unit cell volume of hydrogen sX as a function of temperature; the values at 130 K were recorded over a period of about 7 hours. The decrease of the overall volume indicates the removal of hydrogen from the channels. Bottom right: The c/a ratio and overall unit cell volume of hydrogen sX as a function of time. The increase in volume (primarily along the c-axis) indicates the uptake and incorporation of nitrogen into the chiral channels. In both plots the uncertainties are smaller than the symbols and hence error bars have been omitted.

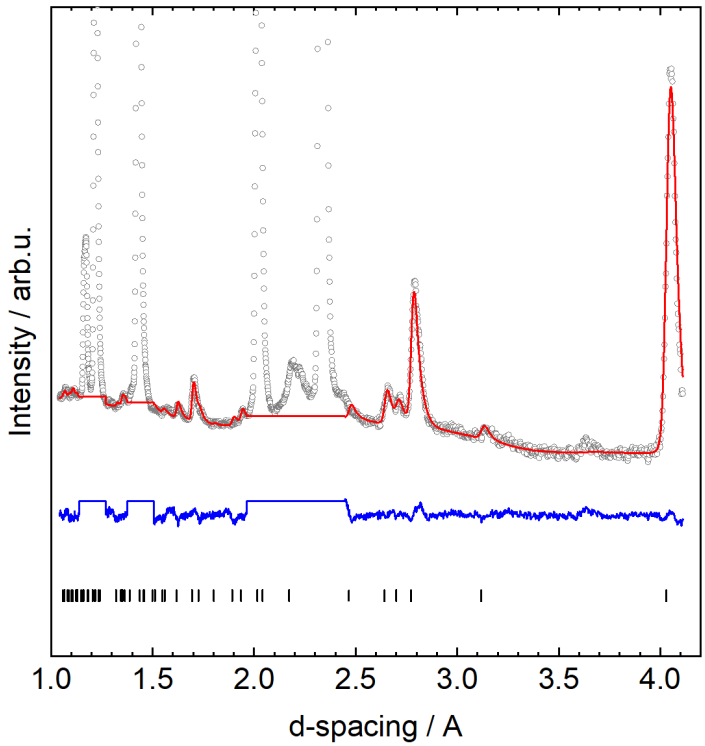

Figure 5.3 *The results of a Rietveld profile refinement of data collected at 0.018 GPa and 130 K using the nitrogen sX structure. Gray circles are measured data points, the red curve gives the calculated pattern, and blue line the difference between observed and calculated profiles. The excluded sections correspond to regions affected by the Bragg reflections of the aluminium pressure cell.*

As shown by del Rosso *et al.*, guest molecules in the s*X* structure are highly mobile and are not locked into one position [257, 258]. This results in a rather continuous nitrogen density along the helical channels. In order to model this continuous nitrogen occupancy in the channels, two nitrogen atoms were placed on two 12-fold sites. The difference in the nitrogen occupancy of these two atoms (0.22(4) and 0.16(2), respectively is most likely a result of statistically preferred positions inside the channel. As both nitrogen atoms sit on equivalent 12c sites, the overall occupancy of nitrogen is 0.19(3) and hence a guest:host ratio of 1:2.6(3) was calculated.

For this model an overall R_w of 0.01386 was achieved and the resulting structural parameters for NH-V are summarised in table 5.2. While the overall fit seems to be reasonable, this refinement resulted in a very short N≡N distance of 0.62(10) Å. In comparison, the tetragonal γ phase (stability region 0.3-3.0 GPa) of pure nitrogen has a N≡N bondlength of about 1.10 Å [263].

Table 5.1 *Unit cell lattice parameters (a and c), oxygen and nitrogen fractional coordinates (x, y, z), occupancies, and multiplicities and Wyckoff positions of the sites for NH-V from neutron diffraction (values obtained at 0.018 GPa and 130 K). The space group of NH-V is either $P6_122$ or $P6_522$ with lattice parameters of $a = 6.240(3)$ Å, and $c = 6.065(2)$ Å.*

Atom	x	y	z	U_{iso}	Occ.
O (6b)	0.764(5)	0.5270(18)	0.250(9)	0.022(15)	1.00(0)
D (6b)	0.377(10)	0.071(6)	0.532(4)	0.024(8)	0.50(0)
D (6b)	0.563(8)	0.335(6)	0.458(3)	0.022(9)	0.50(0)
N (12c)	0.957(10)	0.142(14)	0.652(13)	0.05(7)	0.22(4)
N (12c)	0.213(8)	0.065(12)	0.883(12)	0.04(6)	0.16(2)

A second attempt to refine the structure was made, in which the occupancy of the two nitrogen sites was forced to be equal. This refinement gave an overall R_w of 0.02075, so a slightly worse fit than the first refinement. The occupancy of the nitrogen sites here was refined to be 0.319(16); this is equivalent to a guest:host ratio of 1:1.56(7). This value is far from the calculated ideal filling ratio for NH-V (see below), however this refinement gave more plausible N-N distances of 0.90(5).

Table 5.2 *Unit cell lattice parameters (a and c), oxygen and nitrogen fractional coordinates (x, y, z), occupancies, multiplicities, and Wyckoff positions of the sites for NH-V from neutron diffraction (values obtained at 0.018 GPa and 130 K). The space group of NH-V is either $P6_122$ or $P6_522$ with lattice parameters of $a = 6.240(3)$ Å, and $c = 6.065(2)$ Å.*

Atom	x	y	z	U_{iso}	Occ.
O (6b)	0.763(5)	0.5270(18)	0.250(9)	0.022(15)	1.00(0)
D (6b)	0.377(10)	0.071(6)	0.532(4)	0.024(8)	0.50(0)
D (6b)	0.563(8)	0.334(6)	0.458(3)	0.022(9)	0.50(0)
N (12c)	0.957(10)	0.130(4)	0.695(8)	0.013(16)	0.319(16)
N (12c)	0.2262(27)	0.0574(24)	0.9012(27)	0.029(4)	-

Please note that neither the lattice parameters nor the position of the water molecules were affected by restraining the occupancy of the nitrogen atoms. This likely indicates that the nitrogen molecules are indeed very mobile and that the data set alone does not suffice to determine the exact position and occupancy of a rather continuous distribution of guests in the channel.

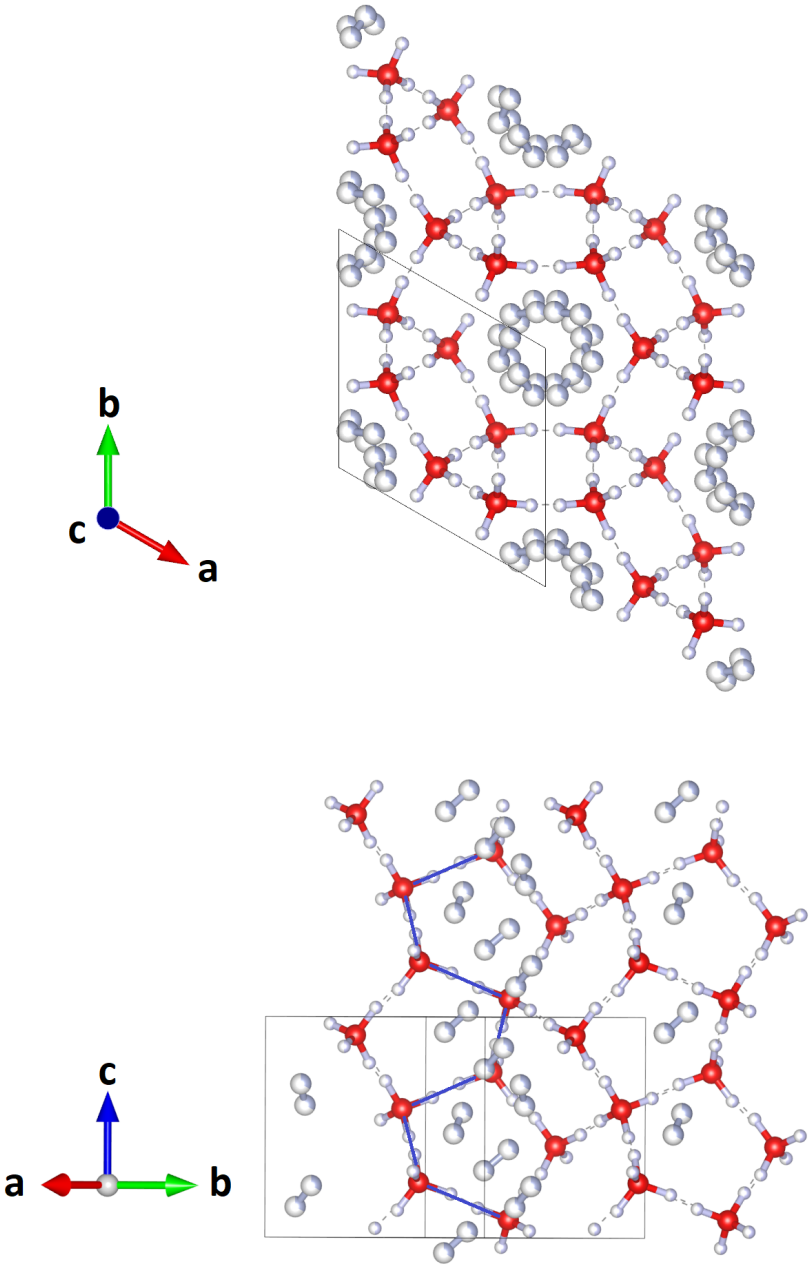

Figure 5.4 *Refined $P6_122$ structure of NH-V (sX-hydrate) from the neutron diffraction data with oxygen atoms (red), deuterium atoms (white), and nitrogen atoms (blue). Fractionally occupied sites are displayed by partially coloured atoms. The structure is projected along the c-axis (top) and normal to it (bottom). The spiral-arranged sequences of hydrogen bonds are indicated by blue lines in the bottom picture.*

For both refinements the occupancies of 0.19(3) and 0.319(16) correspond, on average, to 2.28 and 3.828 molecules per unit-cell. Thus, from this model it can be assumed that in each cell at least two molecules are present. The guest molecules are located on one of the 12 nitrogen sites that are arranged in a spiral-like configuration inside the [001] channels of the water framework. However, from the structure of the γ-phase of solid nitrogen it can be assumed that the shortest N–N intermolecular contact should not be less than 3.46 Å. Therefore, if the first site is occupied by a nitrogen, the next-nearest occupied site should be 6 to 8 sites down along the channel (intermolecular distance of 3.29(6) Å and 3.80(5), respectively). This makes the first occupancy of 0.19(3) more plausible - despite the unrealistic nitrogen bondlength of 0.62(10) Å.

Table 5.3 *Interatomic distances in NH-V at 0.018 GPa and 130 K as obtained from neutron powder diffraction data.*

	Distance / Å		Distance / Å
O-O	2.749(10)	N1-O	2.12(6)
O-O'	2.715(12)	N2-O	2.37(5)
N1-D1	1.58(7)	N2-D1	2.11(5)
N1-D2	2.27(6)	N2-D2	2.16(5)
O-D1	0.95(5)	N1-N2	0.90(5)
O-D1'	1.80(5)	N1-N1'	1.40(3)
O-D2	0.96(6)	N1-N2'	1.68(4)
O-D2'	1.76(5)		

The structure obtained from the second refinement is shown in figure 5.4. As mentioned in the introduction, NH-V (at 180 bar and 130 K) has a helical water network (indicated by the blue lines) with the covalent O-D bonds having a length of 0.95(5) and 0.96(6) Å, respectively; the hydrogen bonds are 1.80(5) and 1.76(5) Å, respectively. These are typical values for clathrate hydrates (c.f. Sloan (2008) [77]). On looking at the list of N–D distances between the nitrogen molecules and deuterium atoms (see Table 5.3), the N1-D1 contact appears to be shorter than 1.8 Å. This clearly suggests a weak attractive interaction from the nitrogen molecules. The particularly short interatomic distance of 1.58(7) indicates a hydrogen bonding between guests and host-lattice here.

In addition to this experimental work, DFT simulations were carried out [1]. The reason for this study was of a twofold nature; first, to further support the presented structure which is based on a meagre diffraction pattern and second, to obtain the ideal filling ratio of nitrogen sX. The calculated relative atom positions are summarised in table 5.4 and are in good accordance with the parameters found experimentally. This further supports the structure presented here but also sheds light on the error on the nitrogen positions inside the channel and the respective filling ratios.

Table 5.4 *Fractional coordinates (x, y, z) and Wyckoff positions of the sites for NH-V from from a GO calculation with lattice parameters of $a = 6.263$ Å, $c = 6.065$ Å. The filling ratio is 1:2 for a pressure of 4 GPa (the minimum pressure of convex hull plot, see figure 5.5).*

Atom	x	y	z
O (6b)	0.7641	0.5282	0.2500
D (6b)	0.3782	0.0692	0.5248
D (6b)	0.5723	0.3361	0.4507
N (12c)	0.8236	0.1003	0.4860
N (12c)	0.1762	0.8997	0.9860

The relative enthalpies of formation, $\Delta H(x)$, for a series of NH-V approximants with guest-host ratio $1 : n$ ($n = 2, 3, 4, 6$; $x \approx 0.67, 0.75, 0.80, 0.86$) are shown in figure 5.5 (a) as a function of pressure. To estimate the stability of intermediate guest-host ratios, a quadratic function is fitted to the formation enthalpies of the four NH-V approximants. The curve segment of the quadratic which forms the convex hull of equation 6.1 corresponds to the most favourable guest-host ratios. For NH-V, guest-host ratios of between 1:2.8 and 1:3 are most stable across the entire pressure range. This can be seen in figure 5.5 (b) which shows the composition-pressure phase diagram of nitrogen hydrates. There is a spread of metastable NH-V structures with similar filling ratios indicated by the dotted region. In comparison, similar calculations on H_2-sX (C_0) and CO_2-sX suggest a guest:host ratios of 1:2 and 1:4 respectively, roughly in agreement with experimental findings [154].

Along a fixed stoichiometry of 1:3 N_2:H_2O, the calculations predict a transition from NH-III to NH-V at around 2.5 GPa. (NH-III is a tetragonal hydrate, sT, in the space group $P4_2/mnm$ and the lattice parameters $a = 6.342$ Å and $c = 10.610$ Å[38].) The latter structure is stabilised by having a smaller molecular volume due to efficient packing of the nitrogen molecules.

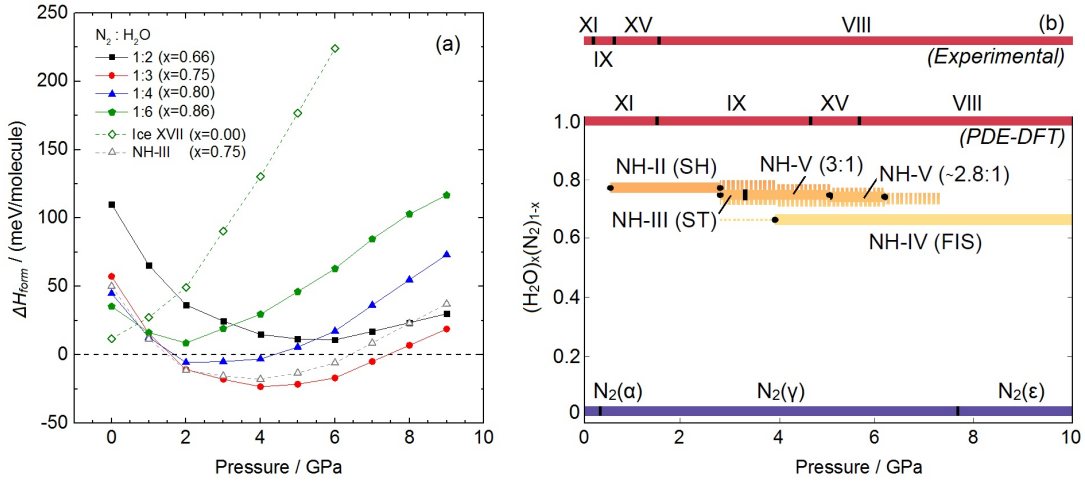

Figure 5.5 *(a) Relative enthalpies of NH-V with a range of filling ratios against decomposition into pure ice and N_2 calculated from equation 6.1. For comparison, the metastability of pure ice XVII is indicated, as well as the formation enthalpy of NH-III hydrate. (b) Composition-pressure phase diagram of nitrogen hydrates. Solid lines correspond to stable points on the convex hull and dotted lines correspond to metastable points within 5 meV of the hull. For comparison, the experimental phase evolution of ice is shown along the top.*

The semi-local exchange-correlation functional used for these calculations does not fully account for longer range dispersion interactions which may be present. As a result, the pressure estimations are higher than seen in experiment, an effect well known for ice [236]. To illustrate this, the experimental low temperature phase evolution of ice in the same pressure range is shown in figure 5.5. However, PBE usually provides at least qualitative agreement with experiment (sometimes much better than that [264]) and taken together with the experimental results provides good evidence for the existence of NH-V.

5.2.2 Decomposition of NH-V

In the experiment, the nitrogen pressure was then increased to 0.300 GPa at 130 K. This led to changes in the diffraction pattern - the intensity of the peak at 4.12 Å decreased, while a new peak at about 3.64 Å slowly emerged, indicating a structural change in the sample (see figure 5.2; the new peak is indicated by a red arrow). To speed this process up, the temperature was increased - first

in 10 K steps to 160 K under a static pressure of 0.300 GPa, then in larger temperature steps. At every temperature, diffraction patterns were collected for about one hour each. A pressure drop in the sample chamber upon every increase in temperature was observed, indicating additional gas uptake. In figure 5.6 the respective diffraction patterns upon heating are depicted, with the first, blue curve being the pattern recorded at 0.018 GPa and 130 K. The newly emerging peak at 3.64 Å is close to a *d*-spacing that would suggest a doubling of the s*X* unit cell (it would be the (211) peak). Upon closer investigation, however, this theory was proven wrong, and it was possible to identify this peak to belong to the hexagonal clathrate structure sH, a high-pressure phase hitherto only observed above 0.85 GPa [57, 70]. This structure comprises two different small cages and one large cage, which runs the length of the unit cell along the *c*-axis. The sH structure is found in many simple gas hydrates (for example, Ar, Kr, Xe, methane, and N_2) but generally in the pressure range $\sim$ 1-2 GPa [42, 57, 162]. Here, the sH structure has the lattice constants $a = 11.82(4)$ Å, and $c = 9.82(4)$ Å.

Upon further heating above 160 K (turquoise curve in figure 5.6) the intensity of sH's peaks stayed constant, whilst the peaks from NH-V (and from the residual ice XVII) decreased. Simultaneously, new peaks belonging to the sII clathrate hydrate structure appeared in the diffraction pattern. Note that only the NH-V peaks disappeared, the peaks assigned to sH remained. This suggests that sII does not form directly from sH but rather that it is formed from NH-V. Analogous observations in the H_2-H_2O system support this hypothesis. Donelly *et al.* found that hydrogen s*X* (C_0) transforms into sII upon heating at 0.300 GPa [41, 261]. Furthermore, it would not be surprising that residual ice XVII, a metastable structure, transformed in the presence of a suitable guest into sII as well. The transformation NH-V $\longrightarrow$ sII therefore gives a second possible route for the decomposition.

Table 5.5 *Space group and unit cell lattice parameters (a, c) for the N_2 variants of sX, sH, sIII, and sII at 0.300 GPa*

Hydrate		Space group	*a* / Å	*c* / Å
NH-V	s*X*	$P6_122$	6.240(3)	6.065(2)
NH-II	sH	$P6/mmm$	11.82(4)	9.82(4)
NH-I	sII	$Fd\bar{3}m$	17.152(4)	17.152(4)
NH-VI	sIII	$P4_2/mnm$	22.914(9)	12.003(7)

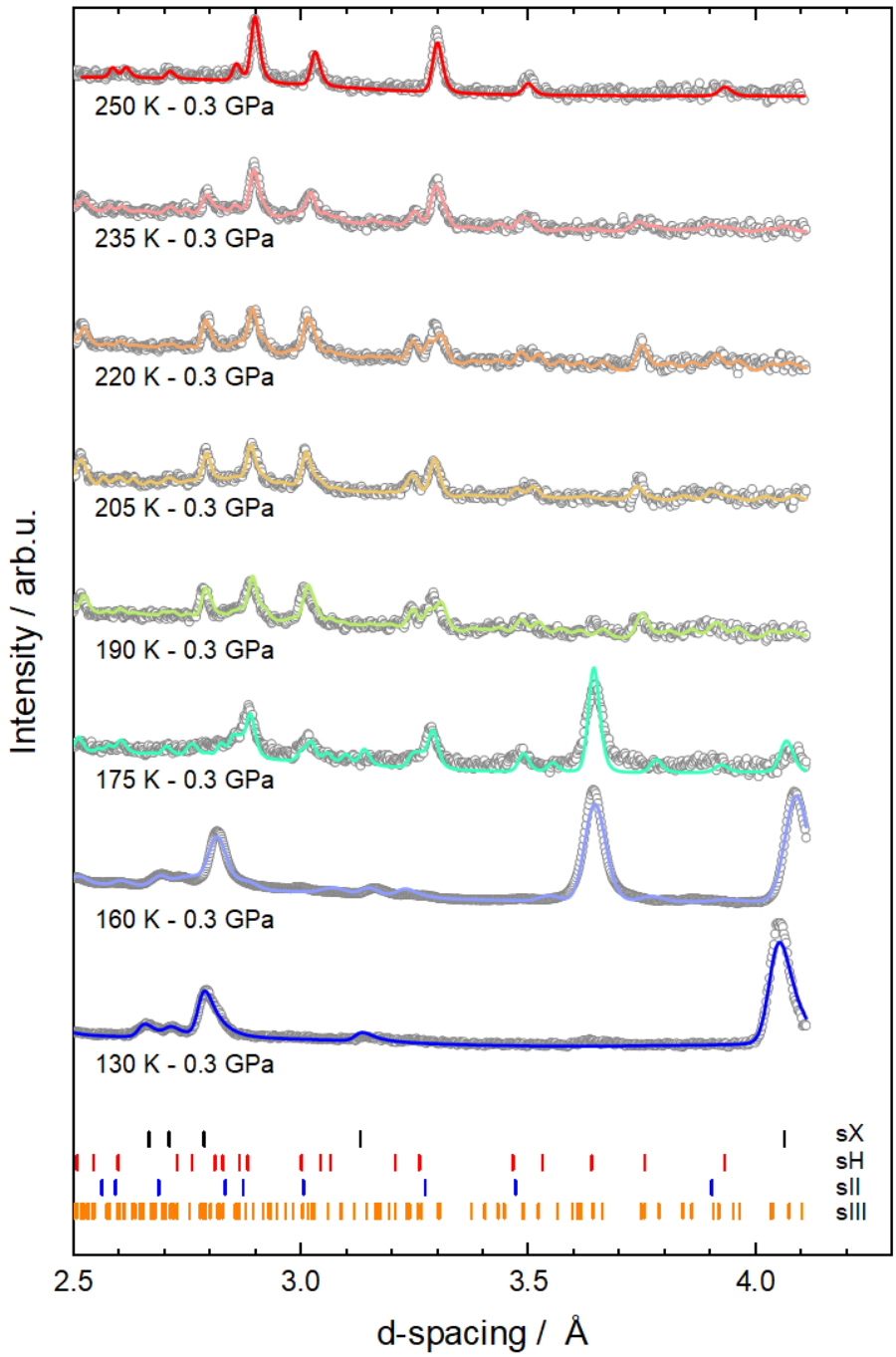

Figure 5.6 *Neutron diffraction patterns recorded while heating the sample at 0.300 GPa. The first curve (blue) gives the pattern of nitrogen sX. The main components of the respective patterns are from bottom to top: sX, sX+sH, sH+sII, sII+sIII, sII+sIII, sII+sIII, sII+sIII, and sII. Gray circles are measured data points, the solid curves give the respective Rietveld fit to the data.*

Upon further heating, the N_2-H_2O mixture undergoes another remarkable transition - the sH peaks start to disappear and another (metastable) phase is formed. This phase could be fitted with the known pattern of a clathrate of the structure III type (sIII). For this purpose, a Rietveld refinement was carried out to match not only the peak positions but also the respective intensities, however, due to the large unit cell and the meager data quality the atom positions had to be fixed. Hitherto this clathrate type has only been known in bromine-water mixtures.[265] Type III clathrate hydrate has a tetragonal structure with space group $P4_2/mnm$ and a cell volume of 6300 Å^3, the largest known unit cell for a clathrate. The cell consists of 172 water molecules which form sixteen 14-hedral cavities ($5^{12}6^2$), four 15-hedral cavities ($5^{12}6^3$), and ten dodecahedral cavities (5^{12}). The lattice parameters obtained from our measurements were $a = 22.914(9)$ Å, and $c = 12.003(7)$ Å. Almost 200 years after the first description of bromine hydrate here is shown that the sIII structure can serve as host to a second molecular guest species [266, 267]. It should be noted that the data quality for this refinement was not particularly good due to a short collection time and hence this clathrate might have been misidentified; however the emergence of 10 new peaks in 2.5-4.0 Å window does support the theory of a large unit cell. The peaks could not be fitted with any other nitrogen, water, or nitrogen hydrate structure, and thus the assignment of those peaks to the type III clathrate seems most plausible until further studies are carried out.
For this nitrogen hydrate the name nitrogen hydrate VI (NH-VI) is proposed. Finally, as it warms close to room temperature NH-VI forms the stable clathrate hydrate of type sII. This transition sequence is an excellent example of Ostwald's rule of stages, an empirical law stating that a meta-stable phase will transform to the stable phase, by passing through metastable phases in order of their Gibbs free energy. All nitrogen hydrates observed in this study are summarised in table 5.5.

5.3 Conclusions

In this chapter is shown that nitrogen-water mixtures can form the chiral clathrate hydrate structure, sX. This new nitrogen hydrate (NH-V) is obtained by refilling ice XVII at 130 K. Neutron diffraction data suggests that nitrogen NH-V is hexagonal with space group $P6_122$ or $P6_522$ and lattice parameters $a = 6.240(3)$ Å and $b = 6.065(2)$ Å. Experimentally a guest:host ratio of 1:2.6(3) per molecule was found, close to DFT calculations that find NH-V stable with

a filling ratio of 1:3 for a fixed stochiometry and 1:2.8 for the minimum of the convex hull fit. The values for the filling ratios obtained from the DFT simulation are well within the error bars of the experimental ones - theory and experiment are therefore in good agreement.

$$\text{NH-V} \longrightarrow \text{NH-II} \longrightarrow \text{NH-VI} \longrightarrow \text{NH-I}$$

At 0.300 GPa nitrogen NH-V transforms into the hexagonal NH-II, however, the transition only occurs very slowly. NH-II (sH) then, upon heating, undergoes transitions into NH-VI (sIII) and finally into NH-I (sII) clathrate hydrates. This is somewhat surprising. The sIII structure is an oddity in that it has so far only been observed in the bromine-water system. To find it in a simple gas system like nitrogen-water is unexpected. Similarly sH is generally found at pressures above ∼1 GPa and the ability to form it as part of a cascade of metastable structures at the much lower pressure of 0.300 GPa may be useful technologically. A phase diagram for the nitrogen hydrates with the respective crystal structures is given in figure 5.7.

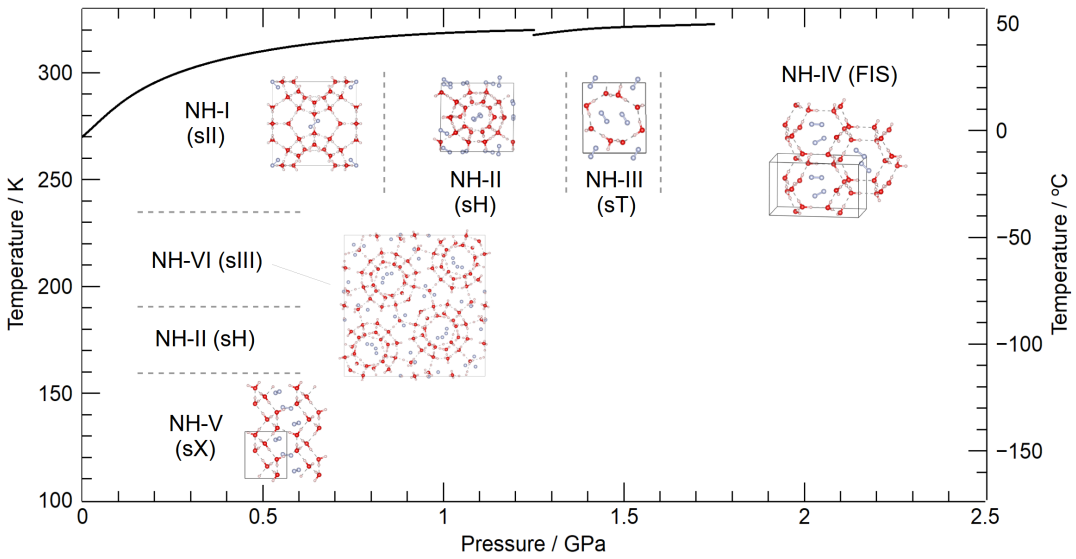

Figure 5.7 *Phase diagram of nitrogen hydrates; the solid line gives the dissociation curve of the respective nitrogen hydrates and the dotted line show the first appearance of the respective phases. Data taken from [1, 38]*

In addition,another possible route for the decomposition of NH-V is reported - heating it at an elevated pressure leads to a direct formation of the stable nitrogen hydrate I (sII).

$$\text{NH-V} \longrightarrow \text{NH-I}$$

Hereby it is demonstrated that ice XVII is a microporous material that can be loaded with different gases. The unique channel layout of the sX network gives it a large amount of flexibility: the guest gases it can absorb span an unusually large size range (from H_2 via N_2 to CO_2), with the gas uptake ratio adjusting accordingly (from 1:2 to 1:4) to avoid steric repulsion of the guest molecules. At the same time, guest species exhibit high mobility along the channels, which makes determinations of the guest content from diffraction difficult. So far, DFT calculations have proved very useful in constraining the guest-host ratio. If necessary, more nuanced descriptions of the electronic structure, e.g. through local-MP2 calculations, could be applied [264].

The universality of the sX host network raises the interesting possibility that if ice XVII can be loaded with oxygen (a molecule of similar size to nitrogen but with a triplet ground state), a magnetic sX-based hydrate might be produced. While this seems not very likely due to the large O_2-O_2 distances and the hexagonal unit cell an ordering along the channels would be possible. An initial attempt to calculate a respective structure with DFT failed; difficulties with the spin polarisation resulted in inconsistent calculations.

Chapter 6

Ammonia Mono Hydrate IV: An Attempted Structure Solution

In chapter 1, it was outlined that the water-ammonia system is of interest since it represents a natural laboratory in which to observe the behavior of materials that contain a mixture of homonuclear and heteronuclear hydrogen bonds. Compared to the previously discussed water-nitrogen system (and other clathrate hydrates), hydrophilic/hydrophobic interactions between the two species play a negligible role. The end-member phases (water ice and solid ammonia), and the stoichiometric hydrates ammonia hemihydrate ($NH_3 \cdot {}^1/_2H_2O$, AHH), ammonia monohydrate ($NH_3 \cdot H_2O$, AMH), and ammonia dihydrate ($NH_3 \cdot 2H_2O$, ADH) (see Loveday *et* Nelmes 2004 [57]) are therefore model systems for understanding far more complex hydrogen-bonded molecules [44].

Beside this mainly academic reason, the water-ammonia system is also of considerable interest to planetary scientists; most astronomical observations and cosmological models indicate that both ammonia (15 %) and water (45 %) are abundant in the outer solar system [268, 269]. Large proportions of the mantle regions Uranus and Neptune (the "ice giants") are likely composed of those two molecules [270]. Furthermore, their abundance on icy moons in our solar system has been confirmed [43, 271] and NH_3-H_2O is presumed to feature prominently in the large number of trans-Neptunian objects and Neptune-like exoplanets [272, 273].

In this astrophysical context, ammonia is considered the most plausible planetary

"antifreeze" agent, despite many open questions. For example, the ammonia yield from various condensation models (and hence the effective composition of planets and satellites) [274], as well as the fate of ammonia once accreted into Titan [43] are still disputed. For conditions in the crust of the outer planets and in moons (up to 5 GPa and 100-300 K), the physical properties of H_2O-NH_3 remain an inconclusively discussed question. The pressure melting curve and the polymorphism of the stoichiometric ammonia hydrates have implications for the internal structure of large icy satellites, leading to phase layering and the possible persistence of deep subsurface oceans [275–279]. Aqueous ammonia is also a candidate substance involved in cryomagmatism on Titan; the melting behavior and densities of liquids and solids in the ammonia-water system must be known to properly model the partial melting and vertical propagation of cryomagma through a planetary crust [280, 281].

At atmospheric pressure ammonia monohydrate crystallizes in an orthorhombic phase below the congruent melting point at 194.15 K [282]. The structure of this low-pressure phase, AMH I was solved in space-group $P2_12_12_1$ (Z=4) using single-crystal X-ray diffraction data at 113 K [283], and subsequently refined from neutron powder diffraction measurements of the deuterated isotopologue at 110 K [57].

The first visual and Raman scattering observations made using diamond anvil cells indicated that AMH possessed no high pressure polymorphs[284]. However, dilatometric studies showed that this assumption was false and the existence of a high-pressure phase, stable above 340 MPa at 195 K, was established [285]. For the full phase diagram of ammonia monohydrate see Figure 6.1.
The first of the high pressure phases, AMH-II, was shortly afterward characterised by neutron powder diffraction; a pattern of AMH-II, collected at 508.9 MPa, was reported from studies using a gas pressure cell on the Polaris diffractometer at Isis. The experimental report states that the diffraction pattern was indexed with an orthorhombic unit cell with a volume of approx. 750 $Å^3$. The first of the high pressure phases, AMH-II, was characterised by Nelmes et Loveday by means of neutron powder diffraction and the pattern of AMH-II, collected at 508.9 MPa, was incorrectly indexed with an orthorhombic unit cell [286]. Finally, the structure was solved in 2009 for a diffraction pattern collected at 443 MPa and 174 K (a= 18.8680(2) Å, b = 6.9477(1) Å, and c = 6.8589(1) Å) [44].

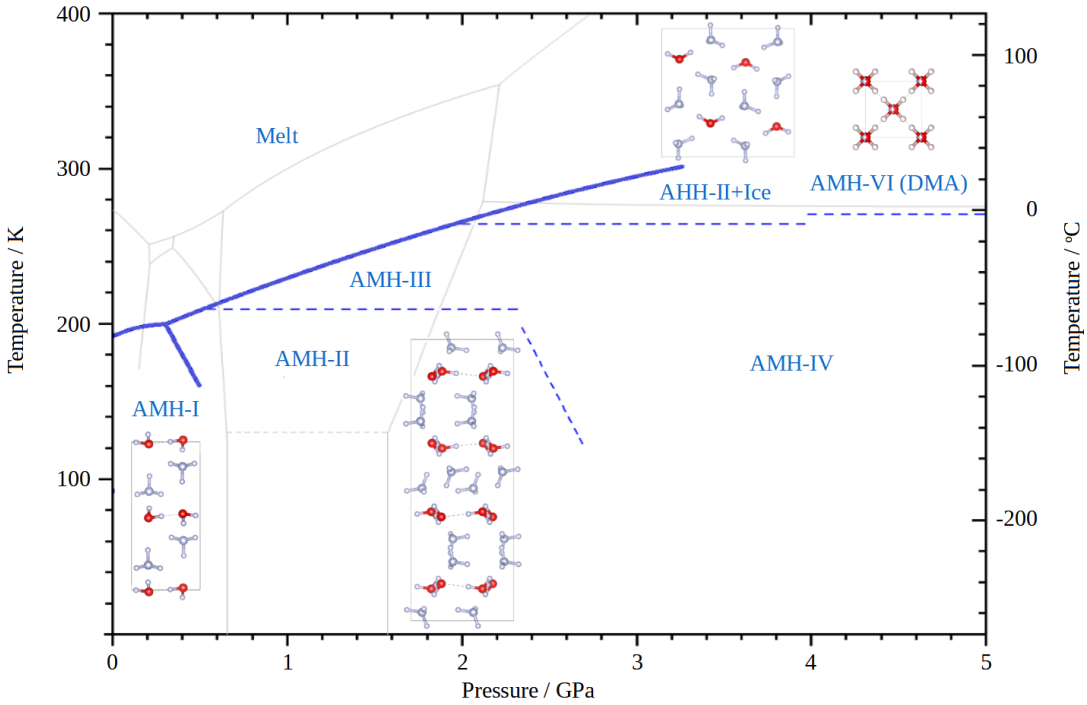

Figure 6.1 *The AMH phases diagram. For the known crystal structures the respective unit cells are shown. Please note that broken lines do not denominate phase boundaries but rather a line at which the respective other phase first appears. The grey lines in the background give the phase diagram of water as a reference. The melting curves and phase boundaries are taken from [13, 42, 43, 45–47, 56]*

Of the remaining three high-pressure phases only the structure of the disordered molecular alloy phase (DMA, formerly AMH-VI) is known. It has been extensively studied [45] and crystallises in the cubic structure ($Im\bar{3}m$) with the lattice parameter a = 3.273 Å. In DMA, the two possible crystallographic sites (0,0,0) and ($^1/_2$,$^1/_2$,$^1/_2$) can be occupied equally by either an ammonia or a water molecule. Together with AMH-III (still unsolved) this structure counts to the "high-temperature" phases of ammonia monohydrate, as they can only be observed at >200 K and >270 K, respectively.

Both AMH-III and VI play a minor role in this study; in this body of work, mainly the structure of ammonia monohydrate IV is investigated. With results based on a neutron diffraction study carried out at the ISIS neutron source, paired with density functional theory (DFT) calculations, a possible structure solution for this - so far, unsolved - polymorph is proposed.

6.1 Material and Methods

The experiment was carried out on a sample of nominal composition $ND_3{\cdot}D_2O$ (AMH) prepared by condensing ND_3 gas (Aldrich Chemicals Co., 99 atom% D) into a Swagelock steel cylinder which was cooled to 77 K in a bath of liquid nitrogen (LN2). The cylinder was then weighed and the contents diluted to the appropriate stoichiometry with D_2O (Aldrich Chemicals Co., 99 atom % D). The resulting mixture was then warmed in a bath of isopropanol and liquid nitrogen at 184 K to stabilise a $ND_3{\cdot}D_2O$ liquid. To crystalise the AMH, the liquid was once again cooled in a bath of LN2 and the so-obtained sample was stored at these conditions; the ideal AMH stoichiometry is 48.598 wt.% ND_3.

The sample was transported to ISIS (RAL, Oxfordshire, UK) where it was cryo-loaded into a PE-press at PEARL. To that purpose the sample was ground to a fine powder under liquid nitrogen and loaded into a pre-cooled gasket. The gasket was sitting on an anvil which was emerged in LN2. After loading, the gasket-anvil assembly was then put into the PE-press and an initial sealing load of 5 t was applied. The sample preparation and the PE-experiment were carried out by Dr John Loveday, Dr Victor Robinson, and Dr Ciprian Pruteanu, but is qualitatively the same as the procedure outlined in chapter 7.

Furthermore, a computational study is mentioned here; calculations of the enthalpies of structural candidates obtained from Rietveld refinements were performed, using density functional theory (DFT) as implemented in the CASTEP code [239]. Exchange-correlation effects were described within the generalised gradient approximation (GGA) using the Perdew-Burke-Ernzerhof (PBE) functional [234] and ultra-soft pseudo-potentials or norm-conserving potentials as generated 'on-the-fly' by CASTEP with cut-off radii of 1.1 Bohr for oxygen and nitrogen, and 0.6 Bohr for hydrogen. Geometry optimisations were performed with plane wave cut-offs of 1000 eV and Monkhorst-Pack [259] k-point spacings of no more than $2\pi \times 0.04$ $Å^{-1}$, until residual forces and stresses were below 0.05 meV/Åand 0.1 GPa, respectively.

6.2 Results and Discussion

After applying a sealing load of 5 t, the sample in the PE-cell was lowered into the diffractometer. A cryostat was then used to increase the temperature of cell and sample - from the loading temperature of 77 K - to 170 K. At this temperature the load was increased incrementally to 40 t (5 t steps). During the pressure increase the sample first transformed into AMH-II and then ultimately into AMH-IV (see phase diagram 1.11 in chapter 1). No pressure marker was used for this experiment to avoid parasitic lead peaks, and therefore the exact pressure is unknown. However, from previous pressure-load curves and the phase diagram of AMH it can be deduced that the sample pressure lies between 3 and 5 GPa. Once the load of 40 t was reached, a powder pattern was recorded.

6.2.1 Density of Ammonia Hydrate

From the initial composition of the water-ammonia mixture and the absence of other known phases of ice, water and ammonia-water mixtures, it is evident that AMH-IV indeed is a 1:1 mixture. This is mentioned because in a previous study the composition of ammonia-water phases was wrongly identified (c.f. the DMA phase in AMH and ADH) [45].

The average volume per molecule for ADH, AMH, and AHH at ambient pressure are, respectively, 30.170(6) $Å^3$, 30.604(2) $Å^3$, and 30.583(2) $Å^3$ [58]. These values are remarkably similar and show no obvious trend between volume per molecule and composition. This trend is also visible in the similarity of the equations-of-state (BM-EoS) of the high pressure phases of both the AMH and ADH [43, 44, 47, 57, 58]. It thus seems reasonable to assume that AMH-IV also shows no significant composition dependence in its equations of state; in the pressure range from 3-5 GPa it should have a density of 1.4-1.8 g/cm^3. The content of a unit cell can be estimated from these densities.

Altogether the data collection resulted in 15 well defined, although broad, peaks and several heavily overlapping ones (see diffraction data below). The relatively small number of peaks imposes an upper limit on the size of unit cells that can be meaningfully tested. In this case, refinements unit cells larger than 400 $Å^3$ proved to be very unstable unless a high-symmetry space group was used.

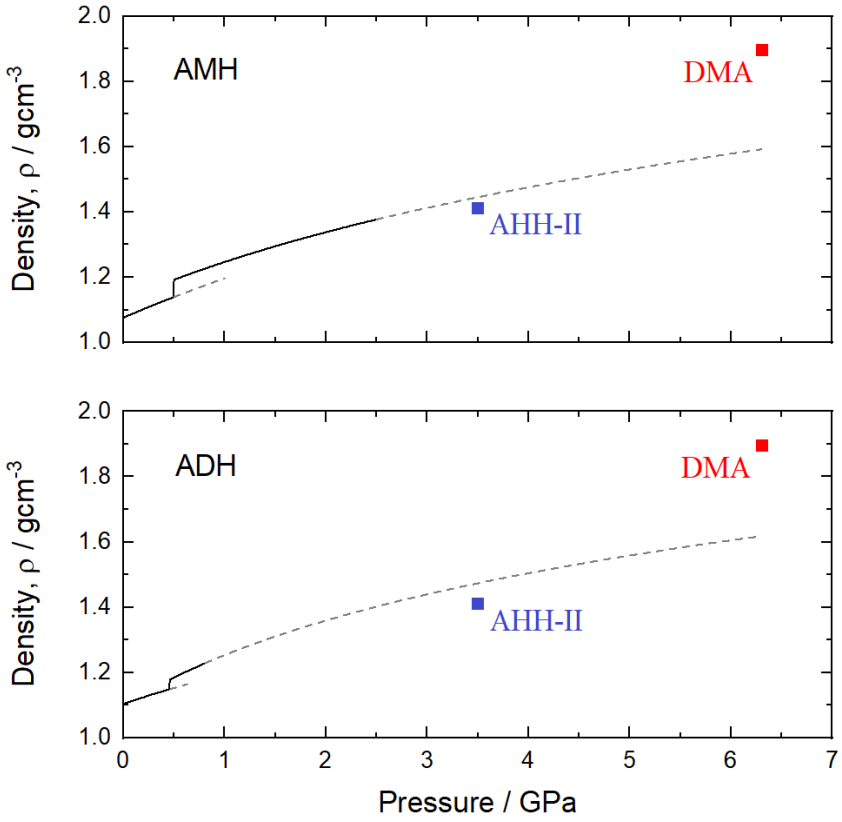

Figure 6.2 *Densities of AMH and ADH as a function of pressure. The solid lines are fits to a BM-EoS at about 180 K and the broken lines are their extrapolation; the solid blue and red square gives the density of AHH-II and the DMA at about 3.6 GPa and 6.3 GPa, respectively. Data taken from [43, 44, 47, 57, 58]*

6.2.2 Initial Indexing

Peaks in the diffraction data were identified by fitting them with pseudo-Voigt functions and then the GSAS-II indexing routine was run. In general the indexing of cubic, hexagonal, and trigonal crystal systems resulted in unit cells too large (> 1000 Å^3) for the data set and hence were mostly discarded. This indexing resulted in 108 possible cells, not including a triclinic lattice. A list of the remaining 108 possible cells is given in an appendix to this chapter in Table 6.4 ranked according to their figure of merit (FoM).

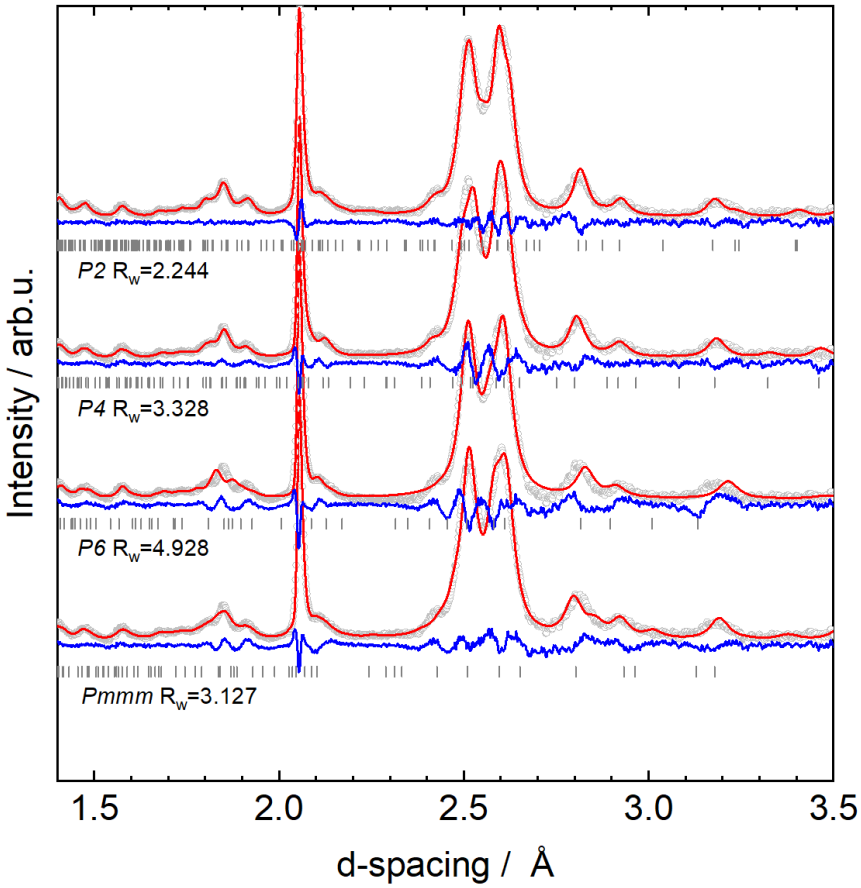

Figure 6.3 *Le-Bail fits (red) to the data of AMH-IV (grey) for cells that showed a high FoM in GSAS-II. Please note that the P*4*, P*6 *and the Pmmm cells here show relatively low R_w values even though the fits show a missmatch with the data for at least one experimentally observed peak.*

A Le-Bail (LB) refinement (see chapter 2) was carried out in the respective lowest symmetry space group for this crystal system to account for all possible peaks in the powder pattern. Altogether, 60 cells showed promising Le-Bail fits and were used for the next step of the data analysis. The respective R_w values for the LB fits are shown in the appendix as well. Please note that most of the 60 cells have several possible space groups with higher symmetries that also fit the pattern equally well.

Several LB-refinements with small R_w values still showed a missmatch in one or more of the peaks between data and fitted model; hence a sole evaluation of the cells based on R_w is not sensible. As an example, a small subset of the Le-Bail fits for a monoclinic, ($P2$), tetragonal ($P4$), hexagonal ($P6$), and orthorhombic ($Pmmm$) case are shown in figure 6.3. Only the monoclinic cell has no missmatch between fit and experimentally observed reflections.

6.2.3 Structure Search Using Monte Carlo Simulated Annealing

The technique of choice to obtain structural models was Monte Carlo Simulated Annealing (MCSA; see section 2.3.2). As outlined, MCSA uses atoms, molecules, or molecule fragments and varies their position in the unit cell. This is done by a random-walk approach [192]. For the resulting structure model the peak-intensities are calculated and compared with the intensities from the Le-Bail fit. This procedure is repeated until a convergence criterion is met. As such, MCSA has the advantage that the molecules placed in the unit cell can be chosen in a way that the required density is 1.4-1.8 g/cm^3.
Here, the starting structures for the MCSA consisted of water D_2O and ammonia ND_3. Both molecules were restrained and the position and orientation in the unit cell of these rigid bodies was varied (see table 6.1).

Table 6.1 *Parameters for the MCSA procedure. The first lines show the molecular geometry of the rigid bodies used; for small unit cells 512 individual runs were performed; for larger cells only 256 to reduce the computing time.*

D_2O	O-D	0.97 Å	D-O-D	109.47^o
ND_3	N-D	1.02 Å	D-N-D	109.47^o
Runs	256 or 512			
Start T	3.0			
Final T	0.1			
Trial per T	1500			

The MCSA was considered successful if several runs converged to the same structural model. The obtained structure was then used for individual Rietveld refinements. For the initial refinement the atoms were fixed in the molecular geometry as a rigid body. After refining their positions and isotropic displacement parameters, the restrictions were lifted and a full refinement was carried out. Finally, this procedure was repeated for all possible space groups of higher symmetry of the respective unit cell.

6.2.4 Structure Candidates based on Rietveld Refinements

In most cases a reasonable structure was obtained from the MCSA runs. However, the MCSA-solutions often were not stable against Rietveld refinements. That is, an attempt to refine the structures resulted in physically implausible structures. Only a few Rietveld refinements resulted in feasible structural models and are summarised in table 6.2.

Table 6.2 *Lattice parameters and space groups of structures obtained from MCSA which showed a reasonable Rietveld fit to the experimental data.*

Space group	a / Å	b / Å	c / Å	α	β	γ	R_w (RR)
$P2/n$	7.41	4.89	5.07	90.0	124.2	90.0	0.02328
$P2_1$	7.48	9.73	5.06	90.0	124.5	90.0	0.02463
$P2$	5.62	5.86	5.0	90.0	91.9	90.0	0.02488
$P2_1/c$	4.28	4.51	18.01	90.0	92.6	90.0	0.02249
Pc	5.47	9.51	5.95	90.0	99.2	90.0	0.01663
$P2_1/c$	5.47	19.03	5.96	90.0	99.0	90.0	0.02249

P2/n and $P2_1$

Initially the monoclinic cell with the dimensions $a = 7.41$,$b = 4.89$, $c = 5.07$, and $\beta = 124.2$ was tested and showed promising results for the space groups $P2$, $P2_1$, $P2/n$, $P2_1/n$, Pn, $P2/m$, and $P2_1/m$. Other space groups can be excluded due to systematic absences. For Z=4, a density of 1.75 g/cm^3 was calculated. Of the 7 space groups only one gave a reasonable structural solution. This structure, in the $P2/n$ space group, is depicted in Figure 6.4; the resulting Rietveld fit is shown in Figure 6.5.

This structure appears to be layered along the b-axis; water molecules are only found in the *ac*-plane at y=0, whereas ammonia molecules are found in the plane at y=½. The repetitive layers of ammonia and water molecules are a motive found in nearly all other structure candidates as well; also the known AMH-II phase (space group *Pbca*; see below) shows such a structure and hence it would not be surprising to see yet another high-pressure phase of ammonia and water in a similar arrangement.

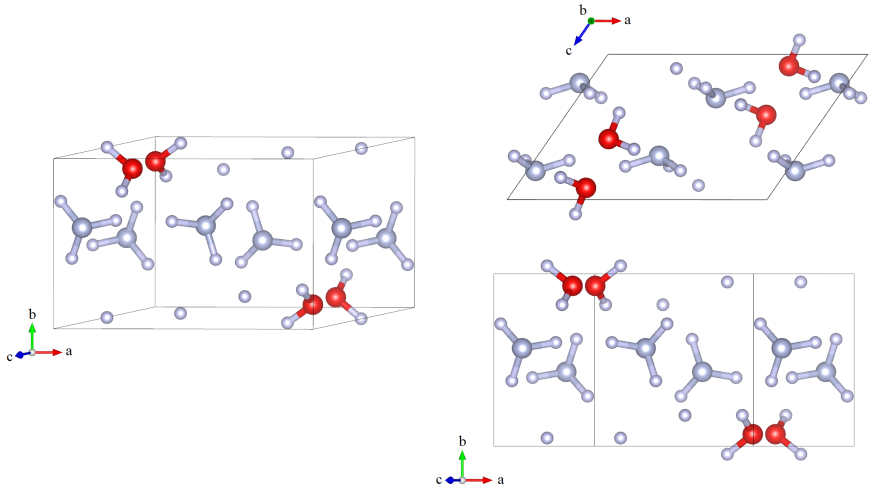

Figure 6.4 *Structure candidate from MCSA in the space group $P2/n$. Ammonia and water form stacked layers along the b axis.*

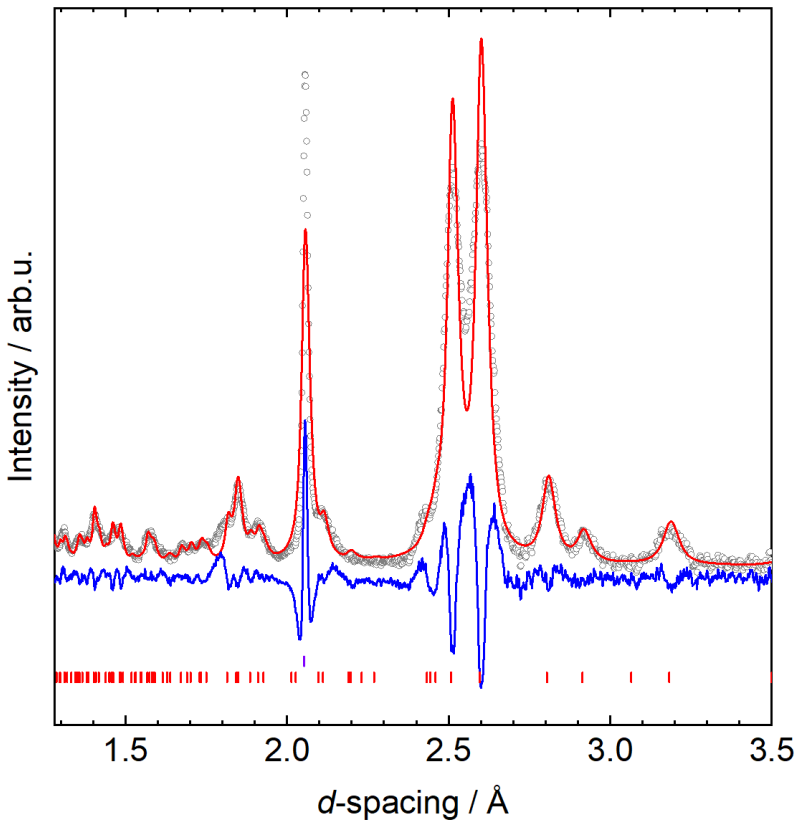

Figure 6.5 *Best fit for $P2/n$. Grey gives the data, red the respective fit, and blue the difference. The positions of sample and anvil peaks are shown in red and blue, respectively.*

The Rietveld fit hereby fits most peaks rather well; only a shoulder at 1.85 Å is not fitted properly. The structure, on the other hand, would be atypical for ammonia hydrates as the model would not allow for a hydrogen-bond network. Several attempts to use this structure and introduce disorder by partially occupying the hydrogen positions did not result in plausible fits to the data. For these refinements, rigid bodies of D_4O and D_4N molecules with partially occupied hydrogen sites ($^1/_2$D for D_4O and $^3/_4$D for D_4N molecules, respectively) were used for MSCA runs. Please note that to this possibility is unlikely; to date, most of the discovered ammonia hydrates are not disordered (with DMA being the exception to the rule).

Finally an attempt was made to use DFT to see whether this structure would be stable. To that end, the cell parameters and atom positions of the structure obtained from the MCSA and Rietveld refinement were used as an input file for a CASTEP calculation (for the exact procedure and input parameters see section 6.2.4; the same input was used for all DFT calculations). A geometry optimisation (GO) was then carried out; the so obtained calculated structure, however, did not resemble the structure from the MCSA/Rietveld. It is not surprising that this new structure did not fit the experimental diffraction pattern. Hence it is very unlikely that this $P2/n$ candidate is feasible.

Amongst the list of possible cells, one other is remarkably similar to the one discussed here. The cell $a = 7.48$ Å,$b = 9.73$ Å, $c = 5.06$ Å, and $\beta = 124.5$ deg has basically the same lattice parameters but is doubled along the b-axis. It was treated in the same fashion as the above case and the MCSA runs resulted in a reasonable structure for the $P2_1$ space group. The structure is shown in Figure 6.6; similarly to the $P2/n$ candidate, the structure is layered along the b-axis. Also in this case, a GO was carried out; the arrangement of molecules seems to be energetically unfavourable resulting in a massive shift of the atom positions during the optimisation. The GO structural model did not fit the experimentally observed pattern and hence this structure can be excluded as well.

P2

The cell $a = 5.62$ Å, $b = 5.86$ Å, $c = 5.01$ Å, and $\beta = 91.9$ deg was tested in a similiar way as described above. A LB-refinements was used to determine the lattice parameters, MCSA to find a plausible structure and space group ($P2$,

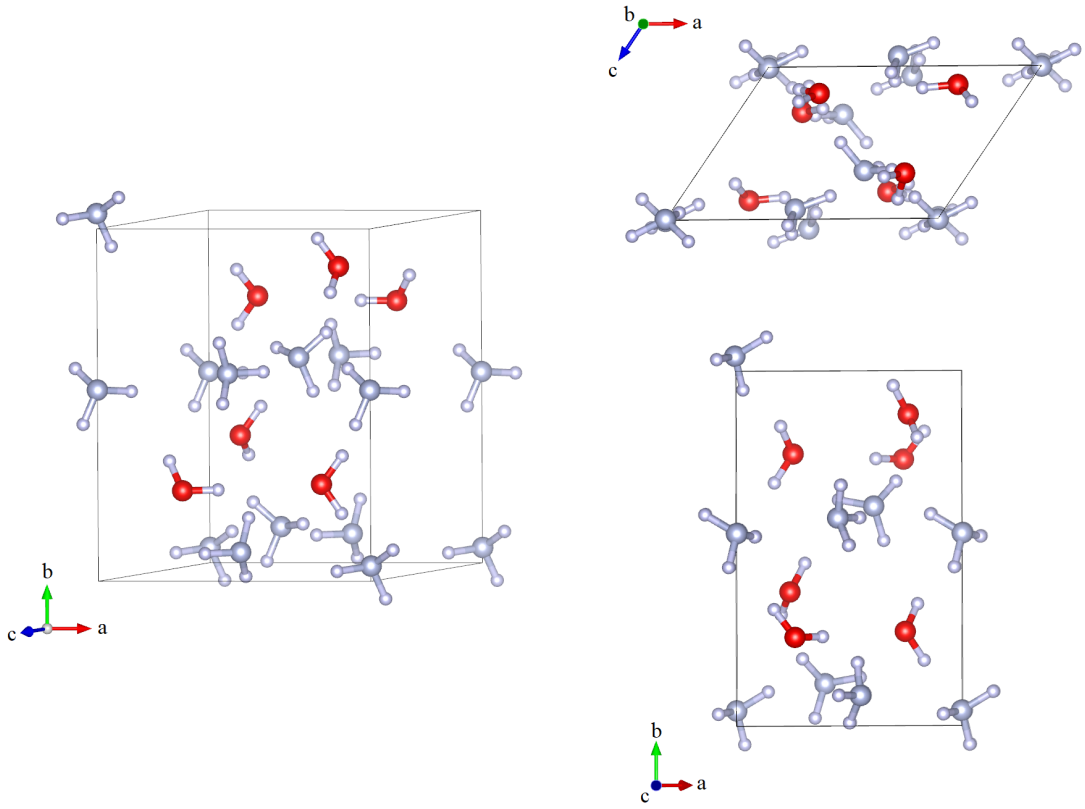

Figure 6.6 *Structure candidate from MCSA in the space group $P2_1$. Again, ammonia and water form stacked layers along the b axis.*

Z=4, ρ = 1.62 g/cm^3), and the geometry of the structure was then optimised using CASTEP. However, the Rietveld refinements carried out resulted in a physically implausible structure with the two water molecules occupying the same crystallographic site. This would mean a largely reduced density as well as a wrong (AHH) composition. While dehydration in case of the AMH-IV $\xrightarrow{\Delta T}$ AHH-II + ice VI has been observed, the lack of water reflections in the experimental pattern suggests that this is not the case here. Hence this candidate structure was discarded.

$P2_1/c$ the First

The first $P2_1/c$ cell presented here, $P2_1/c$ (I) had the lattice parameters a = 4.379(3) Å, b = 4.502(4) Å, c = 17.770(5) Å, and β = 92.39(2) deg. This structure shows similarity to that of AMH-II (*Pbca*). Compared to the density of AMH-II (1.190 g/cm^3, Z=16), its density is higher (1.52 g/cm^3, Z=12) [56].

The monoclinic cell deviates from an ideal orthorhombic cell by only ≈ 2.4 deg. Second, from the MCSA in the space group $P2_1/c$ a structure model was obtained which employed – very similar to AMH-II – a motif of partially layered ammonia and water [56]. The layers of ammonia are stacked along the c-axis at $z = 0$ and $z = 0.5$ and ammonia and water mixes and intertwines between those layers. Furthermore, pure layers of ammonia and water are stacked along the a-axis.

A Rietveld refinement on this structure was stable with an $R_w = 0.02784$ for 32 parameters and the Rietveld fit to the data is given in Figure 6.7. The structural parameters were then used as an input for a geometry optimisation in CASTEP, and a Rietveld fit of the GO-optimised structure is shown in Figure 6.7. The geometry optimisation did not result in massive shifts of molecule positions (average displacement of 0.964(3) Å of the molecular centres between the GO and the Rietveld solution) and resulted in a physically plausible structure. To verify further that the structure is plausible, phonon calculations were carried out. The Γ-point was sampled and resulted in real phonon frequencies only. While the Rietveld fit of the geometry optimised structure reproduces the main features of the experimental data (see Figure 6.7), many peaks - particularly in the high-Q range (d-spacings 1.3-1.9) - are poorly fitted by this structure.

$P2_1/c$ the Second

The second monoclinic cell in this space group, $P2_1/c$ (II), that showed promising results has the dimensions $a = 5.487(3)$ Å, $b = 19.068(4)$ Å, $c = 5.989(3)$ Å, and $\beta = 99.537(16)$ deg. A Rietveld fit to the experimental data is given in figure 6.8. Compared to the above discussed structure, $P2_1/c$ (II) seems to fit all main features of the diffraction pattern quite well. To verify further that the structure is plausible, phonon calculations were carried out. The Γ-point was sampled and resulted in real phonon frequencies only. Furthermore, an extensive DFT study was carried out and its details will be discussed in section 6.2.5. A density of about 1.30 g/cm^3 was calculated for the above mentioned lattice parameters (Z=12). While this density is at the lower end of the reasonable densities, the $P2_1/c$ discussed here is still the most plausible structure so far.

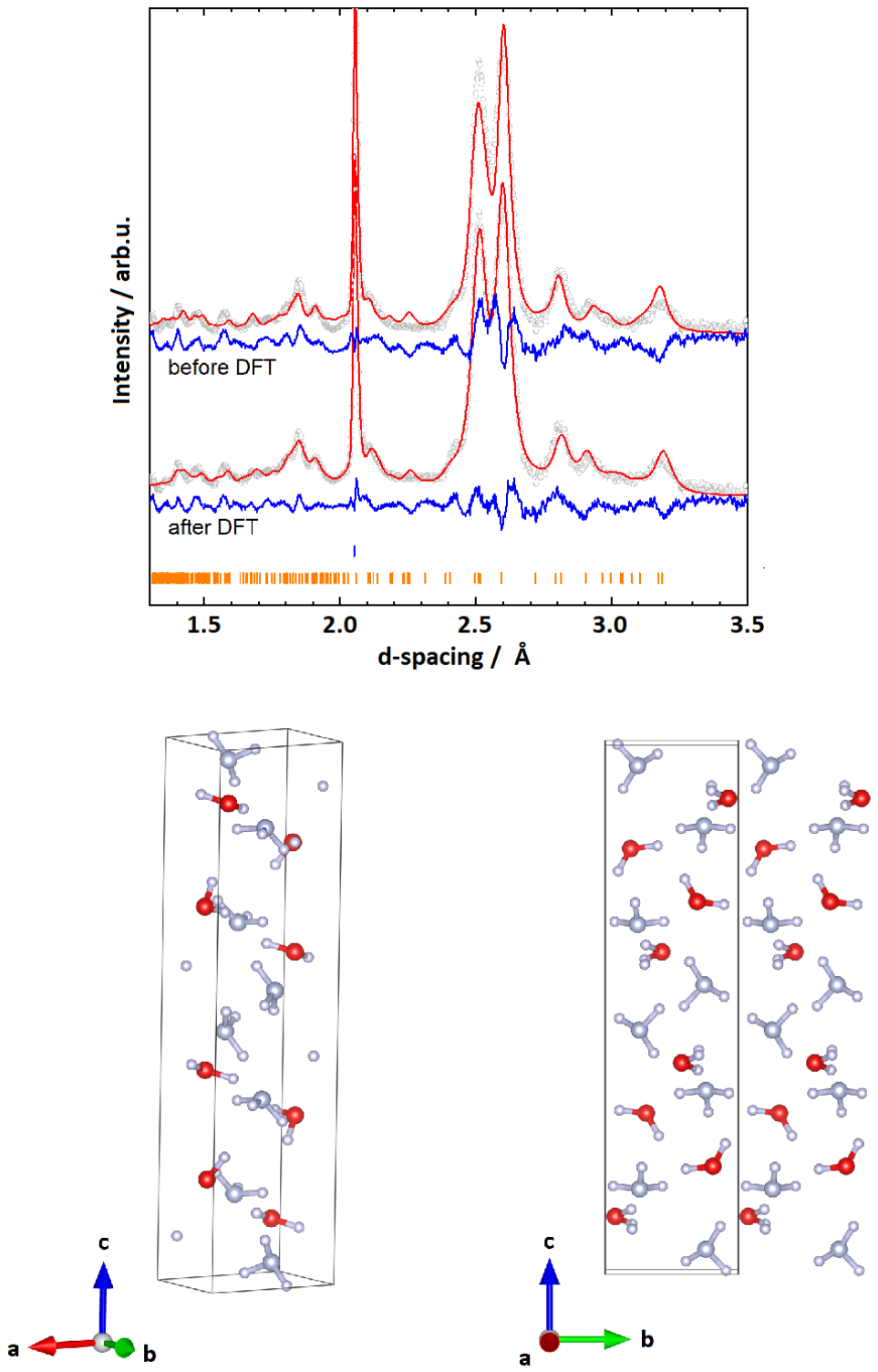

Figure 6.7 *Rietveld fits to experimental data and respective structures for the monoclinic cell $a = 4.379(3)$ Å, $b = 4.502(4)$ Å, $c = 17.770(5)$ Å, and $\beta = 92.39(2)$ deg in the space group $P2_1/c$. The top plot shows the model obtained directly from MCSA, the bottom one the same structure after optimising its geometry using DFT.*

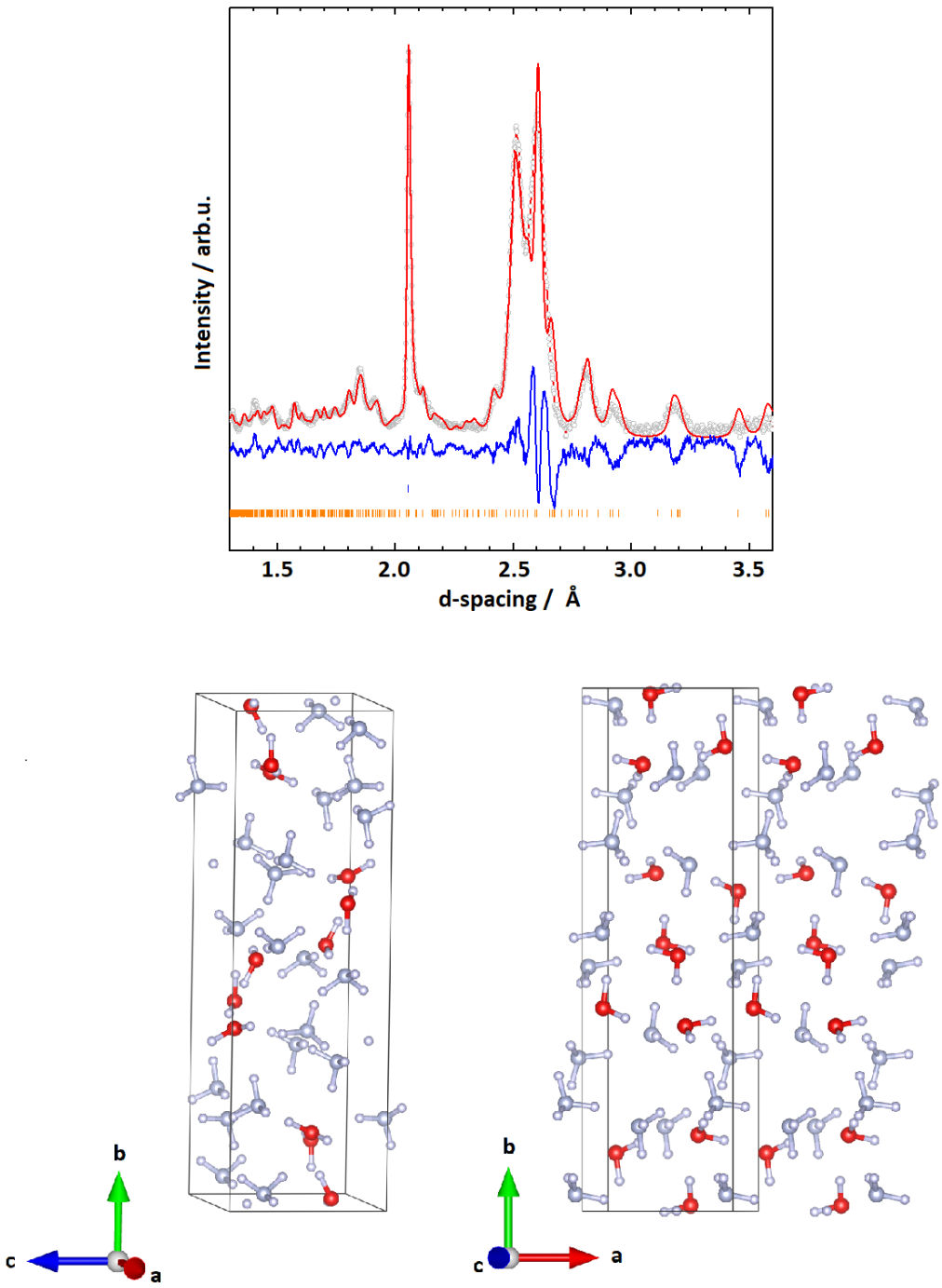

Figure 6.8 *Rietveld fits to experimental data and respective structures for the monoclinic cell* $a = 5.487(3)$ *Å,* $b = 19.068(4)$ *Å,* $c = 5.989(3)$ *Å, and* $\beta = 99.537(16)$ *deg in the space group* $P2_1/c$.

6.2.5 Structure and DFT study of $P2_1/c$ (II)

As mentioned in the section above, the best fit to the diffraction pattern of AMH-IV resulted from a unit cell with the dimensions $a = 5.487(3)$ Å, $b = 19.068(4)$ Å, $c = 5.989(3)$ Å, and $\beta = 99.537(16)$ deg and the $P2_1/c$ symmetry; the values were obtained from the Rietveld refinement shown in figure 6.8. The overall fit gave resulted in R_w=0.04725, and - as stated above - accounts for nearly all features in the diffraction pattern. However, due to the limited number of well resolved peaks and the large unit cell volume of 613.30(8) Å^3 the molecular geometry had to be fixed with rigid bodies. Furthermore, a high symmetry spacegroup had to be chosen in order not to exceed the empirical $3n$-rule of refinable parameters which states that for every parameter, three peaks for fitting are needed. As the data quality is meager, additional DFT calculations were needed to evaluate the structure. The atom positions and isotropic displacement parameters for the proposed structure of AMH-IV are summarised in table 6.3.

Table 6.3 *Atom site, position and isotropic displacement parameters for AMH-IV in space group $P2_1/c$; lattice parameters $a = 5.487(3)$ Å, $b = 19.068(4)$ Å, $c = 5.989(3)$ Å, and $\beta = 99.537(16)$ deg.*

Atom	Site	x	y	z	U_{iso}
D1	4e	0.062(9)	0.433(4)	0.724(9)	0.165(15)
D2	4e	-0.105(9)	0.394(4)	0.522(9)	0.165(15)
D3	4e	0.545(6)	0.5092(18)	0.266(5)	0.006(5)
D4	4e	0.388(6)	0.5531(18)	0.069(5)	0.006(5)
D5	4e	0.372(5)	0.2823(12)	0.558(3)	0.177(16)
D6	4e	0.343(5)	0.2607(12)	0.285(3)	0.177(16)
D7	4e	0.288(5)	0.3429(12)	0.359(3)	0.177(16)
D8	4e	0.986(5)	0.2022(12)	0.838(3)	0.066(8)
D9	4e	0.755(5)	0.2596(12)	0.776(3)	0.066(8)
D10	4e	0.733(5)	0.1949(12)	0.960(3)	0.066(8)
D11	4e	0.644(5)	0.370(2)	0.032(7)	0.021(7)
D12	4e	0.747(5)	0.294(2)	0.105(7)	0.021(7)
D13	4e	-0.032(4)	0.9612(7)	0.112(4)	0.026(6)
D14	4e	0.212(4)	0.9968(7)	0.275(4)	0.026(6)
D15	4e	-0.053(4)	0.9870(7)	0.375(4)	0.026(6)
N1	4e	0.274(5)	0.2912(12)	0.401(3)	0.177(16)
N2	4e	0.798(5)	0.2084(12)	0.815(3)	0.066(8)
N3	4e	0.024(4)	0.9980(7)	0.234(4)	0.026(6)
O1	4e	0.048(9)	0.419(4)	0.566(9)	0.165(15)
O2	4e	0.440(6)	0.5501(18)	0.231(5)	0.006(5)
O3	4e	0.599(5)	0.321(2)	0.054(7)	0.021(7)

An attempt was made to remove the rigid body restriction and to reduce the symmetry of the space group to $P2_1$, both of which remained fruitless. The former resulted in unreasonable O-H and N-H distances of < 0.8 Å, paired with an asymmetry in bond lengths in the H_2O and NH_3 molecules. However, the overall structure remained intact. In the latter case of lowering the symmetry, the structure completely fell apart. Without access to additional data of better quality these limitations are necessary and due to these restrictions, some peaks are still not fitted perfectly.

Two motifs seem to repeat in this structure, a planar quadrilateral and an "envelope shaped" quadrilateral (see figure 6.9). The rings constitute of alternating NH_3 and H_2O molecules and are interconnected by hydrogen bonds. The former are stacked along the a-axis either oriented with the two NH_3 up or down. The latter quadrilaterals form alternating stacks that are tilted either +25 deg relative to the *bc*-plane, or -25 deg relative to the *bc*-plane.

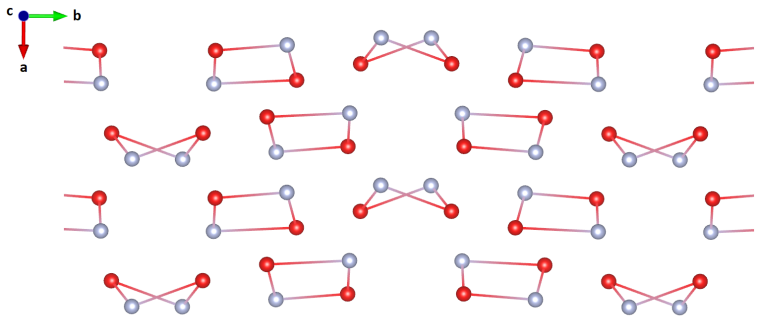

Figure 6.9 *Reduced structure without hydrogen/deuterium along the unique axis (b-axis). Two structural motifs repeat along this axis, a planar quadrilateral and an "envelope shaped" quadrilateral.*

Please note that all considerations so far have assumed a hydrogen-ordered structure; this is based on the observation that the structures of most ammonia hydrates (AMH-I, AMH-II, ADH-I, AHH-I, AHH-II [47, 57]) are ordered and the low temperature at which the data were collected; the DMA phase, on the other hand, is highly disordered [45]. The possibility that AMH-IV is also (partially) disordered can hence not be completely ruled out. However, given the data quality on the structural complexity it is not possible to test for disorder in a meaningful way.

The enthalpy calculations based on density functional theory (DFT) were performed using the CASTEP code [239, 287] on the ammonia monohydrate structure obtained by MCSA. Additionally, calculations were performed on the structures of AMH-I, AMH-II, and the ionic $P4/nmm$ phase; the latter of these phases was chosen as a reference structure. To calculate stable compounds, enthalpy values H were compared according to $H = U + PV$ where U is the internal energy per molecule and P and V are the pressure and molecular volume respectively. To determine the relative stability, the formation enthalpies at every pressure point from 1 to 15 GPa relative to the reference structure at the same pressure was plotted according to

$$\Delta H(P) = H(P) - H(P)_{ref}. \tag{6.1}$$

This data is shown in figure 6.10. The semi-local exchange-correlation functional used for these calculations does not fully account for longer range dispersion interactions which may be present. As a result, the pressure estimations are higher than seen in experiment, an effect well known for ice [236].

At ambient pressure, AMH-I is the most stable compound. Upon an increase in pressure, AMH-II starts to compete with AMH-I and becomes energetically favourable at 4 GPa. This is also observed in experiments at a transition pressure of about 0.5 GPa. AMH-I, despite not being the dominant species anymore, was traced to 15 GPa. The kink in the enthalpy curve at 12 GPa indicates an ionisation of two of the four water-ammonia pairs to NH_4^+ and OH^-. Spontaneous ionisation of this form has been observed in several DFT studies before [288, 289]. Between 4 and 5 GPa, Griffiths' ionic $P4/nmm$ phase becomes the energetically favourable phase and remains so for the whole pressure regime studied here. While this behaviour has been observed by Griffiths *et al.* as well [288], experimentally no ionisation of this sort has been observed to date. From neutron diffraction experiments it is known that AMH-II transforms into AMH-IV at 2.2 GPa (upon pressure increase) or into AMH-III at 210 K (upon heating); see Loveday and Nelmes (2004) [57].

The $P2_1/c$ (II) structure of AMH-IV was tracked in the same way and remains energetically unfavourable in the whole pressure range. This would indicate metastability of the phase, but could also be a result of the temperature difference between the DFT-study (0 K) and the experiment (170 K). Similar

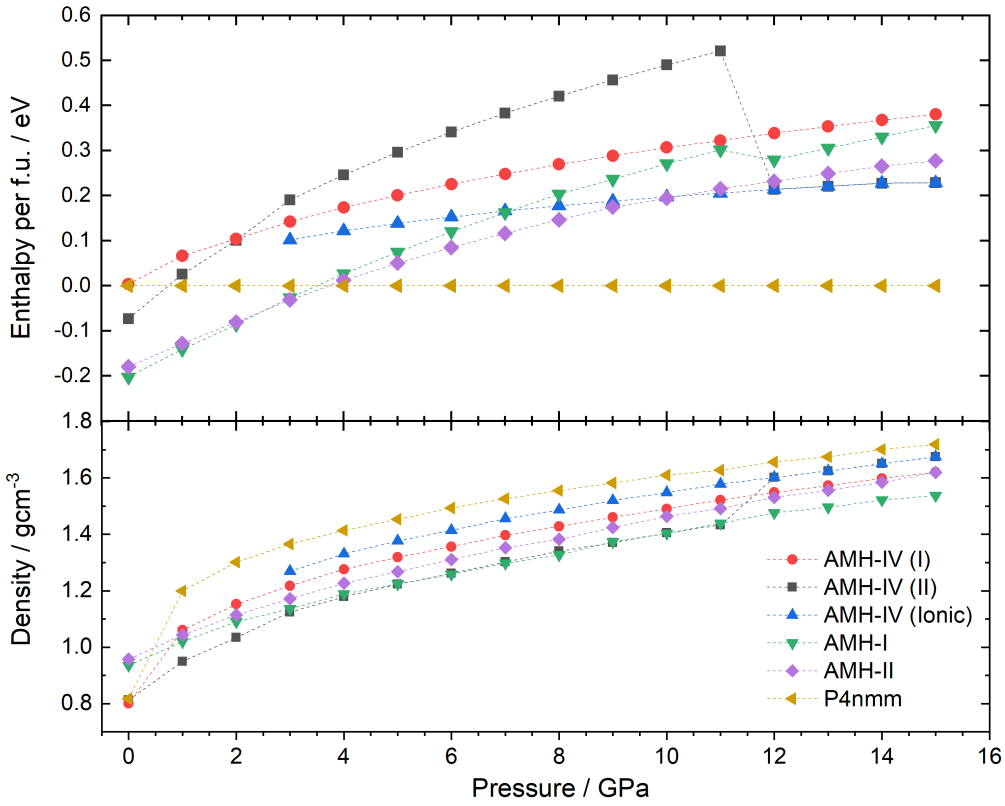

Figure 6.10 *Top: Enthalpies of the ammonia monohydrate phases AMH-I, AMH-II, Griffith's $P4/nmm$ phase and the proposed $P2_1/c$ structure of AMH-IV as a function of pressure. AMH-IV spontaneously ionises at 12 GPa and changes its unit cell.*
Bottom: Densities of the ammonia monohydrate phases as a function of pressure.

to AMH-I, AMH-IV partially ionises at 12 GPa; two of the twelve formula units form $NH_4^+ \cdots OH^-$ pairs. The ionisation goes hand in hand with a change in lattice parameters to a=5.79316 Å, b=16.59557 Å, c=4.67090 Å, α=89.5249 deg, β=88.4048 deg, and γ=76.2010 deg (at 12 GPa). Furthermore, a jump in energy of -0.3 eV per formula unit can be observed. This jump is remarkable, much larger than in AMH-I, despite only 2-of-12 molecules ionising vs 2-of-4 in AMH-I. The reason for this is the transition to a completely new (theoretical) phase. Also this structure was traced (see red curve in Figure 6.10) along the pressure axis. No transition back to a purely molecular phase could be observed from 3 to 15 GPa.

Since the triclinic, partially ionic structure is energetically much more favourable, an attempt was made to use it as an input structure for a Rietveld refinement, however, the experimentally observed pattern did not match this triclinic structure at all. The unit cell of this structure can be seen in Figure 6.11.

To reduce the fitting parameters, a higher symmetry, molecular equivalent of this structure in space group $P2_1$, was carefully constructed (a=16.5956 Å, b=4.6709 Å, c=5.7932 Å, and β=76.201 deg), but also this second attempt remained fruitless.

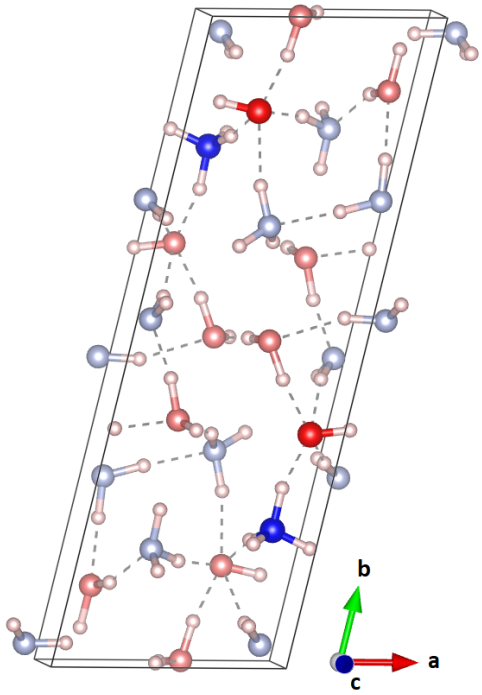

Figure 6.11 *Unit cell of the triclinic, partially ionic structure obtained from DFT; the ionic units are highlighted. This structure does not fit the experimentally observed powder patter.*

6.3 Conclusions

A neutron powder diffraction study was carried out to investigate the structure of ammonia monohydrate IV. To that end a neutron diffraction pattern, collected at 170 K at elevated pressure of 3-4 GPa by Loveday, Robinson and Pruteanu, was used. Considerations based on the density of other ammonia-water phases suggest a density of 1.4-1.8 g/cm^3 and a proton ordered structure. Due to the data quality and number of peaks the structure search was restricted further to unit cells not larger than 400 Å^3.

An initial indexing of the broad diffraction peaks using the Gsas-II software suit led to 108 possible unit cells (see appendix 6.3); carrying out LB-intensity extractions, this number was reduced to 60 possible cells. Structure-candidates were then obtained by performing Monte-Carlo Simulated-Annealing (MCSA) in all plausible space groups of the respective cell. The MCSA procedure used rigid

bodies of NH_3 and H_2O. The obtained structures were then further refined using the Rietveld method.

The most plausible structure which accounts for all features in the experimental pattern was found in the $P2_1/c$ space group and has the lattice parameters $a = 5.487(3)$ Å, $b = 19.068(4)$ Å, $c = 5.989(3)$ Å, and $\beta = 99.537(16)^o$. DFT calculations revealed a high formation enthalpy relative to other ammonia monohydrate phases which could indicate its metastability.

Another possible explanations for this energy difference could be that the assumption of an ordered structure is wrong. However, the data quality, due to the nature of the broad and heavily overlapping reflections, was not sufficient to test disordered structures. A proton-disordered or a disordered molecular alloy variant of the structure can hence not be ruled out completely. Finally, it is possible that too high a symmetry for the cell was chosen; this includes the possibility for a triclinic unit cell, which was not investigated based on the same data-quality reasoning as above.

To address the above mentioned concerns in the future, an X-ray diffraction study would prove helpful. First and foremost a diffraction pattern with less information, i.e. without information of the hydrogen positions, simplifies the search for a suitable unit cell and a structure based on X-ray data is not affected by any hydrogen-disorder.

Appendix Chapter 6

Table 6.4 *Lattices that showed a high FoM for the indexing routine in GSAS-II*

Cell	a	b	c	α	β	γ	FoM	R_w (LB)
Monoclinic	9.56	3.89	12.64	90.0	91.5	90.0	63	2.349
Monoclinic	5.47	9.51	5.95	90.0	99.2	90.0	60	2.208
Monoclinic	11.21	6.80	5.19	90.0	106.3	90.0	57	1.901
Monoclinic	5.64	9.54	6.37	90.0	121.7	90.0	56	2.072
Monoclinic	6.62	2.60	7.43	90.0	130.5	90.0	54	3.249
Monoclinic	7.98	5.02	8.85	90.0	99.2	90.0	52	2.154
Monoclinic	21.26	4.03	8.47	90.0	140.3	90.0	49	3.342
Monoclinic	7.41	4.89	5.07	90.0	124.2	90.0	48	2.624
Monoclinic	6.82	10.40	3.97	90.0	93.5	90.0	47	2.118
Monoclinic	15.92	3.59	9.06	90.0	108.8	90.0	41	1.957
Monoclinic	4.77	9.54	9.09	90.0	112.2	90.0	34	1.853
Monoclinic	5.61	9.54	7.95	90.0	111.7	90.0	34	2.766
Monoclinic	10.26	11.67	9.08	90.0	122.0	90.0	34	2.614
Monoclinic	16.01	5.81	11.69	90.0	139.1	90.0	34	1.955
Monoclinic	7.73	5.42	8.90	90.0	93.0	90.0	33	2.111
Monoclinic	4.43	4.47	17.39	90.0	93.1	90.0	31	2.604
Orthorombic	9.12	9.83	10.41	90.0	90.0	90.0	31	2.111
Monoclinic	5.37	5.63	13.99	90.0	101.9	90.0	30	2.590
Monoclinic	3.55	10.48	9.82	90.0	127.9	90.0	30	2.515
Monoclinic	10.59	6.69	6.14	90.0	103.5	90.0	29	2.157
Monoclinic	10.15	3.75	9.02	90.0	135.2	90.0	28	2.337
Monoclinic	3.92	10.42	9.18	90.0	120.1	90.0	27	2.103
Monoclinic	8.41	3.52	15.73	90.0	135.7	90.0	26	2.245
Monoclinic	17.68	6.31	4.06	90.0	97.7	90.0	26	2.254
Monoclinic	10.45	2.76	10.20	90.0	93.1	90.0	25	5.843
Monoclinic	10.79	12.70	3.81	90.0	135.9	90.0	24	2.402
Monoclinic	3.56	8.42	7.63	90.0	115.7	90.0	23	2.263
Monoclinic	2.95	9.54	9.33	90.0	127.2	90.0	22	6.580
Monoclinic	5.94	5.72	8.52	90.0	99.3	90.0	21	2.279
Monoclinic	14.83	3.45	6.37	90.0	128.1	90.0	20	2.792
Monoclinic	11.66	9.56	4.06	90.0	138.3	90.0	18	2.190
Monoclinic	7.27	3.80	6.35	90.0	112.9	90.0	18	2.691
Monoclinic	8.81	2.97	7.27	90.0	107.9	90.0	17	2.652
Monoclinic	8.99	6.08	5.51	90.0	135.0	90.0	17	2.690
Orthorombic	3.24	9.85	13.46	90.0	90.0	90.0	17	2.868
Monoclinic	7.28	2.96	10.75	90.0	101.9	90.0	17	2.516
Orthorombic	4.86	5.84	11.42	90.0	90.0	90.0	17	3.461
Monoclinic	14.38	3.69	6.99	90.0	125.5	90.0	17	2.928

Cell	a	b	c	α	β	γ	FoM	R_w (LB)
Monoclinic	10.10	3.61	7.00	90.0	117.2	90.0	16	2.602
Orthorombic	3.58	8.75	11.57	90.0	90.0	90.0	16	2.759
Monoclinic	4.34	8.75	7.18	90.0	124.1	90.0	16	3.364
Monoclinic	3.05	10.40	10.38	90.0	104.9	90.0	16	2.273
Orthorombic	5.62	6.83	8.78	90.0	90.0	90.0	16	2.798
Monoclinic	6.40	3.69	10.51	90.0	97.8	90.0	15	2.437
Monoclinic	5.87	5.61	7.32	90.0	106.9	90.0	15	2.714
Monoclinic	5.62	5.85	5.02	90.0	91.5	90.0	15	2.687
Orthorombic	5.47	6.02	11.71	90.0	90.0	90.0	14	2.875
Monoclinic	9.08	3.38	6.45	90.0	101.5	90.0	14	3.461
Orthorombic	5.85	7.61	8.36	90.0	90.0	90.0	14	3.074
Monoclinic	3.23	8.30	7.87	90.0	104.5	90.0	14	2.573
Monoclinic	5.31	13.34	4.09	90.0	117.6	90.0	13	2.933
Orthorombic	5.33	5.61	11.67	90.0	90.0	90.0	13	3.910
Orthorombic	4.41	5.48	16.92	90.0	90.0	90.0	13	2.951
Orthorombic	4.04	10.28	11.26	90.0	90.0	90.0	13	2.401
Orthorombic	4.12	8.33	10.05	90.0	90.0	90.0	13	2.454
Orthorombic	3.43	8.45	12.15	90.0	90.0	90.0	13	2.687
Monoclinic	4.17	4.13	10.39	90.0	105.1	90.0	13	2.669
Orthorombic	5.60	6.36	7.50	90.0	90.0	90.0	12	2.441
Orthorombic	3.19	4.87	11.70	90.0	90.0	90.0	12	3.197
Monoclinic	6.66	4.38	5.90	90.0	107.7	90.0	12	2.620
Orthorombic	3.17	7.77	12.16	90.0	90.0	90.0	12	3.740
Orthorombic	3.80	5.85	11.21	90.0	90.0	90.0	12	3.832
Orthorombic	3.19	7.54	9.19	90.0	90.0	90.0	11	2.994
Orthorombic	2.92	6.88	10.77	90.0	90.0	90.0	11	4.133
Orthorombic	2.92	6.88	10.77	90.0	90.0	90.0	11	4.178
Monoclinic	8.81	5.03	8.50	90.0	136.8	90.0	11	2.507
Orthorombic	4.54	9.64	11.70	90.0	90.0	90.0	11	2.667
Orthorombic	6.11	6.36	10.03	90.0	90.0	90.0	11	2.755
Orthorombic	3.18	4.89	11.68	90.0	90.0	90.0	11	3.895
Orthorombic	3.48	4.94	15.88	90.0	90.0	90.0	11	3.750
Orthorombic	3.12	8.46	9.53	90.0	90.0	90.0	11	3.208
Orthorombic	3.12	8.46	9.53	90.0	90.0	90.0	11	3.208
Orthorombic	3.18	7.54	9.16	90.0	90.0	90.0	11	3.065
Orthorombic	5.63	9.32	10.11	90.0	90.0	90.0	10	3.088
Orthorombic	2.61	8.80	9.21	90.0	90.0	90.0	10	3.231
Orthorombic	5.61	6.36	7.51	90.0	90.0	90.0	10	2.560
Orthorombic	5.22	7.39	8.03	90.0	90.0	90.0	10	3.932

Cell	a	b	c	α	β	γ	FoM	R_w (LB)
Hexagonal	9.71	9.71	8.19	90.0	90.0	120.0	5	3.835
Orthorombic	3.42	8.80	9.70	90.0	90.0	90.0	9	3.019
Monoclinic	3.56	3.85	12.94	90.0	119.9	90.0	9	2.821
Orthorombic	4.28	6.36	7.51	90.0	90.0	90.0	9	3.744
Tetragonal	5.59	5.59	11.67	90.0	90.0	90.0	7	3.156
Orthorombic	2.80	5.52	11.71	90.0	90.0	90.0	6	3.025
Orthorombic	4.12	7.89	13.01	90.0	90.0	90.0	5	3.009
Orthorombic	6.84	8.71	10.43	90.0	90.0	90.0	5	2.936
Hexagonal	5.79	5.79	12.04	90.0	90.0	120.0	5	4.073
Monoclinic	4.05	10.30	8.73	90.0	129.4	90.0	5	3.692
Monoclinic	7.75	5.42	8.88	90.0	92.8	90.0	5	3.065
Hexagonal	9.69	9.69	8.19	90.0	90.0	120.0	4	4.177
Monoclinic	5.62	5.62	13.92	90.0	103.4	90.0	4	2.983
Hexagonal	8.89	8.89	11.61	90.0	90.0	120.0	4	4.768
Hexagonal	13.20	13.20	6.19	90.0	90.0	120.0	4	2.930
Tetragonal	8.25	8.25	9.97	90.0	90.0	90.0	4	3.096
Orthorombic	9.01	5.66	7.67	90.0	90.0	90.0	4	3.550
Monoclinic	5.71	9.16	13.52	90.0	89.9	90.0	4	2.759
Orthorombic	6.64	9.28	13.53	90.0	90.0	90.0	4	3.268
Hexagonal	13.20	13.20	6.19	90.0	90.0	120.0	4	2.930
Tetragonal	8.25	8.25	9.97	90.0	90.0	90.0	4	3.189
Orthorombic	9.01	5.66	7.67	90.0	90.0	90.0	4	3.550
Orthorombic	6.84	8.71	10.44	90.0	90.0	90.0	3	2.936
Hexagonal	5.79	5.79	12.04	90.0	90.0	120.0	3	4.073
Hexagonal	9.71	9.71	8.19	90.0	90.0	120.0	3	3.792
Monoclinic	5.48	9.55	5.96	90.0	99.6	90.0	3	1.879
Hexagonal	8.89	8.89	11.61	90.0	90.0	120.0	3	4.768
Monoclinic	4.02	12.72	11.34	90.0	138.4	90.0	3	1.865

Chapter 7

A new ternary structure in ND_3-D_2O-CD_4

In chapters 1 and 6 it was outlined that methane, ammonia and water are the basis of the 'mineralogy' of the outer planets Uranus and Neptune as well as icy moons like Europa (Jupiter), Titan (Saturn), and Triton (Neptune) all of which contain significant proportions of some or all of these ices [81]. Modelling the evolution of these bodies rests on knowledge about the properties of ices and their mixtures [164, 290].

For example, studies of methane clathrate hydrate [42] showed that, rather than decomposing into ice and methane at high pressure as had been thought, methane clathrate hydrate underwent a series of structural phase transitions (see chapter 6). Based on this result, a model for the source of Titan's atmospheric methane was proposed [42], which stimulated new modelling of Titan [291]. This modelling suggested that outgassing of methane from Titan's interior has been episodic and that we are currently witnessing the final outgassing event [291].

In another recent work, it has been shown that ammonia hemihydrate is the dominant composition of ammonia hydrate above 2 GPa [58]. This result implies that solid ammonia water mixtures above this pressure exist as mixtures of ice and ammonia hemihydrate II. Furthermore, this gave rise to the possibility of liquid water on those planets with ammonia acting as an anti-freeze agent.
It also has been shown that above 6 GPa ammonia hydrates are significantly ionised and this is likely to affect the electrical conductivity of ammonia hydrates

with possible implications for the magnetism of icy planets [46].

However, almost all work (including chapter 6 in this thesis) focuses on the behaviour of planetary ices at high pressure has been carried out on binary mixtures (methane-water and ammonia-water), while the actually relevant system to the planets is the ternary one, consisting of methane, water, ***and*** ammonia. While the ternary system is of interest, the only measurement of this mixture is a combined Raman, X-ray diffraction, and observation study of the melting/decomposition behaviour up to 3 GPa of an ammonia-methane-water mixture of unknown composition by Kurnosov *et al.* in 2006 [60].

The experiments here were carried out at the PEARL diffractometer (ISIS, Oxfordshire, UK) and aimed to verify or falsify the claimed increase in the melting temperature and to look for evidence of an incorporation of ammonia into the water lattice of methane hydrate. The former was (at least partially) successful as it was possible to show that up to 1.6 GPa the melting temperature stayed constantly at 320 K. Furthermore, evidence is given that the ternary system crystallises in a so far not reported structure strongly supporting the latter.

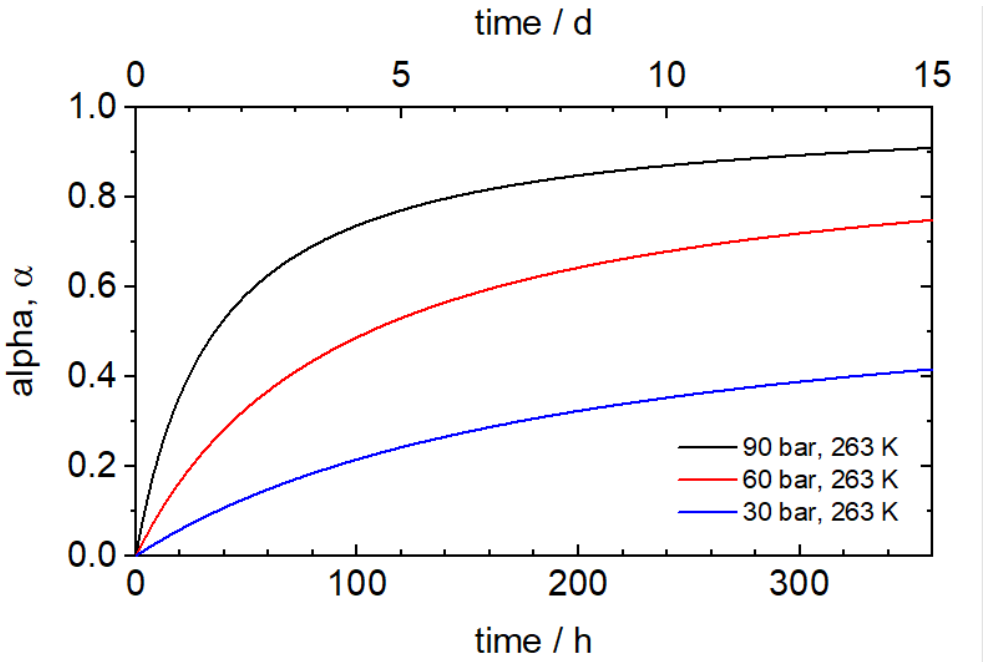

Figure 7.1 *Methane hydrate I to ice I_h ratio α as a function of time as given by Kuhs et al. [59]. The growth rate increases with both the temperature and with the (gas) pressure.*

7.1 Material and Methods

Prior to this experiment, the two hydrates methane hydrate I (MH-I) and ammonia hemihydrate (AHH), were prepared separately. The used set-up and technique to form the methane hydrate was similar to the one reported by Kuhs *et al.* [59]. In brief, deuterated water (Sigma-Aldrich, D_2O, >99.99% deut.) was powderised by spraying it into liquid nitrogen in a water-free atmosphere to prevent hydrogenated water condensing onto the sample. The largely increased surface area of the so produced very fine powder accelerates the synthesis of MH-I significantly. The sample growth is determined by two mechanisms: the formation of a hydrate on the outside of a particle and the subsequent diffusion into the interior thereof (see Figure 7.4). While the rate for the former process is high, it is small for the latter and hence is the rate-limiting step for the process.

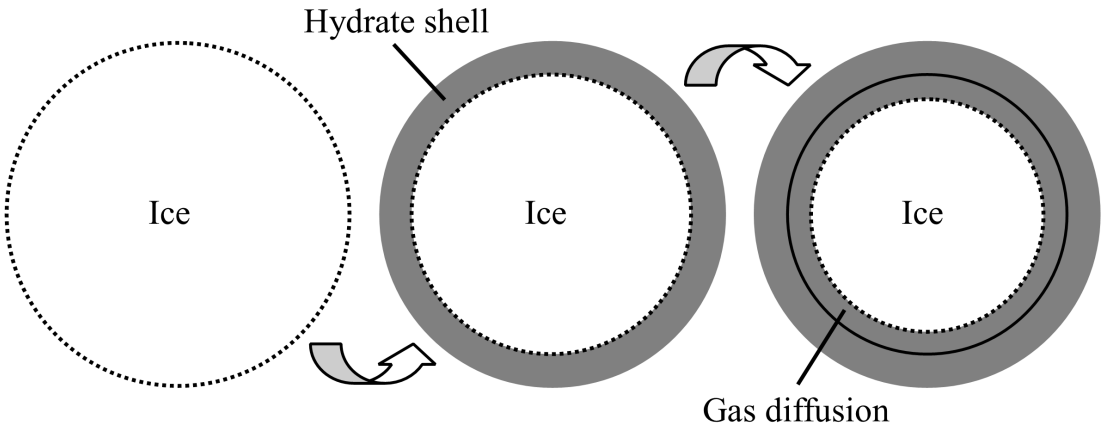

Figure 7.2 *The formation of MH-I is a two-step process. In the first step methane gets absorbed on the surface of an ice crystallite and a layer of methane hydrate is formed. In the second step methane diffuses through the MH-I layer into the interior of the particle and the MH-I layer grows inwards. Figure taken from Kuhs et al. [59].*

The powder was then transfered into a Swagelok pressure cylinder and pressurised with deuterated methane (Cambridge Isotope Laboratories, CD_4, >99% deut.) to about 50 bar (the bottle pressure). The pressure cylinder was then stored in a freezer at -5℃ (268K). In figure 7.1, the MH-I/I_h ratio, α, as a function of time is shown (data taken from Kuhs *et al.* 2006 [59]). From this data and a maximal pressure of 50 bar, a growth-time of about three months was estimated to form a sample of α >0.95.

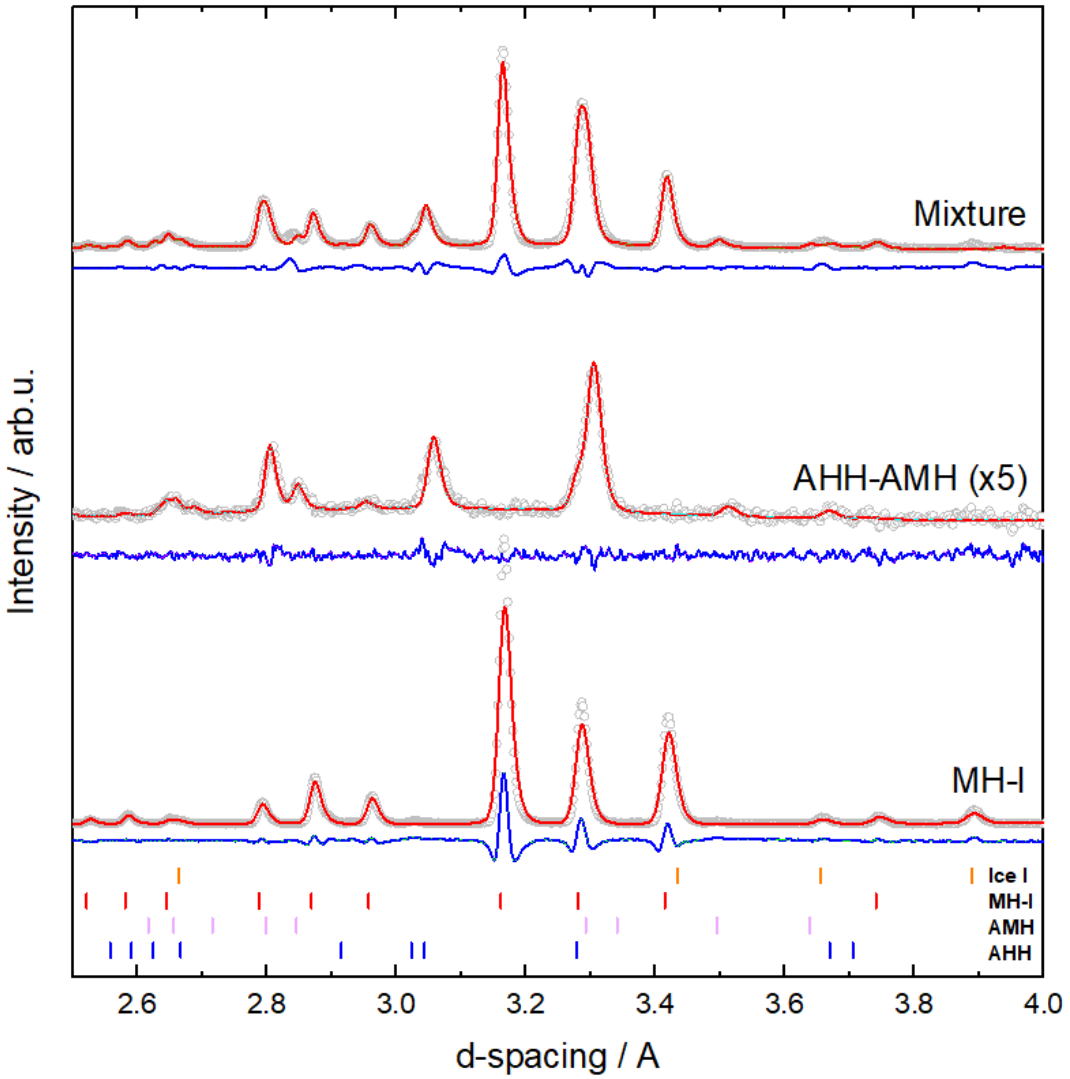

Figure 7.3 *Neutron diffraction patterns of the samples that were used for the experiment; Methane Hydrate CD_4-D_2O (bottom), ammonia hemihydrate ND_3-$0.5H_2O$ (mid) and the pattern of the mixture (top).*

In a similar set-up, the ammonia hemihydrate was produced by condensing deuterated ammonia (Sigma-Aldrich, N_3, >99.99% deut.) into a Swagelok bottle cooled with liquid nitrogen and filled with deuterated water (Sigma-Aldrich, D_2O, >99.99% deut.). The 2:1 mixture was then allowed to warm to room temperature and was cooled back to 166 K in an Isopropanol/LN2 bath to stabilise a liquid mixture of D_2O-ND_3. This mixture was then cooled with liquid nitrogen to 77 K to form a solid. (Due to the rapid cooling from 166 K to 77 K an amorphous solid is formed which crystallises at approximately 120 K on heating to the hydrate).

To establish the water-gas ratio in the sample, the two gas hydrates as well as a roughly 1:1 mixture of them were transferred into an Orange-type cryostat and diffraction patterns were collected for about 1 h at the PEARL beam-line, at the ISIS neutron source at the Rutherford Appleton Laboratory (RAL, Oxfordshire, UK) [221]. The respective diffraction patterns are given in Figure 7.3. Finally, the water-methane, water-ammonia and the water-methane-ammonia ratios were obtained from a Rietveld fit to the respective patterns.

The analysis of all diffraction patterns was carried out by Rietveld profile refinement using the GSAS-II crystallographic software package [183].

7.2 Results and Discussion

From the Rietfeld fits shown in figure 7.3 molar ratios of 46.0:8.2 D_2O:CD_4 for the MH-I sample and 2.0:1.5 ND_3:D_2O for the AHH/AMH sample were determined. For methane hydrate this corresponds to an occupancy of the cavities of 100%. Taking the phase fractions of the mixture into account, this results in a molar ratio of 13.3:56.7:8.2 for ND_3:D_2O:CD_4; hence, the sample had and ammonia content of 17.0 wt%.

For the high-pressure experiment, the mixture of D_2O-ND_3-CD_4 was cryo-loaded into a PE-cell; as a pressure marker a small amount of lead was added. Below 1 GPa the diffraction peaks of MH-I were clearly visible and above this pressure, the sample transformed into MH-II. The sample was then pressurised in steps to 1.6 GPa; after every pressure step the sample was heated to the melt and then allowed to re-crystallise.

7.2.1 The Melting Temperature of D_2O-ND_3-CD_4

In 2006, Kurnosov *et al.* first reported a massive increase above 1.2 GPa in the decomposition temperature in a NH_3-CH_4-H_2O system relative to the pure CH_4-H_2O system – with a total increase of 70 K at 2.0 GPa [60]. The influence of ammonia on the melting behaviour of methane hydrate has hence been the subject of several other studies; Choukroun *et al.* found a lower melting curve for

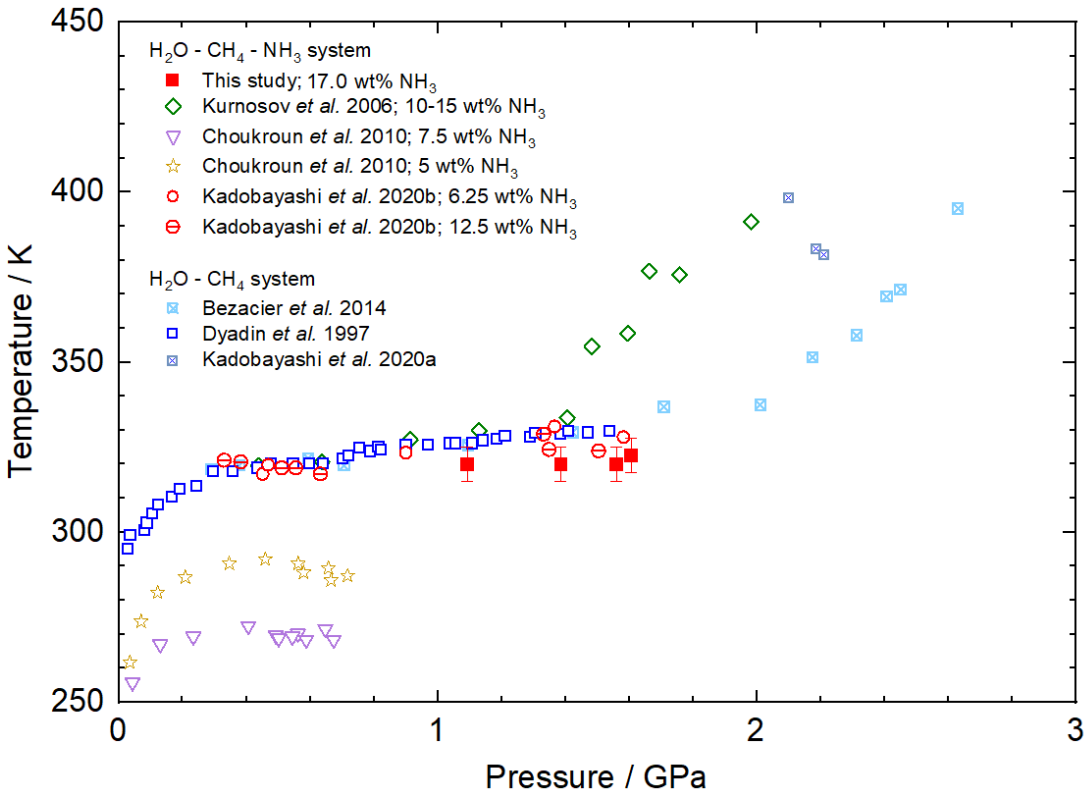

Figure 7.4 *Summary of melting curves of methane hydrate in the water-methane–ammonia system. Blue squares indicate the dissociation of pure methane hydrate and the other open symbols indicate the dissociation conditions of MH in mixed samples with different ammonia concentrations. The open green diamonds indicate those reported by Kurnosov et al. (ammonia concentration 10-15 wt%). Full red squares are the melting points of deuterated methane-ammonia-water in this study. Data taken from [60–66].*

the ternary system at pressures <0.8 GPa. For methane hydrate I, the melting temperature is lowered by about 30 K and 50 K for samples with 5 and 7.5 wt% ammonia, respectively [65]. On the contrary, data published by Kadobayashi *et al.* suggests a melting curve for the D_2O-ND_3-CD_4 system indistinguishable from the melting curve of pure methane hydrate for pressures <2 GPa (6.25 and 12.5 wt% ammonia). However, in the stability region of MH-III they reported a lower melting temperature for methane hydrate in the presence of ammonia [63, 64, 292]. Please note that these studies show that methane hydrate can co-exist with aqueous ammonia, but none of them report any effect of ammonia on the solid-solid transitions MH-I $\longrightarrow$ MH-II and MH-II $\longrightarrow$ MH-III.

Figure 7.4 shows the reported decomposition curves for methane hydrate in the

presence of ammonia along with the curves for pure methane hydrate [60–66]. Data of the melting temperatures this study on the deuterated ternary mixture are shown as red squares.

It was not possible to reproduce the predicted increase in the dissociation temperature; up to a pressure of 1.6 GPa the melting curve stayed flat at about 320 K and in agreement with the curves for pure methane hydrate published by Bezacier *et al.* [61] and Dyadin *et al.* [66]. It should be emphasised that in all other studies shown here, hydrogenous samples where used but this study was carried out on a deuterated sample. Therefore an isotope effect reducing the overall melting temperature can not be excluded but seems unlikely as the melting curve below 1 GPa does not differ from the hydrogenous ones. Furthermore, no (significant) isotope effect on the melting of methane hydrate in such low a pressure regime has been observed so far.

7.2.2 Incorporation of ND_3 into the CD_4-D_2O Network: Evidence for a Ternary Phase Above 1.6 GPa

In figure 7.6 the powder patterns collected at each pressure after melting are shown. The open symbols show the diffraction data and the solid line is a Rietveld fit to the data. Up to a pressure of 1.48 GPa, it was possible to index all peaks in the diffractograms either as methane hydrate-II (MH-II) or as ice VI. Please note that ammonia hydrates only crystallise above 3 GPa at room temperature.

After heating at 1.6 GPa, new peaks emerged alongside the methane hydrate and ice VI peaks (cf. arrows in Figures 7.5 and 7.6). It was not possible to fit any known methane hydrate, ammonia hydrate, or high pressure ice structure to this pattern. A comparison of the known crystal structures of ammonia, methane, water, and their mixtures is shown in Figure 7.5. This indicates that the NH_3-CH_4-H_2O system forms a new crystal structure above this pressure.

An analysis of the space group of MH-II with the subgroup tool on the Bilbao crystallographic server [293] was hence carried out. Most subgroups of$P6/mmm$ could not explain the emerging peaks, only the space group $Cmmm$, a *translatsionsgliche* subgroup of $P6/mmm$ could explain the peaks. A transformation to

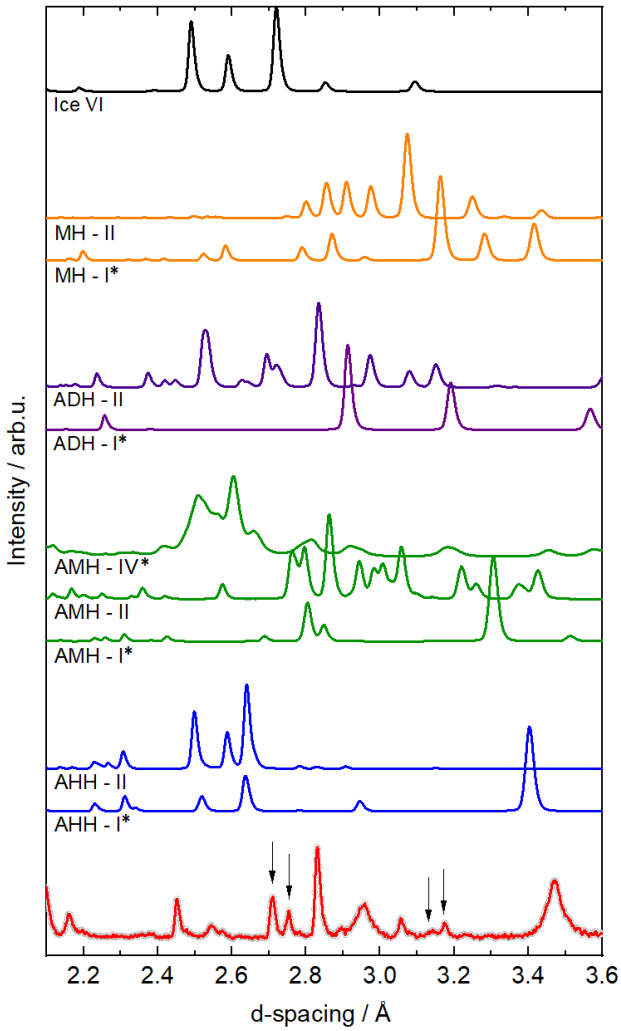

Figure 7.5 *Comparison with other structures of the D_2O, ND_3-D_2O and CD_4-D_2O systems which have been observed at similar P/T-conditions.*

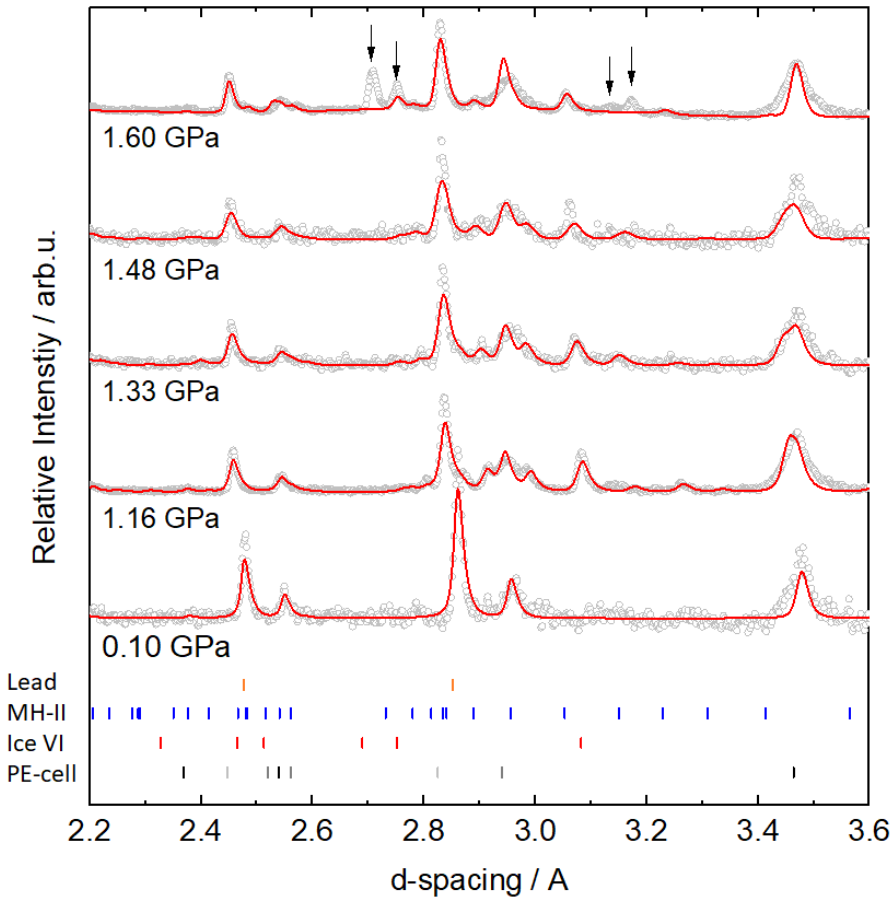

Figure 7.6 *Neutron diffraction patterns for the compression of ND_3-CD_4-D_2O system. After each pressure step the sample was heated to the melt. Open circles are collected data, lines are the respective Rietveld fits. The tick mark*

this space group resulted in the lattice parameters a=20.50748 Å, b=11.84000 Å, and c=9.92200 Å. A Le-Bail fit was then carried out and is shown in figure along with the transformed MH-II unit cell in space group $Cmmm$ (R_w=0.0884). Ammonia could therefore be incorporated into the existing MH-II water lattice resulting in a reduction of crystal symmetry and a slight distortion of the unit cell to a=20.128(6) Å, b=11.8157(31) Å, and c=9.902(4) Å (at 1.6 GPa).

Two mechanisms could be possible here; either ammonia substitutes a D_2O molecule in the water lattice, or ammonia occupies a cage and forms a mixed clathrate. An incorporation into the water lattice seems more plausible at first due to the hydrophilic nature of ND_3 (cf. chapters 1 and 6). However, Shin *et al.* postulated an incorporation of ammonia into the clathrate cages; based on a series of vapor deposition experiments paired with molecular simulations

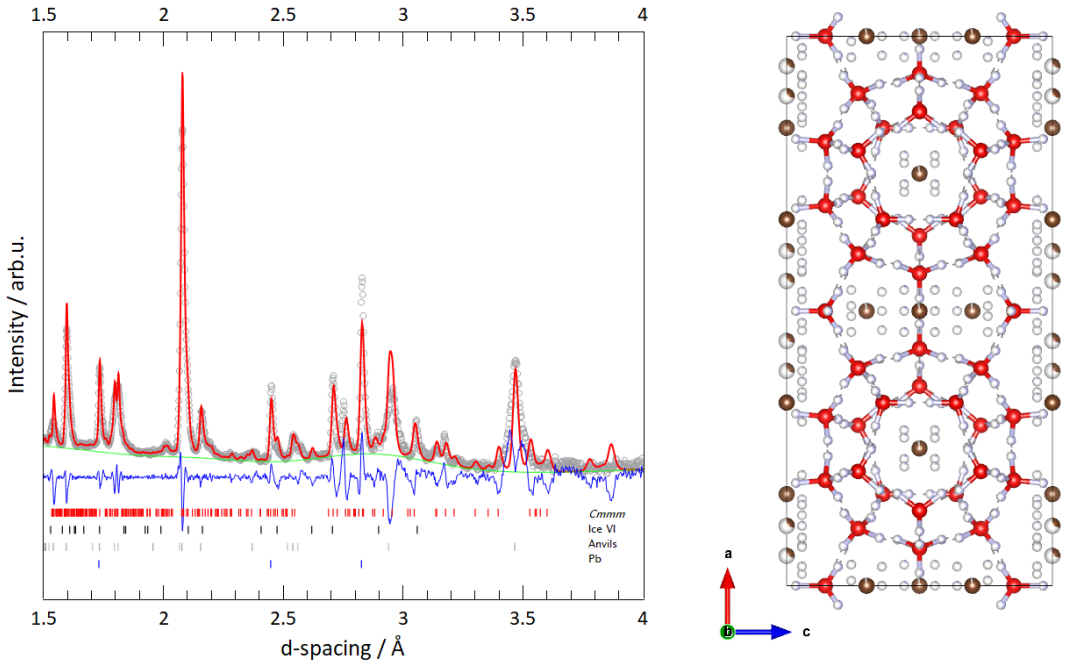

Figure 7.7 *Left: A LeBail fit for MH-II in the Cmmm space group could explain the emerging peaks. The resulting lattice parameters are a=20.49949 Å, b=11.42588 Å, and c=9.5209 Å. Right: MH-II, a hexagonal clathrate hydrate (sH), in the orthorombic Cmmm space group.*

they were able to show that ammonia can occupy both small and large cages in the sI and sII structures [86]. Hence, the mixed cage occupation seem more plausible. However, the observation of hydrogen bonding between the ammonia guest molecules and the water molecules is highly unusual for clathrates as it was believed that a hydrogen-bonding guest would result in the break-down of the cage-like water network (cf. Sloan [77]).

A quick initial test to rule out a substitution of ammonia into the water lattice was tried. To that end, every D_2O position in the MH-II phase was also occupied with an ammonia molecule. The two molecules were then constrained to give a total occupancy of 1 and the occupancies were refined using the Rietveld method. Similarly, the the sites of the CD_4 guest molecules were occupied with constraint ammonia molecules and refined as well. However, the overall fit to the data did not improve and the new peaks could not be explained by these (very simple) models. This is most likely due to the poor data quality as most peaks in the high q-region are heavily overlapping with parasitic anvil, ice VI, or Pb peaks.

Another possibility for the ternary mixture could be the formation of a completely new crystal structure, unrelated to any known binary hydrates. In this case it is likely that 1.6 GPa was not a sufficiently high enough pressure to convert all of the MH-II into the new phase. Based on the limited data set it was not possible to investigate this possibility closely and an attempt for structure search (see chapter 6) was once again complicated by the existence of many parasitic anvil, ice VI, and PE-press peaks. A more detailed study should be carried out in the future.

7.3 Conclusions

A neutron powder diffraction study was carried out to investigate the ternary mixture of ammonia, water, and methane. To that end a 1:1 mixture of AHH and MH-I was cryo-loaded into a PE-press and then allowed to warm to room temperature. The reason for this study was twofold. First, to verify or falsify the claimed increase of the melting temperature of methane hydrate in the presence of ammonia and second, to look for evidence of incorporation of ammonia into the MH-I lattice.
For the former of the two goals, the sample was then incrementally compressed to 1.6 GPa. At each step, the sample was heated to the melt and then re-cooled to room temperature. Here no evidence of an increase in the melting behaviour of MH-II in the presence of ammonia was found as our melting curve is in good agreement with the melting curve of pure MH-II as given by Bezacier *et al.* [62]. It should be noted though, that both Kurnosov *et al.* and Bezacier *et al.* used hydrogenous samples whereas this study was carried out on a deuterated sample - and an isotope effect is hence possible but unlikely.

As for the latter goal, it was possible to identify four novel reflections at 1.6 GPa. These peaks do not fit any of the known crystal structures of the ammonia hydrates or the methane hydrates. This evidence gives credence to the existence of a ternary crystal structure. Due to many parasitic peaks of AMH, ice VI and the cell it was not possible to determine the exact structure. A follow-up experiment was originally scheduled for a further investigation of the ternary system but had to be cancelled due to the outbreak of a global pandemic in 2020/21. Still the report of a ternary phase in the ammonia-methane-water system has many implications on how we see and model the outer planets and the icy moons.

Chapter 8

Carbonic Acid at High Pressure: Carbonate Formation in TiZr-Gaskets

The investigation of small gases dissolved in water is of importance to many different fields such as astrophysics, biology and environmental science [70]. In particular, the carbon dioxide-water system is of considerable importance as both molecules are abundant in the Solar system - in cosmic dust as well as in the interior of planets and moons [294, 295]. However, more importantly carbon dioxide and water are the principal volatile components of the Earth's mantle and their behaviour at pressure is important to models of the Earth's carbon and water cycles. As such, solid CO_2-hydrates may be a possibility for carbon dioxide sequestration [296].

Historically, the first evidence for the existence of CO_2 hydrates dates back to the year 1882, when Wróblewski [297–299] reported clathrate formation while studying carbonic acid. He noted that the gas hydrate was a white material resembling snow, and could be formed by raising the pressure in the H_2O-CO_2 system. He also estimated the CO_2-hydrate composition to be approximately $CO_2 \cdot 8\ H_2O$. The composition found by Wróblewski was falsified in 1954, when von Stackelberg and Muller [300] determined the crystal structure of CO_2 hydrate to be a type-I clathrate hydrate (sI); this type of clathrate allows for a H_2O:CO_2 ratio of 5.75:1 [70].

The first high pressure phase of CO_2 and H_2O was reported by Hirai *et al.* in 2010 [67]. Formed by compressing sI (space group $Pm3n$) using diamond anvil cells

and a helium-refrigeration cryostat, this phase was revealed at pressures above approximately 0.6 GPa and below 1.0 GPa. Above this pressure, the new phase decomposes to dry ice (space group $P\bar{a}3$) and ice VI (space group $P4_2/nmc$). The exact phase boundaries were later determined by Massani *et al.* [39]. Tulk *et al.* tried to solved the structure of this new phase in 2014 using neutron-diffraction data and computer models and proposed a filled ice structure in the space group *Imma* for the high-pressure phase of CO_2 hydrate [301]. However, Amos *et al.* showed that this phase is in fact part of the chiral sX clathrate family [154].

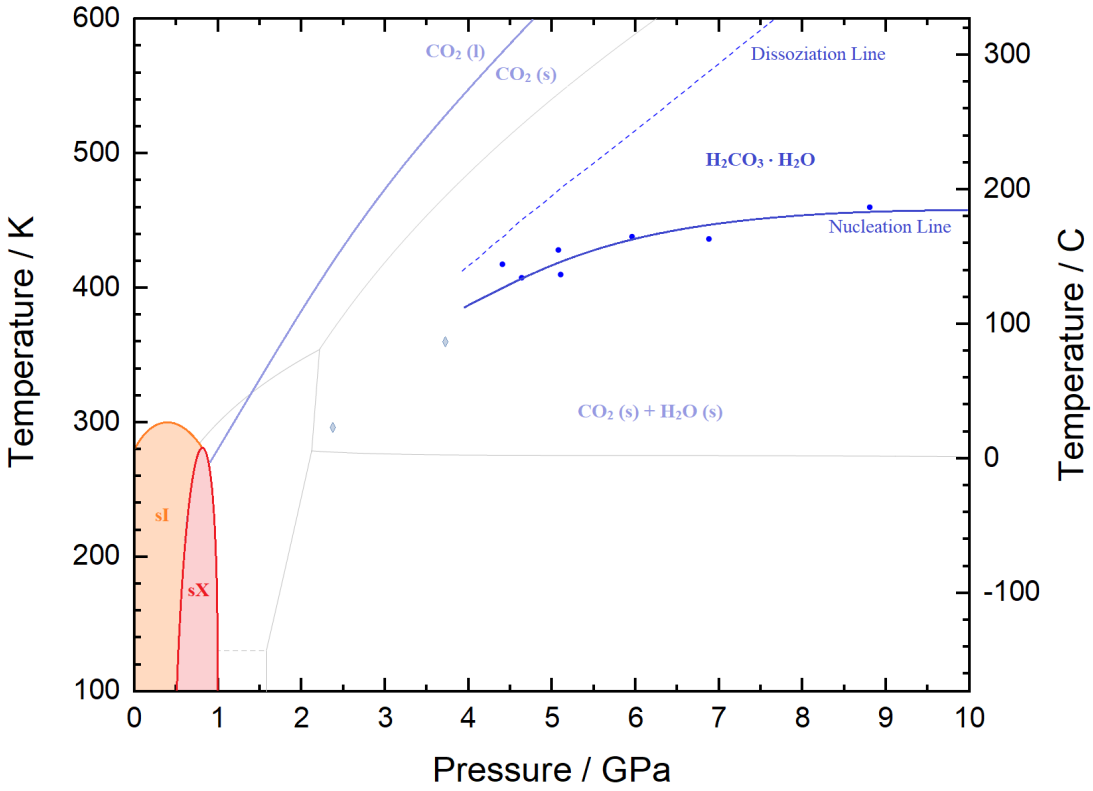

Figure 8.1 *Phase diagram of water and carbon dioxide. The coloured areas show the stability region of sI and sX, respectively. The dark blue line shows the nucleation line above which carbonic acid monohydrate ("S3") can be found, and the dashed line gives its dissociation curve. The light grey and blue lines show the phase diagram of pure water and CO_2, respectively. Data taken from [39, 67, 68].*

Figure 8.1 shows the phase diagram of carbon dioxide-water as published by Abramson *et al.* in 2017 [68]. At 4.4 GPa and about 400 K they found a kink in the Ice-VII+CO_2 melt-curve and observed a new solid phase ("S3") forming. They interpret the kink as a quadruple point for the equilibrium between ice VII, solid CO_2, S3, and fluid F1. Above this pressure they observed a peritectic line

which separates F1+S3 from CO_2+F1 (dotted line) and an eutectic line which separates Ice-VII+S3 from S3+F1 (not shown). Abramson *et al.* also observed that S3 formed over the course of a few hours from mixtures of solid ice VII and solid CO_2 when warmed above 155^{o}C. The solid blue points in figure 8.1 show the pressures and temperatures where this was observed. Finally S3 was observed to decompose on decompression and the open diamonds denote the conditions where decomposition was observed. However, the exact location of the phase boundary that separates ice-VII+CO_2 from S3 remains to be determined [68].

Abramson *et al.* have also been able to characterise the S3 phase with Raman spectroscopy and X-ray diffraction; based on the Raman spectra they concluded that S3 is carbonic acid. From single crystal X-ray diffraction follows that S3 is the monohydrate of carbonic acid ($H_2CO_3 \cdot H_2O$) and has a triclinic structure (a=5.88 Å, b=6.59 Å, c=6.99 Å, α=88.7^o, β=79.7^o, γ=67.7^o, V=246.5 Å^3)[302].

The work described in this chapter arises from an attempt to determine the hydrogen positions in carbonic acid monohydrate (CMH) by means of neutron diffraction. The attempt was unsuccessful, but revealed a more complex behaviour of carbonic acid at elevated pressures and temperatures. In particular, the absence of carbonic acid in the presence of titanium – a metal which is commonly used in neutron experiments as a component of null-scattering TiZr alloy. As such it has an influence on the experimental design of neutron experiments experiments involving CO_2 and H_2O or carbonic acid.

8.1 Material and Methods

The *ex-situ* Raman experiments were carried out with in a Confocal Raman Microscope, Labram 300, which employs a 632.81 nm (red) 15-mW He-Ne laser. The *in-situ* experiments were carried out using a green 514.5 nm laser. The DACs (200 μm culet, Re gasket) were loaded using the 'bubble-method' [154]; first liquid D_2O (S-A, 99.999%, >99.9% deut.) was filled into the gasket hole and the cell was closed lightly and in a manner that the water was still able to evaporate. Upon the formation of a bubble of suitable size, the cell was closed and the sample frozen in liquid N_2; the cell was opened again and gaseous CO_2 was condensed into the cavity in the sample chamber.

The neutron diffraction experiments were conducted in a PE-press at the PEARL beam-line, Rutherford Appleton Laboratory [221]. To that end, a fine powder of CO_2 and D_2O (roughly 1:1 in volume) was ground together and then cryo-loaded into a PE-press [197, 200]. A set of ZTA ceramic anvils (ZrO and Al_2O_3) was used and the gasket material consisted of a null-scattering TiZr alloy [221, 303]. The press was sealed with an initial load (sample pressure less than 0.5 GPa) and then put onto the instrument.
The analysis of the diffraction patterns was carried out by either Rietveld profile refinement using the GSAS-II crystallographic software package [183].

8.2 Results and Discussion

8.2.1 Initial Raman Experiments

In order to find any possible isotope effects Abramson's Raman experiment in a diamond anvil cell was repeated with D_2O [68]. To this end, carbon dioxide and deuterated water were loaded into a DAC using the bubble-method. The sample was then brought to 4.5 GPa, at which pressure it was heated to 445 K; after

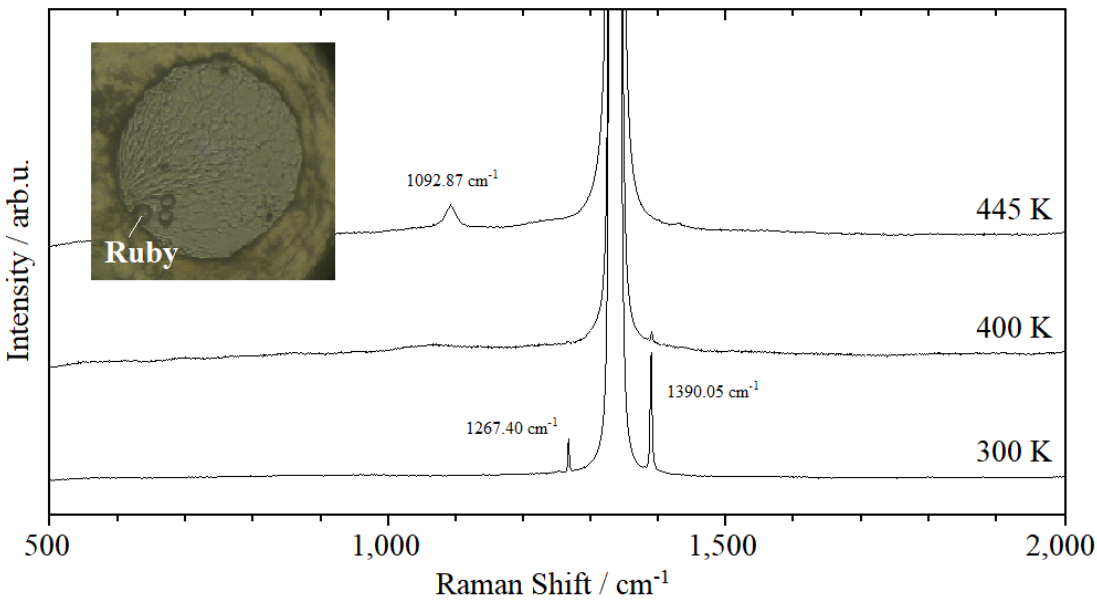

Figure 8.2 *Raman spectra of CO_2 and D_2O at 300 K, after heating to 400 K and 445 K at 4.5 GPa. The two peaks before and after the massive diamond peak at app. 1380 cm^{-1} are CO_2. The emerging peak at app. 1090 cm^{-1} is a carbonic acid mode.*

cooling back to room temperature the sample was characterised by *ex-situ* Raman spectroscopy. The Raman data of this experiment in shown in figure 8.2. The two peaks before and after the massive diamond peak at 1380 cm^{-1} are assigned to CO_2 Fermi-dyade, a peak doublet found in Raman bands of symmetric molecules; it is a consequence of wavefunction mixing which results in a shift of the energies and intensities of the respective modes. The emerging peak at 1090 cm^{-1} after heating to 445 K at 4.5 GPa is a carbonic-acid mode belonging to CO_3^{2-}. The inset in figure 8.2 shows a microscope picture of the sample after heating.

To determine the exact formation condition of carbonic acid, the same experiment was then carried out *in-situ*. The respective spectra are shown in figure 8.3. The first evidence of the presence of $D_2CO_3 \cdot D_2O$ can be observed at 425 K; a carbonic acid mode appears at 1090 cm^{-1} while the Fermi-dyade due to of solid CO_2 and the water modes at 3300-3500 cm^{-1} disappear. The onset of the dissociation of D_2CO_3 can be seen at 440 K (which is in good agreement with the phase

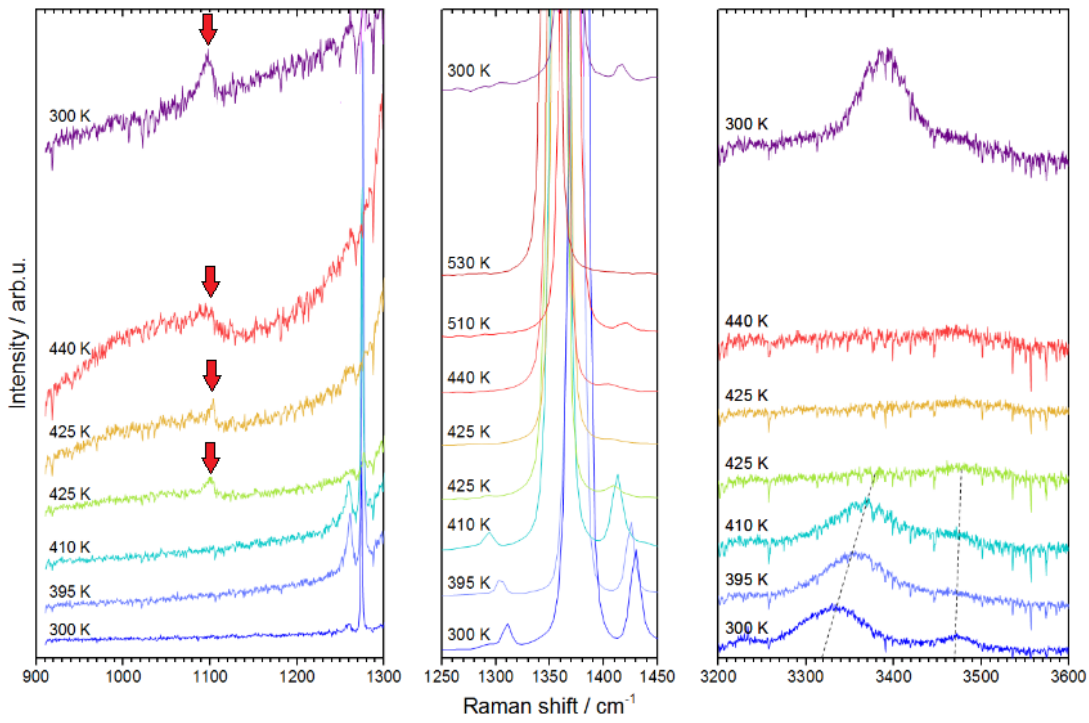

Figure 8.3 *In-situ Raman spectra of CO_2 and D_2O upon heating from room temperature to 530 K at 4.5 GPa. The two peaks before and after the massive diamond peak at app. 1380 cm^{-1} are CO_2. The emerging peak at app. 1090 cm^{-1} is a carbonic acid mode. The two peaks between 3300-3500 cm^{-1} show water modes.*

diagram given in [68]); visual observation of the gasket hole also suggested a partial liquification of the sample at this temperature. Please note that part of the CO_2 remains solid - and therefore visible in the Raman spectra - up to 510 K. The top violet curve in Figure 8.3 thereby depicts the spectrum after cooling the sample back to room temperature and once again shows the presence of carbonic acid.

8.2.2 Powder-Neutron Diffraction at ISIS: A Failed Attempt to Find the Hydrogen Positions

In order to determine the hydrogen/deuteron positions in carbonic acid monohydrate a similar experiment as described in 8.2.1 was carried out at the ISIS neutron source (RAL, Oxfordshire, UK).

To that end, a fine powder of CO_2 and D_2O (roughly 1:1 in volume) was ground together and then cryo-loaded into a PE-press. The sample was step-wise compressed to 4.0 GPa (app. 0.5 GPa steps) while powder data was recorded. The slightly lower starting pressure (cf. DAC experiment 4.5 GPa) was chosen to compensate for a pressure increase due to thermal expansion upon heating.

In figure 8.4 the respective data is shown; the open symbols give the diffraction data, while the solid red line is the corresponding Rietveld fit to the data. The pressures given were determined from the BM-EoS of carbon dioxide; solid CO_2 has no phase transition in the respective pressure range and stays solid upon heating (see section 8.2.1). Note that the mixture is initially liquid; upon reaching about 2 GPa the sample starts to crystallise as ice VII and CO_2(I). As expected, no further phase transition can be observed during this compression.
At 4.0 GPa a diffraction pattern was recorded for about 6 h and from this the composition of the sample was determined; the weighted Rietveld refinement suggests a molar CO_2:D_2O ratio of 1:0.48.

Subsequently, the ice VII-CO_2 sample was heated at 4.0 GPa to 480 K. The diffraction data for the temperature increase is given in figure 8.5; the open circles are measured data points and the solid red line gives the respective Rietveld fit to the data. During the heating, the pressure increased due to thermal expansion

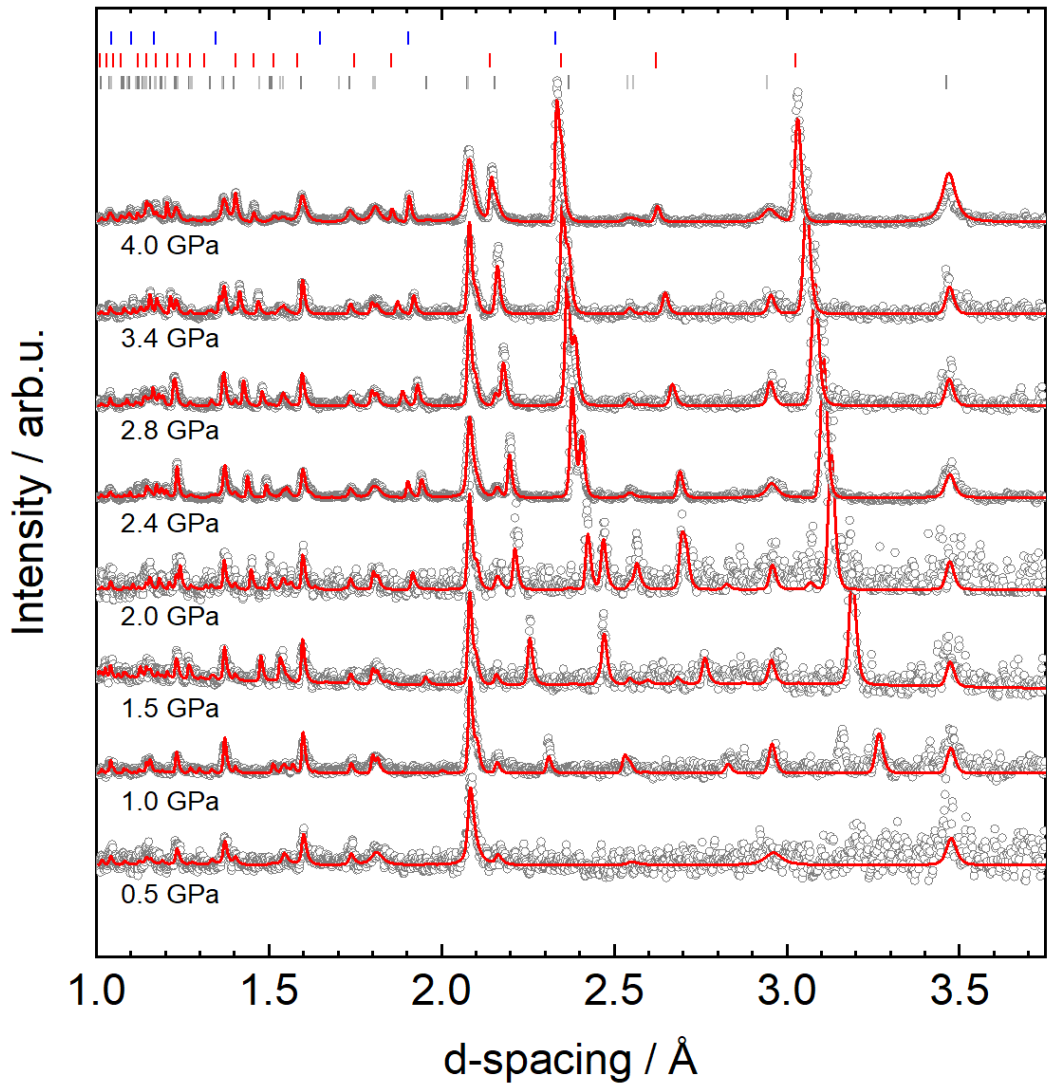

Figure 8.4 *Powder diffraction data for the compression of CO_2 and D_2O at room temperature. The open circles give the diffraction data; the solid red line is a Rietveld fit to the data. The tick-marks are from bottom to top: anvils (Al_2O_3 and ZrO), CO_2 (I) and ice VII.*

to 5.1 GPa at 480 K, which should be in the stability region of the carbonic-acid monohydrate. However, no changes in the diffraction pattern can be observed during the heating.

In a second attempt to form carbonic acid monohydrate, a mixture of ice VII and solid CO_2 was brought to 2.65 GPa (12 t load) and then heated to 480 K (diffraction patterns not shown here). At this temperature, the diffraction peaks caused by solid CO_2 in the sample vanish due to the melting. Simultaneously the appearance of a broad halo-peak (liquid CO_2) was observed. At this temperature

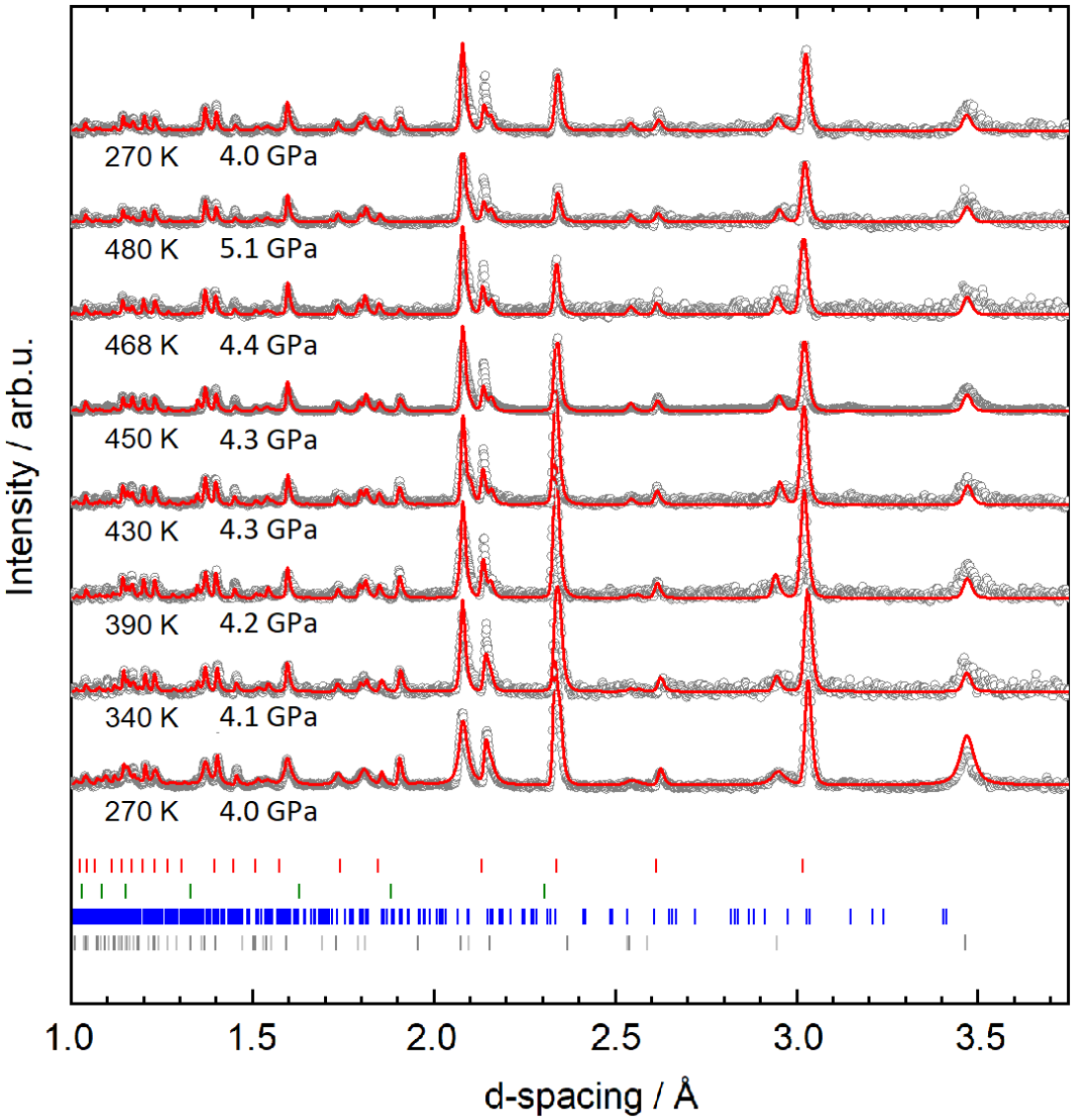

Figure 8.5 *Powder diffraction data for the heating of CO_2 and D_2O at 4.0 GPa. The open circles give the diffraction data; the solid red line is a Rietveld fit to the data. The tick-marks are from bottom to top: anvils (Al_2O_3 and ZrO), $D_2CO_3{\cdot}D_2O$, ice VII, and CO_2 (I).*

the sample was then pressurised in order to obtain $D_2CO_3{\cdot}D_2O$ from the melt. However, also in this case the main diffraction peaks were identified as ice VII and dry ice peaks. The respective powder diffraction pattern at 4.8 GPa and 480 K is shown in figure 8.6; the open circles show the collected data (collection time 6 h) and the red line is a Rietveld fit to the data.

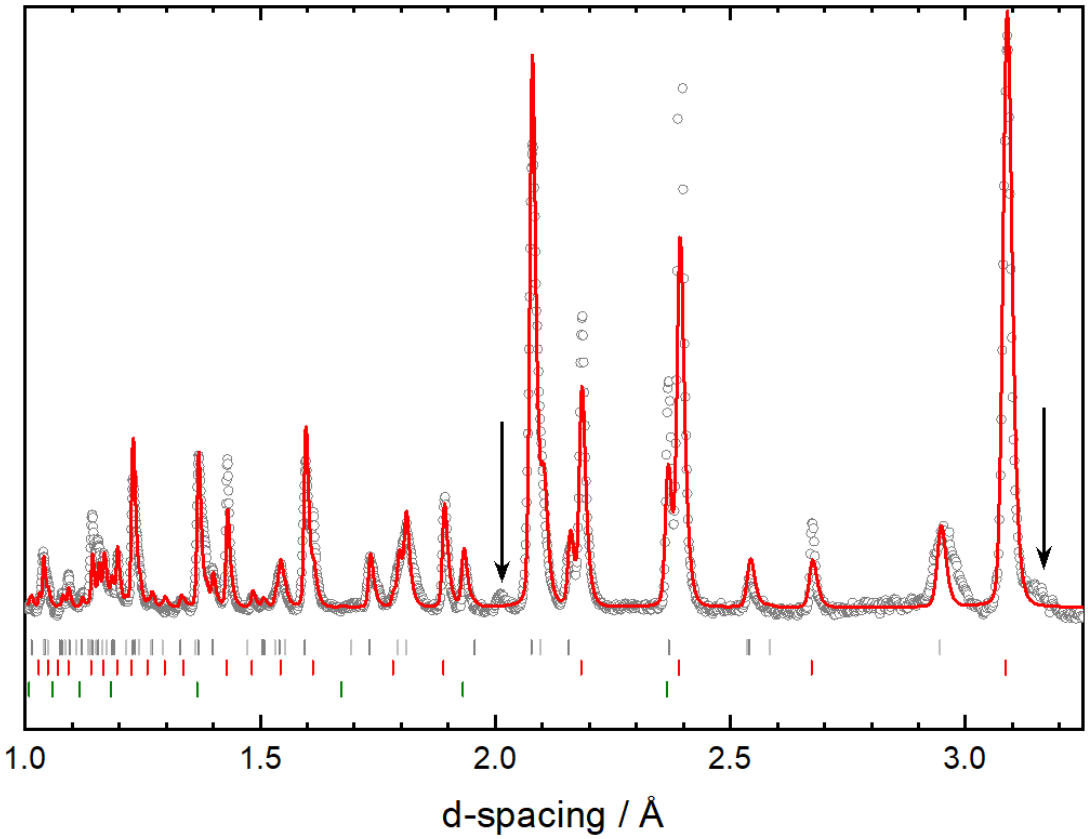

Figure 8.6 *Powder diffraction data for CO_2 and D_2O at 4.8 GPa and 480 K after compression at elevated temperature. The arrows indicate newly emerged peaks not visible before compression. The open circles give the diffraction data; the solid red line is a Rietveld fit to the data. The tick-marks are from top to bottom: anvils (Al_2O_3 and ZrO), CO_2(I), and ice VII.*

8.2.3 The Influence of the Gasket Material on the Formation of H_2CO_3 and D_2CO_3

In the data shown in figure 8.6 two small peaks were observed that could not be indexed by either the anvils, CO_2, or ice VII. The respective peaks are indicated by arrows in figure 8.6. A first attempt to fit the peaks with $D_2CO_3 \cdot D_2O$ failed; as only two peaks were observed, an indexing of this observed phase is impossible.

Additionally it was observed that the intensity of the sample peaks relative to the intensity of the anvil peaks decrease during the heating experiment (cf. Fig. 8.5). This led to the conclusion that the sample somehow reacted during the experiment. Since the formation of carbonic acid was excluded by the lack of the

respective peaks in the diffraction pattern, another possible pathway for the loss of water and carbon dioxide had to be found.

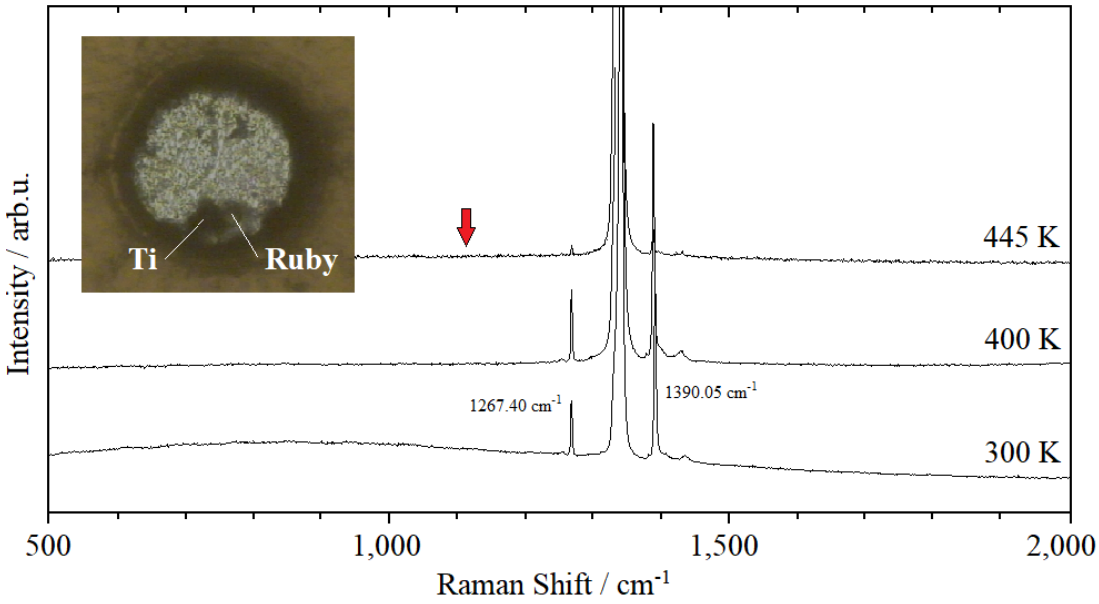

Figure 8.7 *Raman spectra of CO_2 and D_2O in the presence of Ti upon heating form RT to 445 K at 4.5 GPa. The two peaks before and after the massive diamond peak at app. 1380 cm^{-1} are CO_2. The arrow shows the position at which the carbonic acid mode should emerge.*

The only change in the experiments carried out in a diamond anvil cell and in the Paris-Edinburgh press was the different gasket material; while the DAC employed a rhenium gasket, the PE-press used a TiZr gasket. As D_2CO_3 is a strong acid a reaction of carbonic acid with the gasket material would be possible according to

$$2\ D_2CO_3 + Ti \rightarrow Ti(CO_3)_2 + 2\ D_2 \quad \text{and/or}$$
$$2\ D_2CO_3 + Zr \rightarrow Zr(CO_3)_2 + 2\ D_2.$$

An investigation of the gasket was not possible as it was disposed of before a post-experimental examination could be carried out.

The Raman experiment described above was hence repeated in presence of titanium. This was due to the availability of Ti powder. The respective spectra are shown in figure 8.7. While the intensity of the CO_2 bands clearly decreases upon heating, no carbonic acid could be found in these experiments (cf. top spectrum in fig. 8.7). It is therefore likely that the formed carbonic acid indeed

reacts with the gasket material in the PE-press which explains why it was not found. As Ti on its own showed a reaction (see below) a repetition in the presence of Ti *and* Zr - as in a TiZr alloy - was foregone.

While it was not possible to fit a known $Ti(CO_3)_2$ or $Zr(CO_3)_2$ to the two unknown reflections in the powder diffraction data, here an indirect proof of this assumption is discussed. Deuterium phase I (D-I) crystallises in a hexagonal unit cell in the space group $P6_3/mmc$. The most intense peak of D-I is the 101 reflection. As shown in figure 8.8, the powder pattern fitted only with ice VII and CO_2(I) fits particularly poorly in this d-spacing region; however the fit is slightly improved by adding D-I to the phase mixture. The unit cell volume of D_2 (29.3(4) Å^3) is consistent with literature values (28.8 Å^3) at the respective pressure of 4 GPa [110].
The existence of hydrogen in the sample can hence be interpreted as an indication that the concentrated carbonic-acid reacts with the gasket to a carbonate - and that the reaction releases D_2.

8.3 Conclusion

An attempt to make carbonic acid and study its crystal structure and in particular to verify the positions of hydrogens in the crystal structure; while a structure for (hydrogenous) carbonic acid monohydrate has been published based on X-ray diffraction by Abramson *et al.* in 2008 [302], this publication lacks measured hydrogen positions due to the inherent nature of X-ray diffraction.

In a first attempt, it was possible to reproduce Abramson *et al.*'s measurements successfully in a diamond anvil cell using a deuterated sample. The formation of $D_2CO_3{\cdot}D_2O$ was thereby observed using spectroscopy; in an *ex-situ* Raman experiment it formed at a pressure of 4.5 GPa and elevated temperatures. Furthermore, it was confirmed that it can be recovered to room temperature. Secondly, the exact formation temperature at 4.5 GPa was measured in an *in-situ* Raman experiment and found to be 425 K.

A similar experiment was then carried out at a larger scale using a PE-press at the ISIS neutron facility to obtain a diffraction pattern of carbonic acid monohydrate. Diffraction data at 4.0 GPa was recorded up to 480 K at which the pressure

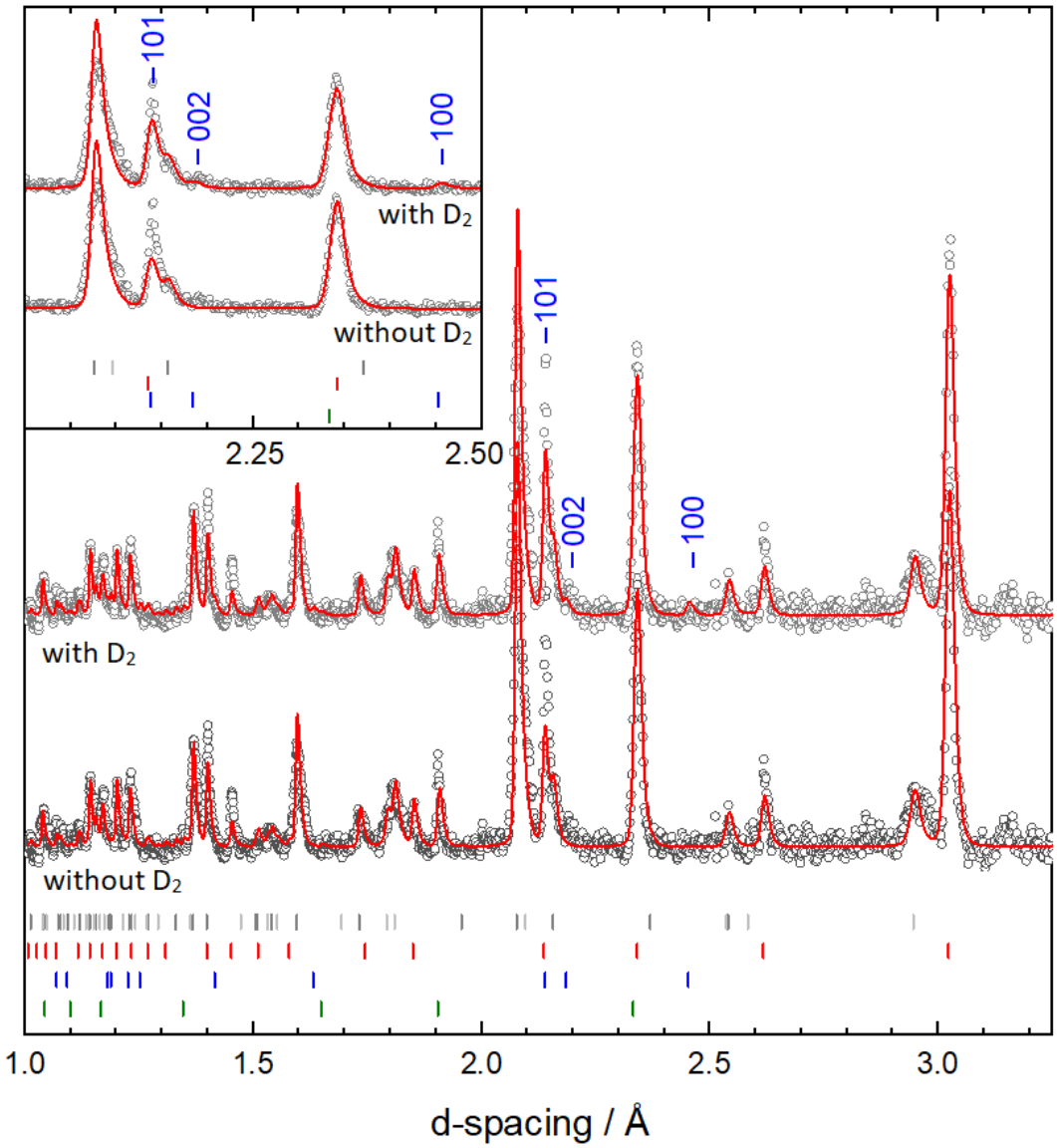

Figure 8.8 *Powder diffraction data for the heating of CO_2 and D_2O at 4.0 GPa. The open circles give the diffraction data; the solid red line is a Rietveld fit to the data. The tick-marks are from top to bottom: anvils (Al_2O_3 and ZrO), CO_2 (I), D_2(I), and ice VII.*

increased to 5.1 GPa, but no reflections associated with $D_2CO_3{\cdot}D_2O$ could be identified. A second attempt to obtain carbonic acid by cooling the mixture from the melt also failed.

Investigating the reason why $D_2CO_3{\cdot}D_2O$ did not form in the PE-press led to the conclusion that the gasket material reacted with the sample. While a rhenium gasket was used for the DAC experiments, PE-press gaskets were machined from an titanium-zirconium alloy. When the DAC experimented was repeated in the

presence of Ti, also no carbonic acid was found. Pure carbonic acid, while not stable at ambient conditions in aqueous solution, is considered a strong acid. It is therefore very likely that it reacts with the gasket material according to

$$2\ D_2CO_3 + Ti \rightarrow Ti(CO_3)_2 + 2\ D_2 \quad \text{and/or}$$
$$2\ D_2CO_3 + Zr \rightarrow Zr(CO_3)_2 + 2\ D_2.$$

While it was not possible to identify any new reflections as $Ti(CO)_3$ or $Zr(CO)_3$, it was possible to improve the Rietveld fit by adding D_2 to ice VII and carbon dioxide. This further reinforces the argument that carbonic acid reacts to a carbonate with Ti or Zr. This evidence that a reaction between carbonic acid and TiZr occurs has important consequences for the design of neutron experiments. TiZr is widely used for sample cans and pressure cells because it produces no Bragg peaks (null-scattering). Experiments involving carbon dioxide, water, and TiZr have the potential to react negating the experiment and potentially damaging the sample can.

As it was not possible to obtain a diffraction pattern of $D_2CO_3{\cdot}D_2O$, and hence to obtain the hydrogen/deuterium positions in its crystal structure, further experiments are necessary in the future. To avoid a reaction with the gasket material, they should be carried out in a large-volume DAC suitable for neutron diffraction using a rhenium gasket.

Chapter 9

Summary and Final Remarks

9.1 Single Crystal Neutron Diffraction in DACs

As outlined in chapter 4 it was shown that it is possible to obtain structurally meaningful data from single-crystal neutron diffraction in diamond anvil cells. It was possible to resolve the diffraction pattern of a DKDP crystals of nDAC size (0.028 mm^3) at the TOPAZ and SNAP beamlines at the Spallation Neutron Source (SNS) at Oak Ridge National Laboratory (ORNL). In the same study it was shown that the same crystal can be resolved in the sample environment of a diamond anvil cell. These proof-of-concept experiment show that obtaining meaningful structural data by means of single crystal diffraction is possible at high flux neutron sources. Furthermore, a case study for an ice VI crystal under pressure was presented which shows the applicability of this technique for real samples.
This proves particularly useful as progress has been made in the development of diamond anvil cells for neutron diffraction; Reinhard Boehler *et al.* at Oak Ridge National Laboratories recently presented a design for a piston-cylinder cell capable of megabar pressure. Their new cell is based on a ball-bearing design and achieved a new pressure record for neutron scattering of about 120 GPa (paper to be published in the near futur).

It was possible to obtain enough structure factors to refine DKDP and ice VI with similar accuracy as literature values for the respective samples and – in case of the DKDP - the bare crystal. However, the errors on the structural parameters increased. The studies presented here are pushing the limits of the

current possibilities of neutron diffraction and hence it is not surprising that the data quality is improvable [2].

For the future several improvements should be implemented to make this technique more accessible and user friendly. First and foremost, I would like to mention the integration algorithms for single crystal reflections. So far only a very basic integration based on two ellipsoids can be used to obtain structure factors on the SNAP beam line; an algorithm integrates single crystal Bragg peaks by summing the number events in a 3D ellipsoidal peak region in reciprocal space and subtracts an estimate of the background obtained from an ellipsoidal shell (see *IntegrateEllipsoids* documentation [246]). This method works well for reflections in 'free' reciprocal space but fails if a Bragg peak lies close to a powder line (usually caused by the gasket material). If the single crystal peak sits on a powder line, the (non-linear) intensity of the powder line is treated as a constant (i.e. averaged) background. This ultimately leads to a wrong count in the integration process and hence to wrong structure factors.

Currently, all single crystal reflections with similar d-spacings as the ones of the gasket material have to be discarded. Hence the overall number of recorded structure factors is largely reduced. In theory it is possible to fit the background with a Gaussian (or a more elaborate function) and use this background in the integration process. The possibility was discussed but was considered too time-consuming for this project especially since the existing routines yielded a sufficient data quality for the planned single crystal experiments on hydrogen/deuterium.

A second remark should also be made with regards to the absorption correction. As outlined prior in this work, the absorption of scattered neutrons was only treated in a very crude way, i.e. the gasket, which is the main neutron absorber, was treated as a hollow sphere and the diamond was not treated for at all; unavoidably, recorded Bragg reflections differ from the real structure factors. This error is highly dependent on the spacial direction of the scattered neutrons. However, due to the multiplicity of most peaks the error is relatively small and a more sophisticated model did not improve the overall data quality significantly. Once again this systematic error was assessed and considered negligible for the overall goal of this project. For the future, however, a proper model and a ray-tracing approach should be considered, based on the dimensions and the geometry

of the sample environment.

Altogether, single-crystal diffraction on SNAP is possible and does yield sufficient data quality despite the required long collection times of 6+ h per orientation. With this powerful tool, several controversies can be investigated - the first and foremost of them the study of the high-pressure phases of hydrogen and deuterium; using a single crystal could finally shed light on the exact nature of the broken-symmetry transition between hydrogen I and II. Furthermore, single-crystal study would prove useful to determine the exact hydrogen positions during the (continuous) transition from ice VII/VIII to ice X.

9.2 Gas Hydrates under pressure

In the second half of this work various gas hydrates of nitrogen, ammonia, and to some lesser degree carbon dioxide were discussed. Thus it seems plausible to split this section into three parts as well.

Nitrogen sX

In this section, the possibility to re-fill empty ice XVII with nitrogen at 130 K and 0.3 GPa was shown . In previous works it has been shown that ice XVII has the possibility to be used as a storage material for hydrogen as H_2 can be reversibly removed from the respective clathrate [154, 257, 258]. Here it was shown that that the empty structure can also be re-filled with a larger molecule, N_2, and that the water network stay intact. (Later, a similar experiment was conducted with oxygen and with neon [262].) This adds the sX hydrate to the list of nitrogen hydrate and the name nitrogen hydrate V (NH-V) was proposed for this structure.

The overall structure for sX is supported by experimental data as well as by DFT calculations and was shown to be in the space group $P6_122$ (or $P6_522$) with lattice parameters $a = 6.240(3)$ Å and $b = 6.065(2)$ Å. However, the nitrogen sX dissociation pathway still needs more attention; it was found that the NH-V hydrate - upon heating under pressure - undergoes transformations according to Ostwald's step rule.

$$\text{NH-V} \longrightarrow \text{NH-II} \longrightarrow \text{NH-VI} \longrightarrow \text{NH-I}$$

First, at 160 K, NH-II (sH) is formed; this nitrogen clathrate has been observed before, albeit at pressures above 0.85 GPa. NH-II then, at 205 K, transforms into a new - so far unobserved structure. The name NH-VI for this structure was proposed. It was possible to index the diffraction pattern with the sIII structure so far only observed in Br_2 hydrate [300]. A Rietveld refinement (with the atom positions fixed) also matched the respective peak intensities with the recorded pattern. However, this result should not be over-interpreted as the diffraction pattern itself was of a meager quality and sIII has the largest of all unit cells for hydrates. A further study could shed light on the exact filling ratios during the decomposition as well as on the structure of NH-VI. For this, an X-ray study might prove more useful than a neutron diffraction study as it simplifies the diffraction pattern, i.e. a simpler pattern without information of the hydrogen positions.

Furthermore, the universality of the sX host network raises the interesting possibility that also other guest-molecules could be found to form this structure; so far H_2, Ne, CO_2, O_2 and N_2 have been reported. Other candidates are the other noble gases and small clathrate formers such as CO, NO_x, or SO_2.

Ammonia Monohydrate and the Ternary Ammonia-Methane-Water System
Amongst the known ammonia monohydrates, two have not been characterised from a structural point of view - ammonia monohydrate III and ammonia monohydrate IV. In this work a possible structure based on neutron diffraction and DFT calculations is presented.

In brief, ammonia monohydrate (AMH-I) was cryo-loaded into a PE-press, and compressed at 170 K. Diffraction data were collected at 170 K after compression to 3-5 GPa; no pressure marker was used to avoid any parasitic peaks in the collected pattern and hence, the exact pressure is not known.

The initial indexing of the broad diffraction peaks led to the large number of 108 possible unit cells were indexed (for unit cell volumes up to 400 $Å^3$). LeBail-intensity extractions and Monte-Carlo Simulated-Annealing (MCSA) for the respective cell resulted in 6 possible structure candidates that fitted the data adequately. The MCSA procedure used rigid bodies of NH_3 and H_2O and the obtained structures were further refined using the Rietveld method.

Of the structures, the most plausible one was found in the $P2_1/c$ space group and has the lattice parameters $a = 5.487(3)$ Å, $b = 19.068(4)$ Å, $c = 5.989(3)$ Å, and $\beta = 99.537(16)^o$. As the data quality was too meager for a definitive structure solution, additionally DFT calculations were performed and the structure presented here, was stable against geometry optimisation; to further verify that the structure is plausible, phonon calculations were carried out at the Γ-point, and resulted in real phonon frequencies only. However, the structure revealed a high formation enthalpy relative to other ammonia monohydrate phases which could indicate its metastability or a wrong unit cell.

To address the concerns of a possibly wrong structure, an X-ray diffraction study would prove helpful. A diffraction pattern with less information, i.e. without any information of the hydrogen positions, would simplify the search for a suitable unit cell. Furthermore, a structure based on X-ray data is not affected by any hydrogen-disorder. Such an X-ray study should also include a further investigation of the phase diagram of ammonia monohydrate. To that end, a 1:1 stochiometric mixture of water and ammonia should be compressed at 220-230 K from < 1 GPa to 5 GPa. This path takes the sample from the melt via AMH-III into the stability region of AMH-IV. Three results could be obtained from this experiment; first, an X-ray diffraction pattern of AMH-IV would shed light on the validity of the above presented results; second, the exact transition of AMH-III to AMH-IV could be studied; third, a diffraction pattern of AMH-III could be obtained with the goal to reveal the structure of this polymorph of ammonia monohydrate as well.
The Exreme Conditions Beamline (ECB, P02.2) at the Deutsches Elektronen-Synchrotron (DESY) would be suitable for this study, and a proposal for the outlined experiment is currently in preparation.

While most research is carried out on binary mixtures of water-ammonia and water-methane, in the outer planets, usually a ternary mixture is present. Hence, a study on the ternary mixture of ammonia, water, and methane was carried out and presented here. The aim was to measure the melting curve of the ternary and to verify or falsify the claimed increase of the melting temperature of methane hydrate in the presence of ammonia [62] and second, to look for evidence of incorporation of ammonia into the hydrate lattice.

In brief, a 1:1 mixture of ammonia hemihydrate (AHH) and methane hydrate I (MH-I) was cryo-loaded into a PE-press (together with a Pb pressure marker). The sample was pressurised in steps to 1.6 GPa; after every pressure step the sample was heated to the melt and then allowed to re-crystallise. No evidence of an increase in the melting behaviour of MH-II in the presence of ammonia was found, however, four novel reflections in the diffraction pattern were observed after recrystallising the sample at 1.6 GPa. These peaks do not fit any of the known crystal structures of the ammonia hydrates or the methane hydrates.

This evidence gives credence to the existence of a ternary crystal structure in the ammonia-methane-water system at elevated pressures. The exact structure could not be determined, however, two possible explanations are the incorporation of ammonia into the water network of methane hydrate or the formation of a completely new crystal structure. As a starting point, a Raman study of the hydrogenous and deuterated ternary in the pressure range up to 10 GPa is currently planned. While this might help to determine any possible deuteration effects and add more data points to the melting curve only diffraction experiments will be able to explain the four observed peaks. Thus, a combined X-ray and neutron diffraction study to investigate the appearance of the new peaks should be carried out in the future.

Carbonic Acid Monohydrate

In the last chapter of this work an attempt was made to synthesise carbonic acid monohydrate and study its crystal structure and in particular to measure the positions of hydrogen (deuterium) atoms in the crystal structure; while a structure for (hydrogenous) carbonic acid monohydrate has been published based on X-ray diffraction by Abramson *et al.* in 2008 [302], this publication lacks measured hydrogen positions due to the inherent nature of X-ray diffraction.

In a first attempt, it was possible to reproduce Abramson *et al.*'s measurements successfully in a diamond anvil cell using a deuterated sample. However, a similar experiment in a Paris-Edinburgh Press - with the aim to obtain a diffraction pattern - remained unsuccessful. Diffraction data was recorded in the published stability region of carbonic acid monohydrate, but no reflections associated with $D_2CO_3 \cdot D_2O$ could be identified.

An investigating why $D_2CO_3 \cdot D_2O$ did not form in the PE-press led to the conclusion that the gasket material most likely reacted with the sample according to

$$2\ D_2CO_3 + Ti \rightarrow Ti(CO_3)_2 + 2\ D_2 \quad \text{and/or}$$
$$2\ D_2CO_3 + Zr \rightarrow Zr(CO_3)_2 + 2\ D_2.$$

As it was not possible to obtain a diffraction pattern of $D_2CO_3 \cdot D_2O$, and hence to obtain the hydrogen/deuterium positions in its crystal structure, further experiments are necessary in the future. To avoid a reaction with the gasket material, they should be carried out in a large-volume DAC suitable for neutron diffraction using a rhenium gasket.

A Final Remark

Once again I would like to thank my supervisors, Dr John Loveday and Dr Malcolm Guthrie, and all my collaborators and colleagues for their support. Thank you!

Bibliography

[1] B. Massani, L. J. Conway, A. Hermann, and J. Loveday. On a new nitrogen sX hydrate from ice XVII. *Journal of Chemical Physics*, 151:104305, 2019.

[2] B. Massani, J. S. Loveday, J. J. Molaison, A. M. dos Santos, X. P. Wang, L. L. Daemen, B. Haberl, R. Boehler, and M. Guthrie. On single-crystal neutron-diffraction in DACs: quantitative structure refinement of light elements on SNAP and TOPAZ. *High Pressure Research*, pages 1–19, 05 2020.

[3] B. Massani, C. G. Pruteanu, L. J. Conway, V. N. Robinson, A. Hermann, and J. S. Loveday. Ammonia mono hydrate iv: An attempted structure solution. *Crystals*, 12(2), 2022.

[4] R. L. Mills and E. R. Grilly. Melting curves of H_2, D_2, and T_2 up to 3500 kg/cm^2. *Physical Review*, 101(4):1246–1247, 1956.

[5] V. Kechin. Melting curve equations at high pressure. *Physical Review B*, 65(5):1–4, 2001.

[6] P. Dalladay-Simpson, R. T. Howie, and E. Gregoryanz. Evidence for a new phase of dense hydrogen above 325 gigapascals. *Nature*, 529(7584):63–67, 2016.

[7] I. F. Silvera and R. J. Wijngaarden. New low-temperature phase of molecular deuterium at ultrahigh pressure. *Physical Review Letters*, 47(1):39–42, 1981.

[8] H. Mao and R. J. Hemley. Ultrahigh-pressure transitions in Solid Hydrogen. *Reviews of Modern Physics*, 66(2):671–692, 1994.

[9] L. Cui, N. H. Chen, S. J. Jeon, and I. F. Silvera. Megabar pressure triple point in solid deuterium. *Physical Review Letters*, 72(19):3048–3051, 1994.

[10] C. J. Pickard and R. J. Needs. Structure of phase III of solid hydrogen. *Nature Physics*, 3(7):473–476, 2007.

[11] C. J. Pickard, M. Martinez-Canales, and R. J. Needs. Density functional theory study of phase IV of solid hydrogen. *Physical Review B*, 85(21):214114, 2012.

[12] G. E. Walrafen. Raman spectral studies on water structure. *Journal of Chemical Physics*, 40:3249–3256, 1964.

[13] A. N. Dunaeva, D. V. Antsyshkin, and O. L. Kuskov. Phase diagram of H_2O: Thermodynamic functions of the phase transitions of high-pressure ices. *Solar System Research*, 44(3):202–222, 2010.

[14] P. W. Bridgman. Water in the Liquid and Five Solid Forms under Pressure. *Proceedings of the American Academy of Arts and Sciences*, 47(13):441–558, 1911.

[15] O. Grasset. Calibration of the R ruby fluorescence lines in the pressure range [0-1 GPa] and the temperature range [250-300 K]. *High Pressure Research*, 21(3-4):139–157, 2001.

[16] Grasset, O. and et al. Pressure measurements within optical cells using diamond sensors: Accuracy of the method below 1 GPa. *High Pressure Research*, 25(4):255–265, 2005.

[17] I. Chou and J. G. Blank and A. F. Goncharov and H. Mao and R. J. Hemley. In situ Observations of a High Pressure Phase of H_2O. *Science*, 281:809–811, 1998.

[18] C. W. F. T. Pistorius, M. C. Pistorius, J. P. Blakey, and L. J. Admiraal. Melting curve of ice VII to 200 kbar. *Journal of Chemical Physics*, 38(3):600–602, 1963.

[19] O. Mishima and S. Endo. Melting curve of ice vii. *Journal of Chemical Physics*, 68:4417–4418, 1978.

[20] Y. Fei, H. Mao, and R. J. Hemley. Thermal expansivity, bulk modulus, and melting curve of H_2O-ice VII to 20 GPa. *Journal of Chemical Physics*, 99(7):5369–5373, 1993.

[21] F. Datchi, P. Loubeyre, and R. LeToullec. Extended and accurate determination of the melting curves of argon, helium, ice (H_2O), and hydrogen (H_2). *Physical Review B*, 61(10):6535–6546, 2000.

[22] N. Dubrovinskaia and L. Dubrovinsky. Whole-cell heater for the diamond anvil cell. *Review of Scientific Instruments*, 74(7):3433–3437, 2003.

[23] R. Frank, Y. Fei, and J. Hu. Constraining the equation of state of fluid H_2O to 80 GPa using the melting curve, bulk modulus, and thermal expansivity of Ice VII. *Geochimica et Cosmochimica Acta*, 68(13):2781–2790, 2004.

[24] B. Schwager, L. Chudinovskikh, A. Gavriliuk, and R. Boehler. Melting curve of H_2O to 90 GPa measured in a laser-heated diamond cell. *Journal of Physics Condensed Matter*, 16(14):1177–1179, 2004.

[25] B. Schwager and R. Boehler. H_2O: another ice phase and its melting curve. *High Pressure Research*, 28(3):431–433, 2008.

[26] G. S. Kell and E. Whalley. Equilibrium line between ice I and III. *Journal of Chemical Physics*, 48(5):2359–2361, 1968.

[27] A. J. Leadbetter, R. C. Ward, J. W. Clark, P. A. Tucker, T. Matsuo, and H. Suga. The equilibrium low-temperature structure of ice. *Journal of Chemical Physics*, 82(1):424–428, 1985.

[28] C. M. B. Line and R. W. Whitworth. A high resolution neutron powder diffraction study of D_2O ice XI. *Journal of Chemical Physics*, 104(24):10008–10013, 1996.

[29] W. B. Durham, H. C. Heard, and S. H. Kirby. Experimental Deformation of Polycrystalline H_20 Ice at High Pressure and Low Temperature: Preliminary Results. *Journal of Geophysical Research*, 88(Supplement):B377–B392, 1983.

[30] A. J. Brown and E. Whalley. Preliminary Investigation of the Phase Boundaries between Ice VI and VII and Ice VI and VIII. *Journal of Chemical Physics*, 45:4360–4361, 1966.

[31] C. W. F. T. Pistorius, E. Rapoport, and J. B. Clark. Phase Diagrams of H_2O and D_2O at High Pressures. *Journal of Chemical Physics*, 48(12):5509–5514, 1968.

[32] G. P. Johari. Dielectric properties of ice VII and VIII and the phase boundary between ice VI and VII. *Journal of Chemical Physics*, 61(10):4292, 1974.

[33] P. W. Bridgman. The Phase Diagram of Water to 45,000 kg/cm^2. *Journal of Chemical Physics*, 5(12):964–966, 1937.

[34] M. Song, H. Yamawaki, H. Fujihisa, M. Sakashita, and K. Aoki. Infrared observation of the phase transitions of ice at low temperatures and pressures up to 50 GPa and the metastability of low-temperature ice VII. *Physical Review B - Condensed Matter and Materials Physics*, 68(2), 2003.

[35] A. F. Goncharov, V. V. Struzhkin, H. Mao, and R. J. Hemley. Raman Spectroscopy of Dense H_2O and the Transition to Symmetric Hydrogen Bonds. *Physical Review Letters*, 83(10):1998–2001, 1999.

[36] C. G. Salzmann, G. Radaelli, E. Mayer, and J. L. Finney. Ice XV: A new thermodynamically stable phase of ice. *Physical Review Letters*, 103(10):1–4, 2009.

[37] T. M. Gasser, A. V. Thoeny, L. J. Plaga, K. W. Koester, M. Etter, R. Boehmer, and T. Loerting. Experiments indicating a second hydrogen ordered phase of ice VI. *Chemical Science*, 7(1):1–11, 2018.

[38] J. S. Loveday and R. J. Nelmes. High-pressure gas hydrates. *Physical Chemistry Chemical Physics*, 10(7):937–950, 2008.

[39] B. Massani, C. Mitterdorfer, and T. Loerting. Formation and decomposition of CO_2-filled ice. *Journal of Chemical Physics*, 147(13):134503, 2017.

[40] K. A. Lokshin, Y. Zhao, D. He, W. L. Mao, H. Mao, R. J. Hemley, M. V. Lobanov, and M. Greenblatt. Structure and dynamics of hydrogen molecules in the novel clathrate hydrate by high pressure neutron diffraction. *Physical Review Letters*, 93(12):1–4, 2004.

[41] M. E. Donnelly. *Neutron Diffraction of Hydrogen Inclusion Comounds Under Pressure*. PhD thesis, University of Edinburgh, Edinburgh, 2016.

[42] J. S. Loveday, R. J. Nelmes, M. Guthrie, S. A. Belmonte, D. R. Allan, D. D. Klug, J. S. Tse, and Y. P. Handa. Stable methane hydrate above 2 GPa and the source of Titan's atmospheric methane. *Nature*, 410(6829):661–663, 2001.

[43] A. D. Fortes, I. G. Wood, M. Alfredsson, L. Vocadlo, K. S. Knight, W. G. Marshall, M. G. Tucker, and F. Fernandez-Alonso. The high-pressure phase diagram of ammonia dihydrate. *High Pressure Research*, 27(2):201–212, 2007.

[44] A. D. Fortes, G. I. G. Griffiths, C. J. Pickard, and R. J. Needs. Crystal Structure of Ammonia Monohydrate Phase II. *Journal of Chemical Physics*, 136(17):13508–13515, 2009.

[45] J. S. Loveday and R. J. Nelmes. Ammonia monohydrate VI: A hydrogen-bonded molecular alloy. *Physical Review Letters*, 83(21):4329–4332, 1999.

[46] C. W. Wilson, C. L. Bull, G. W. Stinton, D. M. Amos, M. E. Donnelly, and J. S. Loveday. On the stability of the disordered molecular alloy phase of ammonia hemihydrate. *Journal of Chemical Physics*, 142(9), 2015.

[47] G. I. G. Griffiths, A. D. Fortes, C. J. Pickard, and R. J. Needs. Crystal structure of ammonia dihydrate II. *Journal of Chemical Physics*, 136(174512), 2012.

[48] A. Bravais. Mémoire sur les systèmes formés par les points distribués régulièrement sur un plan ou dans l'espace. *J. École Polytech.*, (19):1—-128, 1850.

[49] M. Guthrie, R. Boehler, C. A. Tulk, J. J. Molaison, A. M. dos Santos, K. Li, and R. J. Hemley. Neutron diffraction observations of interstitial protons in dense ice. *PNAS*, 110(26):10552–10556, 2013.

[50] W. G. Thomason. The ISIS Spallation Neutron and Muon Source — The first thirty-three years. *Nuclear Instruments and Methods in Physics Research Section A: Accelerators, Spectrometers, Detectors and Associated Equipment*, 917:61–67, 2019.

[51] ISIS neutron scattering facility. High pressure gas cells, *www.isis.stfc.ac.uk/Pages/How-ISIS-works–in-depth.aspx*, 2020.

[52] Rutherford Appelton Laboratories. How ISIS works, *www.isis.stfc.ac.uk/Pages/How-ISIS-works–in-depth.aspx*, 2018.

[53] Dan Amos. *High Pressure Hydrates of CO2 & Materials for Carbon Storage*. PhD thesis, School for Physics and Astronomy, The University of Edinburgh, Edinburgh, July 2015.

[54] H. Mao, J. Xu, and P. M. Bell. Calibration of the ruby pressure gauge to 800 kbar under quasi-hydrostatic conditions. *Journal of Geophysical Research*, 91(B5):4673, 1986.

[55] W. F. Kuhs, J. L. Finney, C. Vettier, and D. V. Bliss. Structure and hydrogen ordering in ices VI , VII , and VIII by neutron powder diffraction. *Journal of Chemical Physics*, 3612(81):3612–3623, 1984.

[56] A. D. Fortes, I. G. Wood, L. Vočadlo, K. S. Knight, W. G. Marshall, M. G. Tucker, and F. Fernandez-Alonso. Phase behaviour and thermoelastic properties of perdeuterated ammonia hydrate and ice polymorphs from 0 to 2 GPa. *Journal of Applied Crystallography*, 42(5):846–866, 2009.

[57] J. S. Loveday and R. J. Nelmes. The ammonia hydrates - Model mixed-hydrogen-bonded systems. *High Pressure Research*, 24(1):45–55, 2004.

[58] C. W. Wilson, C. L. Bull, G. Stinton, and J. S. Loveday. Pressure-induced dehydration and the structure of ammonia hemihydrate-II. *Journal of Chemical Physics*, 136(9):094506, 2012.

[59] W. F. Kuhs, D. K. Staykova, and A. N.Salamatin. Formation of methane hydrate from polydisperse ice powders. *Journal of Physical Chemistry B*, 110(26):13283–13295, 2006.

[60] A. Kurnosov, L. Dubrovinsky, A. Kuznetsov, and V. Dmitriev. High-pressure/high-temperature behavior of the methane-ammonia-water system up to 3 GPa. *Zeitschrift fur Naturforschung B*, 61(12):1573–1576, 2006.

[61] L. Bezacier, G. Tobie, O. Bollengier, O. Grasset, E. Le Menn, and A. Oancea. Dissociation temperatures of methane hydrates at high pressure : Implications for the differentiation of Titan's interior. *EPSC Abstracts*, 6(259285):6–7, 2013.

[62] L. Bezacier, B. Journaux, J. P. Perrillat, H. Cardon, M Hanfland, and I. Daniel. Equations of state of ice VI and ice VII at high pressure and high temperature. *Journal of Chemical Physics*, 141(10):104505, 2014.

[63] H. Kadobayashi, H. Hirai, K. MacHita, H. Ohfuji, M. Muraoka, S. Yoshida, and Y. Yamamoto. High-pressure phase transition of methane hydrate in water-methane-ammonia system. *Journal of Physics: Conference Series*, 1609(1):18–24, 2020.

[64] H. Kadobayashi, H. Hirai, H. Ohfuji, H. Kawamura, M. Muraoka, S. Yoshida, and Y. Yamamoto. Effect of ammonia on methane hydrate stability under high-pressure and high-temperature conditions. *Journal of Physical Chemistry A*, 124(51):10890–10896, 2020.

[65] M. Choukroun, O. Grasset, G. Tobie, and C. Sotin. Stability of methane clathrate hydrates under pressure: Influence on outgassing processes of methane on Titan. *Icarus*, 205:581–593, 2010.

[66] Y. A. Dyadin, E. Y. Aladko, and E. G. Larionov. Decomposition of methane hydrates up to 15 kbar. *Mendeleev Communications*, 7(1):34–35, 1997.

[67] H. Hirai and K. Komatsu and M. Honda and T. Kawamura and Y. Yamamoto and T. Yagi. Phase changes of CO_2 hydrate under high pressure and low temperature. *Journal of Chemical Physics*, 133(12):124511, 2010.

[68] E. H. Abramson, O. Bollengier, and J. M. Brown. Water-carbon dioxide solid phase equilibria at pressures above 4 GPa. *Scientific Reports*, 7(1):1–6, 2017.

[69] K. P. C. Vollhardt and N. E. Schore. *Organische Chemie*. W.H. Freeman and Company, New York, 6 edition, 2011.

[70] E. D. Sloan and C. A. Koh. *Clathrate Hydrates of Natural Gases*. CRC Press, Boca Raton, London, New York, third edition edition, 2007.

[71] J. A. Ripmeester, J. S. Tse, C. I. Ratcliffe, and B. M. Powell. A new clathrate hydrate structure. *Nature*, 325(6100):135–136, 1987.

[72] L. Yang, C. A. Tulk, D. D. Klug, I. L. Moudrakovski, C. I. Ratcliffe, J. A. Ripmeester, B. C. Chakoumakos, L. Ehm, C. D. Martin, and J. B. Parise. Synthesis and characterization of a new structure of gas hydrate. *PNAS*, 106(15):6060–6064, 2009.

[73] N.J. Carron. *An Introduction to the Passage of Energetic Particles Through Matter*. CRC Press, Boca Raton, London, New York, 1 edition, 2006.

[74] H. E. Suess and H. C. Urey. Abundance of the Elements. *Reviews of Modern Physics*, 28(1):53–74, 1956.

[75] D. Prialnik. *An Introduction to the Theory of Stellar Structure and Evolution*. Camebridge University Press, Camebridge, 2 edition, 2009.

[76] J. M. Berg, J. L. Tymoczko, and L. Stryer. *Biochemistry*. W. H. Freeman, Oxford, New York, 5 edition, 2002.

[77] E. Sloan and C. Koh. *Clathrate Hydrates of Natural Gases*. CRC Press, 3rd edition, 2008.

[78] I. Goncharenko and P. Loubeyre. Neutron and x-ray diffraction study of the broken symmetry phase transition in solid deuterium. *Nature*, 435:1206–1209, 2005.

[79] C. Cavazzoni, G. L. Chiarotti, S. Scandolo, E. Tosatti, M. Bernasconi, and M. Parrinello. Superionic and Metallic States of Water and Ammonia at Giant Planet Conditions. *Science*, 283:44–46, 1999.

[80] M. Millot, S. Hamel, J. R. Rygg, P. M. Celliers, G. T. W. Collins, F. Coppari, D. E. Fratanduono, R. Jeanloz, D. C. Swift, and J. H. Eggert. Experimental evidence for superionic water ice using shock compression. *Nature Physics*, (14):297–302, 2018.

[81] T. Guillot. The Interior of Gas Planets: Models and Outstanding Questions. *Annual Review of Earth and Planetary Sciences*, 33:493–530, 2005.

[82] R. Helled, J. D. Anderson, M. Podolak, and G. Schubert. Interior models of Uranus and Neptune. *Astrophysical Journal*, 726(1):15, 2011.

[83] W. B. Hubbard. Neptune's Deep Chemistry. *Science*, 275:1279–1280, 1997.

[84] J. S. Loveday and R. J. Nelmes. High-pressure neutron diffraction and models of Titan. *High Pressure Research*, 7959, 2003.

[85] G. Tobie, O. Grasset, J. I. Lunine, A. Mocquet, and C. Sotin. Titan's internal structure inferred from a coupled thermal-orbital model. *Icarus*, 175:496–502, 2005.

[86] K. Shin, R. Kumar, K. A. Udachin, S. Alavi, and J. A. Ripmeester. Ammonia clathrate hydrates as new solid phases for Titan, Enceladus, and other planetary systems. *PNAS*, 109(37):14785–14790, 2012.

[87] I. F. Silvera. The solid molecular hydrogens in the condensed phase: Fundamentals and static properties. *Rieview of Modern Physics*, 52(2):393–452, 1980.

[88] L. Cui, N. H. Chen, and I. F. Silvera. Excitations, order parameters, and phase diagram of solid deuterium at megabar pressures. *Physical Review B*, 51(21):14987–14997, 1995.

[89] H. Mao and R. Hemley. Ultrahigh transitions in solid hydrogen. *Reviews of Modern Physics*, 66(2):671–692, 2001.

[90] G. Geneste and M. Torrent and P. Loubeyre. Strong Isotopic Effect in Phase II of Dense Solid Hydrogen and Deuterium. *Physical Review Letters*, (109):155303, 2012.

[91] D. Duang, Y. Liu, F. Tian, D. Li, X. Huang, Z. Zhao, H. Yu, B. Liu, W.Tian, and T. Cui. Pressure-induced Metallization of Dense $(H_2S)_2H_2$ with High-T_c Superconductivity. *Scientific Reports*, 4(6968):30–32, 2014.

[92] A. P. Drozdov, M. I. Eremets, I. A. Troyan, V. Ksenofontov, and S. I. Shylin. Conventional superconductivity at 203 kelvin at high pressures in the sulfur hydride system. *Nature*, (525):73–76, 2015.

[93] Ge Yanfeng, Fan Zhang, and Yao Yugui. First-principles demonstration of superconductivity at 280 K in hydrogen sulfide with low phosphorus substitution. *Physical Review B*, (93):224513, 2016.

[94] M. Somayazulu, M. Ahart, A. K. Mishra, Z. M. Geballe, M. Baldini, Y. Meng, V. Struzhkin, and R. J. Hemley. Evidence for superconductivity above 260 k in lanthanum superhydride at megabar pressures. *Phys. Rev. Lett.*, 122:027001, Jan 2019.

[95] G. Yanfeng, F. Zhang, and R. J. Hemley. Room-temperature superconductivity in boron- and nitrogen-doped lanthanum superhydride. *Phys. Rev. B*, 104(214505), 2021.

[96] E. Snider, N. Dasenbrock-Gammon, R. McBride, M. Debessai, H. Vindana, K. Vencatasamy, K. Lawler, A. Salamat, and R. P. Dias. Room-temperature superconductivity in a carbonaceous sulfur hydride. *Nature*, 586(1):373–377, 2020.

[97] L. Gao, Y. Xue, F. Chen, Q. Xiong, R. L. Meng, D. Ramirez, C. W. Chu, J. H. Eggert, and H. K. Mao. Superconductivity up to 164 K in $HgBa_2Ca_{m-1}Cu_mO_{2m+2+\delta}$ (m=1, 2, and 3) under quasihydrostatic pressures. *Physical Review B*, 50(6):4260–4263, 1994.

[98] X. Chen, V. Struzhkin, Y. Yu, A. F. Goncharov, C. Lin, H. Mao, and R. J. Hemley. Enhancement of superconductivity by pressure-driven competition in electronic order. *Nature*, 466(7309):950–953, 2010.

[99] L. Pauling. The Structure and Entropy of Ice and of Other Crystals with Some Randomness of Atomic Arrangement. *Journal of the American Chemical Society*, 57(12):2680–2684, 1935.

[100] E. O. Wollan, W. L. Davidson, and C. G. Shull. Neutron Diffraction Study of the Structure of Ice. *Physical Review*, 75:1348–1352, 1949.

[101] J. van Kranendonk. *Solid Hydrogen - Theory of the Properties of Solid H_2, HD, and D_2*. Plenum Press, New York and London, 1983.

[102] I. Langmuir. The Dissociation of Hydrogen into Atoms. Calculation of the Degree of Dissociation and the Heat of Formation. *Journal of the American Chemical Society*, 37:417–458, 1915.

[103] E. Wigner and H. B. Huntington. On the Possibility of a Metallic Modification of Hydrogen. *Journal of Chemical Physics*, 3(12):764–770, 1935.

[104] N. W. Ashcroft. Metallic Hydrogen: A High-Temperature Superconductor? *Physical Review Letters*, 21(1748), 1968.

[105] E. Babaev and A. Sudbo and N. W. Ashcroft. A superconductor to superfluid phase transition in liquid metallic hydrogen. *Nature*, 431:666–668, 2004.

[106] Eugene Gregoryanz, Alexander F. Goncharov, Kiyoto Matsuishi, Ho-kwang Mao, and Russell J. Hemley. Raman Spectroscopy of Hot Dense Hydrogen. *Physical Review Letters*, 90(17):175701, 2003.

[107] R. T. Howie, P. Dalladay-Simpson, and E. Gregoryanz. Raman spectroscopy of hot hydrogen above 200 GPa. *Nature Materials*, 14(5):495–499, 2015.

[108] I. Mazin, R. Hemley, A. Goncharov, M. Hanfland, and H. Mao. Quantum and Classical Orientational Ordering in Solid Hydrogen. *Physical Review Letters*, 78(6):1066–1069, 1997.

[109] A. F. Goncharov, R. J. Hemley, and H. Mao. Vibron frequencies of solid H_2 and D_2 to 200 GPa and implications for the P-T phase diagram. *Journal of Chemical Physics*, 134(17):174501, 2011.

[110] V. P. Glazkov, S. P. Besedin, I. N. Goncharenko, A. V. Irdova, I. N. Makarenko, V.A. Somenkov, S. M. Stishov, and S. S. Shilshtein. Neutron-diffraction study of the EOS of molecular deuterium at high pressures. *Journal of Experimental and Theoretical Physics Letters*, 47(12):763–766, 1988.

[111] P. Loubeyre, R. LeToullec, D. Hausermann, M. Hanfland M., R. J. Hemley, H. K. Mao, and L. W. Finger. X-ray diffraction and EOS of hydrogen at megabar pressures. *Nature*, 383:702–704, 1996.

[112] A. F. Goncharov, N. Goldman, L. E. Fried, J. C. Crowhurst, I. F. W. Kuo, C. J. Mundy, and J. M. Zaug. Dynamic Ionization of Water under Extreme Conditions. *Physical Review Letters*, 94(12):1–4, 2005.

[113] R. T. Howie, C. L. Guillaume, T. Scheler, A. F. Goncharov, and E. Gregoryanz. Mixed molecular and atomic phase of dense hydrogen. *Physical Review Letters*, 108(12):1–5, 2012.

[114] R. T. Howie, T. Scheler, C. L. Guillaume, and E. Gregoryanz. Proton tunneling in phase IV of hydrogen and deuterium. *Physical Review B*, 86(21):3–8, 2012.

[115] M. I. Eremets, I. A. Troyan, and A. P. Drozdov. Low temperature phase diagram of hydrogen at pressures up to 380 GPa. A possible metallic phase at 360 GPa and 200 K. 2016.

[116] R. Dias, O. Noked, and I. F. Silvera. New low temperature phase in dense hydrogen: The phase diagram to 421 GPa. 2016.

[117] R. P. Dias and I. F. Silvera. Observation of the Wigner-Huntington transition to metallic hydrogen. *Science*, 1579(36):1–10, 2017.

[118] C. E. Mortimer and U. Mueller. *Chemie - Das Basiswissen der Chemie*. Thieme Georg Verlag, 15 edition, 2015.

[119] S. Zumdahl. *Encyclopedia Britannica*. Encyclopedia Britannica Online, 2016.

[120] J. Finney. *Water: A very short introduction*. Oxford University Press, 2015.

[121] L. Pauling. The nature of the chemical bond. iv. the energy of single bonds and the relative electronegativity of atoms. *Journal of the American Chemical Society*, 54:3570–3782, 1932.

[122] A. L. Allred and E. G. Rochow. A scale of electronegativity based on electrostatic force. *Journal of Inorganic and Nuclear Chemistry*, 5:264, 1958.

[123] P. W. Atkins and J. dePaula. *Physical Chemistry*. Wiley-VCH, 2006.

[124] R. C. Weast. *Handbook of Chemistry and Physics*. CRC Press, 1987.

[125] T. Bartels-Rausch, J. H. E. Cartwright, B. Escribano, J. L. Finney, H. Grothe, P. J. Gutierrez, J. Haapala, and W. F. Kuhs. Ice structures, patterns, and processes: A view across the ice fields. *Reviews of Modern Physics*, 84:885–944, 2012.

[126] J. D. Bernal and R. H. Fowler. A theory of water and ionic solution, with particular reference to hydrogen and hydroxyl ions. *Journal of Chemical Physics*, 1:515–548, 1933.

[127] M. Faraday. Experimental research in chemisty and physics. *Journal of the Royal Institution*, 1:85–89, 1859.

[128] S. Gao. Investigation of interactions between gas hydrates and several other flow assurance elements. *Energy Fuels*, 22:3150–3153, 2008.

[129] K. Kvenvolden. A review of the geochemistry of methane in natural gas hydrate. *Organic Geochemistry*, 23:997–1008, 1995.

[130] D. Mahajan, C. E. Taylor, and G. A. Mansoori. An introduction to natural gas hydrate/clathrate: The major organic carbon reserve of the earth. *Journal of Petroleum Science and Engineering*, 56(1-3):1–8, 2007.

[131] B. Buffett and D. Archer. Global inventory of methane clathrate: sensitivity to changes in the deep ocean. *Earth and Planetary Science Letters*, 227:185–199, 2004.

[132] B. A. Buffett. Clathrate hydrates. *Annual Review of Earth and Planetary Sciences*, 28:477–507, 2000.

[133] R. Pellenbarg and M. Max. Gas hydrates: From laboratory curiosity to potential global powerhouse. *Journal of Chemical Education*, 78:7, 2001.

[134] J. Cejka. *Metal-Organic Frameworks Applications from Catalysis to Gas Storage*. Wiley-VCH, Weinheim, Germany, 1 edition, 2011.

[135] J. P. Poirier, C. Sotin, and J. Pyronneau. Viscosity of high-pressure ice VI and evolution and dynamics of Ganymede. *Nature*, 292:225 – 227, 1981.

[136] U. Marboeuf, O. Mousis, J.-M. Petit, B. Schmitt, and H. A. Weaver. On the stability of clathrate hydrates in comets 67P/Churyumov-Gerasimenko and 46P/Wirtanen. *Planets and planetary systems*, 525:4, 2010.

[137] U. Marboeuf, O. Mousis, D. Ehrenreich, Y. Alibert, and A. Cassan. Composition of ices in low-mass extrasolar planets. *Astrophysical Journal*, 2008.

[138] L. E. Senft and S. T. Stewart. Impacts onto H_2O ice: Scaling laws for melting, vaporization, excavation, and final crater size. *Icarus*, 214:724–738, 2011.

[139] K. W. Allen and G. A. Jeffrey. On the structure of bromine hydrate. *Journal of Chemical Physics*, 38(9):2304–2305, 1963.

[140] H. Nakayama, D. D. Klug, C. I. Ratcliffe, and J. A. Ripmeester. Ordering and clathrate hydrate formation in co-deposits of xenon and water at low temperatures. *Chemistry – A European Journal*, 9(13):2969–2973, 2003.

[141] J. A. Ripmeester, L. Ding, and D. D. Klug. A clathrate hydrate of formaldehyde. *Journal of Physical Chemistry B*, 100(32):13330–13332, 1996.

[142] D. Blake, L. Allamandola, S. Sandford, D. Hudgins, and F. Freund. Clathrate hydrate formation in amorphous cometary ice analogs *in vacuo*. *Science*, 254(5031):548–551, 1991.

[143] A. Hallbrucker and E. Mayer. Unexpectedly stable clathrate hydrates formed from microporous vapor-deposited amorphous solid water at low "external" guest pressures and their astrophysical implications. *Icarus*, 90(1):176–180, 1991.

[144] S. Takeya, A. Hori, T. Hondoh, and T. Udachin. In Situ Observation of CO_2 Hydrate by X-ray Diffraction. *Journal of Physical Chemistry B*, 10:973–982, 2000.

[145] R. Sakemoto, H. Sakamoto, K. Shiraiwa, R. Ohmura, and T. Uchida. Clathrate hydrate crystal growth at the seawater/hydrophobic-guest-liquid interface. *Crystal Growth & Design*, 9:1296–1300, 2010.

[146] K. Saito, M. Kishimoto, R. Tanaka, and R. Ohmura. Crystal growth of clathrate hydrate in liquid water saturated with a simulated natural gas. *Crystal Growth & Design*, 11:295–301, 2011.

[147] D. K. Staykova, W. F. Kuhs, A. N. Salamatin, and T. Hansen. Formation of porous gas hydrates from ice powders: Diffraction experiments and multistage model. *Journal of Physical Chemistry B*, 107:10299–10311, 2003.

[148] A. F. Goncharov V. V. Struzhkin Q. Z. Guo J. Z. Hu J. F. Shu R. J. Hemley M. Somayazulu W. L. Mao, H. K. Mao and Y. S. Zhao. Hydrogen clusters in clathrate hydrate. *Science*, 297(5590):2247–2249, 2002.

[149] A. Y. Manakov F. V. Zhurko T. V. Mikina V. Y. Komarov Y. A. Dyadin, E. Y. Aladko and E. V. Grachev. Clathrate formation in water-noble gas (hydrogen) systems at high pressures. *Journal of Structural Chemistry*, 40(5):790–795, 1999.

[150] A. Y. Manakov F. V. Zhurko E. Y. Aladko T. V. Mikina Y. A. Dyadin, E. G. Larionov and V. Y. Komarov. Clathrate hydrates of hydrogen and neon. *Mendeleev Communications*, 5:209–210, 1999.

[151] V. S. Efimchenko, M. A. Kuzovnikov, V. K. Fedotov, M. K. Sakharov, S. V. Simonov, and M. Tkacz. New phase in the water-hydrogen system. *Journal of Alloys and Compounds*, 509(SUPPL. 2):860–863, 2011.

[152] S. Du H. Xu S. C. Vogel J. Han T. C. Germann J. Zhang C. Jin J. S. Francisco X. Yu, J. Zhu and Y. Zhao. Crystal structure and encapsulation dynamics of ice ii-structured neon hydrate. *PNAS*, 111(29):10456–10461, 2014.

[153] C. Baerlocher, L. McCusker, and D. Olson. *Atlas of Zeolite Framework Types*. Elsevier, Amsterdam, 6 edition, 2007.

[154] D. M. Amos, M-E. Donnelly, P. Teeratchanan, C. L. Bull, A. Falenty, W. F. Kuhs, A. Hermann, and J. S. Loveday. A Chiral Gas–Hydrate Structure Common to the Carbon Dioxide–Water and Hydrogen–Water Systems. *Journal of Chemical Physics Letters*, pages 4295–4299, 2017.

[155] C. J. Pickard and R. J. Needs. Hypothetical low-energy chiral framework structure of group 14 elements. *Physical Review B*, 81(1):1–5, 2010.

[156] W. Blase and G. Cordier. $NaGaSn_5$, eine neue Zintl-Phase mit Ga-Sn-Schrauben. *Zeitschrift fuer Naturforschung B*, 43:1017–1019, 1988.

[157] S. Stegmaier, S. J. Kim, A. Henze, and T. F. Faessler. Tetrahedral framework structures: Polymorphic phase transition with reorientation of hexagonal helical channels in the Zintl compound Na_2ZnSn_5 and its relation to $Na_5Zn_{2+x}Sn_{10-x}$. *Journal of the American Chemical Society*, 135(29):10654–10663, 2013.

[158] G. S. Smirnov and V. V. Stegailov. Toward determination of the New Hydrogen Hydrate Clathrate Structures. *Journal of Physical Chemistry Letters*, 4:35603564, 2013.

[159] L. Del Rosso and M. Celli and L. Ulivi. New porous water ice metastable at atmospheric pressure obtained by emptying a hydrogen-filled ice. *Nature Communications*, 7:1–7, 2016.

[160] L. del Rosso, F. Grazzi, M. Celli, D. Colognesi, V. Garcia-Sakai, and L. Ulivi. Refined structure of metastable ice XVII from neutron diffraction measurements. *Journal of Chemical Physics C*, 120(47):26955–26959, 2016.

[161] R. J. Hemley W. L. Vos, L. W. Finger and H. K. Mao. Novel H_2-H_2O Clathrates at High-pressures. *Physical Review Letters*, 71(19):3150–3153, 1993.

[162] J. S. Loveday, R. J. Nelmes, and M. Guthrie. High-pressure transitions in methane hydrate. 350:459–465, 2005.

[163] A. Koumvakalis M. Nicol H. C. Cynn, S. Boone and D. J. Stevensons. Proceedings of the 19th Lunar and Planetary Science Conference. *Cambridge University Press/Lunar and Planetary Institute, 1989*, 1:433, 1989.

[164] J. I. Lunine and D. J. Stevenson. Clathrate and ammonia hydrates at high pressure: Application to the origin of methane on Titan. *Icarus*, 70(1):61–77, 1987.

[165] C. Giacovazzo, H.L. Monaco, D. Viterbo, F. Scordari, G. Gillli, G. Zanotti, and M. Catti. *Fundamentals of Crystallography*, volume 2. 1992.

[166] N. W. Ashcroft and N. D. Mermin. *Solid State Physics*. Brooks/Cole, Belmont, CA, USA, 1976.

[167] E. Wigner and F. Seitz. On the constitution of metallic sodium. *Phys. Rev.*, 43:804–810, May 1933.

[168] C. Giacovazzo, H. L. Monaco, D. Viterbo, F. Scordari, G. Gillli, G. Zanotti, and M. Catti. *Fundamentals of Crystallography*, volume 2. 1992.

[169] W. H. Bragg and W. L. Bragg. The Reflexion of X-rays by Crystals. *Proceedings of the Royal Society of London A*, (88):428—-438, 1913.

[170] P. P. Ewald. Die Berechnung optischer und elektrostatischer Gitterpotentiale. *Annalen der Physik*, (369):253—-287, 1921.

[171] P. P. Ewald. Introduction to the dynamical theory of X-ray diffraction. *Acta Crystallographica*, (25):103—108, 1969.

[172] P. Debye. Zerstreuung von Roentgenstrahlen. *Annalen der Physik*, (351):809—-823, 1915.

[173] P. Scherrer. Bestimmung der inneren Struktur und der Größe von Kolloidteilchen mittels Röntgenstrahlen. *Goettinger Nachrichten Gesellschaft*, (2):98, 1918.

[174] F. Close. *Particle Physics: A very brief introduction*. Oxford University Press, Oxford, New York, 5 edition, 2004.

[175] E. Fermi. Motion of neutrons in hydrogenous substances. *Ricerca Scientifica*, (7):13–52, 1936.

[176] V. F. Sears. Neutron scattering lengths and cross sections Special Feature Neutron scattering lengths and cross sections. *Neutron News*, 3(3):26–37, 1992.

[177] T. M. Michels-Clark, A. T. Savici, V. E. Lynch, X. Wang, M. Chodkiewicz, T. Weber, H. B. Buergid, , and C. M. Hoffmann. Expanding Lorentz and spectrum corrections to large volumes of reciprocal space for single-crystal time-of-flight neutron diffraction. *Journal of Applied Crystallography*, (2016):497–506, 2017.

[178] J. Mayers. The Use of Vanadium as a Scattering Standard for Pulsed Source Neutron Spectrometers. *Nuclear Instruments and Methods in Physics Research*, 221:609–618, 1984.

[179] M. Guthrie, C. G. Pruteanu, M. E. Donnelly, J. J. Molaison, A. M. dos Santos, J. S. Loveday, R. Boehler, and C. A. Tulk. Radiation attenuation by single-crystal diamond windows. *Journal of Applied Crystallography*, 50(1):76–86, 2017.

[180] A. Chatterjee and D. Mikkelson and R. Mikkelson and J. Hammonds and T. Worlton. Coordinated, Interactive Data Visualization for Neutron Scattering Data. *Talk at NOBUGS 2002 Conference, NIST*, 4:194–197, 2002.

[181] B. H. Toby. EXPGUI, a graphical user interface for GSAS. *Journal of Applied Crystallography*, (34):210–213, 2001.

[182] A. C. Larson and R. B. Von Dreele. GSAS Manual. *Los Alamos National Laboratory Report, LAUR*, pages 86–748, 2000.

[183] Von Dreele R. B. Toby, B. H. GSAS-II: the genesis of a modern open-source all purpose crystallography software package. *Journal of Applied Crystallography*, 46:544–549, 2013.

[184] V. Petricek, M. Dusek, and L. Palatinus. Crystallographic computing system jana2006. *Zeitschrift für Kristallographie - Crystalline Materials*, 229:345—-352, 2006.

[185] M. I. Aroyo. *International Tables for Crystallography Volume A: Space-group symmetry*, volume 1. Wiley, 2 edition, 2016.

[186] A. LeBail. Whole Powder Pattern Decomposition Methods and Applications: A Retrospection. *Powder Diffraction*, 20:316, 2005.

[187] H. Rietveld. A profile refinement method for nuclear and magnetic structures. *Journal of Applied Crystallography*, 2:65–71, 1969.

[188] K. N. Trueblood, H. B. Buergi, H. Burzlaff, J. D. Dunitz, and H.H. Schultz. Report of a Subcommittee on Atomic Displacement Parameter Nomenclature. *Acta Crystallografica*, (A52):770–781, 1996.

[189] A. Khachaturyan, S. Semenovskaya, and B. Vainshtein B. Statistical-Thermodynamic Approach to Determination of Structure Amplitude Phases. *Soviet Physics: Crystallography*, 24:519–524, 1979.

[190] A. Khachaturyan, S. Semenovskaya, and B. Vainshtein B. The Thermodynamic Approach to the Structure Analysis of Crystals. *Acta Crystallographica*, A37:742–754, 1981.

[191] Y. G. Andreev and P. Lightfoot and P. G. Bruce. Structure of the polymer electrolyte poly(ethylene oxide)$_3$: $LiN(SO_2CF_3)_2$ determined by powder diffraction using a powerful Monte Carlo approach. *Chemical Communications*, 18:2169, 1996.

[192] N. Metropolis, A. Rosenbluth, M. Rosenbluth, A. Teller, and E. Teller. Equation of State Calculations by Fast Computing Machines. *Journal of Chemical Physics*, 21:1087–1092, 1953.

[193] David Halliday. *Fundementals of Physics*. Wiley, New York, 6^{th} Edition edition, 2001.

[194] R. Feistel and W. Wagner. A new equation of state for H_2O Ice I_h. *Journal of Physical and Chemical Reference Data*, 35(2):1021–1047, 2006.

[195] C. G. Pruteanu, G. J. Ackland, W. C. K. Poon, and J. S. Loveday. When immiscible becomes miscible — Methane in water at high pressures. *Science Advances*, (3):1700240, 2017.

[196] H. Huppertz. Multianvil high-pressure/high-temperature synthesis in solid state chemistry. *Zeitschrift für Kristallographie*, 219(6):330–338, 2009.

[197] S. Klotz. *Techniques in High Pressure in Neutron Scattering*. CRC Press, Boca Raton, 1 edition, 2013.

[198] N. Kawai and S. Endo. The generation of ultrahigh hydrostatic pressures by a split sphere apparatus. *Review of Scientific Instruments*, (41):1178, 1970.

[199] K.D. Leinenweber, J. A. Tyburczy, T. G. Sharp, E. Soignard, T. Diedrich, W. B. Petuskey, Y. Wang, and J. L. Mosenfelder. Cell assemblies for reproducible multi-anvil experiments. *American Mineralogist*, (3):353–368, 2012.

[200] J. M. Besson, R. J. Nelmes, G. Hamel, J. S. Loveday, G. Weill, and S. Hull. Neutron powder diffraction above 10 GPa. *American Mineralogist*, (907):180–181, 1992.

[201] J. S. Loveday, R. J. Nelmes, W. G. Marshall, J. M. Besson, S. Klotz, G. Hamel, and S. Hull. High pressure neutron diffraction studies using the Paris-Edinburgh cell. *High Pressure Research*, 14(4-6):303–309, 1996.

[202] T. Hattori, A. Sano-Furukawa, S. Machida, J. Abe, K. Funakoshi, H. Arima, and N. Okazaki. Development of a technique for high pressure neutron diffraction at 40 GPa with a Paris-Edinburgh press. *High Pressure Research*, pages 417–425, 2019.

[203] A. Jayaraman. Diamond anvil cell and high-pressure physical investigations. *Reviews of Modern Physics*, 55(1):65–108, 1983.

[204] N. Dubrovinskaia, L. Dubrovinsky, N. A. Solopova, A. Abakumov, S. Turner, M. Hanfland, E. Bykova, M. Bykov, C. Prescher, V. B. Prakapenka, S. Petitgirard, I. Chuvashova, B. Gasharova, Yves-Laurent M., P. Ershov, I. Snigireva, and A. Snigirev. Terapascal static pressure generation with ultrahigh yield strength nanodiamond. *Science Advances*, 2(7):1600341, 2016.

[205] M. I. Eremets. *High Pressure Experimental Methods*, volume 1. Oxford Science Publications, 1997.

[206] A. Bocian, C. L. Bull, H. Hamidov, J. S. Loveday, and R. J. Nelmes. Gas loading apparatus for the Paris-Edinburgh press. *Review of Scientific Instruments*, (81):093904, 2010.

[207] S. Klotz, T. Strässle, B. Lebert, M. d'Astuto, and T. Hansen. High pressure neutron diffraction to beyond 20 GPa and below 1.8 K using Paris-Edinburgh load frames. *High Pressure Research*, (36):73–78, 2016.

[208] S. Klotz, T. Strässle, G. Rousse, G. Hamel, and V. Pomjakushin. Angle-dispersive neutron diffraction under high pressure to 10 GPa. *Applied Physics Letters*, 86(3):1–3, 2005.

[209] L. G. Khvostantsev, L. F. Vereshchagin, and A. P. Novikov. Toroid type high-pressure device: History and prospects. *High Pressure Research*, 24:371–383, 1977.

[210] W. Marshall and D. Francis. Attainment of near-hydrostatic compression conditions using the Paris-Edinburgh cell. *Journal of Applied Crystallography*, 35(1):122–125, 2002.

[211] C. E. Weir, E. R. Lippincott, A. van Valkenburg, and E. N. Bunting. Infrared studies in the 1- to 15-micron region to 30,000 atmospheres. *Journal of Research of the National Bureau of Standards Section A: Physics and Chemistry*, 63A(1):55, 1959.

[212] B. Liu, Y. Gao, Y. Han, Y. Ma, and C. Gao. In situ electrical conductivity measurements of H_2O under static pressure up to 28 GPa. *Physics Letters A*, 380(37):2979 – 2983, 2016.

[213] T. Meier. Journey to the centre of the Earth: Jules Vernes' dream in the laboratory from an NMR perspective. *Progress in Nuclear Magnetic Resonance Spectroscopy*, 106:26–36, 2018.

[214] J. S. Loveday. *High-Pressure Physics*, volume 1. CRC Press, 2012.

[215] H. K. Mao and P. M. Bell. High-Pressure Physics: Sustained Static Generation of 1.36 to 1.72 Megabars. *Science*, 4346(200):1145–1147, 1978.

[216] W. A Bassett. Diamond anvil cell, 50th birthday. *High Pressure Research*, 29(2):163–186, 2009.

[217] R. Boehler and K. De Hantsetters. New anvil designs in diamond-cells. *High Pressure Research*, 24(3):391–396, 2004.

[218] R. Boehler, J. J. Molaison, and B. Haberl. Novel diamond cells for neutron diffraction using multi-carat CVD anvils. *Review of Scientific Instruments*, 88(8), 2017.

[219] B. Haberl, S. Dissanayake, F. Ye, L. L. Daemen, Y. Cheng, C. Li, A. Ramirez-Cuesta, J. Timmy, M. Matsuda, J. J. Molaison, and R. Boehler. Wide-angle diamond cell for neutron scattering. *High Pressure Research*, 37(4):495–506, 2017.

[220] B. Haberl, S. Dissanayake, Y. Wu, D. A. A. Myles, A. M. dos Santos, M. Loguillo, G. M. Rucker, D. P. Armitage, M. Cochran, K. M. Andrews, C. M. Hoffmann, H. Cao, M. Matsuda, F. Meilleur, F. Ye, J. J. Molaison, and R. Boehler. Next-generation diamond cell and applications to single-crystal neutron diffraction. *Review of Scientific Instruments*, 89(9), 2018.

[221] C. L. Bull, N. P. Funnell, M. G. Tucker, S. Hull, D. J. Francis, and W. G. Marshall. PEARL: the high pressure neutron powder diffractometer at ISIS. *High Pressure Research*, 36(4):493–511, 2016.

[222] M. Harada, N. Watanabe, M. Teshigawara, T. Kai, T. Kato, and Y. Ikeda. Neutronics of a poisoned para-hydrogen moderator for a pulsed spallation neutron source. *Nuclear Instruments and Methods in Physics Research Section A: Accelerators, Spectrometers, Detectors and Associated Equipment*, 574(3):407–419, 2007.

[223] W. Lu, P. D.Ferguson, E. B. Iverson, F. X. Gallmeier, and I. Popova. Moderator poison design and burn-up calculations at the sns. *Journal of Nuclear Materials*, 377:268–274, 2008.

[224] X. Wang, C. Hoffmann, and A. dos Santos. TOPAZ - Single crystal Diffractometer, 2018.

[225] C. V. Raman and K. S. Krishnan. A New Type of Secondary Radiation. *Nature*, 121:501–502, 1928.

[226] E. Smith and G. Dent. *Modern Raman Spectroscopy: A Practical Approach.* John Wiley & Sons, 1 edition, 2005.

[227] G. J. Piermarini, S. Block, J. D. Barnett, and R. A. Forman. Calibration of the pressure dependence of the R1 ruby fluorescence line to 195 kbar. *Journal of Applied Physics*, 46(6):2774, 1975.

[228] H.K. Mao, P.M. Bell, J.W. Shaner, and D.J. Steinberg. Specific volume measurements of Cu, Mo, Pd, and Ag and calibration of the ruby R1 fluorescence pressure gauge from 0.06 to 1 Mbar. *Applied Physics*, 46:3276, 1978.

[229] G. Shen and Y. Wang and A. Dewaele and C. Wu and D. E. Fratanduono and J. Eggert and S. Klotz and K. F. Dziubek and P. Loubeyre and O. V. F. and P. D. A. and T. Mashimo and R. M. M. Wentzcovitch and *et al.* Toward an international practical pressure scale: A proposal for an ipps ruby gauge (ipps-ruby2020). *High Pressure Research*, 40(3):299–314, 2020.

[230] F. Birch. Finite Elastic Strain of Cubic Crystals. *Physical Review*, 71(11):809–824, 1947.

[231] F. D. Murnaghan. The Compressibility of Media under Extreme Pressures. *PNAS*, 30(9):244–247, 1944.

[232] T. Straessle, S. Klotz, K. Kunc, V. Pomjakushin, and J. S. White. Equation of state of lead from high-pressure neutron diffraction up to 8.9 gpa and its implication for the nacl pressure scale. *Phys. Rev. B*, 90:014101, Jul 2014.

[233] D. Sholl and J. A. Steckel. *Density Functional Theory: A Practical Introduction.* Wiley-Blackwell, 1 edition, 2009.

[234] J. P. Perdew, K. Burke, and M. Ernzerhof. Generalized gradient approximation made simple. *Physical Review Letters*, 77(18):3865–3868, 1996.

[235] M. Hussein, N. Assadi, and D. A. H. Hanaor. Theoretical study on copper's energetics and magnetism in TiO_2 polymorphs. *Journal of Applied Physics*, 113:233913, 2013.

[236] B. Santra, J. Klimes, A. Tkatchenko, D. Alfe, B. Slater, A. Michaelides, R. Car, and M. Scheffler. On the accuracy of van der Waals inclusive density-functional theory exchange-correlation functionals for ice at ambient and high pressures. *Journal of Chemical Physics*, 139(15):154702, oct 2013.

[237] C. J. Pickard and R. J. Needs. Structures at high pressure from random searching. *Physica Status Solidi B: Basic Research*, 246:536–540, 2009.

[238] C. J. Pickard and R. J. Needs. Ab initio random structure searching. *Journal of Physics: Condensed Matter*, 23:053201, 2011.

[239] B. H. Toby and R. B. Von Dreele. First principles methods using CASTEP. *Zeitschrift fuer Kristallographie*, 220:567–570, 2005.

[240] R. Boehler, M. Guthrie, J. J. Molaison, A. M. dos Santos, S. Sinogeikin, N. Pradhan, and C. A. Tulk. Large-volume diamond cells for neutron diffraction above 90 GPa. *High Pressure Research*, 33:546–554, 2013.

[241] M. Guthrie, R. Boehler, J. J. Molaison, B. Haberl, A. M. dos Santos, and C. Tulk. Structure and disorder in ice VII on the approach to hydrogen-bond symmetrization. *Physical Review B*, 99(18), 5 2019.

[242] J. Binns, K. V. Kamenev, G. J. McIntyre, S. A. Moggach, and S. Parsons. Use of a miniature diamond-anvil cell in high-pressure single-crystal neutron Laue diffraction. *IUCrJ*, 3:168–179, 2016.

[243] A. Grzechnik, M. Meven, and K. Friese. Single-crystal neutron diffraction in diamond anvil cells with hot neutrons. *Journal of Applied Crystallography*, (2016):351–356, 2018.

[244] J. E. Tibballs and R. J. Nelmes. The P-T dependence of the crystal-structure of KDP and DKDP above T_c. *Journal of Physics C*, 15(25):L849–L853, 1982.

[245] D. Wang, T. Li, S. Wang, J. Wang, C. Shen, J. Ding, W. Li, P. Huang, and C. Lu. Characteristics of nonlinear optical absorption and refraction for KDP and DKDP crystals. *Optical Materials Express*, 7(2):533, 2017.

[246] O. Arnold, J. C. Bilheuxc, J. M. Borreguero, A. Buts, J. I. Campbell, L. Chapon, M. Doucetc, N. Draper, R. Ferraz, M. A. Gigg, V. E. Lynch, A. Markvardsen, D. J. Mikkelson, J. R. Mikkelson, K. Miller, and J. Zikovsky. Mantid—Data analysis and visualization package for neutron scattering and μSR experiments. *Nuclear Instruments and Methods in Physics Research Section A*, 764:156–166, 2014.

[247] D. E. Lea. Secondary Gamma Rays Excited by the Passage of Neutrons through Matter. *Proceedings of the Royal Society of London. Series A*, 150(13):637–668, 1912.

[248] L. Koester. *Neutron Physics*, volume 1. Springer, 1977.

[249] P. J. Becker and P. Coppens. Extinction within the Limit of Validity of the Darwin Transfer Equations - General Formalisms for Primary and Secondary Extinction and Their Application to Spherical Crystals. *Acta Crystallographica*, A30(129):129–147, 1974.

[250] Mantid Documentation. *IntegrateEllipsoids*, 2019.

[251] A. J. Schultz, M. Jrgensen, R. Vogel, X. Wang, R. L. Mikkelson, D. J. Mikkelson, V. E. Lynch, P. F. Peterson, M. L. Green, and C. M. Hoffmann. Integration of neutron time-of-flight single-crystal Bragg peaks in reciprocal space. *Journal of Applied Crystallography*, 47(3):915–921, 2014.

[252] Mantid Documentation. *IntegratePeaksProfileFitting*, 2019.

[253] P. W. Bridgman. Water, in the Liquid and Five Solid Forms, under Pressure. *Proceedings of the American Academy of Arts and Sciences*, 47(13):441–558, 1912.

[254] B. Kamb. Structure of Ice VI. *Science*, 150(3693):205–209, 1965.

[255] W. F. Kuhs, H. Ahsbahs, D. Londono, and J.L. Finney. In-situ crystal growth and neutron four-circle diffractometry under high pressure. *Physica B: Condensed Matter*, 156-157:684–687, 1989.

[256] J. L. Kuo and W. F. Kuhs. A first principles study on the structure of ice-vi: Static distortion, molecular geometry, and proton ordering. *Journal of Physical Chemistry B*, 110(8):3697–3703, 2006.

[257] L. del Rosso, M. Celli, and L. Ulivi. Ice XVII as a Novel Material for Hydrogen Storage. *Challenges*, 8(1):3, 2017.

[258] L. del Rosso, M. Celli, D. Colognesi, S. Rudic, N. J. English, C. J. Burnham, and L. Ulivi. Dynamics of hydrogen guests in ice XVII nanopores. 065602:1–5, 2017.

[259] H. J. Monkhorst and J. D. Pack. Special points for Brillouin-zone integrations. *Physical Review B*, 13:5188–5192, 1976.

[260] R. Bini, L. Ulivi, J. Kreutz, and H. J. Jodl. High-pressure phases of solid nitrogen by Raman and infrared spectroscopy. *Journal of Chemical Physics*, 112(19):8522–8529, 2000.

[261] M-E. Donnelly, P. Teeratchanan, C. L. Bull, A. Hermann, and J. S. Loveday. Ostwald's rule of stages and metastable transitions in the hydrogen–water system at high pressure. *Physical Chemistry Chemical Physics*, 20:26853–26858, 2018.

[262] M. Catti, L. del Rosso, L. Ulivi, M. Celli, F. Grazzi, and T. C. Hansen. Ne- and O_2-filled ice XVII: A neutron diffraction study. *Physical Chemistry Chemical Physics*, 21(27):14671–14677, 2019.

[263] A. F. Schuch and R. L. Mills. Crystal structures of the three modifications of nitrogen 14 and nitrogen 15 at high pressure. *Journal of Chemical Physics*, 52(12):6000–6008, 1970.

[264] J. Kosata, P. Merkl, P. Teeratchanan, and A. Hermann. Stability of Hydrogen Hydrates from Second-Order Møller–Plesset Perturbation Theory. *Journal of Physical Chemistry Letters*, 9:5624–5629, 2018.

[265] K. A. Udachin, G. D. Enright, C. I. Ratcliffe, and J. A. Ripmeester. Structure, stoichiometry, and morphology of bromine hydrate. *Journal of the American Chemical Society*, 119(47):11481–11486, 1997.

[266] C. J. Loewig. Ueber Brom-Quecksilber, Bromhydrat und ueber Trennung des Broms von Chlor. *Magazin der Pharmazie*, 23:11–13, 1828.

[267] C. J. Loewig. Ueber einige Bromverbindungen und ueber Bromdarstellung. *Annalen der Physik*, 90:485–499, 1828.

[268] J. S. Lewis and R. G. Prinn. Kinetic inhibition of CO and N_2 reduction in the solar nebula. *The Astrophysical Journal*, 238:357, 1980.

[269] R. G. Prinn and B. Fegley Jr. Kinetic inhibition of CO and N_2 reduction in circumplanetary nebulae - Implications for satellite composition. *The Astrophysical Journal*, 249:308, 1981.

[270] H. B. Hubbard and J. J. MacFarlane. Structure and evolution of Uranus and Neptune. *Journal of Geophysical Research: Solid Earth*, 85(225), 1980.

[271] L. A. Young, S. A. Stern, H. A.Weaver, F. Bagenal, R. P. Binzel, B. Buratti, A. F. Cheng, D. Cruikshank, G. R. Gladstone, W. M. Grundy, D. P. Hinson, M. Horanyi, D. E. Jennings, I. R. Linscott, D. J. McComas, W. B. McKinnon, R. McNutt, J. M. Moore, S. Murchie, C. B. Olkin, C. C. Porco, H. Reitsema, D. C. Reuter, J. R. Spencer, D. C. Slater, D. Strobel, M. E. Summers, , and G. L. Tyler. New Horizons: Anticipated Scientific Investigations at the Pluto System. *Space Science Reviews*, 140:93–127, 2008.

[272] Y. Sekine, H. Genda, S. Sugita, T. Kadono, and T. Matsui. Replacement and late formation of atmospheric N_2 on undifferentiated Titan by impacts. *Nature Geoscience*, 4:359–362, 2011.

[273] L. Noack, I. Snellen, and H. Rauer. Water in Extrasolar Planets and Implications for Habitability. *Space Science Review*, 212:877–898, 2017.

[274] O. Mousis, D. Gautier, and A. Coustenis. The D/H ratio in methane in Titan: Origin and history. *Icarus*, 159(1):156–165, 2002.

[275] O. Grasset and C. Sotin. The cooling rate of a liquid shell in Titan's interior. *Icarus*, 123(1):101–112, 1996.

[276] A. D. Fortes, P. M. Grindrod, S. K. Trickett, and L. Vocadlo. Ammonium sulfate on Titan: Possible origin and role in cryovolcanism. *Icarus*, 188(1):139–153, 2007.

[277] O. Grasset, C. Sotin, and F. Deschamps. On the internal structure and dynamics of Titan. *Planetary and Space Science*, 48(7-8):617–636, 2000.

[278] F. Sohl, H. Hussmann, B. Schwentker, T. Spohn, and R. D. Lorenz. Interior structure models and tidal Love numbers of Titan. *Journal of Geophysical Research E: Planets*, 108(12):1–13, 2003.

[279] R. D. Lorenz, B. W. Stiles, R. L. Kirk, M. D. Allison, P. P. Del Marmo, L. Iess, J. I. Lunine, S. J. Ostro, and S. Hensley. Titan's rotation reveals an internal ocean and changing zonal winds. *Science*, 319(5870):1649–1651, 2008.

[280] J. S. Kargel. Ammonia-water volcanism on icy satellites: Phase relations at 1 atmosphere. *Icarus*, 100(2):556–574, 1992.

[281] R. M. C. Lopes, K. L. Mitchell, E. R. Stofan, J. I. Lunine, R. Lorenz, F. Paganelli, R. L. Kirk, C. A. Wood, S. D. Wall, L. E. Robshaw, A. D. Fortes, C. D. Neish, J. Radebaugh, E. Reffet, S. J. Ostro, C. Elachi, M. D. Allison, Y. Anderson, R. Boehmer, G. Boubin, P. Callahan, P. Encrenaz, E. Flamini, G. Francescetti, Y. Gim, G. Hamilton, S. Hensley, M. A. Janssen, W. T. K. Johnson, K. Kelleher, D. O. Muhleman, G. Ori, R. Orosei, G. Picardi, F. Posa, L. E. Roth, R. Seu, S. Shaffer, L. A. Soderblom, B. Stiles, S. Vetrella, R. D. West, L. Wye, and H. A. Zebker. Cryovolcanic features on Titan's surface as revealed by the Cassini Titan Radar Mapper. *Icarus*, 186(2):395–412, 2007.

[282] D. L. Hildenbrand and W. F. Giauque. Ammonium Oxide And Ammonium Hydroxide. Heat Capacities And Thermodynamic Properties From 15 To 300 °K. *Journal of the American Chemical Society*, 75(12):2811–2818, 1953.

[283] I. Olovsson and D. H. Templeton. The crystal structure of ammonia monohydrate. *Acta Crystallographica*, 12(11):827–832, 1959.

[284] A. Koumvakalis. *High pressure study of ammonia monohydrate*. PhD thesis, University of California, Los Angeles, 1988.

[285] D. L. Hogenboom, J. S. Kargel, G. J. Consolmagno, T. C. Holden, L. Lee, and M. Buyyounouski. The ammonia-water system and the chemical differentiation of icy satellites. *Icarus*, 128(1):171–180, 1997.

[286] R. J. Nelmes and J. S. Loveday. Isis experimental report rb9859. *CCLRC Rutherford Appleton Laboratory*, 1998.

[287] M. C. Payne, M. P. Teter, D. C. Allan, T.A. Arias, and J. D. Joannopoulos. Iterative minimization techniques for ab initio total-energy calculations - molecular-dynamics and conjugate gradients. *Reviews of Modern Physics*, 64:1045–1097, 1992.

[288] G. I. G. Griffiths, A. J. Misquitta, A. D. Fortes, C. J. Pickard, and R. J.Needs. High pressure ionic and molecular crystals of ammonia monohydrate within density functional theory. *Journal of Chemical Physics*, 137(6):064506, 2012.

[289] V. Robinson, Y. Wang, Y. Ma, and A. Hermann. Stabilization of ammonia-rich hydrate inside icy planets. *PNAS*, 114(34):9003–9008, 2017.

[290] S. Stanley and T. Bloxham. Convective-region geometry as the cause of Uranus' and Neptune's unusual magnetic fields. *Nature*, 428:151, 2004.

[291] G. Tobie, J. Lunine, and C. Sotin. Episodic outgassing as the origin of atmospheric methane on Titan. *Nature*, 440:61–64, 2006.

[292] H. Kadobayashi, H. Hirai, K. Suzuki, H. Ohfuji, M. Muraoka, S. Yoshida, and Y. Yamamoto. Sequential *in situ* Raman spectroscopy for observing dissociation behavior of filled-ice I_h of methane hydrate at high pressure. *Journal of Raman Spectroscopy*, 51(12):2536–2542, 2020.

[293] M. I. Aroyo, J. M. Perez-Mato, C. Capillas, E. Kroumova, S. Ivantchev, G. Madariaga, A. Kirov, and H. Wondratschek. Bilbao Crystallographic Server I: Databases and crystallographic computing programs. *Zeitschrift fuer Kristallographie*, 221(1):15–27, 2006.

[294] J. Klinger. Extraterrestrial ice: A review. *Journal of Physical Chemistry*, 87:4209–4214, 1983.

[295] J. Waite, M. Combi, W. H. Ip, T. Cravens, R. McNutt, W. Kasprzak, R. Yelle, J. Luhmann, H. Niemann, D. Gell, B. Magee, G. Fletcher, J. Lunine, and W. L. Tseng. Cassini Ion and Neutral Mass Spectrometer: Enceladus Plume Composition and Structure. *Science*, 311:1419—-1422, 2006.

[296] Y. Park, D. Y. Kim, J. W. Lee, D. G. Huh, K. P. Park, J. Lee, and H. Lee. Sequestering carbon dioxide into complex structures of naturally occurring gas hydrates. *PNAS*, 103:12690–12694, 2006.

[297] Z. F. Wroblewski. "Sur la combinaison de l'acide carbonique et de l'eau" [On the combination of carbonic acid and water]. *Comptes Rendus de l'Académie des Sciences*, (94):212–213, 1882.

[298] Z. F. Wroblewski. "Sur la composition de l'acide carbonique hydrate" [On the composition of the hydrate of carbonic acid]. *Comptes Rendus de l'Académie des Sciences*, (94):254–258, 1882.

[299] Z. F. Wroblewski. "Sur les lois de solubilité de l'acide carbonique dans l'eau sous les hautes pressions" [On the laws of solubility of carbonic acid in water at high pressures]. *Comptes Rendus de l'Académie des Sciences*, (94):1355–1357, 1882.

[300] M. von Stackelberg and H. R. Müller. "Feste Gashydrate II. Struktur und Raumchemie" [Solid gas hydrates II. Structure and space chemistry]. *Zeitschrift für Elektrochemie, Berichte der Bunsengesellschaft für physikalische Chemie*, 58(1):25–39, 1954.

[301] C. A. Tulk, S. Machida, D. D. Klug, H. Lu, M. Guthrie, and J. J. Molaison. The structure of CO_2 hydrate between 0.7 and 1.0 GPa. *Journal of Chemical Physics*, 141(174503), 2014.

[302] E. H. Abramson, O. Bollengier, J. M. Brown, B. Journaux, W. Kaminsky, and A. Pakhomova. Carbonic acid monohydrate. *American Mineralogist*, 103(9):1468–1472, 2018.

[303] K. Komatsu, S. Klotz, A. Shinozaki, R. Iizuka, L. E. Bove, and H. Kagi. Performance of ceramic anvils for high pressure neutron scattering. *High Pressure Research*, 34(4):494–499, 2014.

Publication List

2022 | A Possible Crystal Structure of Ammonia Monohydrate IV
B. Massani, C. Pruteanu, L. Conoway, A. Herrmann, and J. S. Loveday
Crystals, 12(2), 135

2020 | On single-crystal neutron-diffraction in DACs: Quantitative structure refinement of light elements on SNAP and TOPAZ
B. Massani, J. S. Loveday , J. J. Molaison , A. M. dos Santos , X. P. Wang , L. L. Daemen , B. Haberl , R. Boehler, and M. Guthrie
HPR, 40(3), 339-357

2019 | On a New Nitrogen sX Hydrate from Ice XVII
B. Massani, L. J. Conway, A. Hermann, and J. Loveday
J. Chem. Phys., 151, 104305

2019 | Amorphous and Crystalline Ices Studied by Dielectric Spectroscopy
L. J. Plaga, A. Raidt, V. Fuentes Landete, K. Amann-Winkel, B. Massani, T. Gasser, C. Gainaru, T. Loerting, and R. Böhmer
J. Chem. Phys., 150, 244501

2019 | Structural Features and Pore Formation in Decomposing CO_2 Clathrate Hydrate
S. Arzbacher, N. Rahmatian, A. Ostermann, B. Massani, T. Loerting, J. Petrasch
PCCP, 147, 134503

2017 | Formation and Decomposition of CO_2-Filled Ice
B. Massani, C. Mitterdorfer, T. Loerting
J. Chem. Phys., 147, 134503

2017 | Diffusive dynamics during the high-to-low density transition in amorphous ice
F.Perakis, K. Amann-Winkel, F. Lehmkuehler, M. Sprung, D. Pettersson, J. Sellberg, H. Pathak, A. Spaeh, F. Cavalca, D. Schlesinger, A. Ricci, A. Jain, B. Massani, F. Aubree, C. J. Benmore, T. Loerting, G. Gruebel, L. Pettersson, A. Nilsson
Proc. Natl. Acad. Sci., 114, 8193-8198

HIGH PRESSURE RESEARCH
https://doi.org/10.1080/08957959.2020.1767100

Taylor & Francis
Taylor & Francis Group

On single-crystal neutron-diffraction in DACs: quantitative structure refinement of light elements on SNAP and TOPAZ

B. Massani[a], J. S. Loveday[a], J. J. Molaison[b], A. M. dos Santos[b], X. P. Wang[b], L. L. Daemen[b], B. Haberl[b], R. Boehler[b] and M. Guthrie[a,c]

[a]SUPA, School of Physics and Astronomy, and Centre for Science at Extreme Conditions, The University of Edinburgh, Edinburgh, UK; [b]Neutron Scattering Division, Neutron Sciences Directorate, Oak Ridge National Laboratory, Oak Ridge, TN, USA; [c]European Spallation Source, ERIC, Lund, Sweden

ABSTRACT

Quantitative single crystal neutron-diffraction in diamond anvil cells has so far been limited by the neutron flux available at the various neutron sources. As a result, highly precise measurements of the exact position of light elements have not been possible preventing, for example, structural studies of hydrogen and hydrogen bonds under pressure. Here we report experiments carried out on SNAP at the Spallation Neutron Source (ORNL, TN, USA) to explore the possibility and current limits of such studies. Furthermore, we benchmarked the obtained data quality with reference experiments carried out on TOPAZ, a dedicated single-crystal instrument.

We show that measuring single-crystal diffraction intensities on SNAP is possible to such a precision that we are able to resolve the hydrogen bonds in potassium dideuterium phosphate (DKDP) as well as in ice VI.

ARTICLE HISTORY
Received 19 March 2020
Accepted 5 May 2020

KEYWORDS
Single-crystal; neutron-diffraction; H-bonds; DAC; SNAP; TOPAZ

1. Introduction

The crystal structures of many important simple-molecular systems - such as hydrogen/deuterium, ammonia, methane, ice - are surprisingly poorly understood under high pressure. For example, solid, compressed hydrogen is the most abundant substance in our solar system, yet not even the H-H bondlength was directly measured at any elevated pressure and the space group of the high-pressure phases remain unknown [1]. Similarly, ice, ammonia, methane, and their binary and ternary mixtures exhibit a wealth of phases and phenomena such as H-bond centring and superionicity [2,3], all materials which are poorly characterised from a structural point of view.

Accurate structural information on these systems is vital to solve a wide range of scientific problems. The outer solar system is dominated by hydrogen and hydrogen-rich materials and knowledge of their high-pressure structures is vital to develop models of phenomena such as the existence and strength of magnetic dynamos, the internal structure of gas-giants & moons, and even to the evolution and composition of atmospheres [4–10]. The long-standing problem of the formation of metallic hydrogen is an important

CONTACT B. Massani b.massani@sms.ed.ac.uk SUPA, School of Physics and Astronomy, and Centre for Science at Extreme Conditions, The University of Edinburgh, Edinburgh, UK

model for the behaviour of solids when quantum effects become significant [11–14]. The behaviour of protons in H-bonded systems like ice are proxys for more complex biological systems (see for example [15]). Finally, the recent discovery of high temperature superconductivity in hydrogen-rich systems like hydrogen sulphide and lanthanum super-hydride provides further need for accurate structural information at high pressure. The superconductivity is believed to be driven by the high polarisability of the hydrogen atoms, which leads to strong electron-phonon coupling with high coupling frequencies [16–19]. However, to date, no full structure (including hydrogen positions) of a hydrogen-rich high-temperature superconductor has been determined.

The small scattering cross-section of hydrogen for X-rays makes neutron diffraction the only reliable method to exactly measure the proton (or deuteron) positions in a crystal structure. Such measurements were the first to verify the model of hydrogen bonds proposed by Pauling [20] and by Wollan et al. [21] and revealed the familiar bent shape of the water molecule in ice I_h [21]. However, until the advent of bright spallation sources, the measurement of neutron powder patterns of sufficient quality for structural refinement has been limited in pressure to 25 GPa due to the large sample volumes required. Some classic examples of large volume devices used at neutron facilities around the world include gas pressure cells ($P_{max} \sim 0.7$ GPa), clamp cells ($P_{max} \sim 2$ GPa), and the Paris-Edinburgh presses ($P_{max} \sim 30$ GPa) (cf. [22,23]).

Recent developments in diamond synthesis have paved the way for larger diamonds and with this large-volume diamond anvil cells (DAC) [24–26]. Combined with extremely bright neutron sources, available at the Spallation Neutron Source (SNS) a facility located in the Oak Ridge National Laboratory, neutron diffraction at a pressure up to 90 GPa has been demonstrated [24,27]. These DACs so far, have mainly been used for powder diffraction and, as such, information obtained from data has its limits. For many crystallographic studies, information from single-crystal techniques are vital in that they provide a much higher (real-space) resolution by enabling access to short d-spacing Bragg reflections that would heavily overlap in a powder study. At pressures >50 GPa powder methods, for example, give the same agreement indices for a 1-site and 2-site model of a hydrogen bond in high-pressure ice (cf. [27]) making it impossible to identify the better model. Of equal importance, single-crystal methods avoid the need to deuterate samples. The concentrated signal from sharp single-crystal Bragg spots remains visible on top of the incoherent scattering originating from protium ^{1}H that would overwhelm distributed powder intensities.

Use of DACs for high-pressure single-crystal neutron diffraction (HP-SCND) therefore paves the way for studies of hydrogen-rich systems to pressures currently inaccessible and with unprecedented structural detail.However, quantitative single-crystal neutron diffraction (SCND) studies under high pressure in DACs remain challenging, albeit successful attempts that have been made. Binns et al. [28] published a set of experiments at ANSTO's KOALA, a neutron Laue diffractometer, using a Merrill-Basset-type diamond cell with conical Boehler anvils ($\varnothing_{culet} = 1$ mm). It demonstrated sufficient data quality for refinement on crystals of typical sizes for X-ray diffraction in a DAC. Furthermore, at Heinz Maier-Leibnitz Zentrum (MLZ)'s four- circle diffractometer HEiDi, monochromatic neutron diffraction was performed in a panoramic DAC with conical Boehler anvils and achieved high-quality data under compression to 1 GPa. Another successful test of the cell/anvil setup with 1.5 mm culets reached 7 GPa [29]. These studies are mainly aiming

for magnetic materials and large unit cells, but do not report a high enough diffraction resolution in the high-Q range to investigate H-bonds.

The goal of this study is to benchmark SNAP, a high-pressure time-of-flight diffractometer at the SNS for the quantitative structure analysis of single crystals containing hydrogen or other light elements in a DAC. As a reference, a similar set of experiment was carried out on TOPAZ, a dedicated single-crystal instrument also at the SNS. We will present a set of trial experiments to investigate the relationship between sample volume and data quality. These properties are inversely related to one another yet, unavoidably, the former is strictly limited in high-pressure studies. The systematic study of the crystallographic limitations of progressively smaller sample volumes is a critical first step in deployment routine quantitative single crystal structure refinement in a DAC.

Furthermore, we will show the influence of the complex sample environment consisting of diamonds and gasket on the data quality. To that end, we examined structural refinements of the deuterated ferroelectric potassium di-hydrogen phosphate (KD_2PO_4, DKDP), as a test case. DKDP is a classic example of a short hydrogen-bonded system, which has already been heavily studied with neutron diffraction – its structural properties are therefore well known up to modest pressures of about 2 GPa [30]. Finally, we will test our data reduction procedure and all necessary corrections against a ice VI single-crystal grown *in-situ* under pressure in a diamond anvil cell.

2. Material and methods

DKDP (KD_2PO_4), is a tetragonal body-centred crystal (space group $I\bar{4}2d$; N° 122), with lattice parameters at ambient pressure and temperature of $a = 7.469(1)$ Å and $b = 6.976(1)$ Å (unit-cell volume 387.29 Å^3). A unit-cell contains four hydrogen-bonded formula units of KD_2PO_4, with all the hydrogen bonds lying in the *ab*-plane [30]. The sample was synthesised at SNS by dissolving KDP (potassium dihydrogen-phasphate, KH_2PO_4) in D_2O and recrystallising out of solution. This procedure was repeated three times and two sample crystals were cut from the deuterated crystal. The larger of the two had a volume of 1.028 mm^3, and the small one had a volume of 0.028 mm^3 (disc-shaped; $\varnothing = 0.6$ mm, $h = 0.1$ mm). The latter volume was chosen because it matches the typical size and geometry of a sample chamber in diamond anvil cells for neutron diffraction [25].

Experiments were carried out at two SNS instruments: TOPAZ, the dedicated single-crystal instrument and SNAP, the high-pressure beam line. TOPAZ is a high-resolution single-crystal diffractometer using the time-of-flight Laue technique with an array of neutron area detectors distributed spherically about the sample. The resulting angular coverage combined with a wide neutron wavelength band of 3.1 Å is well suited for efficient 3D-mapping of Bragg scattering in reciprocal space in the *Q*-range 0.45–25.00 Å^{-1}. As such, TOPAZ is well suited to determine atomic positions and displacement parameters of light elements, such as hydrogen. The high real-space resolution down to 0.25 Å, allows for precise measurements of atom-distances in H-bonds. Due to disorder both the paraelectric phase of DKDP and ice VI have average structures where the equivalent O-H··· O and the O··· H-O positions are occupied equally, resulting in a 50% occupancy on both sites, separated by a distance of less than 0.5 Å[21,31]. A high real-space resolution is critical to resolve such a small displacement. Currently, TOPAZ has 24 of 48 detector ports populated with Anger camera modules covering about 3.0 sr in solid angle.

TOPAZ uses a 18 m long bent focussing guide which focusses the beam to 2.0–4.0 mm. The high-precision goniometer is fixed to $X = 135^\circ$ and samples can be freely rotated about two axis, Φ and Ω (see Figure 1) [32].

The Spallation Neutrons and Pressure (SNAP) instrument is a high-flux diffractometer primarily used for powder diffraction [33]. SNAP uses area detectors of the same type as TOPAZ arranged in two 3×3 detector banks which allow for a Q-coverage of $Q = 0.7$ -24.0 Åin the equatorial plane, depending on the detector positions (horizontal and vertical coverage: $\pm 22.5^\circ$). Compared to the neutron optics used on TOPAZ, the beam-focusing optics on SNAP are significantly shorter (guide length: 2.4 m; source-to-sample distance: 15 m), allowing for a high neutron flux at the expense of a higher divergence and complex beam profile. The instrument is hence well suited to deal with various complex sample environments for high-pressure studies. SNAP's capabilities for a full structural refinement of SCND data have so far not been tested.

aSNS is operating at about 1.33 MW. The accumulated proton charge for the conducted experiments lay between $8.9 \cdot 10^{12}$ and $1.4 \cdot 10^{13}$. All data were normalised to the monitored proton current during the respective experiment.

Patterns of the bare crystals mounted on a Kapton-pin were collected for about 3 h per orientation both on SNAP and on TOPAZ. From this initial measurement on TOPAZ we were able to refine the deuteration ratio of the DKDP to be $> 94\%$. This compares well with that determined from the c/a ratio which is strongly dependent on the deuteration ratio [30,31].

Subsequently, the small crystal was placed in a DAC (SNAP) and a mock-DAC (TOPAZ). The mock-DAC was used because the sample stage on TOPAZ cannot support the weight of a real DAC. The DAC comprises a cell body made from hardened steel or beryllium-copper that drives two opposing diamonds together against the sample, which is contained by a metal gasket (for the detailed design see [25,26,34]). The mock-DAC had the same basic parts but held together by a much lighter aluminium scaffolding instead of the heavy cell body. In both cases a circular, incident-beam collimator of 3 mm in diameter was chosen. The same collimator size was used to collect a Vanadium spectrum, a standard

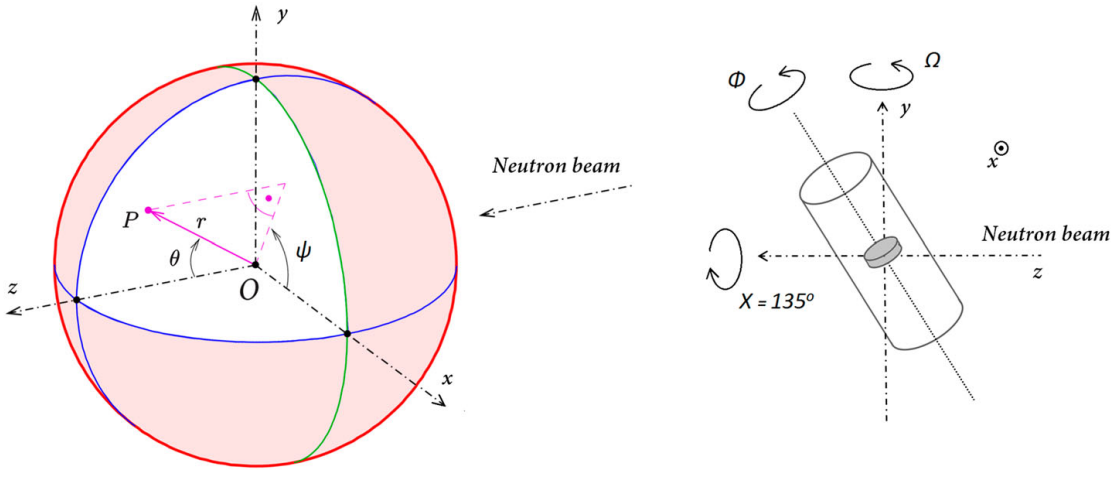

Figure 1. Left: Coordinate system on TOPAZ and SNAP. The beam direction is along the z-axis. The angle θ shown on between z and r is the scattering angle (twice the Bragg angle). The angles θ and Ψ give the direction of the diffracted beam. Right: The goniometer angles X, Φ, and Ω. On TOPAZ X is fixed to 135°; on SNAP X and Φ are fixed to 0°.

sample for the beam-profile calibration (see for example [33]). We then collected patterns of the crystal in the mock-DAC on TOPAZ for ten orientations (3×10 h and 7×6 h). Similarly, six orientations on SNAP were recorded (the sample rotation on SNAP is limited to a single vertical axis whereas TOPAZ has a two-axis orienter). The primary beam entered the cell through the gasket (see schematic sketch in Figure 4). On SNAP data collection was limited to only 3 h collections per orientation.

In order to asses the methods developed here for SCND in a real DAC, a single-crystal of ice VI of a similar size as the small DKDP crystal was grown in a diamond anvil cell by repeatedly melting and re-crystalising a powder of ice VI in an ammonia-water pressure medium (Sigma-Aldrich,ND_4OD-D_2O, 25%, >99.99% deut.).

The data reduction was carried out using the MANTID data analysis and visualisation package [35]. All crystallographic refinements were carried out using EXPGUI [36], the graphical user interface for the GSAS-I software suite [37].

3. Results and discussion

3.1. Crystal size: effects on data quality

As a first step, we investigated the volume restrictions and the influence of the sample environment on the data quality using an instrument fully bench-marked for quantitative single crystal diffraction. To that end we measured the small, DAC-sized crystal on TOPAZ, the dedicated single crystal instrument at SNS. This marks the smallest crystal measured on this instrument to date. As mentioned above, ten orientations of the crystal were measured for 3 h each; each orientation contributed about 100 reflections to the overall data set of 1044 reflections, after outliers had been removed as per standard procedure.

The structural refinement of the data set obtained from this experiment yielded values consistent with those reported in the literature, as obtained by Tibballs and Nelmes [30]. The respective structural information is given in Table 4 (cf. appendix). This data set was used as a baseline for all subsequent measurements. In general, the deviation of the structural parameters from the literature values is very small and might be a feature introduced by a slightly different deuteration ratio of our sample compared to that of Tibballs et al. As mentioned above, the ratio of KDP ($a = 7.4521(4)$, $c = 6.974(2)$, $a/c = 0.936$) to DKDP ($a = 7.469(1)$, $c = 6.976(1)$, $a/c = 0.934$) has a large influence on the lattice parameter a=b; KDP expands more in the ab-plane than along the c-axis when deuterated. This behaviour is due to all the H-bonds being arranged in this plane. However, the obtained structural parameters are afflicted with larger errors of about one order of magnitude higher compared to the results published by Tibballs et al. Note that this is a direct result of the small sample volume, with the low intensites (high-Q) having a greater statistical uncertainty.

In general, our measurements are accurate but not as precise as the literature values. Still, these results show that even in a DAC-sized crystal it is possible to resolve the exact hydrogen/deuteron positions accurately on a well-calibrated neutron diffractometer.

3.2. Effect of the DAC on data quality

Subsequently, the crystal was placed in the mock-DAC and patterns were recorded. Because of the contributions of the single-crystal diamond peaks, and the powder lines

of the steel gasket, an increased background, and an increased signal-to-noise ratio, data-reduction routines that are well established on TOPAZ failed here. In the following, problems encountered and approximations used for the data reduction and analysis are discussed.

3.2.1. Increased background

While light elements (*e.g.* C, N, O, F, Ne) cause mainly the emission of an alpha or beta radiation, heavier elements (*e.g.* Fe and Re) produce high enough gamma radiation if exposed to a neutron beam [38]. The Anger cameras as used on SNAP and TOPAZ detect neutrons but are also sensitive to gamma rays. Since steel, beryllium-copper, or rhenium gaskets are most commonly used in DACs, the background is significantly increased if the primary beam hits the gasket.

While it is possible to minimise the gamma ray emission if the primary beam enters the cell through the one of the diamonds, this geometry limits the accessible orientations of the single-crystal for existing cell geometries. Far more orientations can be measured if the primary beam enters the cell through the gasket, inevitably resulting in a significant background increase.

For SNAP, the diffraction patterns for the empty instrument (black), the sample on a vanadium pin (blue), and the fully-assembled DAC are given in Figure 2(a). All plots are normalised to the proton-current and corrected for instrumental effect by normalising to a measurement of a vanadium standard. The green curve shows the background in which the primary beam enters the cell through the diamonds only, while the red curve is the background for the case in which the primary beam enters the cell through the gasket. Note, that the background level for the high-Q data are of a similar magnitude in both cases; the background increases significantly in the high-Q regime if the gasket is in the primary beam path. For most elements, the absorption cross section σ^a is inversely proportional to the wave vector $k = \frac{2\pi}{\lambda}$. This leads to more neutrons being absorbed at higher wavelengths and hence more gamma rays being emitted [39]. In Figure 2(b) the same data are shown for an experiment on TOPAZ and, similar to the experiments carried out on SNAP, an increased background is observed. (The four red curves show the variation of the background levels for four cell orientations.) However, the background does not increase at low-Q to the same extent as on SNAP.

A background reduction could likely be achieved by a reduction of the beam diameter from 3 mm to the actual dimensions of the sample chamber, however, rather high-precision alignment would be required to ensure the sample is fully bathed by the beam.

It should also be noted that He-based tubes are not expected to suffer from the same issue. Evaluation of this is in progress at SNS's CORELLI beamline, but is outside the scope of this paper.

3.2.2. Gasket contamination

Gaskets for these experiments consist of poly-crystalline steel and add a parasitic signal to the data. Unlike the parasitic Bragg signal from the single crystal diamond - which is well defined in 3D-reciprocal space - powder lines emanating from the metal gasket pollute entire *d*-spacing ranges on the detector. In Figure 3(a), a sample reflection on top of a powder line is shown. Technically, it should be possible to fit the powder-line and subtract the powder-line from the peak. Such an algorithm has not yet been written for MANTID;

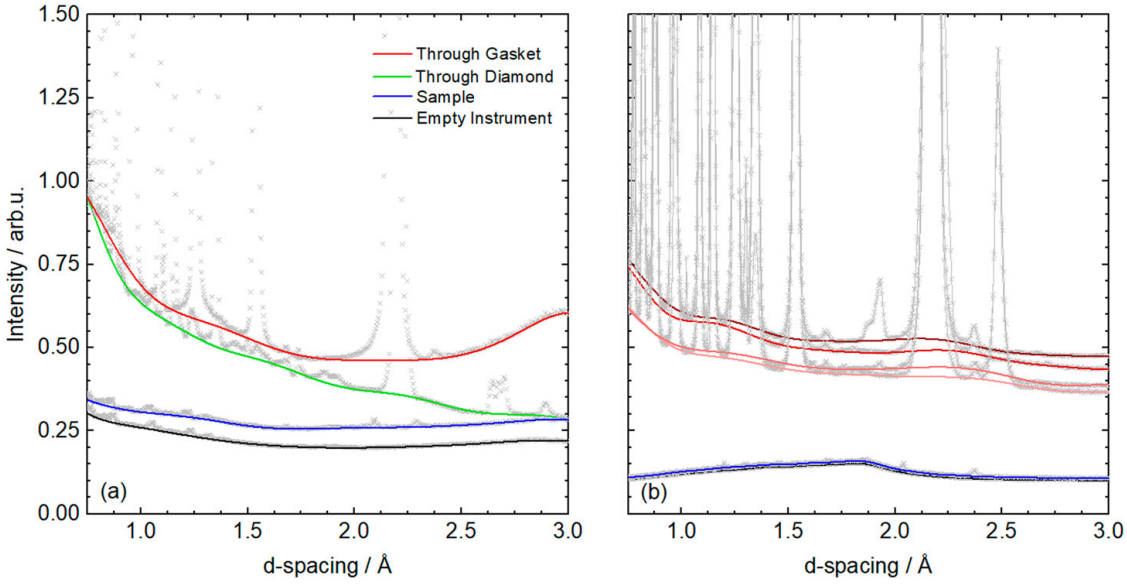

Figure 2. Comparison of background levels on SNAP (a) and TOPAZ (b) for the empty instrument (black), the sample on a vanadium pin (blue), and the full assembled DAC. SNAP: the green curve shows the background in which the primary beam enters the cell through the diamonds only, while the red curve is the background for the case in which the primary beam enters the cell through the gasket. TOPAZ: The four red curves give the background on TOPAZ for various orientations of the cell. All plots are normalised to the proton-current and vanadium-corrected.

Here, we hence excluded all sample reflections overlapping with the *d*-spacing range of gasket-lines. This approximately halved the accessible Q-range for this experiment.

3.2.3. Signal-to-noise ratio

While it is not possible to reduce the background with a longer collection time, the signal-to-noise ratio improves with time. As a threshold for the peak integration we chose $I/\sigma = 3$. For the measurement of one orientation, the number of integrable reflections above the s/n ratio doubled with time - after 3, 6, and 8 h the number of integrable reflections were 5–10, 20–30, and >45, respectively.

3.2.4. Attenuation correction

The sample volume of the DAC-sized crystal was about 0.028 mm^3. In comparison, a metal gasket of a diameter 6.0 mm and a height of 0.5 mm has a volume of 14.137 mm^3 - about 500 times larger. Even if the neutron beam does not illuminate the whole gasket, its illuminated volume exceeds the sample volume. For the attenuation correction, only the contributions of the steel gasket were taken into consideration. A spherical model was used with the radius of the attenuation sphere chosen to be 1.5 mm - the radius of the beam used for this experiment - and consisted of Fe, Cr and Ni in their respective abundance. (Stainless steel as used for this experiment is an alloy composing of roughly 70% Fe, 20% Cr, and 10% Ni. The other elements in stainless steel such as Mg, Si, P and C were omitted in this model for their abundance is usually less than 2% and the attenuation of these elements is low).

Furthermore, we tried to improve the attenuation model using an analytical beam-tracing approach; To that end, a 3-dimensional model of a diamond anvil cell was

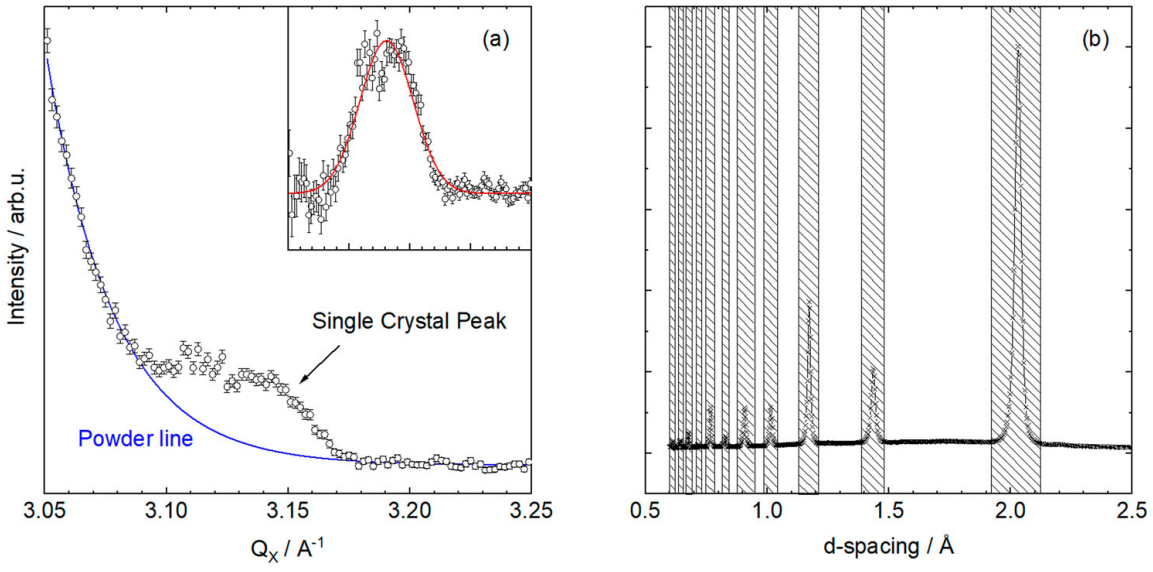

Figure 3. (a) The $31\bar{2}$ single crystal peak of DKDP on top of a powder line caused by the metal gasket of a DAC. The blue curve being gives an exponential fit to the powder line and the insert shows the single crystal peak after the subtraction of the powder line. (b) Integration over the whole detector area after masking all single crystal peaks. The resulting powder lines are caused by the metal gasket (shaded d-spacing regimes); those regions were excluded during the data reduction.

created in Python (cf. inset in the left panel of Figure 4). This model has the same frame of reference as the TOPAZ instrument and is freely rotatable in 3D about Φ, χ and Ω (cf. TOPAZ specification sheet [32]). Instead of a diamond with a pavilion-angle of 49° (as in a real DAC), we modelled the diamond as a cylinder with the same radius as the culet. This simplification can be justified by two reasons. Firstly, as can be seen in Figure 4(b) the overall path-length through the diamond is small compared to the path-length through the gasket. And secondly, the scattering cross-sections of carbon ($\sigma_s = 5.551$

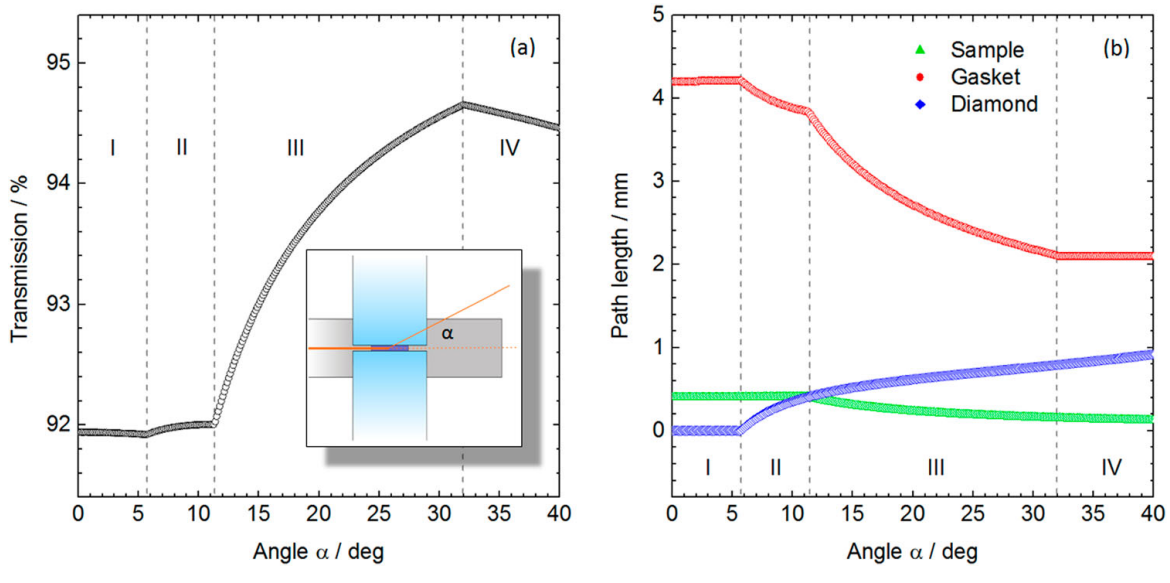

Figure 4. (a) Transmission of a steel gasket for the geometry $\Phi = -15°$, $X = 135°$ and $\Omega = 0°$. The model of a DAC used for this experiment is shown in the inset. For the beam, four cases for the path can be distinguished: (I) diamond-only, (II) diamond-gasket, (III) gasket-diamond-gasket, and (IV) gasket-only. (b) The respective path lengths through diamond and gasket.

barns, $\sigma_a = 0.004$ barns) relative to those of iron ($\sigma_s = 11.62$ barns, $\sigma_a = 2.56$ barns), chromium ($\sigma_s = 3.49$ barns, $\sigma_a = 3.05$ barns), and nickle ($\sigma_s = 18.50$ barns, $\sigma_a = 4.49$ barns) results in a smaller contribution of diamond to the total attenuation [39].

The total beam-path $D_i = d_i^{in} + d_i^{out}$ was calculated, with d^{in} and d^{out} being the path lengths through the respective materials to the centre of the sample chamber and from the centre out of the cell, respectively. The un-attenuated intensities, I_0, can then be calculated according to Beer's law from the observed intensities, I_{obs} as

$$I_{obs} = I_0 \cdot \prod_{i=1}^{n} \exp\left(-\rho_i D_i \sigma_i^s - \rho_i D_i \sigma_i^{a,\ddagger} \cdot \frac{m_{neut}\lambda}{h} \cdot 2200\frac{m}{s}\right). \quad (1)$$

In this equation ρ_i are the atom densities in atoms/m^3, D_i are the path-lengths, σ_i^s are the scattering cross-section and $\sigma_i^{a,\ddagger}$ are the absorption cross-section at 1.798 Å($v = 2200$ m/s); see [39,40]. For most nuclides, the scattering lengths and cross-sections are independent of the incident neutron wave vector in the thermal neutron region, while the absorption cross-sections are inversely proportional to v, the velocity of the neutron [39,41].

The calculated transmission as a function of the angle α (the angle of a beam relative to the gasket plane) for the geometry $\Phi = -15^\circ$, $X = 135^\circ$ and $\Omega = 0^\circ$ is given in Figure 4. It can be seen that the intensities of the reflected beam in this case vary by about 3%, with beams that are in plane with the gasket being attenuated strongest. This model, although more accurate than the spherical model, did not improve the R_w for the refinements significantly.

An attempt to refine anisotropic thermal parameters was made but proved unstable because the number of observed reflections was insufficient.

In a TOF neutron diffraction experiment, where the incident neutron beam travels through a single-crystalline diamond, neutrons with certain wavelengths will fulfil the Bragg condition and and hence be scattered. This can be seen in the transmission spectrum by 'diamond dips', which further decreases the intensity of incident neutrons around certain wavelengths [42]. Loveday et al. [43] showed that this effect is negligible at low pressures but becomes much more pronounced with pressure. Since experiments in this work were a) carried out in a way that the primary beam enters the cell through the gasket and b) were not carried out at high enough pressures, this effect was ignored in this work. At higher pressures and other geometries, an additional correction for 'diamond dips' also has to be applied.

3.2.5. Extinction correction

For the extinction correction a first-order Lorenzian model from GSAS-I was used. A better result for the bare crystal was obtained using the extinction models by Becker and Coppens [44] as employed by the JANA software package, but was not used here since all other error sources for this experiment outweighed the error due to extinction.

3.2.6. Integration and refinements

Several routines for the integration of the Bragg reflections obtained from the experiment were investigated. In figures 5 and 6, the plots show the calculated vs the observed structure factors, F_{calc} and F_{obs}, respectively, for the investigated integration and data-reduction routines. In an ideal case, F_{calc} from the structural model and F_{obs} obtained from the experiment will agree within the statistical error of the measurement, $F_{calc} = F_{obs}$, indicated by

the broken grey line. The insets in the respective plots show the relative difference between F_{obs} and F_{calc} ($|F_{obs} - F_{calc}|/F_{obs}$) as a function of F_{obs}.

First, the integrations were carried out using the standard TOPAZ algorithm (DAC_a), which automatically predicts peaks, finds an orientation matrix (UB-matrix, see [45]), and integrates the respective peaks. This automated algorithm failed here, as can be seen by strong scattered structure factors in Figure 5 (a). It is not surprising, that small structure factors (usually high-Q structure factors) fit particularly poorly. This refinement gave an overall R_w of 0.201, with R_w being the residual factor (R-factor)

$$R_w = \frac{\sum ||F_{obs}| - |F_{calc}||}{\sum |F_{obs}|}. \tag{2}$$

With a refined UB-matrix for every orientation (DAC_{UB}), R_w was reduced to 0.145, suggesting still a bad fit of the model to the data. Hence we picked the peaks manually

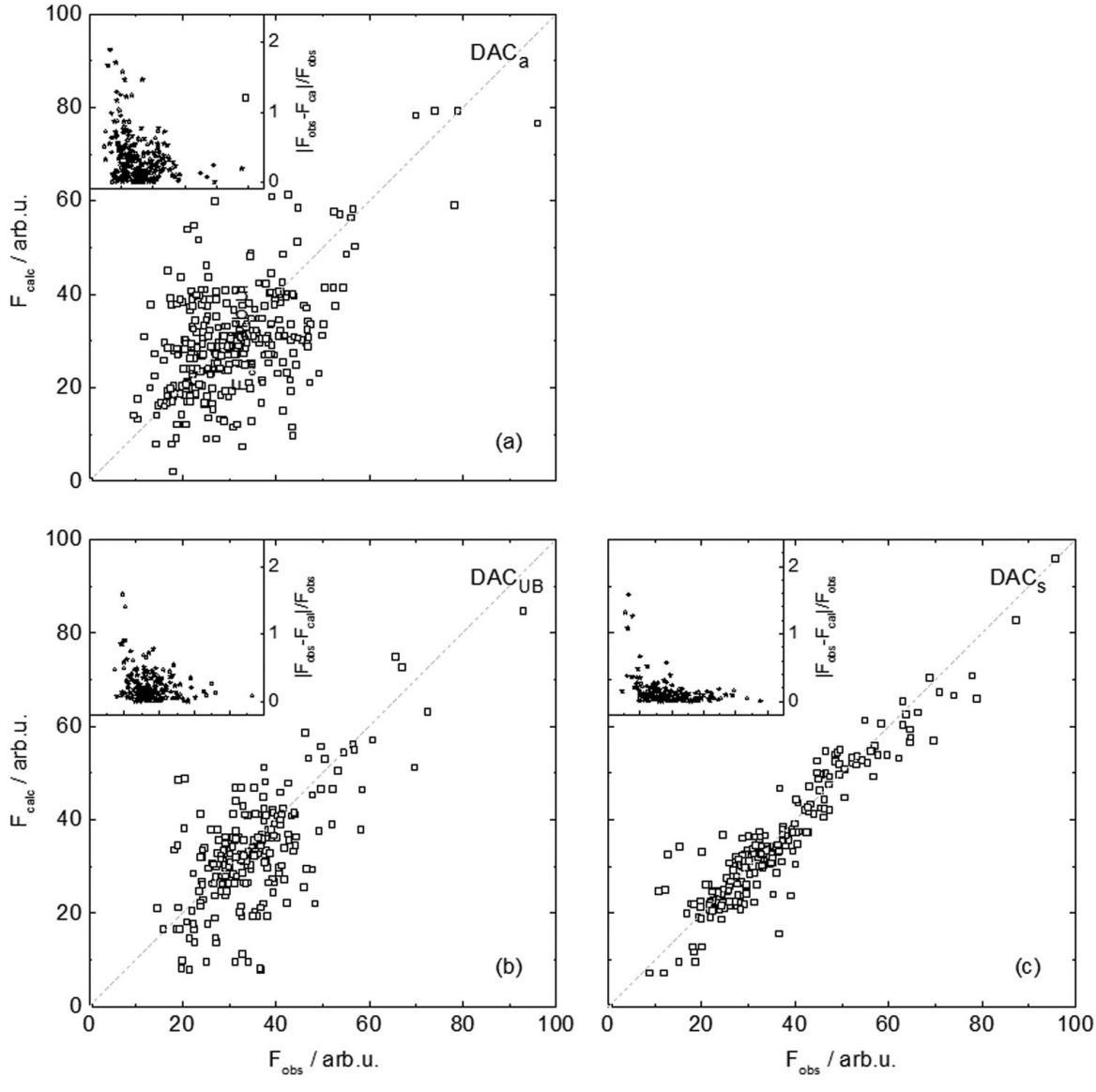

Figure 5. Observed versus calculated structure-factors for: (a) using the standard TOPAZ algorithm (DAC_a), (b) a refined UB for every orientation (DAC_{UB}), and (c) a selected subset of peaks (DAC_s). The insets give the relative difference between observed and calculated structure-factors as $|F_{obs} - F_{calc}|/F_{obs}$ as a function of F_{obs}.

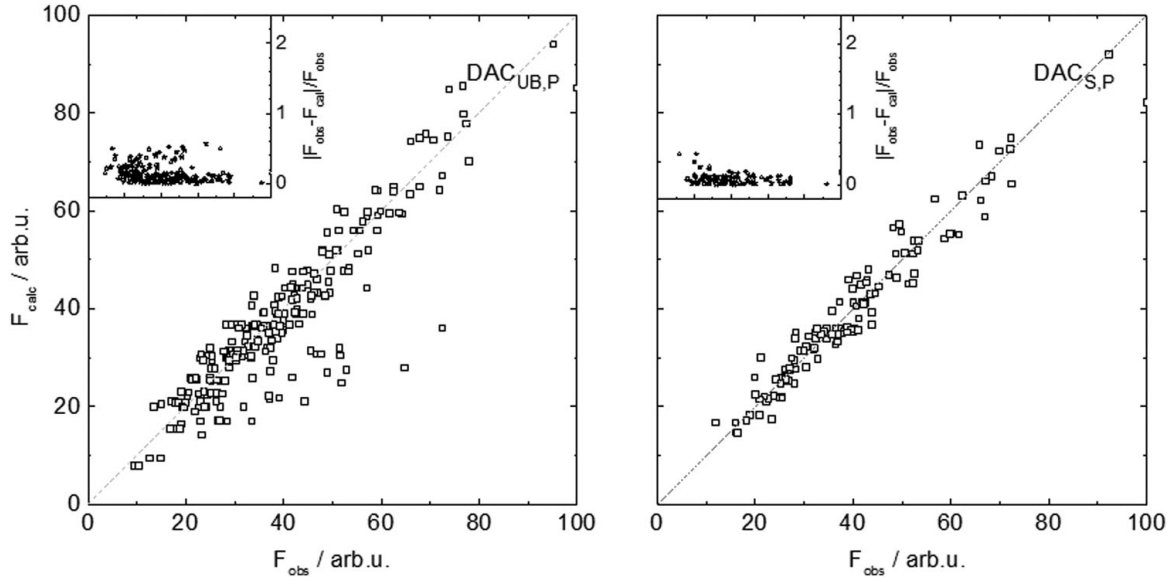

Figure 6. Observed vs Calculated Structure factors for (d) a refined UB for every orientation ($DAC_{UB,P}$), and (e) a selected subset of peaks ($DAC_{S,P}$). The integrations were carried out using the *IntegratePeaksProfileFitting* algorithm. The insets give the relative difference between observed and calculated structur facors as $|F_{obs} - F_{calc}|/F_{obs}$ as a function of F_{obs}.

in order to ensure that the Bragg reflections actually used for the refinement were not overlapped by a powder line or close to a detector edge, and had a sufficient s/n-ratio for the integration. Using this subset of peaks (DAC_S), we obtained an R_w of 0.117, a much better result than for the other routines. The F_{obs} vs F_{calc} plots for the DAC_{UB} and DAC_S routine are depicted in Figure 5(b,c), respectively. The integration discussed above were carried out using the *IntegrateEllipsoids* MANTID-algorithm (see MANTID documentation and [46]).

The same data sets as used in DAC_{UB} and DAC_S were then re-integrated using the *IntegratePeaksProfileFitting* algorithm ($DAC_{UB,P}$ and $DAC_{S,P}$, respecively). This algorithm uses two Gaussians to fit a peak in Q-space, an actual fitting technique. Compared to the *IntegrateEllipsoids* algorithm, the intensities and sigmas of the fitted peaks are in a better agreement with the data, particularly for weak reflections close to the s/n threshold (see MANTID documentation and [46]). The best fit of the data to the model was obtained using this method (cf. Figure 6) with R_w of 0.110 and 0.087, respectively.

The respective results for all the refinements are given in Table 4 in the appendix. Furthermore, all structural parameters are within 1σ of the data obtained from the bare crystal and hence comparable. Note that the data set integrated using the *IntegratePeaksProfileFitting* is not only more accurate than the data from the other routines, it also is 2-3 times more precise. Full structural refinements from single-crystal data in DACs are therefore possible on well-calibrated diffractometers with Anger cameras.

3.3. Is quantitative structure refinement of hydrogen-rich systems in a DAC on SNAP feasible?

SNAP has a much higher flux than TOPAZ, a feature that is needed for high-pressure experiments. However, fully quantitative SXL work on systems containing light elements has not

been explored yet - hence its capabilities for single-crystal diffraction had to be tested. To that end, a single crystal of about 1 mm^3 was placed on a vanadium pin and and diffraction patterns of ten orientations, each measured for 3 h, were collected. Compared to TOPAZ, the detector coverage is more limited and the sample stage deployed for this experiment allowed for rotations about the vertical omega axis only. These limitations significantly reduce the accessible reflections in comparison to TOPAZ. We were able to utilise TOPAZ data-reduction procedures for SNAP.

The results of the refinements for the data collected are given in Table 5 (cf. Table 5 appendix). A total of 1027 reflections were observed and an R_w of 0.067 was obtained. All structural parameters are within 1σ of the reference measurement carried out on TOPAZ (see section 3.1). Note that the lattice parameters in the DAC experiment deviates from the lattice parameter obtained from the bare crystal. This deviation stems from the limited rotation geometry which leads to an under-representation of reflections along the c-axis, and from a broad profile of the sample reflections in this experiment which introduced an error in the calculation of the orientation matrix. While the former is an intrinsic problem of the instrument, the latter was caused by a beam-guide with a suboptimal curvature. The accuracy of the determined lattice parameters greatly improved after an upgrade of the guide in 2018 (see lattice parameters for ice VI in section 3.4. which were determined after the guide-upgrade).

The same experiment as detailed above for TOPAZ was repeated with a DAC-sized crystal and similar results for the refinement were obtained (cf. Table 5). A total of 279 reflections were observed and an R_w of 0.090 obtained. Even though the number of observed reflections dropped by a factor of 4, the structural parameters remained well within 1σ of the larger crystal and within 1-2σ of the reference measurement on TOPAZ. Please note that the error-bars only tripled by reducing the volume by a factor of 35 from 1.028 mm^3 to 0.028 mm^3.

These results show that SNAP as it is setup presents some limitations but in principle similar data quality as on TOPAZ can be achieved and as such can yield accurate structural data.

Finally, the smaller crystal was placed in a real neutron DAC and measured as well. The set-up allows for rotation about ω only with the primary beam entering the cell through the gasket. The DAC was rotated about ω to six orientations and patterns were collected for 3 h each. Despite the short collection time, 56 Bragg peaks with an acceptable I/σ ratio were found and integrated. The empirical 3*n*-rule suggests that for a (isotropic) refinement of DKDP (4 atoms) at least 48 reflections are needed - which was achieved here.

Lattice parameters, and structural parameters of this experiment are shown in Table 5. The fractional refinements carried out on with this small data set resulted in an overall R_w of 0.336. The atomic coordinates obtained from this data set are still correct, but due to the the reciprocal space coverage explored, the uncertainties are very large and in the order of 0.05-0.20. With a similar collection time as on TOPAZ (6–8 h), better results should be possible.

3.4. Application on samples under pressure: a structural study of ice VI

In order to test our method against a sample under pressure, a single crystal of ice VI was measured. The sample was grown under a pressure of 1.1 GPa in a DAC ($\varnothing_{culet} = 1.43$ mm;

Table 1. Comparison of structural parameters of ice VI as reported by Kuhs et al. [31] (top) and this study (bottom).

	x	*y*	*z*	Occ.	U_{iso}
O1 (2a)	0.7500(00)	0.2500(00)	0.7500(00)	1	0.0299(49)
O2 (8g)	0.7500(00)	0.5295(43)	0.1339(38)	1	–
D1 (8g)	0.7500(00)	0.4628(92)	−0.0131(86)	0.5	0.0380(51)
D2 (8g)	0.7500(00)	0.3103(64)	−0.1365(101)	0.5	–
D3 (8g)	0.7500(00)	0.6812(10)	0.1248(18)	0.5	–
D4 (16h)	0.1325(41)	0.5301(51)	0.1844(51)	0.5	–
O1 (2a)	0.7500(00)	0.2500(00)	0.7500(00)	1	0.0208(25)
O2 (8g)	0.7500(00)	0.5337(25)	0.1306(23)	1	–
D1 (8g)	0.7500(00)	0.4450(40)	−0.0120(50)	0.5	0.0211(27)
D2 (8g)	0.7500(00)	0.3850(60)	−0.1423(29)	0.5	–
D3 (8g)	0.7500(00)	0.6799(32)	0.1330(40)	0.5	–
D4 (16h)	0.1333(27)	0.5330(30)	0.7930(25)	0.5	–

Notes: Data were collected on SNAP.

steel gasket, $\varnothing_{hole} = 800$ m, indented to 136 μm; pressure from the EOS of ice VI as given by Bezacier et al. [47]) by repeatedly melting and re-crystallising an ice VI powder resulting in the formation of a single-crystal. The cell containing the sample was then aligned on the SNAP instrument and patterns for three orientations were collected (about 12h per orientation). Altogether, 84 structure factors were obtained after the data reduction procedure and outlier removal. From the UB-matrices, the lattice parameters of the single-crystal were found to be $a = b = 6.205(6)$ Åand $c = 5.709(2)$ Å.

Similarly to DKDP, ice VI is a well known structure and has been studied thoroughly [31,47–50]. Ice VI shows a tetragonal crystal system with the space group $P4_2/nmc$; its unit cell contains 10 water molecules and has the dimensions $a = 6.1845(1)$ Åand $c = 5.6981(1)$ Åat 1.26 GPa [47]. The oxygen atoms are on a 2a and 8g site, and the hydrogens are located on three 8g sites and one 16h site - hence, only 17 parameters are needed for a structural refinement with isotropic atomic displacement parameters.

A preliminary refinement for the 17 parameters in an ice VI crystal resulted in an overall weighted R-factor of $R_w = 0.1302$; constraining the isotropic atomic displacement parameters for the two atoms dropped the R_w further to 0.1109. (Similar to the DKDP a refinement with anisotropic thermal parameters was attempted but gave no physically sensible results.)

The structural parameters for ice VI as given by Kuhs et al. [31] and the values for this refinement are shown in Table 1.

Table 2. Summary of the refinements for the crystals and the crystal in a DAC-sample environment for SNAP and TOPAZ, respectively.

Crystal	Small	Large	Small	DAC	DAC	DAC
Sample	DKDP	DKDP	DKDP	DKDP	DKDP	Ice VI
Instrument	TOPAZ	SNAP	SNAP	TOPAZ	SNAP	SNAP
Orientations	10	6	6	10	6	3
Collection time	3 h	3 h	3 h	6–8 h	3 h	12 h
Reflections	1044	1027	279	167	56	84
R_w	0.045	0.067	0.090	0.087	0.336	0.1302

Notes: The collection time per orientation is give as well as the number of reflections after outlyer removal. Only best refinements are shown - for detailed information see tables 4 and 5 in appendix.

4. Conclusion

We performed several neutron-scattering experiments on the TOPAZ and SNAP beam lines at the Spallation Neutron Source (SNS) at Oak Ridge National Laboratory (ORNL). As a samples, we used deuterated potassium dihydrogen-phasphate (DKDP) and water ice VI. Results of our suite of experiments on single-crystal neutron-diffraction in diamond anvile cells promising results that are summarised in Table 2.

In a first trial experiment we showed that it is possible to obtain data of high quality from a DAC-sized crystal. Our results are in good accordance with the crystal structure published by Tibballs and Nelmes [30], indicating that it is feasible to reduce the sample size to a volume smaller than that of a typical netron-DAC cavity. We repeated the experiment in the sample environment of a diamond anvil cell. Despite the - not surprising - loss of data quality, we were able to obtain enough structure factors to refine the structure with the same accuracy as in the case of the bare crystal, however, the errors on the structural parameters increased significantly.

In a second step, we bench-marked SNAP, an instrument primarily used for powder diffraction, for quantitative analysis of single crystal data. We were able to show that quantitative single crystal diffraction on hydrogen-rich materials on SNAP is possible and that the data is of similar quality to TOPAZ. Subsequently, we collected patterns of a DAC-sized sample to test the volume limitations of SNAP. We were able obtain 279 structure factors - enough to refine the structure to $R_w = 0.090$.

Finally, we collected patterns of a single crystal samples of DKPD and ice in a diamond anvil cell on SNAP. Due to time restrictions, we only obtained 56 reflection from 6 orientations measured for 3 h each; a similar experiment carried out on TOPAZ (10 orientations for 6–8 h each) in comparison resulted in about 300 structure factors. Nevertheless was it possible to refine the structure from the obtained data, however, the large errors on the atomic coordinates suggest that a similar collection time as on TOPAZ is needed for precise results.

The data reduction procedure was then tested against a crystal of ice VI which was grown in a DAC. Diffraction patterns of three orientations (measured for 12h each) resulted in 84 observed structure factors - enough to carry out a refinement that reproduced the published structure of ice VI, proving that quantitative HP-SCND on SNAP in a DAC is possible.

Acknowledgments

This work was conducted at the Spallation Neutron Source (SNS), a Department of Energy (DoE) user facility BM, JJM, XW, AMS, MG and JSL conducted the experiments. BM analysed the data. LDD synthesised the samples. BH and RB contributed to the context of pressure experimentation. All authors contributed to discussions of the work, analysis and to the writing of the manuscript. We would like to thank Vickie E. Lynch for discussion and advice regarding MANTID.

BM acknowledges funding under SUPA's PECRE scheme, by the Shull Wollan center at ORNL and by the ESF through the Hecate grant.

Disclosure statement

Funding

The authors acknowledges funding under SUPA's PECRE scheme, by the Shull Wollan center at ORNL and by the European Research Council through the Hecate grant no. 695527.

References

[1] Goncharenko I, Loubeyre P. Neutron and X-ray diffraction study of the broken symmetry phase transition in solid deuterium. Nature. 200507;435:1206–1209.
[2] Cavazzoni C, Chiarotti GL, Scandolo S, et al. Superionic and metallic states of water and ammonia at giant planet conditions. Science. 1999;283:44–46.
[3] Millot M, Hamel S, Rygg J, et al. Experimental evidence for superionic water ice using shock compression. Nat Phys. 2018;14:297–302.
[4] Guillot T. The interior of gas planets : models and outstanding questions. Ann Rev Earth Planet Sci. 2005;33:493–530.
[5] Helled R, Anderson JD, Podolak M, et al. Interior models of uranus and neptune. Astrophys J. 2011;15:726.
[6] Hubbard WB. Neptune's deep chemistry. Science. 1997;275:1279–1280.
[7] Loveday JS, Nelmes RJ. High-pressure neutron diffraction and models of titan. High Press Res. 2003;23:41–47.
[8] Tobie G, Grasset O, Lunine JI, et al. Titan's internal structure inferred from a coupled thermal-orbital model. Icarus. 2005;175:496–502.
[9] Shin K, Kumar R, Udachin KA, et al. Ammonia clathrate hydrates as new solid phases for Titan, Enceladus, and other planetary systems. Proc Natl Acad Sci. 2012;109(37):14785–14790.
[10] Bezacier L, Tobie G, Bollengier O, et al. Dissociation temperatures of methane hydrates at high pressure: implications for the differentiation of Titan's interior (259285). Vol. 6; 2013. p. 6–7.
[11] Silvera IF. The solid molecular hydrogens in the condensed phase: fundamentals and static properties. Rev Modern Phys. 1980;52(2):393–452.
[12] Cui L, Chen NH, Silvera IF. Excitations, order parameters, and phase diagram of solid deuterium at megabar pressures. Phys Rev B. 1995;51(21):14987–14997.
[13] Mao H k., Hemley R. Ultrahigh transitions in solid hydrogen. Rev Mod Phys. 2001;66(2):671–692.
[14] Geneste G, Torrent M, Loubeyre P, Strong isotopic effect in phase II of dense solid hydrogen and deuterium. (phase II); 2012.
[15] Berg JM, Tymoczko JL, Stryer L. Biochemistry. 5th ed. Oxford: W.H. Freeman; 2002.
[16] Gao L, Xue Y, Chen F, et al. Superconductivity up to 164 K in $HgBa_2Ca_m - 1Cu_mO_2m + 2 + \delta$ (m=1, 2, and 3) under quasihydrostatic pressuresSuperconductivity up to 164 K in $hgBa_2Ca_m - 1Cu_mO_2m + 2 + \delta$ (m=1, 2, and 3) under quasihydrostatic pressures. Phys Rev B. 1994;50(6):4260–4263.
[17] Chen X, Struzhkin V, Yu Y, et al. Enhancement of superconductivity by pressure-driven competition in electronic order. Nature. 2010;466(7309):950–953.
[18] Duang D, Liu Y, Tian F, et al. Pressure-induced metallization of dense $(H_2S)_2H_2$ with high-T_c superconductivity pressure-induced metallization of dense $(H_2S)_2H_2$ with high-T_c superconductivity. Sci Rep. 2014;4(6968):30–32.
[19] Drozdov AP, Eremets MI, Troyan IA. Conventional superconductivity at 203 Kelvin at high pressures in the sulfur hydride system. Nature. 2015;525:73–76.
[20] Pauling L. The structure and entropy of ice and of other crystals with some randomness of atomic arrangement. J Am Chem Soc. 1935;57(12):2680–2684.

[21] Wollan EO, Davidson WL, Shull CG. Neutron diffraction study of the structure of ice. Phys Rev. 1949;75(9):1348.
[22] Besson J, Nelmes R, Hamel G, et al. Neutron powder diffraction above 10 GPa. Am Mineral. 1992;907:180–181.
[23] Klotz S. Techniques in high pressure in neutron scattering. 1st ed. Boca Raton: CRC Press; 2013.
[24] Boehler R, Guthrie M, Molaison JJ, et al. Large-volume diamond cells for neutron diffraction above 90 GPa. High Press Res. 2013;33:546–554.
[25] Boehler R. Novel diamond cells for neutron diffraction using multi-carat CVD anvils. Rev Sci Inst. 2017;88:08390.
[26] Haberl B, Dissanayake S, Wu Y, et al. Next-generation diamond cell and applications to single-crystal neutron diffraction. Rev Sci Instrum. 2018;89(9):092902.
[27] Guthrie M, Boehler R, Molaison JJ, et al. Structure and disorder in ice VII on the approach to hydrogen-bond symmetrization. Phys Rev B. 2019;99:184112.
[28] Binns J, Kamenev KV, McIntyre GJ, et al. Use of a miniature diamond-anvil cell in high-pressure single-crystal neutron Laue diffraction. IUCrJ. 2016;3:168–179.
[29] Grzechnik A, Meven M, Friese K. Single-crystal neutron diffraction in diamond anvil cells with hot neutrons research papers. J Appl Cryst. 2018;51:351–356.
[30] Tibballs JE, Nelmes RJ. The P-T dependence of the crystal-structure of KDP and DKDP above T_cThe P-T dependence of the crystal-structure of KDP and DKDP above T_c. J Phys C Solid State Phys. 1982;15(25):L849–L853.
[31] Kuhs WF, Finney JL, Vettier C, et al. Structure and hydrogen ordering in ices VI, VII, and VIII by neutron powder diffraction. J Chem Phys. 1984;81:3612–3623.
[32] Wang X, Hoffmann C, TOPAZ - single crystal diffractometer; 2018. Available from: https://neutrons.ornl.gov/sites/default/files/TOPAZ.pdf.
[33] Calder S, An K, Boehler R, et al. A suite-level review of the neutron powder diffraction instruments at Oak Ridge National Laboratory. Rev Sci Instrum. 2018;89(9):092701.
[34] Haberl B, Dissanayake S, Ye F, et al. Wide-angle diamond cell for neutron scattering. High Press Res. 2017;37(4):495–506.
[35] Arnold O, Bilheuxc JC, Borreguero JM, et al. Mantid–data analysis and visualization package for neutron scattering and μSR experimentsMantid–Data analysis and visualization package for neutron scattering and μSR experiments. Nucl Instrum Meth Phys Res Sect A. 2014;764:156–166.
[36] Toby BH. EXPGUI, a graphical user interface for GSAS. J Appl Cryst. 2001;34:210–213.
[37] Larson A, Dreele RV, GSAS manual; 2000. Los Alamos National Laboratory Report, LAUR 86-748.
[38] Lea DE. Secondary gamma rays excited by the passage of neutrons through matter. Proc R Soc Lond Ser A. 1912;150(13):637–668.
[39] Sears VF. Neutron scattering lengths and cross sections special feature neutron scattering lengths and cross sections. Neutron News. 1992;3(3):26–37.
[40] Giacovazzo C, Monaco H, Viterbo D. Fundamentals of crystallography. Vol. 2. 3rd edn. Oxford: Oxford University Press; 1992.
[41] Koester L. Neutron physics. Vol. 1. Berlin: Springer-Verlag; 1977.
[42] Guthrie M, Pruteanu C, Donnelly M-E, et al. Radiation attenuation by single-crystal diamond windows. J App Cryst. 2017;50(1):76–86.
[43] Loveday JS, McMahon MI, Nelmes RJ. The effect of diffraction by the diamonds of a diamond-anvil cell on single-crystal sample intensities. J Appl Crystallogr. 1990;23(5):392–396.
[44] Becker PJ, Coppens P. Extinction within the limit of validity of the Darwin transfer equations - general formalisms for primary and secondary extinction and their application to spherical crystals. Acta Cryst. 1974;A30(2):129–147.
[45] Busing WR, Levy HA. Angle calculations for 3- and 4-circle X-ray and neutron diffractometers. Acta Crystallogr. 1967;22(4):457–464.
[46] Schultz AJ, Jørgensen MRV, Wang X, et al. Integration of neutron time-of-flight single-crystal Bragg peaks in reciprocal space. J Appl Crystallogr. 2014;47(3):915–921.
[47] Bezacier L, Journaux B, Perrillat JP, et al. Equations of state of ice VI and ice VII at high pressure and high temperature. J Chem Phys. 2014;141(10):104505. doi:10.1063/1.4894421

[48] Bridgman PW. Water, in the liquid and five solid forms, under pressure. Proc Am Acad Arts Sci. 1912;47(13):441–558.
[49] Kuhs WF, Ahsbahs H, Londono D, et al. In-situ crystal growth and neutron four-circle diffractometry under high pressure. Physica B. 1989;156-157:684–687.
[50] Kuo JL, Kuhs WF. A first principles study on the structure of ice-vi: static distortion, molecular geometry, and proton ordering. J Phys Chem B. 2006;110(8):3697–3703.

Appendix

Table A1. Orientations of the DKDP crystal.

Sample	DKDP			DKDP			DKDP		
Size	Small			Small (DAC)			Large		
Diffractometer	TOPAZ			TOPAZ			SNAP		
Orientation	*X* / deg	Φ / deg	Ω / deg	*X* / deg	Φ / deg	Ω / deg	*X* / deg	Φ / deg	Ω / deg
1	135.00	0.02	0.00	135.00	−15.00	−0.02	0.00	0.00	129.98
2	135.00	−26.70	105.95	135.00	−15.00	29.99	0.00	0.00	149.96
3	135.00	28.71	−149.95	135.00	−15.00	−30.01	0.00	0.00	169.96
4	135.00	−177.09	−174.68	135.00	20.00	−25.00	0.00	0.00	189.96
5	135.00	−51.33	10.75	135.00	20.00	25.02	0.00	0.00	209.95
6	135.00	116.75	10.14	135.00	55.00	20.03	0.00	0.00	229.96
7	135.00	44.88	31.08	135.00	55.00	80.02	0.00	0.00	249.96
8	135.00	−130.16	14.12	135.00	55.00	43.99	0.00	0.00	269.96
9	135.00	52.44	140.49	135.00	55.00	69.01	0.00	0.00	289.96
10	135.00	14.35	100.26	135.00	40.00	47.00	0.00	0.00	299.96

Sample	DKDP			DKDP		
Size	Small			Small (DAC)		
Diffractometer	SNAP			SNAP		
Orientation	*X* / deg	Φ / deg	Ω / deg	*X* / deg	Φ / deg	Ω / deg
1	0.00	0.00	64.97	0.00	0.00	−60.02
2	0.00	0.00	79.98	0.00	0.00	−74.98
3	0.00	0.00	94.96	0.00	0.00	−89.96
4	0.00	0.00	109.96	0.00	0.00	−104.96
5	0.00	0.00	124.96	0.00	0.00	−119.96
6	0.00	0.00	139.96	0.00	0.00	−134.96

Notes: The respective goniometer angles *X*, Φ, and Ω in degree are given. Note that on TOPAZ *X* is fixed to 135°, and on SNAP *X* and Φ are fixed to 0°.

Table A2. Comparison of refinements of data of DKDP in a diamond anvil cell (V =0.028 mm^3).

Crystal	KDP*	DKDP*	DKDP	DKDP	DKDP	DKDP	DKDP	DKDP
Sample Environment	None	None	None	DAC	DAC	DAC	DAC	DAC
Int. Method			Auto	DAC_a	DAC_{UB}	DAC_S	$DAC_{UB,P}$	$DAC_{S,P}$
Note	Nelmes '82	Nelmes '82						
Obs	–	–	1044	359	216	222	323	167
Rw(Fobs)	0.022	0.055	0.045	0.201	0.145	0.117	0.110	0.087
a	7.4521(4)	7.4645(3)	7.4505(12)	7.4534(10)	7.4534(4)	7.4660(7)	7.4713(3)	7.4652(8)
c	6.974(2)	6.9678(4)	6.9679(15)	6.9701(8)	6.9732(4)	6.9733(6)	6.9722(2)	6.9779(7)
a/*c*	0.936	0.934	0.933	0.935	0.936	0.934	0.933	0.934
O–O	2.4944(5)	2.5286(4)	2.5322(4)	2.37(2)	2.3923(4)	2.51(2)	2.507(9)	2.511(9)
O–P	1.5402(4)	1.54207(19)	1.53717(16)	1.51(1)	1.59568(16)	1.551(10)	1.545(4)	1.541(7)
O–D	1.0657(12)	1.0419(3)	1.062(8)	1.13(9)	0.97830(14)	1.071(11)	1.05(1)	1.05(1)
D–D	0.367(3)	0.4511(4)	0.420(16)	0.31(8)	0.44359(6)	0.404(6)	0.45(2)	0.42(6)
x(D)	0.14757(12)	0.14861(2)	0.14844(23)	0.1331(21)	0.1444(18)	0.1528(23)	0.1467(10)	0.1474(18)
y(D)	0.22559(15)	0.22011(2)	0.2217(10)	0.258(11)	0.2204(11)	0.2250(40)	0.2222(12)	0.2220(35)
z(D)	0.12161(47)	0.12041(3)	0.1196(10)	0.146(6)	0.12173(6)	0.1140(40)	0.1229(14)	0.1250(40)
x(O)	0.14839(3)	0.14888(1)	0.14891(11)	0.1438(17)	0.15215(14)	0.1472(15)	0.1494(5)	0.1486(9)
y(O)	0.08264(3)	0.08073(1)	0.08070(11)	0.0909(13)	0.08957(12)	0.0836(12)	0.0822(6)	0.0818(11)
z(O)	0.12584(5)	0.12643(2)	0.12566(11)	0.1166(9)	0.12942(8)	0.1299(21)	0.1254(4)	0.1258(8)
UISO (D)	–	–	0.0279(8)	−0.017(6)	0.17(6)	0.0288(16)	0.0256(16)	0.033(4)
USIO (O)	–	–	0.0183(12)	0.045(9)	0.064(26)	0.0179(21)	0.0146(8)	0.0166(20)

Notes: The data was integrated using the standard TOPAZ algorithm (DAC_a), a refined UB for every orientation (DAC_{UB}), and a selected subset of peaks (DAC_s) to exclude peaks on powder lines. While for the first integrations were carried out using the *IntegrateEllipsoid* algorithm, the last column (DAC_p) was treated as the DAC_s data but integrated using the *IntegratePeaksProfileFitting* algorithm. The well established routine for bare crystals as used on TOPAZ is labelled *Auto*.

Table A3. Sequentially deteriorating data quality with the crystal size (large about 1 mm^3; small about 0.028 mm^3) and the complexity of the sample environment.

Crystal	KDP*	DKDP*	DKDP (s)	DKDP (l)	DKDP (s)	DKDP (s)
Diffractometer			TOPAZ	SNAP	SNAP	SNAP
Sample Environment	None	None	None	None	None	DAC
Int. Method			Auto	Auto	Auto	DAC_m
Note	Nelmes '82	Nelmes '82				
Obs	–	–	1044	1027	279	56
Rw(Fobs)	0.022	0.055	0.045	0.067	0.090	0.336
a	7.4521(4)	7.469(1)	7.4505(12)	7.4871(7)	7.4871(7)	7.486(3)
c	6.974(2)	6.976(1)	6.9679(15)	7.0025(8)	6.9909(8)	7.002(10)
a/*c*	0.936	0.934	0.933	0.934	0.934	0.936
O–O	2.4944(5)	2.5286(4)	2.5322(4)	2.535(3)	2.530(8)	2.42(8)
O–P	1.5402(4)	1.54207(19)	1.53717(16)	1.5478(12)	1.544(4)	1.61(5)
O–D	1.0657(12)	1.0419(3)	1.062(8)	1.056(3)	1.066(8)	0.99(12)
D–D	0.367(3)	0.4511(4)	0.420(16)	0.430(5)	0.404(13)	0.5(3)
x(D)	0.14757(12)	0.14861(2)	0.14844(23)	0.14868(24)	0.1487(10)	0.142(14)
y(D)	0.22559(15)	0.22011(2)	0.2217(10)	0.22150(18)	0.2233(8)	0.219(15)
z(D)	0.12161(47)	0.12041(3)	0.1196(10)	0.1199(4)	0.1209(15)	0.124(20)
x(O)	0.14839(3)	0.14888(1)	0.14891(11)	0.14901(11)	0.1488(5)	0.161(4)
y(O)	0.08264(3)	0.08073(1)	0.08070(11)	0.08096(10)	0.0810(5)	0.088(5)
z(O)	0.12584(5)	0.12643(2)	0.12566(11)	0.12577(13)	0.1260(5)	0.121(8)
UISO (O)	–	–	0.0183(12)	0.02612(4)	0.01755(5)	0.006(10)
UISO (D)	–	–	0.0279(8)	0.01664(5)	0.01709(8)	0.023(33)

On a New Nitrogen sX Hydrate from Ice XVII

B. Massani,[1] L. J. Conway,[1] A. Hermann,[1, a)] and J. Loveday[1, b)]
SUPA, School of Physics and Astronomy and Centre for Science at Extreme Conditions, The University of Edinburgh, Edinburgh EH9 3FD, United Kingdom

(Dated: 18 April 2019)

Recently a new gas hydrate structure has been discovered. This structure, sX, is unique in a sense that it is so far the only gas hydrate with chiral channels. It is formed by hydrogen-water or carbon dioxide-water mixtures at pressures above 0.3 GPa and it has been shown that it is the only clathrate hydrate that is refillable with hydrogen. This property makes it a possible storage material for gases. By analysing neutron diffraction data and calculations based on density-functional theory, we show that sX is also refillable with nitrogen; the guest:host ratio will be shown to be 2.7. Furthermore we report sX's decomposition behaviour and give evidence that it undergoes several transitions into the exotic hydrates sH and sIII that have not been observed at these pressure and temperature conditions - before forming the stable nitrogen hydrate sII.

PACS numbers: Valid PACS appear here
Keywords: Gas hydrate, Neutron diffraction, DFT

I. INTRODUCTION

Water has a very complex phase diagram with at least eighteen recorded crystal structures[1–4], three amorphous[5–8] and one, possibly two, liquid phases[9] - depending on temperature and pressure. When incorporated into binary mixtures additional rich complexity is observed. At present there are at least ten guest host structures reported in which a small "guest" molecule is confined in a "host" lattice consisting of water[10–13]. Some of these are based on cages, so called clathrate hydrates where the water network forms cage-like structures (from *kleithron*, Greek: door bar). Others are based on ice structures with the guest molecules filling holes in a water network based on a known ice structure[12], and another, sX, is based on a network of spiral channels[13–15].

The structures are stabilised by the interplay between hydrogen bonds and other interactions. The host network is held together by hydrogen-bonded water molecules, while the guest-host interaction is mainly of a hydrophobic nature (exceptions exist[16]). Hence, gas hydrates provide the means to probe van der Waals, hydrophobic and hydrogen-bond forming interactions and their interplay[17]. These forces are crucial in many biochemical processes such as protein and DNA folding, protein-ligand interaction, formation of the cell wall and the overall structure of the cell[18,19]. Gas hydrates provide relatively simple model systems against which to test models of intermolecular potentials[20]. Furthermore, they they also occur commonly in nature, e.g. methane clathrate hydrate present on the ocean floor makes up most of Earths methane reserve[17,21,22]. Methane hydrate is also believed to have been the dominant methane-containing phase in the nebula from which the outer planets and their satellites formed (For example Enceladus and Titan[23]). Finally, gas hydrates have potential technological applications, for example, in the transport and storage of gases, e.g. hydrogen[24].

Amongst the hydrate water networks, sX, first discovered as part of the C_0 structure of hydrogen hydrate[25], stands out: it is chiral, has channels rather than cages, is not based on a stable ice structure, and its network does not have an analogue in either silica or zeolite structures[13,26]. It does, however, exist in some ternary Zintl compounds and has been suggested as a metastable group-14 structure[27–29]. The structure proposed initially was based on channels that contained sites partially occupied by non-hydrogen bonded water molecules[25]. Based on the observed high mobility of hydrogen in this structure[25] and molecular-dynamics modelling, Smirnov *et al.* proposed what emerged to be the correct structure: they suggested that the water molecules in the channels were in fact nitrogen molecules that had been absorbed from the liquid storage medium between recovery and the diffraction measurement[30]. Subsequently, del Rosso *et al.* were able to empty C_0 of hydrogen and to identify the structure as a new form of ice, ice XVII[3,14]. Finally, Amos *et al.* found that sX also exists in the carbon dioxide:water system and determined the full structure of both hydrogen and carbon dioxide hydrates *in situ* using neutron diffraction[13].

Due to the high guest-host ratio, the reversibility of the filling and emptying, and the high mobility of hydrogen in the cavities, the sX/ice XVII system has been proposed as a possible hydrogen storage material[31,32]. Other possible applications, however, have not been discussed. With its channel structure, and high surface area, ice XVII resembles activated charcoal and could therefore be used as a low-temperature molecular sieve. Here, we show using high-pressure neutron diffraction data that ice XVII

a)https://www.ph.ed.ac.uk/people/andreas-hermann; Electronic mail: a.hermann@ed.ac.uk
b)https://www.ph.ed.ac.uk/people/john-loveday; Electronic mail: j.loveday@ed.ac.uk

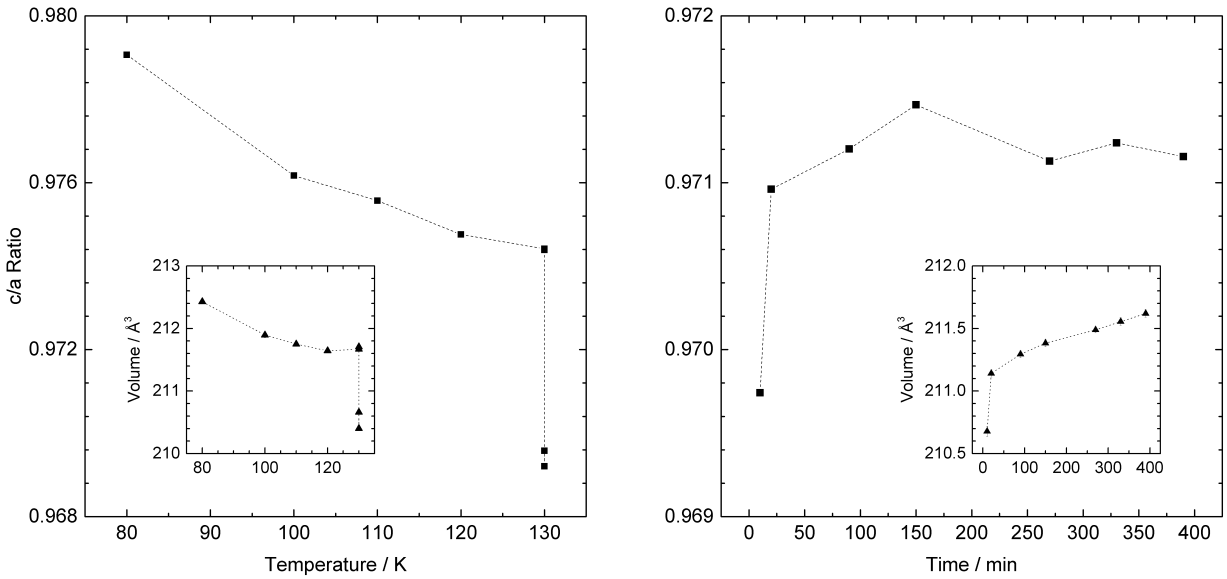

FIG. 1. Left: The c/a ratio and overall unit cell volume of hydrogen sX as a function of temperature (the three values at 130K were recoreded over a period of about 7 hours). The shrinking of the overall volume indicates the removal of hydrogen from the channels. Right: The c/a ratio and overall unit cell volume of hydrogen sX as a function of time. The increase in volume (primarly along the c-axis) indicates the uptake and incorporation of nitrogen into the chiral channels.

can, indeed, absorb nitrogen molecules. Furthermore we show that nitrogen sX undergoes a series of transformations into other, exotic, hydrate types before forming the stable sII structure.

II. METHODS

We have conducted this experiment in an aluminium gas pressure cell at the PEARL beam-line, the dedicated high-pressure powder instrument at the ISIS neutron source at the Rutherford Appleton Laboratory (RAL, Oxfordshire, UK)[33]. This instrument has access to a d-spacing range out to beyond 4 Å, which is necessary to record sX's (101) Bragg reflection at 4.1 Å. This peak is very sensitive to the guest site occupation. The analysis of the diffraction patterns was carried out by either Rietveld or LeBail profile refinement using the GSAS-II crystallographic software package[34].

Enthalpy calculations based on density functional theory (DFT) were performed using the CASTEP code[35] on sets of approximant sX structues with a range of tractable guest-host ratios as well as fully filled nitrogen hydrate III (NH-III). Exchange-correlation effects were described within the generalized gradient approximation (GGA) using the Perdew-Burke-Ernzerhof (PBE) functional[36] and ultrasoft pseudopotentials as generated 'on-the-fly' by CASTEP with radii cut-offs of 1.1 Bohr for oxygen and nitrogen, and 0.6 Bohr for hydrogen. Geometry optimisations were performed with plane wave cut-offs of 1000 eV and a Monkhorst-Pack[37] k-point spacings of no more than $2\pi \times 0.04$ Å^{-1}. The calculations were performed on water networks with ordered hydrogen bonds arranged as to give a zero net dipole. To calculate stable compounds, we compare enthalpy values, $H = U + PV$ where U is the internal energy per molecule and P and V are the pressure and molecular volume respectively. To compare with a decomposition into the pure molecular phases, we also perform calculations on ices XI, IX, XV, VIII and the relevant phases of α-, γ-, and ϵ-N_2[38].

Deuterated water (D_2O)[39] was frozen to produce ice I_h and ground under liquid nitrogen to a fine powder. The powder then was filled into a cooled hydrogen-compatible gas cell at 77 K and pressurised with hydrogen gas to 0.3 GPa. To control the temperature in the cell during the experiment, an ILL pattern 'Orange' helium cryostat was used. Upon heating to 195 K at 0.3 GPa, the H_2-I_h mixture undergoes transitions first to the C_{-1} hydrate at 160 K and than to C_0 (H_2-sX) above 180 K[40,41]. After the full transformation to C_0, the sample was cooled to 80 K and the pressure was released. It is well known that ice XVII can be easily formed by pumping off the hydrogen in sX[3], however, the same can be achieved by heating the hydrogen hydrate at ambient pressure to 130 K[40]. As the hydrogen left the structure, the volume of the unit cell started to decrease, indicating the emptying of the channels in sX. To ensure that the starting material for the experiment is pure ice XVII, diffraction patterns were collected every hour. The transformation was considered complete after about 12 h, at which point the volume of the unit cell did not shrink any further with time (see left panel in Figure 1).

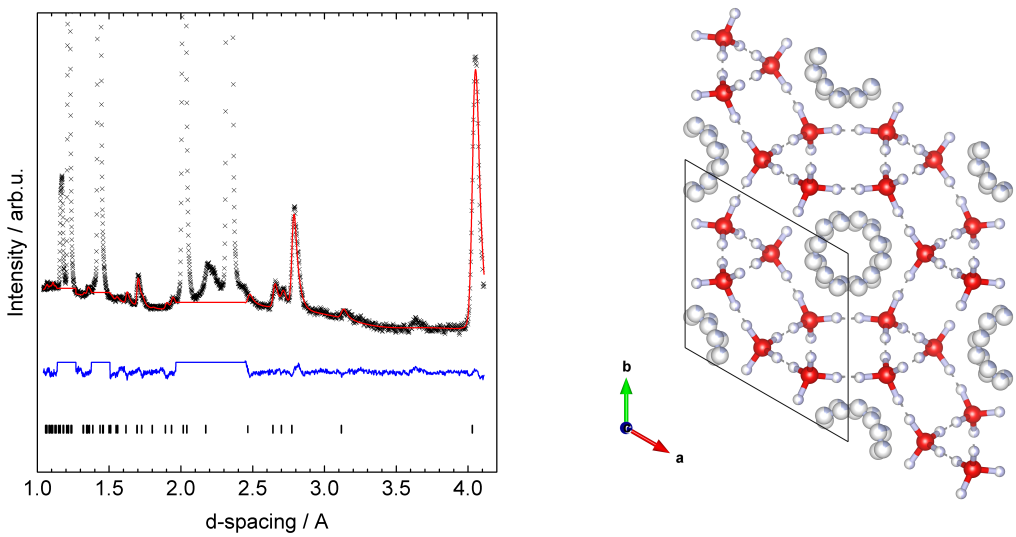

FIG. 2. Left: The results of a Rietveld profile refinement of data collected at 0.018 GPa and 130 K using the nitrogen sX structure. Black crosses are measured data points, the red curve gives the calculated pattern, and blue line the difference between observed and calculated profiles. The excluded sections correspond to regions affected by the Bragg reflections of the aluminium pressure cell. Right: Refined structure from the neutron diffraction data with oxygen atoms (red), deuterium atoms (white), and nitrogen atoms (blue). Disorder is displayed a by partially coloured atoms.

III. REFILLING STUDIES

The emptied C_0 hydrate (ice XVII) was then pressurised with nitrogen to 0.018 GPa (the pressure of a full gas bottle) at 130 K. Uptake of gas was observed. Additional gas had to be added to the system regularly to maintain the pressure, and an expansion of the c-axis of sX (the axis that contracts most on removal of hydrogen) was observed,see right panel in figure 1.

After ∼7 hours the changes in pressure and lattice parameters appeared to have saturated and data was accumulated for about 5 h for full structural analysis. The results of a Rietveld profile refinement are shown in figure 2, together with the refined crystal structure. We were able to fit the known pattern of the sX structure to our data. As in the CO_2 and H_2 hydrates based on sX, the space group is $P6_122$ or $P6_522$. From the refinement we were able to obtain the lattice parameters a=6.240(3) Å and c=6.065(2) Å. According the established numbering methodology, we propose the name nitrogen hydrate V (NH-V) for this new sX-type hydrate. The resulting structural parameters for NH-V are summarised in table I. We find a nitrogen-water guest-host ratio of 1:2.7.

In addition to this experimental work, DFT simulations were carried out to determine the optimal filling ratio of the channels. The relative enthalpy of formation for a series of hydrates approximants with guest-host ratio 1:n (n=2$\cdots$6) are shown in figure 3 as a function of pressure. The canonical filling ratio of the sX structure is 1:2. However, for NH-V, a guest-host ratio of 1:3 is most stable across the entire pressure range. For comparison, calculations suggest a guest:host ratios of 1:2 in H_2-sX (C_0) and 1:4 in CO_2-sX, respectively, roughly in agreement with experimental findings[13]. Interestingly, the calculations predict a transition from NH-III to sX at around 2 GPa. (NH-III is a tetragonal hydrate, sT, in the space group $P4_2/mnm$ and the lattice parameters a=6.342 Å and c=10.610 Å[12].) The latter structure is stabilised by having a much smaller molecular volume due to efficient packing of the nitrogen molecules.

TABLE I. Space group, unit cell lattice parameters (a and c), oxygen and nitrogen fractional coordinates (x, y, z), occupancies, and multiplicities and Wyckoff positions of the sites for NH-V from neutron diffraction.
The values were obtained at 0.018 GPa and 130 K.

Space group	$P6_122$			
a / Å	6.240(3)			
c / Å	6.065(2)			
O (6b)	0.764(5)	0.5270(18)	0.250(9)	1.00(0)
D (6b)	0.377(10)	0.071(6)	0.532(4)	0.50(0)
D (6b)	0.563(8)	0.335(6)	0.458(3)	0.50(0)
N (12c)	0.957(10)	0.142(14)	0.652(13)	0.22(4)
N (12c)	0.213(8)	0.065(12)	0.883(12)	0.16(2)

The calculated structure is in good accordance with the structure obtained from our Rietveld refinements. The calculations suggest the lattice parameters a=5.904 Å, b=5.962 Å, and c=6.003 Å at 4 GPa and a filling ratio of 1:3. In comparison, the experimental values were a=b=6.240(3) Å and c=6.065(2) Å and a filling ratio of 1:2.7. As can be seen, the values obtained for the filling ratios from the DFT simulation are well

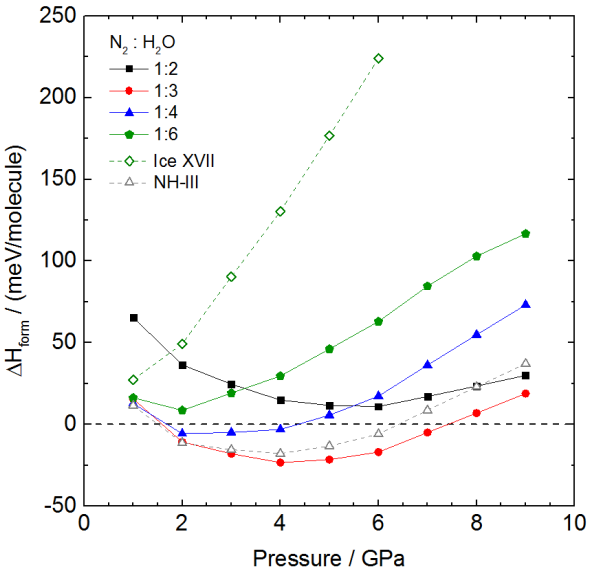

FIG. 3. Stability of nitrogen sX for various filling ratios from DFT calculations, against decomposition into pure ice and N_2. For comparison, the metastability of pure ice XVII is indicated, as well as the formation enthalpy of NH-III hydrate.

within the error bars of the experimental ones.

The nitrogen pressure was then increased to 0.30 GPa at 130 K. This led to changes in the diffraction pattern – the intensity of the peak at 4.12 Å decreased, while a new peak at about 3.64 Å slowly emerged, indicating a structural change in the sample. To speed this process up, the temperature was increased - first in 10 K steps to 160 K under a static pressure of 0.30 GPa, then in larger temperature steps. At every temperature, diffraction patterns were collected for about one hour each. A pressure drop in the sample chamber upon every increase in temperature was observed, indicating additional gas uptake. In figure 4 the respective diffraction patterns upon heating are depicted, with the first, blue curve being the pattern recorded at 0.018 GPa and 130 K. The newly emerging peak at 3.64 Å is close to a d-spacing that would suggest a doubling of the SX unit cell (it would be the (211) peak). Upon closer investigation, however, this theory was proven wrong, and we could identify this peak to belong to the hexagonal clathrate structure sH, a high-pressure phase hitherto only observed above 0.85 GPa[17,42]. This structure comprises two different small cages and one large cage, which runs the length of the unit cell along the c-axis. The sH structure is found in many simple gas hydrates (for example, Ar, Kr, Xe, methane, and N_2) but generally in the pressure range $\sim$ 1-2 GPa[42–44]. Here, the sH structure has the lattice constants a=11.82(4) Å, and c=9.82(4) Å.

Upon further heating above 160 K (turquoise curve in figure 4) the intensity of sH's peaks stayed constant, whilst the peaks from NH-V (and from the residual ice XVII) decreased. Simultaneously, new peaks belonging to the sII clathrate hydrate structure appeared in the diffraction pattern. Note that only the NH-V peaks disappeared, the peaks assigned to sH remained. This suggests that sII does not form directly from sH but rather that it is formed from NH-V. Analogous observations in the H_2-H_2O system support this hypothesis. Donelly *et al.* found that hydrogen sX (C_0) transforms into sII upon heating at 0.3 GPa.[40,41] Furthermore, it would not be surprising that residual ice XVII, a metastable structure, transformed in the presence of a suitable guest into sII as well. The transformation NH-V $\longrightarrow$ sII therefore gives a second possible route for the decomposition.

TABLE II. Space group and unit cell lattice parameters (a, c) for the N_2 variants of sX, sH, sIII, and sII.

Hydrate		Space group	a / Å	c / Å
NH-V	sX	$P6_122$	6.240(3)	6.065(2)
NH-II	sH	$P6/mmm$	11.82(4)	9.82(4)
NH-I	sII	$Fd\bar{3}m$	17.152(4)	17.152(4)
NH-VI	sIII	$P4_2/mnm$	22.914(9)	12.003(7)

Upon further heating, the N_2-H_2O mixture undergoes another remarkable transition - the sH peaks start to disappear and another (metastable) phase is formed. This phase could be fitted with the known pattern of a clathrate of the structure III type (sIII). Hitherto this clathrate type has only been known in bromine-water mixtures.[11] Type III clathrate hydrate has a tetragonal structure with space group $P4_2/mnm$ and a cell volume of 6300 Å^3, the largest known unit cell for a clathrate. The cell consists of 172 water molecules which form sixteen 14-hedral cavities ($5^{12}6^2$), four 15-hedral cavities ($5^{12}6^3$), and ten dodecahedral cavities (5^{12}). The lattice parameters we obtained from our measurements are a=22.914(9) Å, and c=12.003(7) Å. Almost 200 years after the first description of bromine hydrate we show that the sIII structure can serve as host to a second molecular guest species[45,46]. For this nitrogen hydrate we propose the name nitrogen hydrate VI (NH-VI). Finally, as it warms close to room temperature NH-VI forms the stable clathrate hydrate of type sII. This transition sequence is an excellent example of Ostwald's rule of stages, an empirical law stating that a meta-stable phase will transform to the stable phase, by passing through metastable phases in order of their Gibbs free energy . All nitrogen hydrates observed in this study are summarised in table II.

IV. CONCLUSIONS

We have shown that nitrogen-water mixtures can form the chiral clathrate hydrate structure, sX. This new nitrogen hydrate (NH-V) is obtained by refilling ice XVII at 130 K. Neutron diffraction data suggests that nitrogen NH-V is hexagonal with space group $P6_122$ or $P6_522$ and lattice parameters a=6.240(3)) Å and b=6.065(2) Å. Experimentally a guest:host ratio of 1:2.7 per molecule was found, close to DFT calculations that find NH-V stable with a filling ratio of 1:3. The values

for the filling ratios obtained from the DFT simulation are well within the error bars of the experimental ones - theory and experiment are therefore in good accordance.

$$\text{NH-V} \longrightarrow \text{NH-II} \longrightarrow \text{NH-VI} \longrightarrow \text{NH-I}$$

At 0.3 GPa we found that nitrogen NH-V transforms into the hexagonal NH-II, however, the transition only occurs very slowly. NH-II (sH) then, upon heating, undergoes transitions into NH-VI (sIII) and finally into NH-I (sII) clathrate hydrates. This is somewhat surprising. The sIII structure is an oddity in that it has so far only been observed in the bromine-water system. To find it in a simple gas system like nitrogen-water is unexpected. Similarly sH is generally found at pressures above ∼1 GPa and the ability to form it as part of a cascade of metastable structures at the much lower pressure of 0.3 GPa may be useful technologically.

In addition, we report another possible route for the decomposition of NH-V - heating it at an elevated pressure leads to a direct formation of the stable nitrogen hydrate I (sII).

$$\text{NH-V} \longrightarrow \text{NH-I}$$

We have hereby demonstrated that ice XVII is a microporous material that can be loaded with different gases. The unique channel layout of the sX network gives it a large amount of flexibility: the guest gases it can absorb span an unusually large size range (from H_2 via N_2 to CO_2), with the gas uptake ratio adjusting accordingly (from 1:2 to 1:4) to avoid steric repulsion of the guest molecules. At the same time, guest species exhibit high mobility along the channels, which makes determinations of the guest content from diffraction difficult. So far, DFT calculations have proved very useful in constraining the guest-host ratio. If necessary, more nuanced descriptions of the electronic structure, e.g. through local-MP2 calculations, could be applied.[47]

The universality of the sX host network raises the interesting possibility that if ice XVII can be loaded with oxygen (a molecule of similar size to nitrogen but with a triplet ground state), a magnetic sX-based hydrate might be produced. With sufficient cooling this hydrate might be induced to order magnetically.

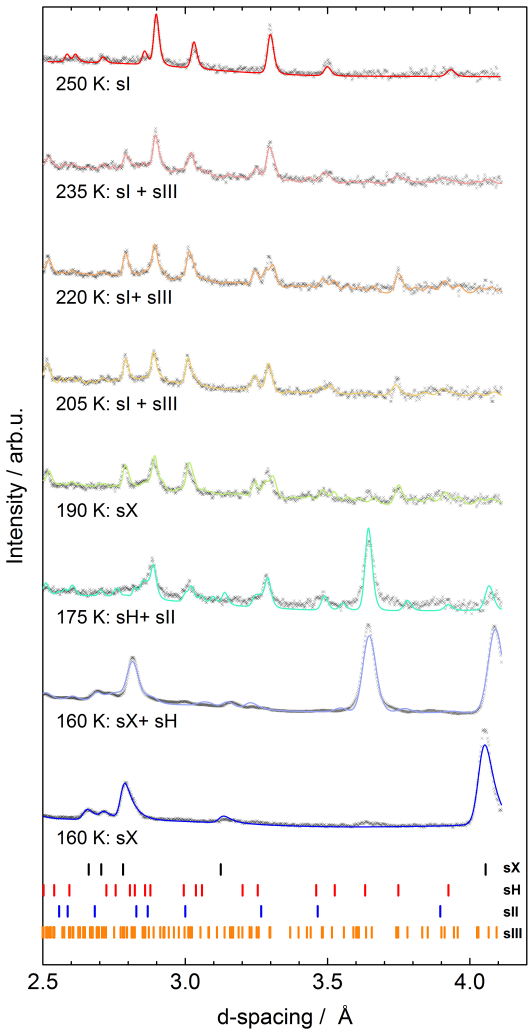

FIG. 4. Neutron diffraction patterns recorded while heating the sample. The first curve (blue) gives the pattern of the pure nitrogen sX. The main components of the respective patterns are from bottom to top: sX, sX+sH, sH+sII, sIII+sII, sIII+sII, sII+sIII, and sII. Black crosses are measured data points, the solid curves give the calculated patterns.

ACKNOWLEDGMENTS

We would like to thank Drs Craig Bull and Nick Funnell (ISIS Facility) for technical assistance with the experiments and the Science, Technology and Facilities Research Council for access to ISIS through the allocation of beamtime. Computing resources provided by the UK national high performance computing service, ARCHER, which is partially funded by EPSRC (EP/P020194), and for which access was obtained via the UKCP consortium funded by EPSRC grant no. EP/P022561/1, are gratefully acknowledged.

LJC acknowledges studentship funding from EPSRC under grant no. EP/L015110/1.

[1] A. N. Dunaeva, D. V. Antsyshkin, and O. L. Kuskov, Solar System Research **44**, 202 (2010).
[2] T. Bartels-Rausch, V. Bergeron, J. Cartwright, H. Julyan, R. Escribano, J. Finney, H. Grothe, P. Gutierrez, J. Haapala, W. Kuhs, J. Pettersson, S. Price, C. Sainz-Diaz, D. Stokes, G. Strazzulla, E. Thomson, H. Trinks, and N. Uras-Aytemiz, Reviews of Modern Physics **84**, 885 (2012), arXiv:1207.3738.
[3] L. Del Rosso, M. Celli, and L. Ulivi, Nature Communications **7**, 1 (2016), arXiv:1607.07617.
[4] T. M. Gasser, A. V. Thoeny, L. J. Plaga, K. W. Koester, M. Etter, R. Boehmer, and T. Loerting, Chemical Science **7**, 1 (2018).
[5] O. Mishima, L. Calvert, and E. Whalley, Nature **310**, 393 (1984).
[6] J. L. Finney, **90**, 303 (2001).
[7] J. L. Finney, *Water: A very short introduction*, first edition ed. (Oxford University Press, Oxford, 2002).
[8] T. Loerting, K. Winkel, M. Seidl, M. Bauer, C. Mitterdorfer,

P. Handle, C. Salzmann, E. Mayer, J. Finney, and D. Bowron, Physical Chemistry Chemical Physics **13**, 8783 (2011).
[9]F. Perakis, K. Amann-Winkel, F. Lehmkühler, M. Sprung, D. Mariedahl, J. A. Sellberg, H. Pathak, A. Späh, F. Cavalca, D. Schlesinger, A. Ricci, A. Jain, B. Massani, F. Aubree, C. J. Benmore, T. Loerting, G. Grübel, L. G. M. Pettersson, and A. Nilsson, Proceedings of the National Academy of Sciences **114**, 8193 (2017).
[10]M. von Stackelberg and H. Mueller, Ann. Chim. Phys. **56**, 25 (1954).
[11]K. A. Udachin, G. D. Enright, C. I. Ratcliffe, and J. A. Ripmeester, Journal of the American Chemical Society **119**, 11481 (1997).
[12]J. S. Loveday and R. J. Nelmes, Physical Chemistry Chemical Physics **10**, 937 (2008).
[13]D. M. Amos, M.-E. Donnelly, P. Teeratchanan, C. L. Bull, A. Falenty, W. F. Kuhs, A. Hermann, and J. S. Loveday, The Journal of Physical Chemistry Letters , 4295 (2017).
[14]L. del Rosso, F. Grazzi, M. Celli, D. Colognesi, V. Garcia-Sakai, and L. Ulivi, Journal of Physical Chemistry C **120**, 26955 (2016), 1609.04996.
[15]B. Massani, C. Mitterdorfer, and T. Loerting, Journal of Chemical Physics **147** (2017), 10.1063/1.4996270.
[16]A. Falenty, T. C. Hansen, and W. F. Kuhs, Nature **516**, 231 (2014).
[17]E. D. Sloan and C. A. Koh, *Clathrate Hydrates of Natural Gases*, third edition ed. (CRC Press, Boca Raton, London, New York, 2007).
[18]J. M. Berg, J. L. Tymoczko, and L. Stryer, *Biochemistry*, 5th ed. (W.H. Freeman, Oxford, New York, 2002).
[19]G. Hummer, S. Garde, A. E. Garcia, M. E. Paulaitis, and L. R. Pratt, Proceedings of the National Academy of Sciences (1998), 10.1073/pnas.95.4.1552.
[20]S. Alavi, J. A. Ripmeester, and D. D. Klug, Journal of Chemical Physics **125** (2006), 10.1063/1.2238864.
[21]B. Buffett and D. Archer, Earth Planet. Sci. Lett. **227**, 185 (2004).
[22]D. Mahajan, C. Taylor, and G. Mansoori, J. Pet. Sci. Eng. **56**, 1 (2007).
[23]J. I. Lunine and D. J. Stevenson, Icarus **70**, 61 (1987).
[24]R. W. Bradshaw, J. A. Greathouse, R. T. Cygan, B. A. Simmons, D. E. Dedrick, and E. H. Majzoub, LDRD Final Report. Sandia report SAND2007-6565 (2008), 10.2172/934586, 1707.04192.
[25]V. S. Efimchenko, M. A. Kuzovnikov, V. K. Fedotov, M. K. Sakharov, S. V. Simonov, and M. Tkacz, Journal of Alloys and Compounds **509**, 860 (2011).
[26]L. O. D. Baerlocher, C.; McCusker, *Atlas of Zeolite Framework Types*, sixth edition ed. (Elsevier, Amsterdam, 2007).
[27]C. J. Pickard and R. J. Needs, Phys. Rev. B - Condens. Matter Mater. Phys. **81**, 1 (2010).
[28]W. Blase and G. Cordier, Zeitschrift für Naturforsch. B **43**, 1017 (1988).
[29]S. Stegmaier, S. J. Kim, A. Henze, and T. F. Fässler, J. Am. Chem. Soc. **135**, 10654 (2013).
[30]V. V. Smirnov, G. S.; Stegailov, J. Phys. Chem. Lett. **4**, 35603564 (2013).
[31]L. del Rosso, M. Celli, and L. Ulivi, Challenges **8**, 3 (2017).
[32]L. del Rosso, M. Celli, D. Colognesi, S. Rudic, N. J. English, C. J. Burnham, and L. Ulivi, **065602**, 1 (2017), arXiv:1706.09350.
[33]C. L. Bull, N. P. Funnell, M. G. Tucker, S. Hull, D. J. Francis, and W. G. Marshall, High Pressure Research **36**, 493 (2016).
[34]. V. D. R. B. Toby, B. H., Journal of Applied Crystallography **46**, 544 (2013).
[35]. V. D. R. B. Toby, B. H., Zeitschrift fuer Kristallographie **220**, 567 (2005).
[36]J. P. Perdew, K. Burke, and M. Ernzerhof, Phys. Rev. Lett. **77**, 3865 (1996), arXiv:0927-0256(96)00008 [10.1016].
[37]H. J. Monkhorst and J. D. Pack, Phys. Rev. B **13**, 5188 (1976).
[38]R. Bini, L. Ulivi, J. Kreutz, and H. J. Jodl, J. Chem. Phys. **112**, 8522 (2000).
[39]We used deuterated reagents to avoid the the incoherent background scattering from hydrogen, .
[40]M. Donelly, *Neutron Diffraction of Hydrogen Inclusion Compounds Under Pressure*, Ph.D. thesis, School for Physics and Astronomy, The University of Edinburgh, Edinburgh (2016).
[41]M. Donnelly, P. Teeratchanan, C. L. Bull, A. Hermann, and J. S. Loveday, Physical Chemistry Chemical Physics **20**, 26853 (2018).
[42]J. S. Loveday and R. J. Nelmes, High Pressure Research **24**, 45 (2004).
[43]J. S. Loveday, R. J. Nelmes, M. Guthrie, S. A. Belmonte, D. R. Allan, D. D. Klug, J. S. Tse, and Y. P. Handa, Nature **410**, 661 (2001).
[44]J. S. Loveday, R. J. Nelmes, and M. Guthrie, **350**, 459 (2005).
[45]C. J. Löwig, Mag. der Pharm. **23**, 11 (1828).
[46]C. Löwig, Ann. Phys. **90**, 485 (1828).
[47]J. Košata, P. Merkl, P. Teeratchanan, and A. Hermann, J. Phys. Chem. Lett. **9**, 5624 (2018).
[48]K. A. Lokshin, Y. Zhao, D. He, W. L. Mao, H. K. Mao, R. J. Hemley, M. V. Lobanov, and M. Greenblatt, Physical Review Letters **93**, 1 (2004).
[49]C. Loewig, Ann. Chim. Phys. **42**, 113 (1829).
[50]K. W. Allen and G. A. Jeffrey, The Journal of Chemical Physics **38**, 2304 (1963).

crystals

MDPI

Article

Ammonia Mono Hydrate IV: An Attempted Structure Solution

Bernhard Massani, Ciprian G. Pruteanu, Lewis J. Conway, Victor N. Robinson, Andreas Hermann and John S. Loveday *

SUPA, School of Physics and Astronomy, Centre for Science at Extreme Conditions, The University of Edinburgh, Edinburgh EH9 3FD, UK; b.massani@ed.ac.uk (B.M.); cip.pruteanu@ed.ac.uk (C.G.P.); L.J.Conway@ed.ac.uk (L.J.C.); victornadenrobinson@gmail.com (V.N.R.); a.hermann@ed.ac.uk (A.H.)
* Correspondence: j.loveday@ed.ac.uk

Abstract: The mixed homonuclear and heteronuclear hydrogen bonds in ammonia hydrates have been of interest for several decades. In this manuscript, a neutron powder diffraction study is presented to investigate the structure of ammonia monohydrate IV at 170 K at an elevated pressure of 3–5 GPa. The most plausible structure that accounts for all features in the experimental pattern was found in the $P2_1/c$ space group and has the lattice parameters $a = 5.487(3)$ Å, $b = 19.068(4)$ Å, $c = 5.989(3)$ Å, and $\beta = 99.537(16)$ deg. While the data quality limits discussion to a proton-ordered structure, the structure presented here sheds light on an important part of the ammonia–water phase diagram.

Keywords: Ammonia hydrate; high pressure; neutron diffraction; density functional theory.

check for updates

Citation: Lastname, F.; Lastname, F.; Lastname, F. Ammonia Mono Hydrate IV: An Attempted Structure Solution. *Crystals* **2022**, *1*, 0. https://doi.org/

Academic Editor: Venu Vangala; Philip Lightfoot; Volodymyr Bon; Helmut Cölfen

Received: 12 October 2021
Accepted: 5 January 2022
Published:

Publisher's Note: MDPI stays neutral with regard to jurisdictional claims in published maps and institutional affiliations.

1. Introduction

The water–ammonia system is of interest for a variety of reasons. First and foremost, it is a model system in which the behaviour of materials that contain homonuclear and heteronuclear hydrogen bonds can be observed; H_2O readily forms H-bonds with itself and with NH_3, while NH_3 tends to donate H-bonds to H_2O. These N-H$\cdots$O and N$\cdots$H-O hydrogen bonds are highly relevant as proxies for the hydrogen bonds in proteins and other biomolecules, where these H-bonds play an important role in folding, replication, and overall functionality [1]. As such, water ice and solid ammonia, as well as their three stoichiometric mixtures—ammonia hemihydrate ($NH_3 \cdot \frac{1}{2}H_2O$, AHH), ammonia monohydrate ($NH_3{\cdot}H_2O$, AMH), and ammonia dihydrate ($NH_3{\cdot}2H_2O$, ADH) [2]—are important proxies for the understanding of more complex hydrogen-bonded molecules.

Of equal importance is the abundance of ammonia (15%) and water (45%) in the outer solar system. This suggests that ammonia–water is one of the main phases in this region of the solar system [3–6] and large proportions of the mantle regions of Uranus and Neptune (the "ice giants") are likely composed of those two molecules, where they experience pressure conditions from the kbar to Mbar range (see Hubart et al. [7] and the phase diagram in Figure 1). Furthermore, their abundance on icy moons in our solar system has been confirmed [8], and NH_3-H_2O is presumed to feature prominently in the interiors of a large number of trans-Neptunian objects and Neptune-like exoplanets [9,10]. In this astrophysical context, ammonia is considered the most plausible planetary 'antifreeze' agent [11].

The flexibility of the hydrogen bond leads one to suspect that NH_3–H_2O mixtures, much like pure water or ammonia, should support a wide range of different phases at different pressures and temperatures, characterised by specific network topologies, density profiles, elastic and viscous properties, etc. The first visual and Raman-scattering observations made using diamond anvil cells indicated that AMH possessed no high-pressure polymorphs [12]. This assumption was proven incorrect; to date, five AMH phases have been identified: AMH-I, AMH-II, AMH-III, AMH-IV and DMA (formerly AMH VI) [2,13]. The first of the high-pressure phases, AMH-II, was characterised by

Nelmes *et* Loveday by means of neutron powder diffraction and the pattern of AMH-II, collected at 508.9 MPa, was incorrectly indexed with an orthorhombic unit cell [14]. Finally, the structure was solved in 2009 for a diffraction pattern collected at 443 MPa and 174 K (a = 18.8680(2) Å, b = 6.9477(1) Å, and c = 6.8589(1) Å) [15].

Of the remaining three high-pressure phases, only the structure of the disordered molecular alloy phase (DMA) is known. It has been extensively studied [13] and crystallises in the cubic structure ($Im\bar{3}m$) with the lattice parameter $a = 3.273$ Å. In DMA, the two possible crystallographic sites (0, 0, 0) and ($\frac{1}{2}$, $\frac{1}{2}$, $\frac{1}{2}$) are equally occupied by either an ammonia or a water molecule. Together with AMH-III (still unsolved), this structure counts towards the 'high-temperature' phases of ammonia monohydrate, as it can only be observed at >200 K and >270 K, respectively. The p/T phase diagram for AMH is shown in Figure 1.

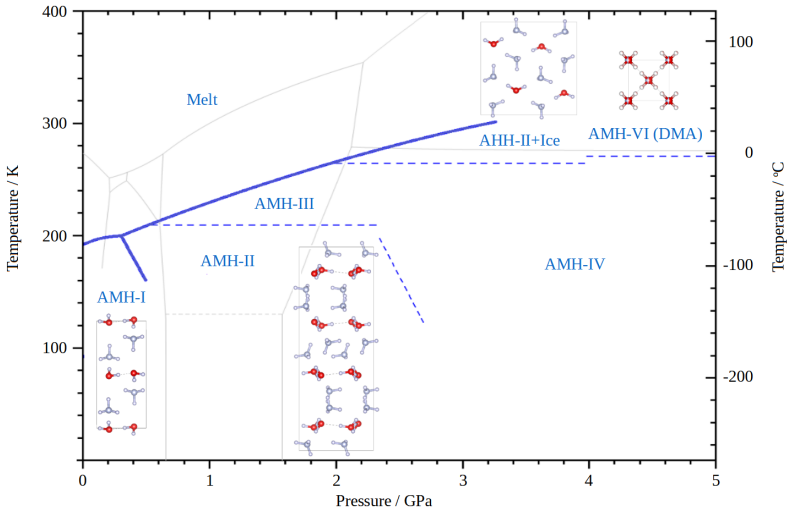

Figure 1. The AMH phases diagram. For the known crystal structures, the respective unit cells are shown. Please note that broken lines do not denominate phase boundaries, but rather a line at which the respective other phase first appears. The grey lines in the background give the phase diagram of water as a reference. The melting curves and phase boundaries are taken from [13,15–20].

In this body of work, we investigate the structure of ammonia monohydrate IV. With results based on a neutron diffraction study carried out at the ISIS neutron source, paired with density functional theory (DFT) calculations, we try to propose a possible structure solution for this—so far, unsolved—polymorph.

2. Materials and Methods

The experiment was carried out on a sample of nominal composition $ND_3 \cdot D_2O$ (AMH), prepared by condensing ND_3 gas (99 atom% D from Aldrich Chemicals Co., Dorset (SP8 4XT), UK) into a Swagelock steel cylinder, which was cooled to 77 K in a bath of liquid nitrogen (LN2). The cylinder was then weighed and the contents diluted to the appropriate stoichiometry with D_2O (Aldrich Chemicals Co., 99 atom% D). The resulting mixture was then warmed in a bath of isopropanol and liquid nitrogen at 184 K to stabilise a $ND_3 \cdot D_2O$ liquid. To crystallise the AMH, the liquid was once again cooled in a bath of LN2 and the so-obtained sample was stored at these conditions; the ideal AMH stoichiometry is 48.598 wt.% ND_3.

The sample was transported to ISIS (RAL, Oxfordshire, UK), where it was cryo-loaded into a Paris-Edinburgh press (PE-press) at PEARL [21,22]. To that purpose, the sample was ground to a fine powder under liquid nitrogen and loaded into a pre-cooled gasket. The gasket was sitting on an anvil (sintered-diamond) that was immersed in liquid nitrogen. After loading, the gasket–anvil assembly was then put into the PE-press and an initial sealing load of 5 t was applied. Data were collected for $81.2° < 2\theta < 98.8°$ ($L_2 = 0.8$ m,

$0.5 < d(\text{Å}) < 4.1$, $\Delta d/d \approx 0.65$ %), the optimised geometry of the PE press. Second frame data were taken but the level of signal was too low to be useful [22].

Diffraction data were analysed (Le Bail, Rietveld, MCSA) using the GSAS-II software suite [23].

We also performed calculations of the enthalpies of structural candidates obtained from Rietveld refinements, using density functional theory (DFT), as implemented in the CASTEP code [24]. Exchange-correlation effects were described within the generalised gradient approximation (GGA) using the Perdew–Burke–Ernzerhof (PBE) functional [25] and ultra-soft pseudo-potentials or norm-conserving potentials as generated 'on-the-fly' by CASTEP with cut-off radii of 1.1 Bohr for oxygen and nitrogen, and 0.6 Bohr for hydrogen. Geometry optimisations were performed with plane wave cut-offs of 1000 eV and Monkhorst-Pack [26] k-point spacings of no more than $2\pi \times 0.04$ Å^{-1}, until residual forces and stresses were below 50 meV/Å and 0.1 GPa, respectively.

3. Results

After applying a sealing load of 5 t, the sample in the PE-cell was lowered into the diffractometer. A cryostat was then used to increase the temperature of the cell and sample to 170 K. At this temperature, the load was increased incrementally to 40 t. During the pressure increase, the sample first transformed into AMH-II and then, ultimately, into AMH-IV. No pressure marker was used for this experiment to avoid parasitic lead peaks; therefore, the exact pressure is unknown. However, from previous pressure–load curves and the phase diagram of AMH, it can be deduced that the sample pressure lies between 3 and 5 GPa. Once the load of 40 t was reached, a powder pattern was recorded.

3.1. Density of Ammonia Hydrate and Initial Indexing

From the initial composition of the water–ammonia mixture and the absence of other known phases of ice, water and ammonia–water mixtures, it is evident that AMH-IV is a 1:1 mixture. This is mentioned because, in a previous study, the composition of ammonia–water phases was wrongly identified (c.f. the DMA phase in AMH and ADH) [13]).

The average volumes per molecule for ADH, AMH, and AHH at ambient pressure are, respectively, 30.170(6) Å^3, 30.604(2) Å^3, and 30.583(2) Å^3 [27]. These values are remarkably similar and show no obvious correlation with composition. This trend is also visible in the similarity of the equations-of-state of the high-pressure phases of both the AMH and ADH [2,15,17,19,27]. It thus seems reasonable to assume that AMH-IV also shows no significant composition dependence in its equations of state; in the pressure range from 3 to 5 GPa, it should have a density of 1.4–1.8 g/cm^3. The content of a unit cell can be estimated from these densities.

Altogether, the data collection resulted in 15 well-defined, although broad, peaks and several heavily overlapping ones (see diffraction data below). The relatively small number of peaks imposes an upper limit on the size of unit cells that can be meaningfully tested. In this case, refinements of unit cells larger than 400 Å^3 proved to be very unstable unless a high-symmetry space group was used.

Peaks in the diffraction data were identified by fitting them with pseudo-Voigt functions, and then the GSAS-II indexing routine was run. In general, the indexing of cubic, hexagonal, and trigonal crystal systems resulted in unit cells that were too large (>1000 Å^3) for the dataset and, hence, were mostly discarded. This indexing resulted in 108 possible cells, not including a triclinic lattice. A Le–Bail (LB) refinement was carried out in the respective lowest symmetry space group for this crystal system to account for all possible peaks in the powder pattern. Al total of 60 cells showed promising Le–Bail fits and were used for the next step of the data analysis. Please note that most of the 60 cells had several possible space groups with higher symmetries, which fit the pattern equally well [28].

3.2. Structure Search Using Monte Carlo Simulated Annealing

In order to solve the structure for AMH-IV, initially, the GSAS-II charge flipping algorithm was used. However, charge flipping is not well-suited to neutron powder diffraction data; hence, Monte-Carlo-Simulated Annealing (MCSA) was used here. MCSA uses atoms, molecules, or molecule fragments and varies their position in the unit cell [29,30]. This is performed using a random-walk approach [31], as implemented in crystallographic software packages [23]. For the resulting structure model, the peak intensities were calculated and compared with the intensities from the Le–Bail fit. This procedure was repeated until a convergence criterion was met. As such, MCSA has the advantage that the molecules placed in the unit cell can be chosen so that the required density is 1.4–1.8 g/cm^3. Here, the starting structures for the MCSA consisted of water D_2O and ammonia ND_3. Both molecules were constrained to have a fixed internal geometry and the position and orientation in the unit cell of these rigid bodies was varied.

The MCSA was considered successful if several runs converged to the same structural model. The obtained structure was then used for individual Rietveld refinements. For the initial refinement, the atoms were fixed in the molecular geometry as a rigid body. After refining their positions and isotropic displacement parameters, the restrictions were lifted and a full refinement was carried out. To double-check whether the structures were physically plausible, geometry optimisations (GO) were carried out in CASTEP. Finally, this procedure was repeated for all possible space groups of higher symmetry in the respective unit cell.

3.3. Two Structure Candidates Based on Rietveld Refinements

In most cases, a reasonable structure was obtained from the MCSA runs. However, the MCSA solutions often were not stable in Rietveld refinements or in GO. Here, we discuss the only two structures that fulfilled both requirements; as both candidate structures were found in the $P2_1/c$ space group, they are labelled $P2_1/c$ (I) and $P2_1/c$ (II).

The first cell presented here, $P2_1/c$ (I), had the lattice parameters $a = 4.379(3)$, $b = 4.502(4)$, $c = 17.770(5)$, and $\beta = 92.39(2)$ deg. This structure is similar to that of AMH-II (*Pbca*). Compared to the density of AMH-II (1.190 g/cm^3, Z = 16), its density is higher 1.52 g/cm^3 (Z = 12) [32]. The monoclinic cell deviates from an ideal orthorhombic cell by only $\approx$ 2.4 deg. From the MCSA in the space group $P2_1/c$, a structure model was obtained, which employed, similarly to AMH-II, a motif of partially layered ammonia and water [32]. The layers of ammonia are stacked along the *c*-axis at $z = 0$ and $z = 0.5$ and ammonia and water mix and intertwine between those layers. Furthermore, pure layers of ammonia and water are stacked along the *a*-axis. A Rietveld refinement of this structure was stable with R_w = 2.784% for 32 parameters and the Rietveld fit to the data is given in Figure 2.

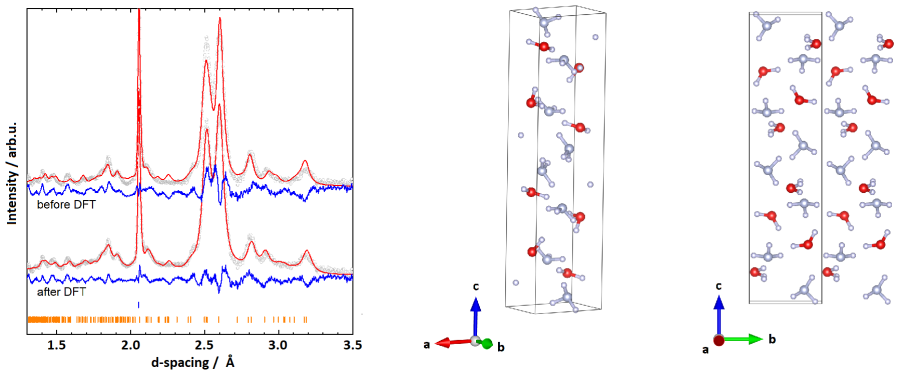

Figure 2. Left: Rietveld fits to experimental data and respective structures for the monoclinic cell $P2_1/c$ (I) with $a = 4.379(3)$, $b = 4.502(4)$, $c = 17.770(5)$, and $\beta = 92.39(2)$ deg. Grey (red, blue) graphs represent diffraction data (Rietveld fits, residuals). Orange ticks represent peak positions of $P2_1/c$ (I), blue ones parasitic peaks from anvils. **Right**: The model obtained from the Rietveld refinement. Red (blue, white) spheres represent oxygen (nitrogen, hydrogen) atoms.

The structural parameters were then used as an input for a geometry optimisation in CASTEP; the respective enthalpy plot is shown in Section 3.4. The geometry optimisation did not result in massive shifts in molecule positions (average displacement of 0.964(3) Å of the molecular centres between the GO and the Rietveld solutions), and resulted in a physically plausible structure. To further verify that the structure is plausible, phonon calculations were carried out at the Γ-point, and resulted in real phonon frequencies only. While the Rietveld fit of the (geometry optimised) structure reproduces the main features of the experimental data (see Figure 2), many peaks—particularly in the high-Q range (d-spacings 1.3–1.9)—are poorly fitted by this structure.

The second monoclinic cell, $P2_1/c$ (II), which showed promising results, has the dimensions $a = 5.487(3)$ Å, $b = 19.068(4)$ Å, $c = 5.989(3)$ Å, and $\beta = 99.537(16)$ deg. A Rietveld fit to the experimental data is given in Figure 3 with an overall R_w of 4.451%. Compared to the structure discussed above, $P2_1/c$ (II) seems to fit all main features of the diffraction pattern quite well. To further verify that the structure is plausible, phonon calculations were carried out, again sampling the Γ-point and confirming real phonon frequencies only. More details of the DFT analyses are discussed in Section 3.4 below.

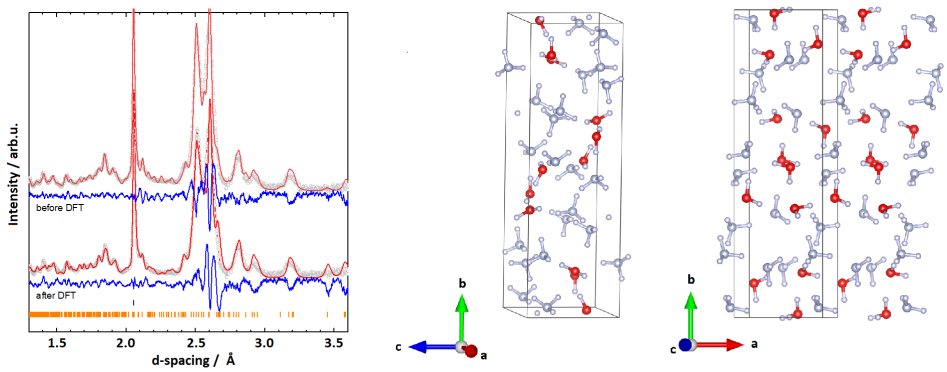

Figure 3. Left: Rietveld fits to experimental data and respective structures for the monoclinic cell $P2_1/c$ (II) with $a = 5.487(3)$ Å, $b = 19.068(4)$ Å, $c = 5.989(3)$ Å, and $\beta = 99.537(16)$ deg. **Right**: The model obtained from the Rietveld refinement. Data representation as explained in the caption of Figure 2.

Compared to the first structure, $P2_1/c$ (II) does not show layers of H_2O or NH_3 in the *ac*-plane (along the *b*-axis). However, the lattice parameters again show a resemblance to the ones of AMH-II, with the *b*-axis being three times as long as the *a* and *c* axis. This seems

plausible, as AMH-IV is an intermediary state between AMH-II and the high-pressure phases AMH-DMA or AHH-II. A density of about 1.30 g/cm^3 was calculated for the above-mentioned lattice parameters (Z=12). While this density is at the lower end of the reasonable densities, $P2_1/c$ (II) is the most plausible structure that we were able to obtain.

3.4. Structure and DFT Study of $P2_1/c$ (II)

As mentioned in the section above, the best fit to the diffraction pattern of AMH-IV resulted from a unit cell with the dimensions $a = 5.487(3)$ Å, $b = 19.068(4)$ Å, $c = 5.989(3)$ Å, and $\beta = 99.537(16)$ deg and the $P2_1/c$ symmetry; the values were obtained from the Rietveld refinement shown in Figure 3. The overall fit resulted in R_w = 4.451%, and—as stated above—accounts for nearly all features in the diffraction pattern. However, due to the limited number of well-resolved peaks and the large unit cell volume of 613.30(8) Å^3 the molecular geometry had to be fixed with rigid bodies. Furthermore, a high symmetry spacegroup had to be chosen to avoid exceeding the empirical $3n$-rule of refinable parameters. The atom positions and isotropic displacement parameters for the proposed structure of AMH-IV are summarised in Table 1.

Table 1. Atom site, position and isotropic displacement parameters for AMH-IV in space group $P2_1/c$ (II); lattice parameters $a = 5.487(3)$ Å, $b = 19.068(4)$ Å, $c = 5.989(3)$ Å, and $\beta = 99.537(16)$ deg.

Atom	Site	x	y	z	U_{iso}
D1	4e	0.062(9)	0.433(4)	0.724(9)	0.165(15)
D2	4e	−0.105(9)	0.394(4)	0.522(9)	0.165(15)
D3	4e	0.545(6)	0.5092(18)	0.266(5)	0.006(5)
D4	4e	0.388(6)	0.5531(18)	0.069(5)	0.006(5)
D5	4e	0.372(5)	0.2823(12)	0.558(3)	0.177(16)
D6	4e	0.343(5)	0.2607(12)	0.285(3)	0.177(16)
D7	4e	0.288(5)	0.3429(12)	0.359(3)	0.177(16)
D8	4e	0.986(5)	0.2022(12)	0.838(3)	0.066(8)
D9	4e	0.755(5)	0.2596(12)	0.776(3)	0.066(8)
D10	4e	0.733(5)	0.1949(12)	0.960(3)	0.066(8)
D11	4e	0.644(5)	0.370(2)	1.032(7)	0.021(7)
D12	4e	0.747(5)	0.294(2)	1.105(7)	0.021(7)
D13	4e	−0.032(4)	0.9612(7)	0.112(4)	0.026(6)
D14	4e	0.212(4)	0.9968(7)	0.275(4)	0.026(6)
D15	4e	−0.053(4)	0.9870(7)	0.375(4)	0.026(6)
N1	4e	0.274(5)	0.2912(12)	0.401(3)	0.177(16)
N2	4e	0.798(5)	0.2084(12)	0.815(3)	0.066(8)
N3	4e	0.024(4)	0.9980(7)	0.234(4)	0.026(6)
O1	4e	0.048(9)	0.419(4)	0.566(9)	0.165(15)
O2	4e	0.440(6)	0.5501(18)	0.231(5)	0.006(5)
O3	4e	0.599(5)	0.321(2)	1.054(7)	0.021(7)

An attempt was made to remove the rigid body restriction and reduce the symmetry of the space group to $P2_1$, both of which remained fruitless. The former resulted in unreasonable O-H and N-H distances of <0.8 Å, paired with an asymmetry in bond lengths in the H_2O and NH_3 molecules. However, the overall structure remained intact. In the latter case of lowering the symmetry, the structure completely fell apart. Without access to additional data of better quality, these limitations are necessary and, due to these restrictions, some peaks are still not perfectly fit.

Two motifs seem to repeat in this structure: a planar quadrilateral and an "envelope shaped" quadrilateral (see Figure 4). The rings constitute of alternating NH_3 and H_2O molecules and are interconnected by hydrogen bonds. The former are stacked along the a-axis, oriented with the two NH_3, either up or down. The latter quadrilaterals form alternating stacks that are tilted either +25 deg relative to the *bc*-plane, or −25 deg relative to the *bc*-plane.

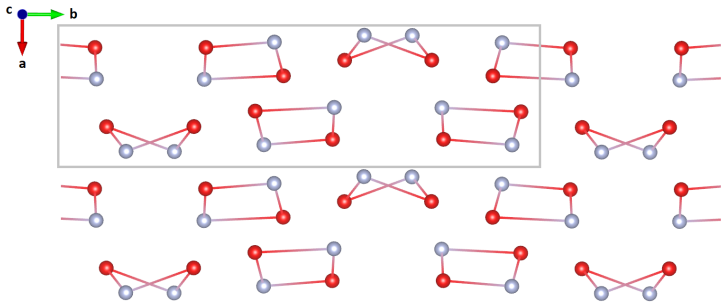

Figure 4. Reduced structure without hydrogen/deuterium along the unique axis (b-axis). The unit cell is indicated by a grey rectangle. Two structural motifs repeat along this axis, a planar quadrilateral and an 'envelope shaped' quadrilateral.

Please note that all considerations so far have assumed a hydrogen-ordered structure; this is based on the observation that the structures of most ammonia hydrates (AMH-I, AMH-II, ADH-I, AHH-I, AHH-II [2,19]) are ordered at the low temperature at which the data were collected; the DMA phase, on the other hand, is highly disordered [13]. The possibility that AMH-IV is also (partially) disordered, therefore, cannot be completely ruled out. This argument is further supported by the isotropic displacement parameter in the Rietveld refinement; the variation in the parameters would suggest disorder. (Please note that a refinement in which all U_{iso} values were fixed to 0.05 remained stable, with an R_w of 5.444%.) However, given the data quality and the structural complexity, it is not possible to test for disorder in a meaningful way.

The enthalpy calculations based on density functional theory were performed using the CASTEP code [24,33] on the ammonia monohydrate structure obtained by MCSA. Additionally, calculations were performed on the structures of AMH-I, AMH-II, and the ionic $P4/nmm$ phase; the latter phase was chosen as a reference structure. To calculate stable compounds, enthalpy values H were compared according to $H = U + PV$, where U is the internal energy per molecule and P and V are the pressure and molecular volume, respectively. To determine the relative stability, the formation enthalpies at every pressure point from 1 to 15 GPa, relative to the reference structure at the same pressure, were plotted according to

$$\Delta H(P) = H(P) - H(P)_{ref}. \quad (1)$$

These data are shown in Figure 5. Please note that the transition pressures obtained from DFT calculations are usually higher than the ones observed in experiments.

At ambient pressure, AMH-I is the most stable compound. Upon an increase in pressure, AMH-II starts to compete with AMH-I and becomes energetically favourable at 4 GPa. This is also observed in experiments at a transition pressure of about 0.5 GPa. AMH-I, despite not being the dominant species anymore, was traced to 15 GPa. The kink in the enthalpy curve at 12 GPa indicates ionisation of two of the four water-ammonia pairs to NH_4^+ and OH^-. The spontaneous ionisation of this form has been observed in several DFT studies before [34,35]. Between 4 and 5 GPa, Griffiths' ionic $P4/nmm$ phase becomes the energetically favourable phase and remains so for the whole pressure regime studied here. While this behaviour has been observed by Griffiths et al. as well [34], experimentally, no ionisation of this sort has been observed in AMH to date. From neutron diffraction experiments, it is known that AMH-II transforms into AMH-IV at 2.2 GPa (upon a pressure increase) or into AMH-III at 210 K (upon heating); see Loveday and Nelmes (2004) [2].

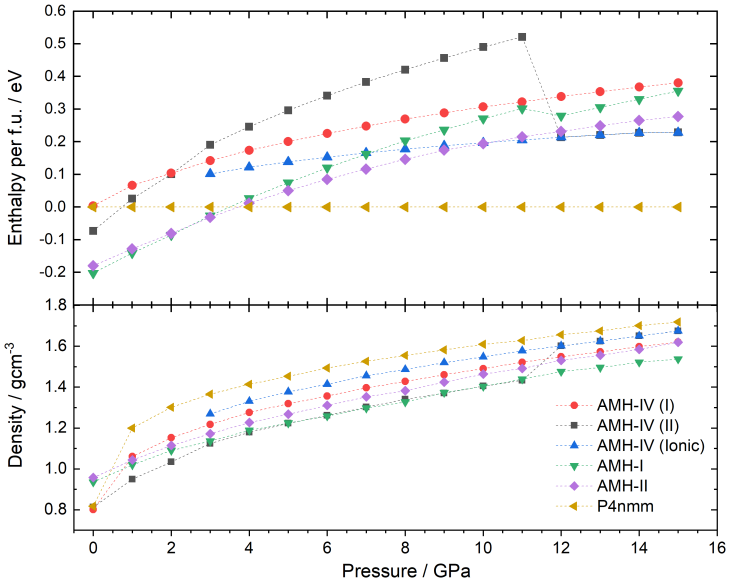

Figure 5. Enthalpy per formula unit and densities of the ammonia monohydrate phases AMH–I, AMH–II, Griffiths' $P4/nmm$ phase and the $P2_1/c$ structures of AMH–IV as a function of pressure. AMH–IV (II) spontaneously ionises at 12 GPa and changes its unit cell.

The $P2_1/c$ (II) structure of AMH-IV was tracked in the same way and remains energetically unfavourable throughout the whole pressure range. This would indicate the metastability of the phase, but could also be a result of the temperature difference between the DFT-study (0 K) and the experiment (170 K). Similar to AMH-I, AMH-IV partially ionises at 12 GPa; two of the twelve formula units form $NH_4^+ \cdots OH^-$ pairs. The ionisation goes hand in hand with a change in lattice parameters to a = 5.79316, b = 16.59557, c = 4.67090, α = 89.5249, β = 88.4048, and γ = 76.2010 (at 12 GPa). Furthermore, a jump in energy of -0.3 eV per formula unit can be observed. This jump is remarkable, much larger than in AMH-I, despite only 2 of the 12 molecules ionising vs. 2 of the 4 in AMH-I. The reason for this is the transition to a completely new (theoretical) phase. Additionally, this structure was traced back (see red curve in Figure 5) along the pressure axis. No transition back to a purely molecular phase could be observed from 15 to 3 GPa.

Since the triclinic, partially ionic structure is energetically much more favourable, an attempt was made to use this as an input structure for a Rietveld refinement. However, the experimentally observed pattern did not match this triclinic structure at all. The unit cell of this structure can be seen in Figure 6. In this cell, α and γ deviated from a monoclinic cell by less than 4 deg. Hence, to reduce the fitting parameters, a higher symmetry, molecular equivalent of this structure in space group $P2_1$, was carefully constructed (a = 16.59557, b = 4.67090, c = 5.79316, and β = 76.2010), but this second attempt proved fruitless.

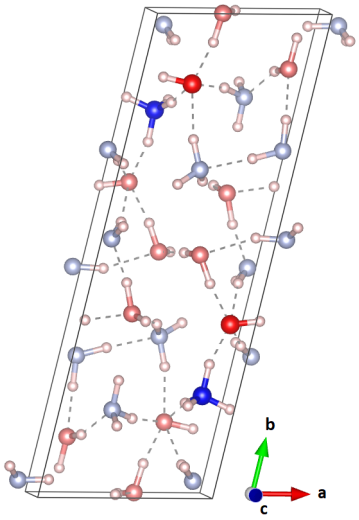

Figure 6. Unit cell of the triclinic, partially ionic structure obtained from DFT; the ionic units are highlighted. This structure does not fit the experimentally observed powder pattern.

4. Conclusions

A neutron powder diffraction study was carried out to investigate the structure of ammonia monohydrate IV. To that end, a neutron diffraction pattern, collected at 170 K at an elevated pressure of 3–4 GPa, was used. Considerations based on the density of other ammonia–water phases suggest a density of 1.4–1.8 g/cm^3 and a proton-ordered structure.

The most plausible structure, which accounts for all features in the experimental pattern, was found in the $P2_1/c$ space group and has the lattice parameters $a = 5.487(3)$ Å, $b = 19.068(4)$ Å, $c = 5.989(3)$ Å, and $\beta = 99.537(16)$ deg. DFT calculations revealed a high formation enthalpy relative to other ammonia monohydrate phases, which could indicate its metastability. Another possible explanation for this energy difference could be that the assumption of an ordered structure is wrong. A disordered structure could also explain the U_{iso} parameters obtained in the Rietveld refinement. However, the data quality, due to the nature of the broad and heavily overlapping reflections, was not sufficient to test disordered structures. Therefore, a proton-disordered or disordered molecular alloy variant of the structure cannot be ruled out. Finally, it is possible that too high a symmetry for the cell was chosen; this includes the possibility of a triclinic unit cell, which was not investigated based on the same data-quality reasoning as above.

To address the above-mentioned concerns in the future, an X-ray diffraction study would prove helpful. First and foremost, a diffraction pattern with less information, i.e. without information on the hydrogen positions, would simplify the search for a suitable unit cell and a structure based on X-ray data would not be affected by any hydrogen disorder.

Author Contributions: B.M. analysed the data and wrote the first draft of the manuscript. J.S.L., V.N.R. and C.G.P. carried out the experiment and J.S.L. and A.H. edited the text. B.M., L.J.C. and A.H. performed the calculations. All authors have read and agreed to the published version of the manuscript.

Funding: Computing resources provided by the UK national high-performance computing service, ARCHER2, which is partially funded by EPSRC (EP/P020194), and for which access was obtained via the UKCP consortium funded by EPSRC grant no. EP/P022561/1 and project d56 "Planetary Interiors", are gratefully acknowledged. LJC acknowledges studentship funding from EPSRC under grant no. EP/L015110/1.

Institutional Review Board Statement: Not applicable.

Informed Consent Statement: Not applicable.

Data Availability Statement: Data was obtained at ISIS neutron source. The data presented in this study are available on request from the corresponding author.

Acknowledgments: We would like to thank Craig Bull (ISIS Facility) for his technical assistance with the experiments and the Science, Technology and Facilities Research Council for offering access to ISIS through the allocation of beamtime.

Conflicts of Interest: The authors declare no conflict of interest.

References

1. Berg, J.M.; Tymoczko, J.L.; Stryer, L. *Biochemistry*, 5th ed.; W. H. Freeman: Oxford, NY, USA, 2002.
2. Loveday, J.S.; Nelmes, R.J. The ammonia hydrates-Model mixed-hydrogen-bonded systems. *High Press. Res.* **2004**, *24*, 45–55. doi:10.1080/08957950410001661990.
3. Lewis, J.S.; Prinn, R.G. Kinetic inhibition of CO and N_2 reduction in the solar nebula. *Astrophys. J.* **1980**, *238*, 357. doi:10.1086/157992.
4. Prinn, R.G.; Fegley, B. Kinetic inhibition of CO and N_2 reduction in circumplanetary nebulae-Implications for satellite composition. *Astrophys. J.* **1981**, *249*, 308. doi:10.1086/159289.
5. Lunine, J.I.; Stevenson, D.J. Clathrate and ammonia hydrates at high pressure: Application to the origin of methane on Titan. *Icarus* **1987**, *70*, 61–77. doi:10.1016/0019-1035(87)90075-3.
6. Cynn, H.C.; Boone, S.; Stevensons, D.J. *Proceedings of the 19th Lunar and Planetary Science Conference*; Cambridge University Press/Lunar and Planetary Institute: Cambridge, UK, 1989; Volume 1, p. 433.
7. Hubbard, H.B.; MacFarlane, J.J. Structure and evolution of Uranus and Neptune. *J. Geophys. Res. Solid Earth* **1980**, *85*, 225–234. doi:doi.org/10.1029/jb085ib01p00225.
8. Young, L.A.; Stern, S.A.; Weaver, H.; Bagenal, F.; Binzel, R.P.; Buratti, B.; Cheng, A.F.; Cruikshank, D.; Gladstone, G.R.; Grundy, W.M.; et al. New Horizons: Anticipated Scientific Investigations at the Pluto System. *Space Sci. Rev.* **2008**, *140*, 93–127.
9. Sekine, Y.; Genda, H.; Sugita, S.; Kadono, T.; Matsui, T. Replacement and late formation of atmospheric N_2 on undifferentiated Titan by impacts. *Nat. Geosci.* **2011**, *4*, 359–362.
10. Noack, L.; Snellen, I.; Rauer, H. Water in Extrasolar Planets and Implications for Habitability. *Space Sci. Rev.* **2017**, *212*, 877–898.
11. Mousis, O.; Gautier, D.; Coustenis, A. The D/H ratio in methane in Titan: Origin and history. *Icarus* **2002**, *159*, 156–165. doi:10.1006/icar.2002.6930.
12. Koumvakalis, A. High Pressure Study of Ammonia Monohydrate. Ph.D. Thesis, University of California, Los Angeles, CA, USA, 1988.
13. Loveday, J.S.; Nelmes, R.J. Ammonia monohydrate VI: A hydrogen-bonded molecular alloy. *Phys. Rev. Lett.* **1999**, *83*, 4329–4332. doi:10.1103/PhysRevLett.83.4329.
14. Nelmes, R.J.; Loveday, J.S. *ISIS Experimental Report RB9859*; CCLRC Rutherford Appleton Laboratory: Chilton, WI, USA, 1998.
15. Fortes, A.D.; Suard, E.; Lemee-Cailleau, M.H.; Pickard, C.J.; Needs, R. Crystal Structure of Ammonia Monohydrate Phase II. *JACS* **2009**, *131*, 13508–13515. doi:10.1021/ja9052569.
16. Loveday, J.S.; Nelmes, R.J.; Guthrie, M.; Belmonte, S.A.; Allan, D.R.; Klug, D.D.; Tse, J.S.; Handa, Y.P. Stable methane hydrate above 2 GPa and the source of Titan's atmospheric methane. *Nature* **2001**, *410*, 661–663. doi:10.1038/35070513.
17. Fortes, A.D.; Wood, I.G.; Alfredsson, M.; Vocadlo, L.; Knight, K.S.; Marshall, W.G.; Tucker, M.G.; Fernandez-Alonso, F. The high-pressure phase diagram of ammonia dihydrate. *High Press. Res.* **2007**, *27*, 201–212. doi:10.1080/08957950701265029.
18. Wilson, C.W.; Bull, C.L.; Stinton, G.W.; Amos, D.M.; Donnelly, M.E.; Loveday, J.S. On the stability of the disordered molecular alloy phase of ammonia hemihydrate. *J. Chem. Phys.* **2015**, *142*, 094707. doi:10.1063/1.4913684.
19. Griffiths, G.I.G.; Fortes, A.D.; Pickard, C.J.; Needs, R.J. Crystal structure of ammonia dihydrate II. *J. Chem. Phys.* **2012**, *136*, 174512.
20. Dunaeva, A.N.; Antsyshkin, D.V.; Kuskov, O.L. Phase diagram of H_2O: Thermodynamic functions of the phase transitions of high-pressure ices. *Sol. Syst. Res.* **2010**, *44*, 202–222. doi:10.1134/S0038094610030044.
21. Besson, J.M.; Nelmes, R.J.; Hamel, G.; Loveday, J.S.; Weill, G.; Hulld, S. Neutron powder diffraction above 10 GPa. *Phys. B Condens. Matter* **1992**, *180*, 907–910. doi.org/10.1016/0921-4526(92)90505-M.
22. Bull, C.L.; Funnell, N.P.; Tucker, M.G.; Hull, S.; Francis, D.J.; Marshall, W.G. PEARL: The high pressure neutron powder diffractometer at ISIS. *High Press. Res.* **2016**, *36*, 493–511. doi:10.1080/08957959.2016.1214730.
23. Toby, B.H.; Dreele, R.B.V. GSAS-II: The genesis of a modern open-source all purpose crystallography software package. *J. Appl. Crystallogr.* **2013**, *46*, 544–549.
24. Clark, S.J.; Segall, M.D.; Pickard, C.J.; Hasnip, P.J.; Probert, M.I.J. .; Refson, K.; Payne, M.C. First principles methods using CASTEP. *Z. Fuer Krist.* **2005**, *220*, 567–570.
25. Perdew, J.P.; Burke, K.; Ernzerhof, M. Generalized gradient approximation made simple. *Phys. Rev. Lett.* **1996**, *77*, 3865–3868, doi:10.1103/PhysRevLett.77.3865.
26. Monkhorst, H.J.; Pack, J.D. Special points for Brillouin-zone integrations. *Phys. Rev. B* **1976**, *13*, 5188–5192.
27. Wilson, C.W.; Bull, C.L.; Stinton, G.; Loveday, J.S. Pressure-induced dehydration and the structure of ammonia hemihydrate-II. *J. Chem. Phys.* **2012**, *136*, 094506. doi:10.1063/1.3686870.

28. Lebail, A. Whole Powder Pattern Decomposition Methods and Applications: A Retrospection. *Powder Diffr.* **2005**, *20*, 316. doi:doi:10.1154/1.2135315.
29. Khachaturyan, A.; Semenovskaya, S. Statistical-Thermodynamic Approach to Determination of Structure Amplitude Phases. *Sov. Phys. Crystallogr.* **1979**, *24*, 519–524.
30. Khachaturyan, A.; Semenovskaya, S. The Thermodynamic Approach to the Structure Analysis of Crystals. *Acta Crystallogr.* **1981**, *A37*, 742–754. doi:doi:10.1107/S0567739481001630.
31. Metropolis, N.; Rosenbluth, A.; Rosenbluth, M.; Teller, A.; Teller, E. Equation of State Calculations by Fast Computing Machines. *J. Chem. Phys.* **1953**, *21*, 1087–1092. doi:doi:10.1063/1.1699114.
32. Fortes, A.D.; Wood, I.G.; Vocadlo, L.; Knight, K.S.; Marshall, W.G.; Tucker, M.G.; Fernandez-Alonso, F. Phase behaviour and thermoelastic properties of perdeuterated ammonia hydrate and ice polymorphs from 0 to 2 GPa. *J. Appl. Crystallogr.* **2009**, *42*, 846–866. doi:10.1107/S0021889809027897.
33. Payne, M.C.; Teter, M.P.; Allan, D.C.; Arias, T.; Joannopoulos, J.D. Iterative minimization techniques for ab initio total-energy calculations-molecular-dynamics and conjugate gradients. *Rev. Mod. Phys.* **1992**, *64*, 1045–1097.
34. Griffiths, G.I.G.; Misquitta, A.J.; Fortes, A.D.; Pickard, C.J.; Needs, R. High pressure ionic and molecular crystals of ammonia monohydrate within density functional theory. *J. Chem. Phys.* **2012**, *137*, 064506. doi:10.1063/1.4737887.
35. Robinson, V.; Wang, Y.; Ma, Y.; Hermann, A. Stabilization of ammonia-rich hydrate inside icy planets. *Proc. Natl. Acad. Sci. USA* **2017**, *114*, 9003–9008. doi:10.1073/pnas.1706244114.